Phase Behaviour Studies Related To Biodiesel Production Using Supercritical Methanol

Sultan Said Abdallah Al-Habsi

A thesis submitted in partial fulfilment of the requirements for the degree of Doctor of Philosophy and the Diploma of Imperial College London

Department of Chemical Engineering
Imperial College London
London SW7 2AZ, United Kingdom

March 2019

Originality Declaration

I herewith certify that all material in this dissertation which is not my own work has been properly acknowledged.

Sultan Said Abdallah Al-Habsi

Copyright Declaration

Dedicated to my wife and kids

Acknowledgments

This work would never have been completed without the contribution of amazing individuals. First and foremost, I would like to express my sincerest gratitude to my supervisor Professor J P Martin Trusler for his excellent guidance, great support, and patience through the long journey of this research. I will always be thankful for his invaluable advice, encouragement and commitment, which made everything easier. My deepest gratitude are also extended to the first man I met at Imperial who is my co-supervisor Dr. Saif Al-Ghafri. Your dedicated guidance, experience, priceless vision have always inspired me. It was a great honour to be working with you.

I would also like to extend my special gratitude to all the wonderful friends and colleagues whom I have met through these four years at Imperial. I can never thank enough Lorena Souza, Benaiah Anabaraonye, Claudio Calabrese, Hao Bian, Theodor Videnberg, Florence Chow, Malami Mohammed, Rayane Hoballah, Chidi Efika, Mihaela Stevar, Chidi Efika, Ines da Graca, Geraldine Ollarves, Caroline Jones, Malyanah Binti Mohammed Taib and Humera Ansari for the support I received from you, sincere friendship, joy and making my PhD journey unforgettable and enjoyable.

Special thanks go to the electrical and mechanical workshop staff, mainly Chin Lang, Gavin Barnes and Richard Wallington for the support and help they provided during these years.

Last but not least, it is always hard for me when it comes to expressing my gratitude to my beloved wife and family. Words are so limited but all what I can say to you is that I am extremely grateful for all the support, care, deep love and understanding you showed through the good and hard times. Your best wishes, truthful prayers and inspiring letters have considerably provided me the strength and encouraged me to move forward.

Sultan Al Habsi

March 2019

Abstract

Biodiesel is a promising renewable and sustainable fuel that can replace fossil fuels. Among the different techniques used to produce biodiesel, the transesterification process is currently the preferred method. The conventional transesterification process is based on acid-base catalysis, but this technique has many drawbacks including a requirement for high-purity feedstocks, and costly pre-treatment and downstream processes. A recent alternative process, using a supercritical alcohol (preferably methanol) without a catalyst, may offer some advantages. This process can utilise a wide range of potential feedstocks (especially wastes), shows high production efficiency, and requires only simple post-processing. However, this technique requires conditions of high temperature and high pressure which increase the utility costs and may restrict the economic feasibility and sustainability of the process. In order to fully explore these issues and to optimise the process conditions, better understanding of the phase behaviour of the mixtures involved in the biodiesel process is required. The components of interest include fatty acids, esters alcohols and co-solvent such as carbon dioxide and the conditions include high pressures and wide ranges of temperature. Phase equilibrium studies on systems relevant to biodiesel production with supercritical methanol available in the literature are very limited. The principal focus of this project is the experimental investigation of the phase behaviour of representative mixtures with small molecular chains, which exist during biodiesel production, over wide ranges of temperatures and pressures. In addition to the experimental work, the research will include both modelling works on the mixtures of interest supported by a simulation for the process using gPROMS, a simulation tool developed by Process Systems Enterprise (PSE) company.

In this project, new fluid-phase equilibrium measurements have been carried out on two relevant representative binary systems: (methyl propanoate + carbon dioxide) and (butanoic acid + carbon dioxide) using a high-pressure quasi-static analytical apparatus with compositional analysis using a gas chromatography. The measurements for the (methyl propanoate + carbon dioxide) mixture were made along six isotherms at temperatures from (298.15 to 423.15) K and at pressures up to near the mixture critical pressure at each temperature while for the mixture (butanoic acid + carbon dioxide) the measurements were made along eight isotherms at temperatures from (323.13 to 423.2) K and pressures up to the mixture critical pressures. Vapour-liquid equilibrium (VLE) data obtained for the mixtures have been compared with the predictions of SAFT-γ Mie model, a group-contribution version of the Statistical Associating Fluid Theory (SAFT). The group interaction parameters in SAFT-γ Mie reported in literature have been revised by fitting to the new experimental VLE data. After

parameters optimisation, the model was found to be in a good agreement with the measured VLE data for both bubble and dew points. The experimental data were also compared with the description of Peng Robinson equation of state (PR EoS) combined with the classical one-fluid mixing rules integrating one temperature-independent binary interaction parameter for (methyl propanoate + carbon dioxide) system and two temperature-independent binary interaction parameters for (butanoic acid + carbon dioxide) system. The results after tuning show that the PR EoS can also predict well the system measured data, except in the critical regions in which PR EoS shows overprediction. Furthermore, the phase equilibria of (methyl propanoate + propionic acid + carbon dioxide), (*tert*-butanol + water + carbon dioxide) and (toluene + water + carbon dioxide) ternary systems were studied by the means of the high-pressure quasi-static analytical apparatus. Compositions of present phases coexisting in vapour-liquid equilibrium (VLE) for (methyl propanoate + propionic acid + carbon dioxide) mixture were measured along six isotherms at temperatures from (323.12 to 423.11) K and pressures from (1 to 20) MPa at equal feed molar ratio of (methyl propanoate + propionic acid). Phase behaviour measurements were also collected at different compositions of the mixture (methyl propanoate + propionic acid) at fixed temperatures and pressures. Compositions of coexisting phases of the ternary system (*tert*-butanol + carbon dioxide + water) have been obtained along five isotherms at temperatures of (283.2, 298.18, 323.13, 373.10 and 423.17) K and at pressures of (4.0, 8.0, 12.0 and 18.0) MPa with different known feed compositions of (*tert*-butanol + water) while the phase behaviour of the system (toluene + water + carbon dioxide) was investigated along four isotherms at temperatures from (338.15 to 413.15) K and pressures up to the upper critical end point (UCEP). The data obtained for the ternary mixtures have been compared with the descriptions of SAFT-γ Mie and PR equation of states.

Other cross interactions available in biodiesel systems such as (COOH - CH_3OH), (OH_GI - CH_3OH), (CO_2 - CH=), (CH_3OH - CH=), (COOH - CH=) and (H_2O - CH=) were estimated in this work by regression to fluid-phase behaviour data published in literature. The comparison between the predictions of SAFT-γ Mie reported in literature and those of SAFT-γ Mie after refining the parameters were shown. Preliminary designs of one-step process (transesterification) and two-step processes (hydrolysis and esterification) for biodiesel production under supercritical conditions were suggested and simulated using gPROMS ProcessBuilder software. The CO_2 co-solvent effect on the one-step process based on literature data was also examined by a process flowsheet.

The research including new phase behavior measurements, modelling and gPROMS simulation is expected to contribute to optimisation of biodiesel production processes.

Table of Contents

List of Publications

i. Sultan S. A. Al Habsi, Saif ZS. Al Ghafri and J. P. Martin Trusler - Experimental and Modeling Study of the Phase Behavior of (Butanoic Acid + Carbon Dioxide) at Temperatures Between (323.15 and 423.15) K and Pressures up to 20 MPa (In Preparation).

ii. Sultan S. A. Al Habsi, Saif ZS. Al Ghafri, Bamagain, Rami and J. P. Martin Trusler - Experimental and Modeling Study of the Phase Behavior of (Methyl Propanoate + Carbon Dioxide) at Temperatures Between (298.15 and 423.15) K and Pressures up to 20 MPa (In Preparation).

iii. Sultan S. A. Al Habsi, Kirsten Grübel, Saif ZS. Al Ghafri and J. P. Martin Trusler - Experimental and Modeling Study of the Phase Behavior of (*Tert*-butanol + Water + Carbon Dioxide) Mixture at Temperatures Between (283.2 to 423.17) K and Pressures of (4 - 18) MPa (In Preparation).

iv. Sultan S. A. Al Habsi, Saif ZS. Al Ghafri and J. P. Martin Trusler - Experimental and Modeling Study of the Phase Behavior of (Toluene + Water + Carbon Dioxide) Mixture at Temperatures From (338.15 to 413.15) K and pressures up to the UCEP (In Preparation).

v. Sultan S. A. Al Habsi, Saif ZS. Al Ghafri and J. P. Martin Trusler - Experimental and Modeling Study of the Phase Behavior of (Methyl Propanoate + Propionic Acid + Carbon Dioxide) Mixture at Temperatures From (323.12 to 423.11) K and Pressures From (1 to 20) MPa (In Preparation).

List of Figures

List of Tables

Chapter 1: Introduction

1.1 Energy Consumption and CO_2 Emissions

According to the International Energy Agency (IEA) estimates, the demand of global energy grew by 2.1% in 2017 (more than twice the growth rate in 2016) with fossil fuels accounting for 81% of total energy demand [1]. The trends show that global energy-related CO_2 emissions increased by 1.6% in 2017, reaching a significant high record of 32.6 gigatonnes (Gt). The increase was the outcome of weak efforts in global energy efficiency as well as strong global economic growth of 3.7% driving the rise in energy demand. As per current and planned policies, including the Nationally Determined Contributions (NDCs) under the Paris Agreement, energy-related CO_2 emissions are expected to steadily increase to 34.6 Gt by 2030 and to continue increasing afterwards. In order to be on track with the Paris Agreement and reach long-term climate mitigation targets, the IEA's Sustainable Development Scenario (SDS) shows that by 2040 annual CO_2 emissions are required to decrease by 46% below the current levels.

Rapid growth in the world population, global energy demand, and carbon dioxide (CO_2) and greenhouse gases emissions associated with the use of fossil fuels have driven the search for alternative energy sources that are renewable, sustainable and have a lower environmental impact [2]. Among the various alternative renewable energy sources, bioenergy derived from biofuels will play a key role in fulfilling the world's future energy demands [3, 4].

Biofuels are fuels produced directly or indirectly from biomass [5]. They exist in liquid (e.g. bioethanol and biodiesel), solid (e.g. wood chips and pellets) and gaseous (e.g. biogas and syngas) forms [6]. Production of conventional biofuels for transport, which include starch- and sugar-based ethanol, and hydrotreated vegetable oil and oil-crop biodiesel, increased just 2% to reach 81 million tonnes of oil equivalent (Mtoe) in 2017, with average production growth of around 3% a year expected over the next five years as shown in Figure 1.1 [7]. Transport biofuel consumption, on the other hand, needs to triple by 2030 in order for biofuels' share of transport fuel global demand to reach 10% by 2030 as required by the SDS [7]. The biofuels required here are the sustainable fuels produced from non-food crop feedstocks, which do not directly compete with food crops for agricultural land or cause sustainability impacts. A set of biofuels sustainability standards and requirements has been also defined by the European Union's Renewables Directive 2009/28/EC [8], which mandate levels of use of renewable energy within the European Union, for all biofuels (used in transport) and bioliquids and biomass fuels (used for heating and power) produced or consumed in the EU to make sure that they are produced in a sustainable and environmentally friendly manner. Only biofuels

that comply with the standards can count towards national renewable energy targets or get governmental support. The criteria is summarised in Table 1.1.

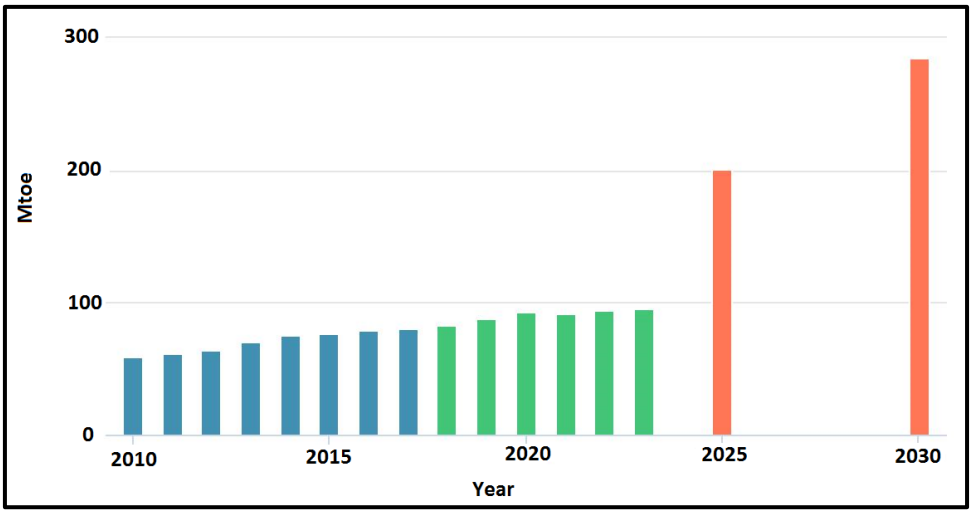

Figure 1.1: Historical and forecasts of global biofuel production versus SDS targets [7]. Blue, green and orange columns represent historical, forecast and SDS targets, respectively.

Table 1.1: European Union's Renewables Directive sustainability criteria [8, 9].

Sustainability Criteria		Requirements
1	Greenhouse gas savings	Biofuels must achieve greenhouse gas (GHG) savings of at least 35% in comparison to fossil fuels. This requirement rises to 50% in 2017 and to 60% in 2018 but only for new production plants. All life cycle emissions (including cultivation, processing and transport) are considered when calculating greenhouse gas savings.
2	Carbon stock	Biofuels are not grown in areas converted from lands with previously high carbon stock such as wetlands or forests.
3	Biodiversity	Biofuels are not produced from raw materials obtained from lands with high biodiversity such as primary forests or highly biodiverse grasslands.

Biofuels are classified in three main categories known as first, second and third generation biofuels. These classifications depend on the feedstocks and conversion technologies used for the production [10]. The first generation biofuels are produced directly from food crops that contain sugar, oil and starch such as wheat, corn and soybeans. The second generation biofuels are those derived from non-food feedstock, which are lignocellulosic materials such

as agricultural and forest residues, jatropha, and perennial grasses, and organic and industrial solid wastes. The third generation biofuels are produced from microalgae [11].

The production of the first generation biofuels is commercial worldwide with technologies and markets, but this generates significant social, environmental and economic impacts on soil, water, land, food security, and civil development [12]. Much research [2, 6, 13-15] addressed the challenges of sustainable availability of feedstocks for biofuel production and highlighted the food-versus-fuel debate and conflicts. The high demand for water and food keeps on growing with the world's growth population [12]. As a result, food prices and costs of source materials have been increased significantly. Under the pressure of these challenges, the second-generation biofuels are expected to be the major player in the transition to environmentally friendly and sustainable source of energy.

1.2 Biodiesel

Biodiesel is one of the renewable resources of energy that can be a clean alternative for fossil fuels. It is expected to be the largest contribution to renewable liquid fuels. Biodiesel is biodegradable, non-toxic, essentially free of sulphur, and can be produced from a variety of low-value raw materials [16, 17]. Emissions from engines using biodiesel were found to be having less CO, SO_x, and unburned hydrocarbons. Biodiesel can also be used directly in normal diesel engines without modification, so it is a good alternative for fuels [18-20].

1.2.1 Biodiesel Feedstocks and Production

Biodiesel is made from renewable sources and feedstocks such as vegetable oils and animal fats [21]. The waste vegetable oils and animal fats are also potential sources for biodiesel production [22, 23]. Due to its high viscosity, water and free fatty acid content, and low energy content the vegetable oils are generally impractical and not suitable for both direct use and indirect-type diesel engines [21, 24]. Currently, there are four major methods and processes to produce biodiesel which are: pyrolysis, microemulsification, catalytic cracking and transesterification. The reader may refer to a review conducted by Hajar et al. [25] for these production processes. Transesterification of natural glycerides is considered currently as the most common method for biodiesel production. In this process, triglycerides, which are the main components of the plant oils and animal fats, and alcohol such as methanol or ethanol react with each other in the presence of catalyst to form esters (biodiesel). Esters can be Fatty Acid Methyl Ester (FAME) or Fatty Acid Ethyl Ester (FAEE) depending on the alcohol type. The physical properties of the produced biodiesel is so similar to the existing conventional fossil fuel diesel [26]. Glycerol is released from the reaction as a by-product which can be also a valuable in some productions such as hydrogen production.

Triglycerides are made up of three fatty acids connected together by one glycerol [27] as shown in Figure 1.2 which illustrates the structure of triolein, one of the key components in feedstocks. The fatty acids can be classified as saturated fatty acids containing carbon-carbon single bonds and unsaturated acids having one or more carbon-carbon double bond (C=C). They vary in the length of the carbon chain and in the number of unsaturated bonds. The different types and compositions of the fatty acids attached to triglycerides determine degree of saturation/unsaturation and the molecular structure of the feedstocks, and hence they influence quality, costs and both physical and chemical properties of the oils [4, 28].

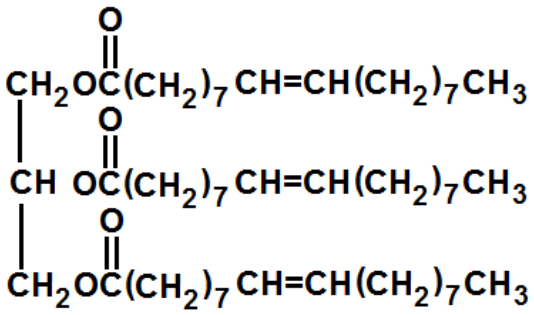

Figure 1.2: Chemical structure of triolein which is derived from glycerol and three units of oleic acid (unsaturated fatty acid).

Much research have been conducted on some edible and non-edible vegetable oils in terms of biodiesel yields and reactions rates via transesterification method [18, 24, 29-34]**.** There are more than 350 oil bearing crops in the world identified as potential sources for biodiesel production [28]. About 26 non-traditional seed oils in India itself were studied and found suitable for biodiesel production and they meet USA, Germany and Europe biodiesel specification standards [35]. Currently, more than 95% of the global biodiesel is produced from edible oil crops such as rapeseed (84%), sunflower oil (13%), palm oil (1%), soybean oil and others (2%) [28, 36, 37]. The dominant fatty acids in the edible and non-edible oils are oleic acid and linoleic acid (unsaturated fatty acids) and palmitic acid and staeric acid (saturated fatty acids). Table 1.2 shows the average compositions of these fatty acids in oils [38-40]. Other fatty acids including myristic acid (C14:0), palmioleic acid (C16:1), stearic acid (C18:0), linolenic acid (C18:3) and arachidic acid (C20:0) are found in very small quantities in the oils, hence their compositions are not included in the table.

Table 1.2: Fatty acids percentages in different feedstocks [38-40].

Source	Saturated fatty acids (wt%)			Unsaturated fatty acids (wt%)	
Acid name	Lauric acid	Myristic acid	Palmitic acid	Oleic acid	Linoleic acid
Lipid numbers (C:D)[a]	12:0	14:0	16:0	18:1	18:2
		Edible			
Canola		0.1	3.8	7.5	**74.0**
Corn (USA)			10.3	**62.4**	20.1
Corn (Brazil)			10.5	25.5	**59.3**
Sun flower (Brazil)		0.1	5.7	24.2	**60.4**
Cottonseed		0.8	21.9	16.9	**70.7**
Soybean (Brazil)		0.1	9.9	21.4	**56.0**
Extra Virgin Olive			8.7	**76.3**	8.6
Peanut		0.0	9.4	**48.7**	31.1
Rice Bran (Brazil)		0.2	16.9	**40.5**	36.2
Palm		1.1	**42.7**	**39.4**	10.6
Coconut	**45.5**	18.8	10.1	7.5	1.8
		Non-edible			
Jatropha		0.0	15.2	**44.6**	32.2
Moringa		0.0	7.6	**66.6**	8.1
Neem		0.3	14.9	**43.9**	17.9
Tobaco		0.1	8.5	11.2	75.6

[a]Notation: C and D in lipid numbers stand for the number of carbons and the number of the double bonds, respectively.

1.2.2 Biodiesel Standards and Properties

Currently, biodiesel and bioethanol are the only primary biofuels that can be applied for combustion engines. Biodiesel has been tested and recommended for heavy duty engines and machines as alternative for petroleum diesel [12]. In order to support the growing use of alkyl esters-based biodiesel and its blends as fuels suitable for automotive, and to run diesel engines and appliances efficiently and safely specifications and standards have been developed and are required to be met. ASTM International (formerly American Society for Testing and Materials) D6751 standard (adopted in USA) and EN 14214 (adopted in Europe) standard establish specifications for key fuel properties for biodiesel. Both standards are the international basis for biodiesel specifications and regulations developed in the other countries in the world. The ASTM D6751 standard defines biodiesel as mono-alkyl esters of

long chain fatty acids, and the type of alcohol is not specified. The specifications of this standard are intended for B100[1] biodiesel or use as a blend component with middle distillate fuels. The standard specifications in Europe, EN 14214, applies only to mono-alkyl esters made with methanol, fatty acid methyl esters (FAME). So, biodiesel produced using different alcohols (e.g. ethanol) are not covered. The minimum ester content is specified at 96.5% by mass. The most important fuel properties include density, viscosity, flash point, ester content, acid value, moisture content and oxidation stability. The biodiesel specifications according to ASTM D6751 and EN 14214 are compared with those of conventional petroleum diesel in Table 1.3.

[1] The 100 in the abbreviation B100 refers to the volume percentage of biodiesel in the blend. B100 is pure biodiesel.

Table 1.3: US and EU Specifications of biodiesel properties [41, 42].

Specification	Units	Biodiesel		Petroleum Diesel
		EN 14214:2012	ASTM D6751-18	(EN 590:2004)
Flash point, min[a]	K	374	366	328
Sulphur, max	mg/kg	10	Two grades:[b] (S15) 15 ppm (S500) 0.05%	350
Sulphated ash, max	%wt	0.02	0.02	
Water, max	mg/kg	500		200
Water & sediment, max	%vol		0.050	
Total contamination, max	mg/kg	24		24
Density (288.15 K)	g/cm^3	0.86-0.90		0.82-0.845
Kinematic Viscosity (313.15 K)	mm^2/s	3.5-5.0	1.9-6.0	2.0-4.5
Distillation temperature	%vol recovered		90%: 633 K max	
Cu corrosion, max	3 h/ 323.15K	1	3	1
Oxidation stability		8 hrs min	3 hrs min	25 (g/m^3) max
Cetane number, min		51	47	51
Acid value	mgKOH /g	0.5 max	0.5 max	
Alcohol control		0.20% wt MeOH max, or 403 K flash point, min	0.20% wt MeOH max	
Ester content, min	%wt	96.5		
Monoglycerides, max	%wt	0.7	0.4	
Diglycerides, max	%wt	0.2		
Triglycerides, max	%wt	0.2		
Free glycerol, max	%wt	0.02	0.02	
Total glycerol, max	%wt	0.25	0.24	
Iodine value, max	g Iod/100 g	120		
Linolenic acid ME, max	%wt	12		
Polyunsaturated ME, max	%wt	1		
Phosphorous, max		4.0 mg/kg	0.001% wt	

[a]Notation: Min and max refer to minimum and maximum, respectively.
[b]Notation: Grade S15 and S500 refer to maximum allowance sulphur content.

1.3 Research Motivation

The current conventional transesterification process is based on acid-base catalysts. Commonly used catalysts for the process are potassium hydroxide and sodium hydroxide. The main factors that transesterification depends on are reaction temperature and pressure, reaction time, molar ratio of glyecrides to alcohol, free fatty acid (FFA) content, water content in the feedstock, and catalysts [21]. There are several drawbacks of the catalytic transesterification such as it required high purity feedstocks and hence costly additional downstream treatment steps are required. Water has to be removed as it can cause hydrolysis of triglycerides to diglycerides and monoglycerides producing fatty acid salts instead of biodiesel. Free fatty acids can also have a negative effect on the process [43].

In 2001, Saka and Kusdiana [29] first proposed a biodiesel production technique using supercritical methanol at temperatures and pressures at or above the critical values of 512 K and 8.1 MPa, respectively. This method does not require any catalysts (so called non-catalytic transesterification) and does not generate significant waste. Pre-treatment of feedstocks (e.g. removing moisture and free fatty acids as in the conventional process) is not required. The supercritical technique is a very promising approach with several key advantages compared to the conventional process, including simple post treatments for the product, no catalyst involved, exhibiting high production efficiency as FFAs and H_2O have positive effect on the process, using so many different potential feedstocks including wastes; however, the conditions are harsh, requiring temperature of 623 K to 673 K and pressure above 20 MPa. Such conditions constrain the economics of this process and, therefore, more experiments and studies are still required to optimise the method.

The study of the fluid-phase behaviour of the mixtures of components involved in biodiesel production including esters, fatty acids, alcohols, and co-solvents (e.g. CO_2) at conditions of high pressure and temperature is required in order to explore the scope for optimisation in the process conditions. The SAFT-γ Mie group contribution approach was reported to calculate accurately both fluid-phase behaviour and second-order derivatives of free energy, such as speed of sound, compressibility, and the heat capacity, of pure components and mixtures [44], hence, it is used in our project to simulate the biodiesel production process.

1.4 Research Scope and Objectives

Experimental and modelling research on the phase equilibria of methanol and reactants (triglyceride), intermediates (diglyceride and monoglyceride) and products (biodiesel and glycerol) play a key role in optimising this process. Reliable experimental data and a robust *Thermodynamic and Kinetic Modelling Framework (TKMF)* are required to optimise and

improve the supercritical technique process. Building a TKMF for the biodiesel process faces several *simultaneous challenges* as follows:

- A few studies on this new technique are reported in the literature, but these research studies, due to the lack of experimental data, still cannot provide sufficient fundamental information that can be used for engineering design and retrofit, hence the predications of existing thermodynamic models cannot be fully reliable. There exists no single thermodynamic model that can describe the entire production process Moreover, there are no complete kinetic studies conducted in the supercritical biodiesel process.
- Reliable pure-component data are of utmost importance as uncertainties in these data have a dramatic influence on the computed phase behaviour. However, for key constituents in biodiesel production (e.g., fatty acids, esters, glycerol) not all required properties can be measured experimentally. The limit of such existing data affects the reliability of the existing models.
- The supercritical process is realized at high temperature and high pressure, and the mixtures involved are highly asymmetric, non-ideal and associating, and hence hard to model.
- To correctly model the phase behaviour observed experimentally in the process (i.e. how the phases in the system change when the mixture is heated) methods for thermodynamic analysis are required for multicomponent reacting systems.

This project aims to develop a thermodynamic and kinetic modelling framework (TKMF) for simulation of innovative biofuel production processes with the aid of experimental work focusing mainly on phase behaviours. The research will include both experimental and modelling works on the supercritical process supported by a simulation for the process using gPROMS. To realise the goals of the project and to address some of the challenges existing in biodiesel production processes, the following overall objectives were tackled during this research:

1. Collection and evaluation of existing experimental phase behaviour data and kinetic data with detailed analysis of their uncertainties.
2. Experimental phase behaviour measurements on representative mixtures with minimum molecular chains (that exist during biodiesel production) required to obtain the functional groups parameters for SAFT-γ Mie.
3. Deployment of a SAFT-γ Mie group contribution approach for estimation and prediction of thermophysical properties of compounds used in biofuel production. This will include determining group interaction parameters that are presently unknown.

4. Use of Peng Robinson EoS model for prediction of fluid-phase behaviour data measured in this work. This is mainly to have a comparison between the prediction of SAFT-γ Mie model and that of PR model.
5. Develop a kinetic model that best fits the available data. This model together with the developed SAFT-γ Mie model will be used later in a process simulation.
6. Evaluation of the performance of the TKMF in a complete process flow diagram (PFD) simulation of biodiesel production with supercritical methanol. This will be realised in the gPROMS modelling platform.

1.5 Thesis Outline

This thesis continues in Chapter 2 with the literature and theoretical background on fluid phase equilibria and chemical kinetics followed in Chapter 3 by a review on the theory and modelling approaches relevant to the present work. A description of the analytical equipment used to carry out experiments in this work, calibration methods and validations are outlined in Chapter 4. The experimental measurements of the phase behavior of binary systems are presented and discussed in detail in Chapter 5 while the details of the ternary systems are given in Chapter 6. The results are compared with the predictions of SAFT-γ Mie and Peng Robinson EoS models. Chapter 7 shows the estimation of other the cross interactions for the functional groups required in describing phase behaviour of biodiesel systems. The simulation of the process flow diagram for the supercritical technology using gPROMS software is presented in Chapter 8. The main conclusions of the present work and recommendations for the future work are summarised in Chapter 9.

Chapter 2: Fluid Phase Equilibria and Chemical Kinetics: Literature and Background

In this Chapter, an introduction to fluid phase equilibria of pure components, binary and multiple mixtures is presented. Then, phase behaviour of biodiesel transesterification process reported in literature is given followed by a brief discussion of the experimental methods to measure phase equilibria. Basics of reaction kinetics and the kinetics of biodiesel transesterification reported in literature are then briefly discussed. The effect of co-solvents on the reaction is briefly reviewed in the last section.

2.1 Phase Equilibria and Phase Diagrams

2.1.1 Introduction

Phase behaviour is usually represented graphically by phase diagrams, which show the boundaries between coexisting phases, and the conditions that occur when the pressure and/or temperature is changed to cross these boundaries. At equilibrium, a system may form of a number of coexisting phases. Three conditions need to be met in the system to be at thermodynamic equilibrium [45, 46]:

- The temperature of the phases must be uniform to satisfy the thermal equilibrium.
- The pressure of the phases must be uniform to satisfy the mechanical equilibrium.
- The chemical potentials of each component throughout all the phases are equal. The Gibbs energy must be at a minimum.

The number of independent intensive variables F, also known as degrees of freedom, required to describe and define the state of a system is expressed by the Gibbs phase rule [47]:

$$F = C + 2 - P. \tag{2.1}$$

Here, C is the number of components and P is the number of phases.

2.1.2 Phase Behaviour of Pure Components

The phase behaviour of a pure component can be described by pressure-temperature (p-T) or pressure-volume (p-v) diagrams. The diagrams show the conditions at which vapour, liquid and solid phases can coexist at equilibrium. An example of such phase diagrams is shown in Figure 2.1. The lines AD, BD and CD in Figure 2.1a are the solid-vapour equilibrium line (also known as sublimation line), the solid-liquid equilibrium (also known as melting curve) and the liquid-vapour line (also known as vapour pressure curve), respectively. The intersection of

these lines (at point D) is called triple point where all the three phases of a pure component can coexist at equilibrium. Point C in the diagram is called critical point where the liquid and vapour phases become indistinguishable. Figure 2.1b is a pressure-volume (*p*-*v*) diagram for a pure component. If a pressure of a compressed liquid, at point A, at a constant temperature below the critical temperature is decreased, its volume will increase until the pressure reaches the vapour pressure, point B, which is the system bubble point. The liquid phase keeps changing into vapour phase as a result of the further increase in the volume of the system at constant pressure until it reaches the dew point, point D, where the last liquid drop is vaporized. As can be seen in the figure, the phase envelope is identified by the bubble and dew point curves. The bubble point and dew point curves are formed by the bubble points and dew points of the system measured at different temperatures, respectively. It can be seen also in the figure that the mixture volume is reduced when the temperature of the system approaches the critical point, point C, where the bubble point curve and dew point curve meet. The fluid is called supercritical when the temperature is above the critical temperature.

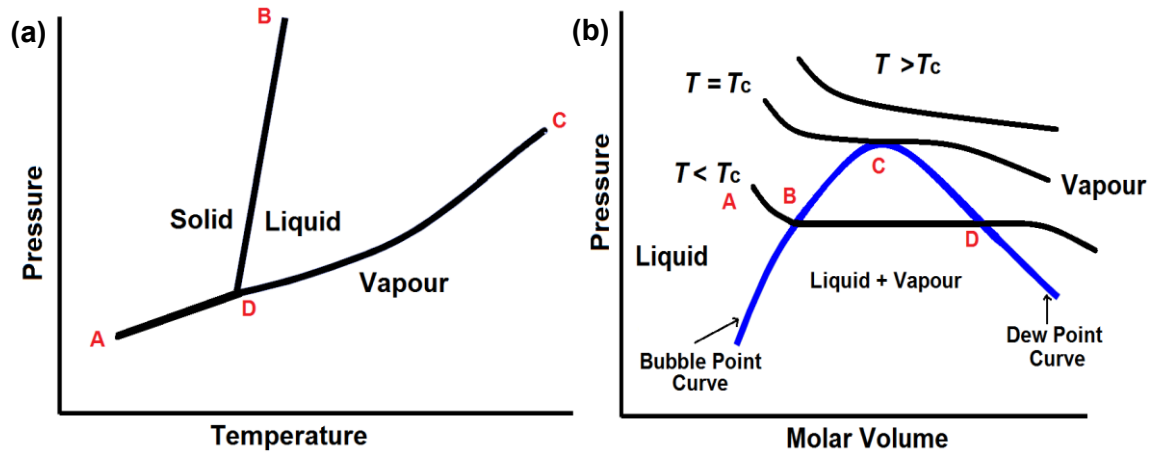

Figure 2.1: Phase diagrams for pure component. (a), *p*-*T* phase envelope; (b), *p*-*v* phase envelope.

2.1.3 Phase Behaviour of Binary Mixtures

In general, the phase behaviour of a mixture of two components (binary system) is more complex than that of a pure component due to the number of degrees of freedom required to describe the system. Pressure, temperature and composition variables are the most convenient experimental variables to describe a binary system. The phase behaviour is commonly represented in (*p, T*), (*p, v*), (*T, x*), and (*p, x*) diagrams. An example of a binary phase diagram is the (*p*, *T*) diagram as shown in Figure 2.2. The diagram shows the conditions at which liquid and vapour phases can coexist at equilibrium. It can be observed in the figure

that the liquid and vapour phases can also coexist above the critical point, C. Point B is the highest pressure and called cricondenbar while point A is the highest temperature and called cricondentherm.

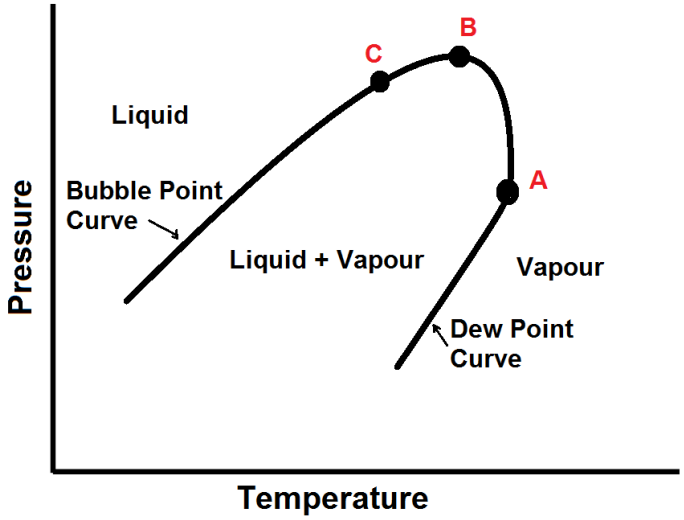

Figure 2.2: *P-T* phase envelope for binary mixture.

According to Van Konynenburg and Scott classification [48, 49], there are six main types of fluid phase behaviour that can be observed experimentally. All these types (expect type VI) can be predicted by an equation of state such as van der Waals EoS. These types are shown in Figure 2.3. The simplest type of phase behaviour is type I, which is typical for binary systems containing compounds with similar molecular size and/or critical properties. The liquid-vapour critical curve is the only critical curve found and it connects the critical point of component one, C_1, with the critical point of component two, C_2. An example of this type is (methane + CO_2) mixture [50]. In type II, the phase diagram presents liquid-liquid separation and limited miscibility at low temperatures due to differences between the two components. In addition to the continuous liquid-vapour critical curve (L=V) there are a liquid-liquid critical curve (L_2=L_1) and a three-phase equilibrium line (L_2L_1V) which intersect at UCEP (Upper Critical End Point). An example of this type is (CO_2 + *n*-alkane shorter than, and up to *n*-dodecane) [51].

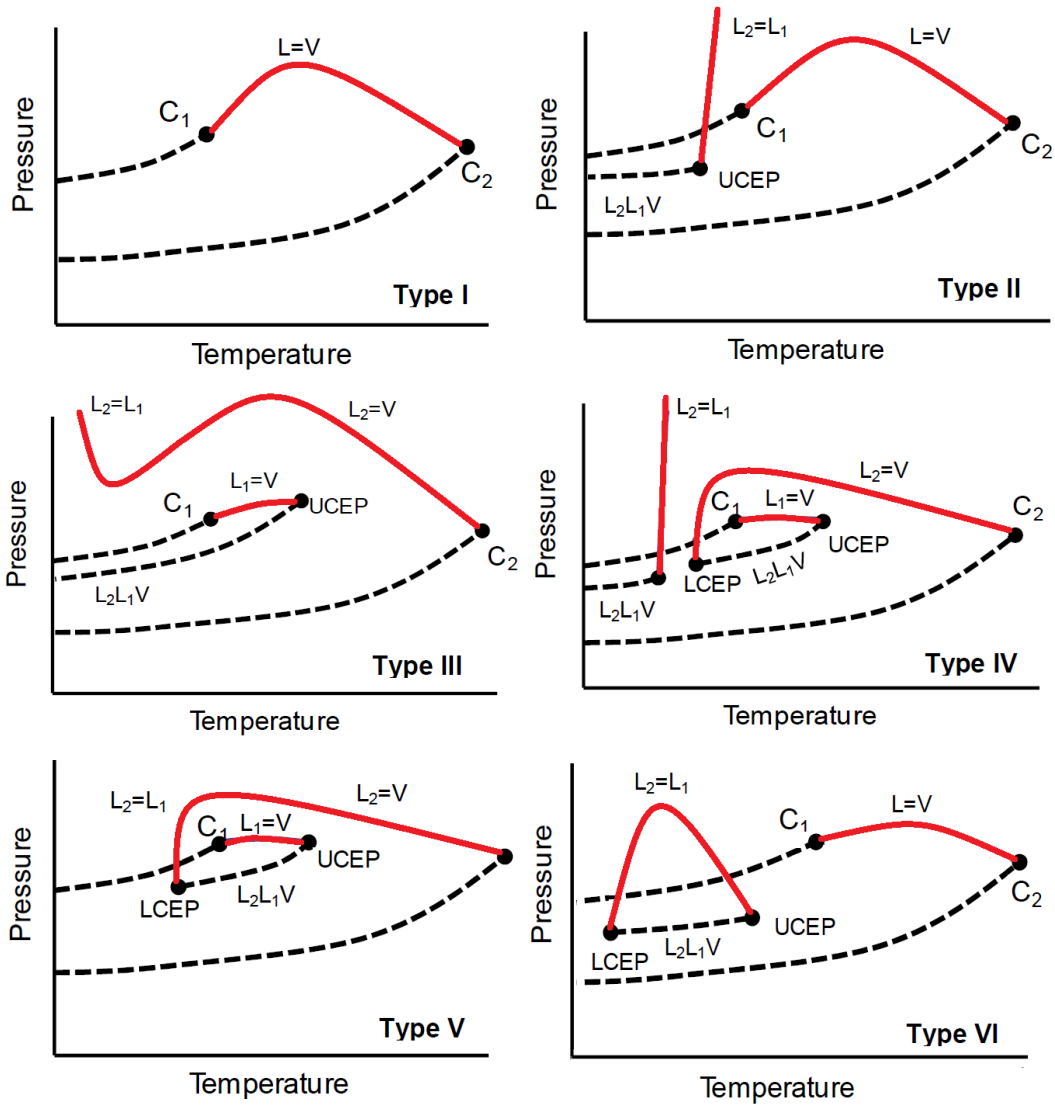

Figure 2.3: (*p*, *T*) projections of phase behaviour diagrams of binary mixture according to Van Konynenburg and Scott classification [48, 49, 52].

In systems with large immiscibility such as mixtures of (water + n-alkane) and (CO_2 + longer *n*-alkanes) [51], as seen in type III, the locus of the liquid-liquid critical line (L_2=L_1) moves to temperature beyond the critical point of the more volatile component, C_1, and merge with the liquid-vapour critical curve (L_2=V). So, the liquid-vapour critical curve has two branches: (L_1=V) line goes from the critical point of the more volatile component, C_1, to the UCEP. The second branch (L_2=V) starts at the critical point of the less volatile component, C_2, and rises with pressure merging into the liquid-liquid critical line (L_2=L_1). In Type IV, the liquid-vapour critical line (L_2=V) starting at the critical point of the less volatile component, C_2, ends at LCEP (Lower Critical End Point) while the other liquid-vapour critical line (L_1=V) starts at the critical point of the more volatile component, C_1, ends at UCEP. A three-phase equilibrium line (L_2L_1V) is bounded between the UCEP and LCEP. The region of immiscibility at low temperature is also

seen and another UCEP exists in this type of phase behaviour. From the second UCEP a liquid-liquid critical line (L_2=L_1) extends to high pressure. Another three-phase equilibrium line (L_2L_1V) is found which extends from the second UCEP to low pressures. An example system of this type is (methane + 1-hexane) mixture [48, 49]. Type V shows a similar behaviour of type IV but the liquid phase is homogeneous in the low temperature region. (Methane + *n*-hexane) binary system [53] is an example of type V. In type VI, LCEP and UCEP are observed, and are connected with each other by liquid-liquid critical curve (L_2=L_1). A three-phase equilibrium line (L_2L_1V) is also found in this type. An example binary mixture of this type is (water + 2-butoxyethanol) [54] and (D_2O + 2-methyl-pyridine) [55].

2.1.4 Phase Behaviour of Ternary Mixtures

An additional independent intensive variable or degree of freedom is required when a new component is added in order to define the state of the system as per the phase rule. This variable can be a second mole fraction. One variable from the four independent variables (T, p, x_1, x_2) of a ternary system needs to be dropped in order to represent the system in a three-dimensional space. Accordingly, the fluid phase behaviour of ternary mixtures can be represented in triangular phase diagrams in prismatic (p, x_1, x_2), (T, x_1, x_2) or (T, p, x) spaces. The first two representations (for isothermal and isobaric conditions, respectively) are the familiar forms of the ternary phase diagrams. These forms can be seen in the ternary mixtures (*tert*-butanol + water + carbon dioxide) and (methyl propanoate + propionic acid + carbon dioxide) which are covered in Chapter 6.

Classification of triangular phase diagrams is more complex than that of binary systems due to the increased number of different possible types of phase behaviour [56]. However, Blume and Deiters [57] suggested a systematic global scheme to classify the phase behaviour of ternary mixtures. They assumed equal size molecules and used the van der Waals EoS [58] with Lorentz-Berthelot combining rules similar to the scheme of Van Konynenburg and Scott classification of binary systems. Eight classes of ternary phase diagram have been classified with combinations of type I, type II and type III of Van Konynenburg and Scott classification as summarised in Table 2.1.

Ternary class T-I is a combination of binary subsystems of type I of Van Konynenburg and Scott classification; hence this class is found on mixtures of similar chemical substances. The phase diagram presents a vapour-liquid critical curve that runs continuously between the critical points of the three components. Ternary class T-II is a combination of two binary subsystems of type I and one subsystem of type II. In this class a liquid-liquid critical plane at low temperatures is observed and it ends at an UCEL (Upper Critical Endpoint Line) at low pressure. The ternary class T-III is seen in mixtures that involve two binary subsystems of type

I and one binary subsystem of type III. There is a continuous transition between vapour-liquid equilibrium (VLE) and liquid-liquid equilibrium (LLE) surfaces. A discontinuity in the vapour-liquid critical surface is seen and its rim is UCEL ending in a tricritical point.

Table 2.1: Ternary phase diagrams classes as per Blume and Deiters [57] classification scheme.

Subsystems			Ternary class
I	I	I	T-I
I	I	II	T-II
I	I	III	T-III
I	II	II	-
I	II	III	T-V
I	III	III	T-IV, T-VI
II	II	II	T-VIII
II	II	III	-
II	III	III	-
III	III	III	T-VII

The combination of binary subsystems of types I, II and III results in appearance of ternary class T-V which is similar to the ternary class T-III but additional liquid-liquid critical surface at low temperatures is seen. The ternary classes T-IV and T-VI are seen in mixtures involving two subsystems of type III and one subsystem of type I. However, the ternary class T-IV appears when two heavy compounds are mixed with a third lighter one while the class T-VI appears in mixtures of two light components and one heavy compound. In both classes there are two critical surfaces. In the class T-IV, one critical surface starts at the critical point of the light component and ends at an UCEL at low temperatures while the other critical surface starts at the critical line connecting the two critical points of the heavy compounds and it runs to high pressure at high temperatures. In the class T-VI, one critical surface starts at the critical point of the heavy component and runs to infinite pressure, whereas the other surface at low pressures starts at the critical line connecting the two critical points of the light compounds and ends at an UCEL. In ternary class T-VII, there are three binary subsystems of type III. Three critical surfaces, each starting from the critical point of each component, are seen in this class: liquid-liquid critical surface running from the heaviest compound to infinite pressure, vapour-liquid critical surface running from the lightest compound to a UCEL, and the third surface showing liquid-liquid critical behaviour when the third component approaches the light component and vapour-liquid critical behaviour when it approaches the heavy compound. The

last ternary class in the table T-VIII is a combination of binary subsystems all of type II. It presents three liquid-liquid critical surfaces at low temperatures and one continuous vapour-liquid critical plane.

2.1.5 Phase Behaviour of Biodiesel Transesterification Process

The study of phase equilibria during synthesis of fatty acid methyl esters (biodiesel) at conditions of high temperature and pressure is crucial for describing the chemical kinetic of the process. The intermediates formed during the reaction, in addition to FAME and glycerol make the system more complex for the analysis of phase behaviour. Producing biodiesel using this technique has been in focus recently. Thus, studying and knowing the phase behaviour and equilibria under medium and high pressures and over a wide range of temperatures is important for further design, development and optimisation in the process, and subsequently for developing our thermodynamic and kinetic modelling framework. The existence of one pseudo homogeneous phase in the non-catalytic process was found to be important for obtaining a high reaction rate between methanol and triglycerides under supercritical conditions [59]. Phase equilibrium of systems containing methyl esters, methanol, glycerol or glycerides (two or multicomponent) at moderate conditions of temperature and pressure has been the subject of area of research from numerous papers published in literature [19, 21, 59-69] as shown in Table 2.2 which was summarised by Glisic and Skala [59].

Triglycerides and methanol form two liquid phases when in contact due to the poor miscibility, which is because of the molecular difference in size and polarity. Due to this immiscibility of methanol and oil and also the reversibility of reactions, large excess of methanol is required in the non-catalytic transesterification [59, 70].

From Table 2.2, the reported research systems can be classified as reactant system, product system and by-product system. However, one of the main aims in this research is to consider all the systems together in explaining the phase equilibrium in order to develop a complete model covering the biodiesel production process.

Table 2.2: The literature review of phase equilibrium for tri-, di-, mono-glycerides, methyl esters and methanol or CO_2 [59].

Ref.	System	Temperatures and Pressures Ranges		Equilibria
		T/K	*p*/MPa	
Weber et al. [65]	(triolein + CO_2)	333 - 353	10 - 50	VLE[a]
Tang et al. [66]	(triolein + methanol)	353 - 463	6 - 10	VLE
Devender et al. [67]	(glycerol + methanol + methyl Oleate)	333 - 408	-	VLLE[b]
Glisic et al. [70]	(triolein + methanol)	473 - 513	3.5 - 6	VLE and VLLE
Andreatta et al. [69]	(methyl oleate + Glycerol + methanol)	313 - 393	0.1 - 0.6	LLE and VLLE
Fang et al. [68]	(methanol + C18 methyl esters)	523 - 573	2.45 - 11.45	VLE
Hegel et al. [71]	(veg. oil + methanol + methyl esters + glycerol)	333, 393 and 423	up to 1	VLE VLLE
Shimoyama et al. [72]	(methyl myristate + methanol), (methyl laureate + methanol)	493 - 543	2.16 - 8.49	VLE
Shimoyama et al. [73]	(glycerol + methanol)	493 - 573	2.16 - 8.49	VLE
Shimoyama et al. [74]	(Methyl myristate + methanol), (methyl laureate + methanol)	493 - 543	6.95 - 19.33	VLE
Srinophakun et al. [75]	(methanol + triglycerides, methanol + glycerol + FAME)	323- 823	0 - 21	VLE
Pin- et al. [76, 77]	(CO_2 + methanol), (CO_2+ soybean) (methyl esters, CO_2 + biodiesel + methanol)	303 - 343	3.5 - 6	VLE

[a]Notation: VLE stands for Vapour-Liquid Equilibrium.
[b]Notation: VLLE stands for Vapour-Liquid-Liquid Equilibrium.

The latest research on the phase behavior area [59, 78] tried to analyze the phase transitions of (vegetable oil and methanol) binary system starting from the triglycerides and methanol reaction to creation of diglycerides and monoglycerides and finally the fatty acid methyl ester (biodiesel) and glycerol. It was admitted in this study [59, 78] that analysis of phase equilibrium for this system was complex. As transesterification reaction proceeds at desired conditions of pressure and temperature, the distribution and composition of liquid phases are changing along with reaction mixture, depending on solubility to oil, methanol or biodiesel [59, 70]. Based on the temperature and pressure conditions, phase transitions during reaction showed four different scenarios. The first type of phase transition was considered as relatively high temperature and low pressure for methanol (T > 443.15 K, p > 1.5 MPa). At the beginning of the synthesis, the mixture is in equilibrium having methanol-rich liquid phase and oil-rich phase with small quantity of dissolved methanol (methanol to oil molar ratio was 1:1 which is three times less than the stoichiometric ratio) which is the reason behind the slow reaction rate [59].

A new liquid phase of (glycerol + methyl ester) is created, and the oil rich phase disappears when conversion of triglycerides is completed. The second scenario of the phase transition occurs at temperatures between 423.15 to 483.15 K and pressure conditions between 1.5 and 5.0 MPa, which are below the critical point of methanol. The mixture (methanol and triglycerides) is in liquid-liquid equilibrium (LLE) at the beginning of reaction with mass ratio of 46:54 where methanol is distributed between two liquid phases. During the reaction, the amount of triglycerides decreases, and after one third of time required to complete the conversion, the liquid 1 phase disappears and the third liquid phase (mainly methyl ester with some glycerol, methanol and some monoglycerides) is formed. At the end of the reaction, one liquid phase exists. Existing of the different phase during the reaction of triglycerides methanolysis is postulated by solubility of the reactants, intermediates, and products. Presence of the by-product (glycerol) can change the equilibrium compositions. The third type could be observed at temperatures near the critical temperature from (513.15 to 543.15) K and a pressure above the critical pressure of methanol from (20 to 28) MPa. The system of (triolein and methanol) was found to be at equilibrium of dense gas (or supercritical phase) but calculations indicated that at 543.15 K and 20.0 MPa the system from beginning to end of reaction dense gas phase was present. Vegetable oil and methanol present in two liquid phases at temperatures up to 543.15 K and pressure slightly below the methanol vapor pressure at this temperature. At temperatures above 543.15 K and pressure higher than the vapor pressure of methanol at this temperature (e.g. 20 MPa) and methanol to oil molar ratio is 42:1 (fourth type), single phase (supercritical or dense gas phase) exists in the whole system.

2.2 Reaction Kinetics

Chemical reaction kinetics can be defined as the study of the rate at which chemical processes take place [79]. In a chemical reaction it is the amount of product that forms or the amount of reactants that are consumed in a given interval of time. Reactions can occur at many different rates; some, such as geological processes, occur on the time scale of years, while others occur very rapidly (e.g. nanoseconds) [80].

2.2.1 Reaction Rates

Rates of reactions can be determined by monitoring the change in concentration of either reactants or products as a function of time [81]. In a plot of the concentration of a reactant or a product against time, the tangential slope of the curve at any time is the corresponding instantaneous rate [79]. Since reactions slow down with time, the instantaneous rates near the beginning (initial rates) could be the best indicator for a reaction rate.

The reaction rates can be affected by several factors such as [82]:

Concentration: when the concentration of reactants increases the probability that molecules of the reactants collide with each other increases.
Temperature: when temperature is increased reactant molecules will gain more kinetic energy and move faster, and hence collide more frequently and with more energy. This can be explained using the Arrhenius equation [83] (explained in section 2.2.3 or, for gases, the Maxwell-Boltzmann distribution.
Catalyst: in general, catalysts speed up reactions by providing alternative pathways and changing the mechanism of the reaction with lower activation energy.
Phase of the reactants: in general, the more homogeneous the mixture of reactants, the faster the molecules can collide and react.

2.2.2 Rate Law

The dependence on concentration of the rate of a chemical reaction is described by its *rate law*. If a reaction is designated symbolically by

$$aA + bB \ldots\ldots \rightarrow cC + dD \ldots, \tag{2.2}$$

then a rate law takes a form such as the following:

$$r = k C_A^{\,x} C_B^{\,y} \ldots. \tag{2.3}$$

Here, r is the rate of reaction, k is the rate constant, C_A, C_B ⋯ are the concentrations of the components A, B ⋯, and x, y ⋯ are reaction orders with respect to A, B ⋯, respectively. The overall order of the reaction is $x + y$. Most simple reactions are of order 0, 1 or 2; however, reaction orders can be fractional. The rate law is always determined experimentally. The form of the rate law above is called a differential rate law. The form can be integrated for different reaction order processes. If the rate law for a reaction is in the form:

$$r = k C_A^{\,n}, \tag{2.4}$$

where n is reaction order, and if the reaction is well behaved, the order of the reaction can be determined graphically using the integrated rate equations. Table 2.3 shows the rate laws and their integrated rate forms for different orders.

Table 2.3: Differential and integrated rate laws for different orders for equation (2.4).

Order	Rate law	Integrated rate forms	Linear plot	slope
0	$r = k$	$C_{A_t} = C_{A_0} - kt$	C_A vs. t	$-k$
1	$r = kC_A$	$\ln C_{A_t} = \ln C_{A_0} - kt$	$\ln C_A$ vs. t	$-k$
2	$r = kC_A^2$	$1/C_{A_t} = 1/C_{A_0} + kt$	$(1/C_A)$ vs. t	k

2.2.3 Relationship Between Reaction Rate and Temperature

The activation energy E_a of a reaction is defined as the minimum amount of energy needed to initiate the reaction. So, it is the energy required to form an activated complex after a collision between reactants. For a given reaction, the relationship between the rate constant k and the temperature T of the system are given by the Arrhenius equation [83]:

$$k = A\exp\left(\frac{-E_a}{RT}\right), \tag{2.5}$$

where R is the gas constant (8.314 $J \cdot mol^{-1} \cdot K^{-1}$), E_a is the activation energy, and A is a constant called the pre-exponential or frequency factor; which is related to the frequency of collisions of reactants.

In the next section, the literature review of the kinetics of biodiesel non-catalytic transesterification process is covered.

2.2.4 Kinetics of Non-Catalytic Transesterification of Biodiesel

There were a few attempts and studies to model the kinetics of non-catalytic transesterification [24, 33, 34, 84-87]. Most studies used relatively simple first order irreversible reaction and the reaction conditions used are summarised in Table 2.4. Some authors assumed and tested three steps kinetic models (reversible or irreversible) [84, 86-88] and here we show briefly one work done by Glisic and Orlović [88].

The kinetics was first modelled using three consecutive steps for the soybean oil transesterification with methanol [86] as follows:

$$\text{Triglyceride} + \text{methanol} \xrightarrow{k_1} \text{diglyceride} + \text{FAME} \tag{2.6}$$

$$\text{Diglyceride} + \text{methanol} \xrightarrow{k_2} \text{monoglyceride} + \text{FAME} \tag{2.7}$$

$$\text{Monoglyceride} + \text{methanol} \xrightarrow{k_3} \text{glycerol} + \text{FAME} \tag{2.8}$$

Triglyceride reacts with methanol and forms diglyceride and fatty acid methyl ester (FAME). Monoglycerides and FAME are formed in the second reaction from the reaction of diglyceride and methanol. Glycerol and again FAME are the final products as shown in the last reaction. The reaction was assumed irreversible because of the large excess of methanol (its concentration was assumed to be constant) and was assumed to be a first order with respect to each reactant. As per Glisic and Orlović, the concentrations of methyl esters and triglycerides calculated from this model were consistent and in a good agreement with the experimental data. The kinetics parameters were calculated at temperatures of 493.15 K and 508.15 K. The rate constants for the first and second reactions were temperature dependent, and they were comparable, and the last step (conversion of monoglyceride to glycerol) was found to be independent of temperature, and the rate constant was lower than the first two steps [86].

The three-step model mechanism was simplified by ignoring the intermediates and using a single overall step as follows [87]:

$$\text{Triglyceride} + 3\,\text{methanol} \rightarrow 3\,\text{FAME} + \text{glycerol} \tag{2.9}$$

The effect of methanol concentration on transesterification reaction of rapeseed oil was ignored due to its large excess, and the reaction was assumed to be a first order with respect to triglyceride. Regarding the rate constants, which were reported at different temperatures (from 473.15 K to 760.15 K), it was found that they increased with temperature. Another study [32] found similar results for soybean oil when they used the same methodology for calculating the reaction kinetics. For instance, at 543.15 K the rate constant from [32] is 7.91×10^{-4} s^{-1} and it is 7×10^{-4} s^{-1} as reported in [87]. It was also noticed [89] that the methanol solubility limits the reaction rates at subcritical conditions. As the reaction proceeds the reaction rate increases because the intermediates (diglycerides and monoglycerides) and products (biodiesel and glycerol) formed can increase the solubility of methanol with oil. Varma and Madras [85] used the simplified single step model in the castor oil and linseed oil transesterification. Activation energies of 35 $kJ \cdot mol^{-1}$ and 47 $kJ \cdot mol^{-1}$ were obtained for castor oil methyl ester and linseed oil methyl ester, respectively, over a temperature range of 473.15 K and 623.15 K. In a following work [26], activation energies between 9 $kJ \cdot mol^{-1}$ and 15 $kJ \cdot mol^{-1}$ for transesterification of (four other oils + methanol) were reported at a temperatures range of 473.15 K and 673.15 K. The activation energies were much lower than those in the previous study [85]. In general, it is expected that an activation energy for a catalytic reaction is lower than that for its similar non-catalytic reaction [90]. The various activation energies that have been reported in the literature show the complicity of transesterification chemical kinetics along with the effects of mixing and phase behaviour.

A comparison of kinetics data for different types of oils was reported by Varma and Madras [85] and Rathore and Madras [26]. In this study, it was found that a triglyceride containing saturated fatty acids has a reaction constant faster than that for one comprising unsaturated acids, and when number of double bonds were increased in the unsaturated acids the reaction became slower. On the other hand, as reported in a separate study [91], unsaturated fatty acids were found to have slightly higher reactivity than did saturated fatty acids.

Table 2.4: The literature review for non-catalytic transesterification (first order assumption) at sub- and supercritical conditions.

Ref.	Oil:Methanol molar ratio	*T* /K	*P*/MPa	Optimum conditions and conversion		
				T/K, *p*/MPa	Reaction time (min)	Conversion (%)
Kusdiana & Saka [92]	1:42[a]	473 to 760	7 to 105	623, 43	4	95
Madras et al. [24]	1:40[b]	473 to 673	20	623, 20	40	96
Bunyakiat et al. [93]	1:42[c]	543 to 623	10 and 19	623, 19	7	95
He et al. [32]	1:40[d]	513 to 613	10 to 40	(373-593)[f], 35	25	96
Varma & Madras [85]	1:40[e]	473 to 623	20	623, 20	40	~100

[a,b,c,d,e]Notations: oil types are rapseed, sunflower, coconut, soybean and canola, respectively.
[f]Notation: temperature increased gradually.

Non-catalytic transesterification is a complex reaction that was represented as three parallel and consecutive reversible reactions of second order in some papers published in literature [59, 78]. In these studies, the overall reaction was assumed to occur as a sequence of three steps, parallel with respect to methanol and consecutive with respect to triglyceride. The reaction scheme is shown below:

$$\text{Triglyceride} + \text{methanol} \underset{k_{12}}{\overset{k_{11}}{\rightleftharpoons}} \text{diglyceride} + \text{FAME} \tag{2.10}$$

$$\text{Diglyceride} + \text{methanol} \underset{k_{22}}{\overset{k_{21}}{\rightleftharpoons}} \text{monoglyceride} + \text{FAME} \tag{2.11}$$

$$\text{Monoglyceride} + \text{methanol} \underset{k_{32}}{\overset{k_{31}}{\rightleftharpoons}} \text{glycerol} + \text{FAME} \tag{2.12}$$

The reversible reactions of diglyceride, monoglyceride and glycerol with FAME control and limit the conversion of triglycerides to biodiesel. The composition of product mixture at the end

of the transesterification consists of mainly methyl esters (biodiesel), large excess of methanol, small amount of glycerol and low concentrations of intermediates. The presence of intermediates in the final product could affect the quality of biodiesel and its compliance with the technical standards [59]. The experiments were carried out under subcritical or supercritical conditions of methanol, and they showed that reaction mixture had complex phase transition associated with mass transfer phenomenon.

2.2.5 Co-Solvent Effects on the Non-Catalytic Supercritical Methanol Process

Cao et al. [94] used propane as a co-solvent in soybean oil with methanol to produce biodiesel. Propane reduced the amount of methanol required and reduced the system pressure as well. In addition, with increasing amounts of propane the mixture critical point decreased, and that allowed a single phase to be formed. A yield of 98% biodiesel in a time interval of 10 min was obtained when the reaction conditions were a temperature of 553.15 K, a system pressure of 12.8 MPa, propane to methanol molar ratio of 0.05, and a methanol to oil ratio of 24. This research team [95] also examined CO_2 as a co-solvent at milder conditions, and the results were similar to those obtained with propane. A 98.5% yield in 10 min was obtained at 553.15 K, a system pressure of 14.3 MPa, a CO_2 to methanol ratio of 0.1, and a methanol to oil ratio of 24. Hexane was also used as a co-solvent to reduce the viscosity of vegetable oil [96]. Interestingly, the methyl ester produced from transesterification reaction can be also used as a co-solvent [97]. The study showed that when FAME is added to the system a single liquid phase exists at 313.15 K. The single homogeneous liquid phase was seen at a methanol to soybean oil molar ratio of 6 and methyl ester concentration of 36 wt.% in the solution.

In general, the kinetics of biodiesel process needs more investigation and research. Moreover, it has been seen that there is lack of research on the kinetics of the reaction of free fatty acid with methanol to produce free fatty methyl ester (biodiesel). It can be said that it has not been considered seriously yet although esterification of free fatty acids occurs much faster than transesterification at lower temperatures [98]. The kinetics for the esterification step, which is the second step in a developed two-step process [29, 98] (the first step is hydrolysis of triglycerides to fatty acids in subcritical water followed by the second step, which is methyl esterification of fatty acids to their methyl esters in supercritical methanol), was first studied based on an autocatalytic model [99]. The model appeared to agree with their experimental data carried out at T = 543.15 K and p = 20 MPa at different methanol to oleic acid ratios, but no reaction rate constants and activation energies were reported [98].

The esterification of a mixture of fatty acids (dominant was oleic acid) with methanol in supercritical state was also investigated in a batch stirred-tank reactor by Alenezi et al. [100]. One step second order reversible reaction was used:

$$\text{Fatty acid} + \text{methanol} \rightleftharpoons \text{water} + \text{biodiesel} \qquad (2.13)$$

The model here was found to fit the experimental data. The calculated kinetics parameters (with molar ratio of methanol to FFA is 7:1) in this study are shown in Table 2.5 [100].

Table 2.5: Kinetic parameters for esterification [100].

T(K)	k_1 [min^{-1} (mol/mol of fatty acid)$^{-1}$]	k_{-1} [min^{-1} (mol/mol of fatty acid)$^{-1}$]
523.15	0.035	0.037
543.15	0.050	0.054
563.15	0.110	0.054
593.15	0.230	0.063
Activation Energy (E_a), kJ·mol^{-1}	72	23.2

The same research group [101] studied also the non-catalytic hydrolysis of sunflower oil with subcritical water at temperatures ranging from (543 to 623) K, a pressure of 20 MPa and reaction times up to 30 min. They considered the intermediates (di- and mono-glycerides) in the reaction: triglycerides were hydrolyzed to diglycerides, the diglycerides were hydrolyzed to monoglycerides, and finally the monoglycerides were hydrolyzed to glycerol, and in each step fatty acids were generated. The activation energies (kJ·mol^{-1}) were reported as 98, 38 and 90 and pre-exponential factors (s^{-1}) as 8.67×10^4, 1.83×10^{-4} and 4.67×10^4 for the three steps, respectively.

Based on the works and researches available in the literatures, further work is required to understand the reaction kinetics for both the transesterification of triglycerides and esterification of fatty acids in sub and supercritical methanol in order to develop the aimed thermodynamic modelling framework. However, in this present work, reaction kinetics reported in literature are used in the process simulation covered in Chapter 8.

Chapter 3: Theory and Modelling

Thermodynamics models play a crucial role in the design and optimisation of chemical processes, and these models need to offer acceptable accuracy to support the design and optimisation of processes. Given the scarcity of experimental data on many systems of interest, in addition to the varied conventional modelling approaches being implemented the development of techniques with predictive capabilities that can be used over a wide range of mixtures and process conditions is needed. In this Chapter, a brief description of some commonly used cubic equation of states and their applications is given. In addition, Statistical Associating Fluid Theory (SAFT) is described. The focus is on SAFT-γ Mie group contribution approach. The systems of interest that are investigated in this work and the procedure of parameters estimation for the functional groups comprising biodiesel production within SAFT-γ Mie are covered.

3.1 Cubic Equations of State

In thermodynamics, an equation of state (EoS) is a thermodynamic equation that provides a mathematical relationship between two or more state variables associated with the matter, such as temperature, pressure and volume. An equation of state can describe and predict thermophysical properties over wide ranges of temperatures and pressures for both pure fluids and mixtures. Among so many different thermodynamic models, cubic equations of state are the most common used in the oil, gas and biofuel industries. They are simple in mathematical calculations and reliable in the prediction of thermophysical properties.

3.1.1 Van der Waals Equation of State (vdW EoS)

The first cubic equation of state was proposed by Johannes D. van der Waals in 1873 in his dissertation titled “On the continuity of the gas and liquid state” [58]. He corrected the pressure and volume terms of the ideal gas equation, taking into account the size of the molecules and molecular interaction forces, and expressed his equation as follows:

$$p = \frac{RT}{V_m - b} - \frac{a}{V_m^2}, \tag{3.1}$$

where p, T and V_m are the pressure, temperature and molar volume, respectively and the parameters a and b are the van der Waals coefficients. The term (a / V_m^2) is called the attractive term and it accounts for the attractive intermolecular forces between molecules while the parameter b is called co-volume and it accounts for the space occupied by the molecules. The

parameters *a* and *b* in the vdW EoS are generally obtained by solving for the conditions of the critical point. The critical point of a fluid is defined as follows:

$$\left(\frac{\partial p}{\partial V_{\mathrm{m}}}\right)_T = 0 \text{ and } \left(\frac{\partial^2 p}{\partial V_{\mathrm{m}}^{\,2}}\right)_T = 0 \tag{3.2}$$

Using these conditions, the values of the two parameters can be obtained as follows:

$$a = \frac{27(RT_c)^2}{64p_c} \text{ and } b = \frac{RT_c}{8p_c}, \tag{3.3}$$

where T_c and p_c are the critical temperature and critical pressure, respectively.

Due to its limitation and failure to predict accurately the Vapour-Liquid equilibria (VLE) of complex fluid mixtures, various modifications on the equation have been made in order to improve its accuracy. The equations of state Soave-Redlich-Kwong (SRK EoS) [46] and Peng-Robinson [102] (PR EoS) are the most widely used in biofuel industry and academia and hence they will be covered in the next sections.

3.1.2 Soave-Redlich-Kwong Equation of State (SRK EoS)

In 1949, Redlich and Kwong [103] modified the vdW EoS by considering temperature-dependent binary interaction parameters in the attractive term in Equation (3.1). The repulsive term was not changed. The modified equation of state showed a capability of predicting the gas-phase properties accurately, but its ability to predict liquid-phase thermodynamic properties and VLE is limited. Soave modified Redlich-Kwong by introducing the acentric factor parameter, ω, in the definition of the attractive term. The acentric factor is a conceptual number used to measure the non-sphericity of molecules, and to take into account the molecular size and shape effects [104]. This modified equation of state has shown more accurate representations of vapour pressures of fluids. It is expressed as follows:

$$p = \frac{RT}{V_m - b} - \frac{a(T)}{V_m(V_m + b)} \tag{3.4}$$

The parameters of the Soave-Redlich-Kwong equation of state (SRK EoS) [46] are calculated for individual components by the following expressions:

$$\left.\begin{aligned} a_i &= 0.42748(R^2 T_{c,i}^2 / p_{c,i})\alpha(T) \\ b_i &= 0.08664(RT_{c,i} / p_{c,i}) \\ \alpha_i(T) &= \left[1 + n_i\left(1 - \sqrt{\frac{T}{T_{c,i}}}\right)\right]^2 \\ n_i &= \left[1 + (0.48508 + 1.55171\omega_i - 0.15613\omega_i^2)\left(1 - \sqrt{\frac{T}{T_{c,i}}}\right)\right]^2 \end{aligned}\right\}, \tag{3.5}$$

where T_c, p_c and ω are the critical temperature, critical pressure and acentric factor, respectively. The Soave alpha function, $\alpha(T)$, appearing in Equation (3.5) determines the temperature dependency of the parameter *a* and is tuned to obtain a good description of the vapour pressures of pure components. The Soave-Redlich-Kwong EoS reduced the critical compressibility factor, $Z_c = p_c V_c / RT_c$, from 0.375 (proposed in vdW EoS) to 0.333. The SRK EoS improved the VLE predictions of pure fluids and mixtures, but it does not show reliable liquid densities and was inaccurate for predicting properties near the critical point.

3.1.3 Peng-Robinson Equation of State (PR EoS)

In 1976, Peng and Robinson [102] made a further modification to the attractive term in order to improve the poor prediction of liquid density property obtained by SRK EoS. They lowered the value of the constant compressibility factor, Z_c, to 0.307. In 1978, Peng and Robinson introduced the acentric factor, ω, in the new version of the equation which showed more accurate predictions of vapour pressures for the heavy fluids. The Peng-Robinson equation of state (PR78) is given by

$$p = \frac{RT}{V_m - b} - \frac{a(T)}{V_m(V_m + b) + b(V_m - b)} \tag{3.6}$$

The parameters are calculated by the following expressions:

$$\left.\begin{aligned} a_i &= 0.45724(R^2 T_{c,i}^2 / p_{c,i})\alpha(T) \\ b_i &= 0.07780(RT_{c,i} / p_{c,i}) \\ \alpha_i(T) &= \left[1 + n_i\left(1 - \sqrt{\frac{T}{T_{c,i}}}\right)\right]^2 \\ n_i &= 0.37464 + 1.54226\omega_i - 0.26992\omega_i^2 \qquad (\omega_i \le 0.491) \\ n_i &= 0.379642 + 1.48503\omega_i - 0.164423\omega_i^2 + 0.016666\omega_i^3 \qquad (\omega_i > 0.491) \end{aligned}\right\}, \tag{3.7}$$

3.1.4 Mixing Rules and Binary Interactions

For the calculations of pure components, the critical temperature T_c, critical pressure p_c, and the acentric factor ω are the only parameters required in the cubic equations of state. To apply the equations of state to mixtures, a mixing rule is used to estimate the values of the parameters a and b of the mixture from those of the pure components. The most commonly used mixing rules are the van der Waals one-fluid mixing rules [58], which are given for n-component mixture as follows:

$$\left.\begin{aligned} a &= \sum_{i=1}^{n}\sum_{j=1}^{n} x_i x_j a_{ij} \\ b &= \sum_{i=1}^{n}\sum_{j=1}^{n} x_i x_j b_{ij} \end{aligned}\right\}, \tag{3.8}$$

where a_{ij} and b_{ij}, are the unlike interactions parameters of the mixture. They can be estimated by using appropriate combining rules such as the rules proposed by van der Waals:

$$\left.\begin{aligned} a_{ij} &= (1-k_{ij})\sqrt{a_i a_j} \\ b_{ij} &= (b_i + b_j)/2 \end{aligned}\right\}. \tag{3.9}$$

Here k_{ij}, is an adjustable binary interaction parameter and commonly obtained by regression to experimental VLE data for the mixture of interest. It corrects the deviation between the prediction of the equation of state and the experimental data. Further modifications to the combining rules can be implemented by introducing the binary interaction parameter, l_{ij}, in the b_{ij} term. The classical mixing rules in Equation (3.8) become as follows:

$$\left.\begin{aligned} a &= \sum_{i=1}^{n}\sum_{j=1}^{n} x_i x_j (1-k_{ij})\sqrt{a_i a_j} \\ b &= \sum_{i=1}^{n}\sum_{j=1}^{n} x_i x_j (1-l_{ij})(b_i + b_j)/2 \end{aligned}\right\}, \tag{3.10}$$

There are unconventional mixing rules that can be used in the predictions of mixtures with strong polar and hydrogen-bonded substances, and the reader can refer to the literature [105, 106].

In this work, PR EoS with van der Waals mixing rules is used in the modelling of the phase behaviour data for the mixtures of interest mentioned below in section 3.2.3 . The binary interaction parameters, k_{ij} and l_{ij}, are correlated as a linear function of inverse temperature as follows:

$$\left.\begin{aligned} k_{ij} &= k_{ij,0} + \frac{k_{ij,1}}{T} \\ l_{ij} &= l_{ij,0} + \frac{l_{ij,1}}{T} \end{aligned}\right\} \tag{3.11}$$

Different approaches were used to fit the PR EoS to the experimental VLE data, and they are summarised as follows:

- The binary interaction parameter, $k_{ij,0}$, in Equation (3.11) was only adjusted and considered constant across all the isotherms in the mixtures. The temperature-dependent parameter, $k_{ij,1}$, was not taken into account and the binary interaction parameter, l_{ij}, was set to zero.
- The temperature-dependent parameter, k_{ij}, was considered and the binary interaction parameter, l_{ij}, was set to zero.
- The temperature-independent binary parameters, $k_{ij,0}$ and $l_{ij,0}$, were only considered in the regression of the experimental data.

Since the dominant experimental uncertainties are in the compositions of phases, and temperature and pressure are measured with small uncertainties, the objective function, S, used in the parameters estimation is defined as follows:

$$S^2 = \frac{1}{N}\sum_{i=1}^{N}\left[\left(x_{2,i} - x_{2,i,\text{calc}}\right)^2 + \left(y_{2,i} - y_{2,i,\text{calc}}\right)^2\right], \tag{3.12}$$

where N is the number of the equilibrium state points, subscript 'calc' denotes values calculated by PR EoS. The values of the critical temperature T_c, critical pressure p_c, and the acentric factor ω, of the pure-fluids used in this work are provided in Table 3.1.

Table 3.1: critical temperature T_c, critical pressure p_c, and acentric factor ω of the pure-fluids used in this work. Data retrieved from Aspen V8.8.

Components	T_c/K	p_c/MPa	ω
Butanoic acid	615.7	4.060	0.675003
Propionic acid	600.8	4.668	0.579579
Methyl propanoate	530.6	4.004	0.346586
Water	647.1	22.064	0.344861
Tert-butanol	506.2	3.972	0.615203
Carbon dioxide	304.2	7.383	0.223621

3.2 Statistical Associating Fluid Theory (SAFT)

3.2.1 Introduction

Cubic equations of states describe well phase behaviour data of fluids composed of simple molecules with weak electrostatic forces. However, due to their lack of detailed molecular description of fluids characterized by strong intermolecular forces and associations especially hydrogen-bonding fluids and polar solvents their descriptive and predictive capability is poor. The statistical mechanical approaches such as perturbation theories [107, 108] are an alternative that can provide useful information of the intermolecular potential function of a fluid in which the thermodynamic properties of the fluid can be determined. The thermodynamic perturbation theory (TPT) proposed by M.S. Wertheim in the mid-1980's [109-113] is one of the perturbation approaches. It was successful in describing the effects of the chain formation and molecular associations on the thermodynamic properties of fluids [114]. This led Chapman et al. [115, 116] to propose an equation of state that combined the Wertheim expressions for association and chain formation to a theory for simple, nonpolar molecules. This approach was called the Statistical Associating Fluid Theory (SAFT). The molecules in the SAFT approach are modelled as associating chains of boned identical spherical monomeric segments interacting through repulsive and dispersion forces. The SAFT EoS is expressed in terms of a Helmholtz free energy, A, as the following:

$$\frac{A}{Nk_BT}=\frac{A^{ideal}}{Nk_BT}+\frac{A^{mono}}{Nk_BT}+\frac{A^{chain}}{Nk_BT}+\frac{A^{assoc}}{Nk_BT}, \tag{3.13}$$

where N is the total number of molecules and k_B is Boltzmann's constant and T is the absolute temperature. The three residual contributions added to the ideal free energy of the fluid (A^{ideal}) are: the monomeric contribution (A^{mono}), which accounts for the repulsion-dispersion interactions between the segments; the contribution (A^{chain}), which accounts for formation of chains, and the short-range intermolecular association contribution (A^{assoc}). Figure 3.1 shows a representation of Wertheim's perturbation scheme where these contributions are shown for construction of an associating fluid. As can be seen in the figure, dispersion forces to spherical segments of a reference monomer fluid are added to form linear chains followed by addition of association sites to the molecules to allow for interactions through hydrogen bonds.

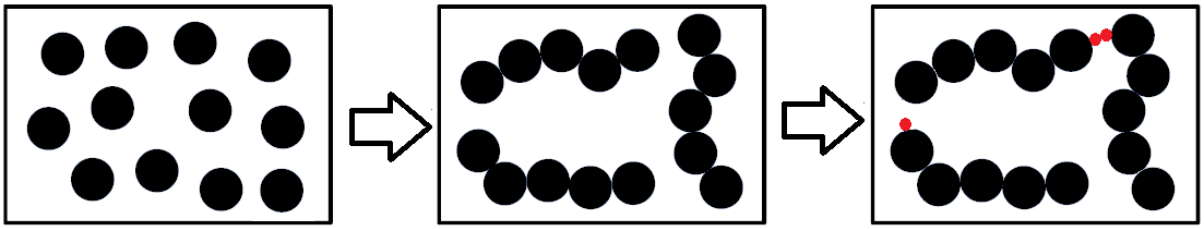

Figure 3.1: Schematic representation of the perturbation scheme for a fluid within SAFT.

Due to the flexibility of the original SAFT EoS different versions of the equation have been developed such as SAFT-LJ (Lennard-Jones) [117-119], SAFT-HR (Huang-Radosz) [120], SAFT-VR (Variable Range) [121, 122], Soft SAFT [123, 124] and PC-SAFT (Perturbed Chain) [125, 126]. In the original SAFT, molecules are modelled as associating chains of Lennard-Jones (LJ) segments, while in the SAFT-HS version the molecules are modelled as associating chains of hard-sphere segments. SAFT-VR models a fluid as associating chains of segments that interact through an attractive potentials of variable range such as the square well and Mie potentials. The properties of the segments in the SAFT-VR are calculated through a Barker and Henderson high temperature perturbation expansion [127, 128] from a hard-sphere reference fluid. In SAFT-PC, the monomer reference system is replaced by a hard-chain reference fluid.

Recently, group contribution (GC) concept has been applied within the framework of SAFT. In a group-contribution approach, molecules are modelled in terms of the functional groups that they comprise, and it is assumed that the thermodynamic properties of any given system of interest can be obtained from appropriate summations over the contributions of the corresponding groups to the properties of the system. Functional group parameters are classically determined by fitting experimental VLE data, and once the parameters that describe given groups have been obtained, a GC model can be used in a straightforward manner for the prediction of the properties of any compound or mixture formed from those groups [44]. GC methods have been developed for the prediction of pure components, binary and multicomponent mixtures [129-131]. GC approaches have been recently developed within the framework of SAFT incorporating heteronuclear molecular models (segments are not necessarily identical) such as SAFT-γ approach [132-134]. Incorporating the versatile Mie intermolecular potential of variable attractive and repulsive range in SAFT-γ approach [135] provided an accurate thermodynamic properties, including both fluid-phase behaviour and second-order derivatives of the free energy, such as speed of sound, compressibility, and the heat capacity, of pure fluids and mixtures [44]. More reviews of the different versions of SAFT can be found in literature [136, 137].

In this work, the experiential phase behaviour data measured in this work and collected from literature were coupled to the SAFT-γ Mie group contribution approach.

3.2.2 SAFT-γ Mie Group Contribution Approach

In SAFT-γ approach, as explained earlier, SAFT with its known capability to describe complex fluid mixtures has been combined with group-contribution methodology [135]. This approach is combined with Mie potential in which the pair interaction energy between segments *k* and *l* is given by:

$$\Phi_{kl}^{Mie}(r_{kl}) = C_{kl}\varepsilon_{kl}\left[\left(\frac{\sigma_{kl}}{r_{kl}}\right)^{\lambda_{kl}^{r}} - \left(\frac{\sigma_{kl}}{r_{kl}}\right)^{\lambda_{kl}^{a}}\right], \tag{3.14}$$

where ε_{kl} is the depth of the potential well, σ_{kl} is the segment diameter, r_{kl} is the distance between the centres of the segments and λ_{kl}^{r} and λ_{kl}^{a} are the repulsive and attractive exponents of the segment-segment interactions, respectively. The parameter C_{kl} is a function of λ_{kl}^{r} and λ_{kl}^{a} and ensures that minimum of the interaction is - ε_{kl}. It can be expressed as follows:

$$C_{kl} = \frac{\lambda_{kl}^{r}}{\lambda_{kl}^{r} - \lambda_{kl}^{a}}\left(\frac{\lambda_{kl}^{r}}{\lambda_{kl}^{a}}\right)^{\frac{\lambda_{kl}^{a}}{\lambda_{kl}^{r} - \lambda_{kl}^{a}}}. \tag{3.15}$$

In the approach of the SAFT-γ Mie group contribution model, the molecular properties are obtained by splitting the molecules into distinct functional groups that represent the chemical structure of a molecule, with appropriate contributions of all the functional groups. An example of the breakdown of a compound into functional groups is shown in Figure 3.2 for Pentanoic acid.

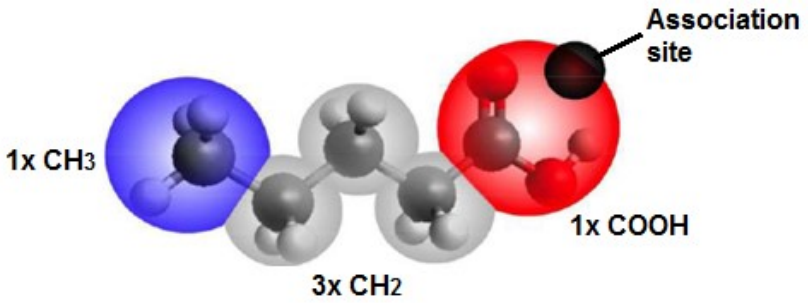

Figure 3.2: SAFT-γ Mie representation of Pentanoic acid ($CH_3(CH_2)_3COOH$). Reproduced based on the work of Dufal, et al. [44].

A functional group can comprise either one or multiple identical Mie segments described by the same set of group parameters. A functional group *k* is fully described by the following parameters: the number of identical segments v^*_k that the group comprises, the energy of interaction ε_{kk} between the segments, the segment diameter σ_{kk}, and the repulsive and attractive exponents λ^r_{kk} and λ^a_{kk}, respectively which determine the form of the interaction potential. Moreover, the range to which the segments of a given group contribute to the overall molecular properties is characterised by the shape factor S_k. In case of associating groups such as H_2O and COH molecules, additional parameters need to be determined: the number of the different site types $N_{ST,k}$, the number of sites $n_{k,a}$ of each type together with the position of the site, and the energy ε^{HB}_{kkab} and range of the association K_{kkab} between different sites [116, 138, 139]. The interactions between different groups (*k* and *l*) are, by extension, described by the corresponding unlike parameters ε_{kl}, σ_{kl}, λ^r_{kl}, λ^a_{kl}, ε^{HB}_{klab} and $K_{kl,ab}$. These unlike group parameters are needed not only to describe mixtures, but also for pure fluids like pentanoic acid shown in Figure 3.2 where the interactions between CH_3 and CH_2 or CH_3 and COOH groups are required to estimate the thermodynamic properties. The interactions are typically determined using combining rules (CR) and refined by regression to experimental VLE data. The unlike segment diameter σ_{kl} is obtained from the Lorentz-arithmetic mean of the like parameters:

$$\sigma_{kl} = \frac{\sigma_{kk} + \sigma_{ll}}{2}. \tag{3.16}$$

The unlike dispersion energy ε_{kl} is obtained by a geometric mean:

$$\varepsilon_{kl} = \frac{\sqrt{\sigma_{kk}^3 \sigma_{ll}^3}}{\sigma_{kl}^3} \sqrt{\varepsilon_{kk}\varepsilon_{ll}}. \tag{3.17}$$

The exponents of the unlike interactions λ^r_{kl} and λ^a_{kl} are obtained by the following combining rule:

$$\lambda_{kl} = 3 + \sqrt{(\lambda_{kk} - 3)(\lambda_{ll} - 3)}. \tag{3.18}$$

In association mixtures, the unlike association energy ε^{HB}_{klab} can be obtained by:

$$\varepsilon^{HB}_{kl,ab} = \sqrt{\varepsilon^{HB}_{kk,aa}\varepsilon^{HB}_{ll,bb}}, \tag{3.19}$$

and the unlike bonding volume K_{klab} is estimated by

$$K_{kl,ab} = \left(\frac{\sqrt[3]{K_{kk,aa}} + \sqrt[3]{K_{ll,bb}}}{2} \right)^3 \tag{3.20}$$

The combining rules (CRs) can provide good initial estimates of the unlike cross interactions between the functional groups; however, it is best to estimate them using experimental VLE data when available in order to capture the features of the interactions more accurately.

3.2.3 Selection Criteria of the Measured Systems

The systems studied in this research were chosen primarily to provide new data of phase behavior in wide ranges of temperatures and pressures for representative mixtures with minimum molecular chains that exist during biodiesel production. The SAFT-γ Mie model developed using the experimental data of these mixtures were used to predict the actual complex systems available in biodiesel production. The functional groups that are required to fully describe the mixtures in biodiesel reactions (reactants, intermediates and products as well as the co-solvents) are collected in a biodiesel matrix shown in Figure 3.3. This matrix highlights the like and unlike interactions that need to be obtained from experimental VLE data.

	CH_3	CH_2	COOH	COO	H_2O	CH_3OH	CH=	OH_GL	COH	CO_2
CH_3	✓									
CH_2	✓	✓								
COOH	✓	✓	✓							
COO	✓	✓	×	✓						
H_2O	✓	✓	✓	×	✓					
CH_3OH	✓	✓	×	×	✓	✓				
CH=	✓	✓	×	✓	×	×	✓			
OH_GL	✓	✓	×	✓	×	×	✓	✓		
COH	✓	✓	×	×	×	×	×	×	✓	
CO_2	✓	✓	×	×	✓	✓	×	×	×	✓

Figure 3.3: SAFT-γ Mie functional groups and unlike cross interactions that are required for the modelling of biodiesel system in our current work. The tick (✓) indicates the like and unlike parameters that have been already obtained and reported in literature while the cross (×) indicates the interactions required to be obtained by experimental data.

In this work, five main systems were investigated, and the experimental data measured were compared with the predictions of SAFT-γ Mie model. The system (butanoic acid + CO_2) was selected to represent a simple model of (fatty acid + CO_2). Phase equilibrium studies on binary systems relevant to saturated and unsaturated fatty acids and carbon dioxide have been published in literature [140-150], however some of these studies only considered one phase; either liquid or vapour phase, and inconsistencies can also be seen in the published date. Butanoic acid ($CH_3(CH_2)_2COOH$), also known as butyric acid, is a short fatty acid containing the COOH functional group found in the fatty acids, which are one of the reactants in biodiesel reactions. Carbon dioxide (CO_2) might be used as a co-solvent to lower the energy requirements in the transesterification reactions [95, 151, 152]. It is also the most common solvent in supercritical fluid extraction processes [153], wherein comprehensive knowledge of the phase behaviour of mixtures containing carbon dioxide is required.

The system (methyl propanoate + CO_2) was selected to be a representative mixture for (fatty acid methyl ester (FAME) + CO_2). Methyl propanoate ($C_2H_5COOCH_3$), also known as propanoic acid methyl ester, is an ester containing the COO functional group found in the fatty acid methyl esters, which are the major components of biodiesel.

The system (methyl propanoate + propionic acid + CO_2) was selected to represent ternary mixtures containing methyl ester, fatty acid, and the co-solvent CO_2. The group parameters for the functional groups of the SAFT-γ Mie model, which esters, fatty acids, glycerides and carbon dioxide are composed of, were estimated using the experimental measurements of the first two systems. The prediction of the model will be tested against the phase behaviour of this ternary system.

The system (*tert*-butanol + H_2O + CO_2) were studied in the present work. *Tert*-butanol is the smallest tertiary alcohols and is miscible with water in all proportions under ambient conditions. It is used as an organic solvent to dissolve methanol and glycerol in the enzymatic transesterification for the production of biodiesel [154]. The presence of water during biodiesel purification processes can cause issues including deterioration of the quality of biodiesel, soap formation, and corrosion of fuel systems. To the best of our knowledge, the system (*tert*-butanol + water + carbon dioxide) has only been studied by Kim et al. [155] at the single temperature of 323.2 K and at pressures from (6 to 12) MPa. Their results showed quite complex phase behaviour of the ternary system under CO_2 addition with extended three phase regions. In this work, experimental measurements of the phase behaviour of the ternary system (*tert*-butanol + water + carbon dioxide) measured along five isotherms at temperatures from (283.2 to 423.17) K with pressures of 4, 8, 12 and 18 MPa were reported. From this

system, cross interactions parameters for SAFT-γ Mie model that are not available in the SAFT databank were estimated.

The system (toluene + H_2O + CO_2) was studied in this work to investigate miscibility of CO_2 with aromatic hydrocarbons in the presence of water. The knowledge of the phase behaviour of the mixtures is crucial in the design of Carbon Capture and Storage (CCS) processes and Enhanced Oil Recovery (CO_2-EOR) operations. There is lack of data in the available literature for this system. Moreover, the accuracy and capability of SAFT-γ Mie model to describe the system was covered.

The rest of the cross interactions in the matrix were estimated and covered in Chapter 7.

3.2.4 Parameter Estimation Within SAFT-γ Mie

The like and unlike group parameters have been covered in the previous section (3.2.2). In this work, similar to the other works with SAFT-γ Mie model [44, 156, 157], only the unlike dispersion energy ε_{kl} and in some cases the unlike repulsive exponent λ_{kl}^{r} are adjusted to fit the experimental VLE data of pure compounds and mixtures that contain the groups of interest. If there are associating interactions between functional groups the unlike association energy $\varepsilon_{klab}^{\mathrm{HB}}$ and the bonding volume $K_{\mathrm{kl,ab}}$ are also tuned. All other parameters including the unlike attraction exponent λ_{kl}^{a} and the unlike segment diameter σ_{kl} are always estimated by the combining rules as discussed in section 3.2.2 . The experimental data of pure components used to estimate the like and also unlike parameters include typically vapour pressure p_{vap} and saturated-liquid densities ρ_{sat} data (at temperatures ranging from the triple point to approximately 90% of the critical point [44]) as well as single-phase densities $\rho_{\mathrm{liq}}(T, p)$ at given temperatures and pressures or even second-order derivative properties, such as speed of sound if available. The objective function used to estimate the group parameters from vapour pressure p_{vap} and saturated-liquid densities ρ_{sat} data is as of the following form:

$$\min_{\Omega} f_{obj} = w_p \sum_{u=1}^{N_{Pvap}} \left[\frac{p_{\mathrm{vap}}^{\mathrm{exp}}(T) - p_{\mathrm{vap}}^{calc}(T)}{p_{\mathrm{vap}}^{\mathrm{exp}}(T)} \right]^2 + w_\rho \sum_{u=1}^{N_{\rho sat}} \left[\frac{\rho_{\mathrm{sat}}^{\mathrm{exp}}(T) - \rho_{\mathrm{sat}}^{\mathrm{calc}}(T)}{\rho_{\mathrm{sat}}^{\mathrm{exp}}(T)} \right]^2, \tag{3.21}$$

where w_{p} and w_ρ are the weight factors and N are the number of the experimental points used in the parameter estimation. The minimization of estimation is performed using the numerical solver available in gPROMS software. In case of mixtures fluid phase behaviour data (vapour-liquid or liquid-liquid equilibria) of binary mixtures comprising the corresponding groups of interest need to be used to estimate the cross interaction parameters.

The comparison between the calculations of SAFT-γ Mie and experimental data is quantified by a percentage average absolute deviation (Δ_{AAD}) defined as:

$$\Delta_{\mathrm{AAD}} = \frac{1}{n_{\mathrm{R}}} \sum_{i=1}^{n_{\mathrm{R}}} \left| \frac{R_i^{\mathrm{exp}} - R_i^{\mathrm{calc}}}{R_i^{\mathrm{exp}}} \right|, \tag{3.22}$$

where n_{R}, ‘exp’ and ‘calc’ superscripts represent number of experimental data points of property R, experimental and calculated quantities, respectively.

Chapter 4: Analytical Apparatus for Fluid Phase Equilibrium Measurements

In this work, a quasi-static analytical apparatus was used to measure the phase equilibria of the systems. The design of the apparatus, setup, operation and control were previously described in detail by Forte [158], who designed and built the original system. In this Chapter, only a summary of the experimental setup is given. The apparatus experimental procedure, calibration, validation measurements and uncertainty analysis are presented.

4.1 Apparatus Design

The quasi-static analytical apparatus is schematically shown in Figure 4.1 [159] and Figure 4.2.

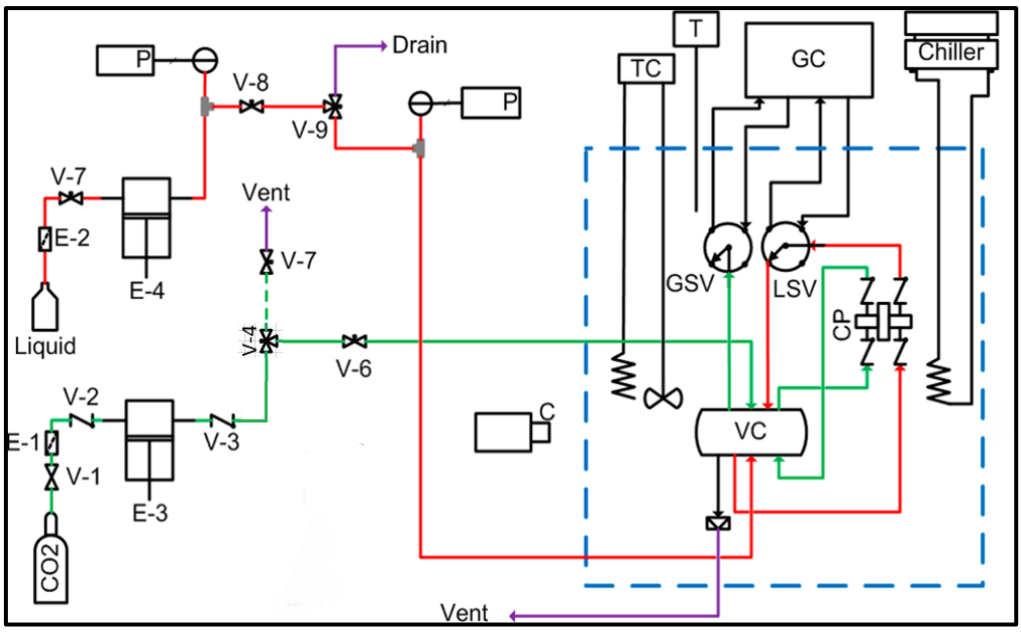

Figure 4.1: Schematic diagram of the quasi-static-analytical apparatus. The abbreviations represent: VC: view cell, GC: gas chromatography, CP: circulation pump, GSV: gas sampling valve, LSV: liquid sampling valve, TC: Temperature controller, C: Camera, P: Pressure transducers, T: Temperature sensor, E1 and E2: filters, E3 and E4: syringe pumps. Green line denotes the gas flow, red line denotes the liquid flow, and the area within the blue dotted line indicates the oil bath area [160].

This apparatus has a maximum operating temperature of 433.15 K and a maximum operating pressure of 20 MPa. The apparatus consisted of a high pressure equilibrium view cell (VC) made from 17-4PH martensitic stainless steel immersed in a thermostatic silicone oil (Dow Corning Corporation, type 200-10) bath and fitted with a magnetic two-channel reciprocating

recirculation pump and electronically-actuated gas- and liquid-sampling valves (GSV and LSV manufactured by VICI AG International) for compositional analysis by online Gas Chromatography (Shimadzu, model GC-2014, Shimadzu Scientific Instruments, Inc.).

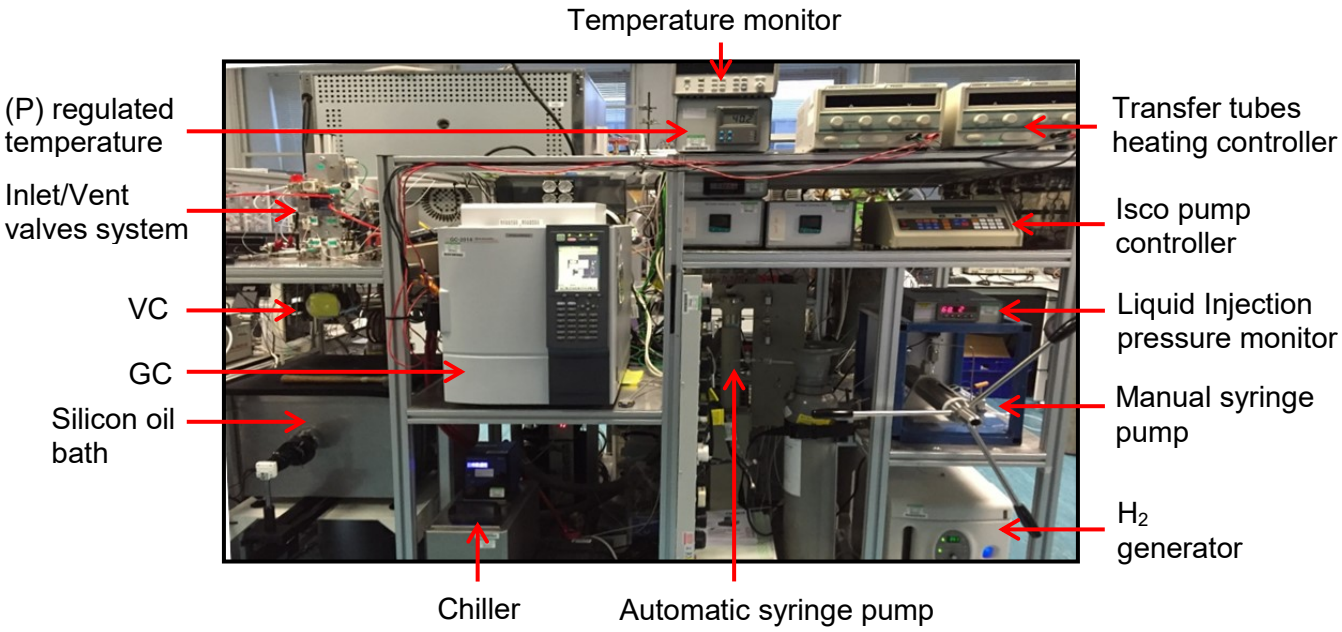

Figure 4.2: Experimental setup of the quasi-static-analytical apparatus.

The view cell was a horizontally orientated cylindrical vessel of internal volume of 35 cm^3 fitted with axially opposed sapphire windows to enable observation of the phase behaviour inside the cell. The temperature of the cell was controlled by the silicone oil bath using a temperature controller (Grant Model, TX150, Grant Instruments Ltd.). An external temperature controller (Huber model CC1, Huber K.ltemaschinenbau GmbH) was used to provide cooling when working at temperatures below 298 K. The bath was equipped with two double-glazed windows aligned with the front and back sapphire windows of the view cell. The recirculation pump was used to recirculate the gas phase and the liquid phase so as to promote equilibration and mass transfer between the two phases. Figure 4.3 shows the circulation of the liquid and vapour inside the view cell; the liquid falls from the top of the cell through the vapour while the vapour bubbles rise from the bottom of the cell passing through all the coexisting liquid phases. Additionally, the cell was rocked to expedite equilibration. The four-port chromatographic liquid-sampling value (LSV), with a 1 µL internal loop, was installed in the liquid recirculation line and used to withdraw samples from the liquid phase for compositional analysis in the GC. The gas phase was sampled by means of a six-port gas-sampling valve (GSV), with a 5 µL external loop, connected to the top of the equilibrium cell

by a short length of a 0.1 mm inner diameter (i.d.) fine-bore capillary. The sampling valves were kept inside the same oil bath as the VC to avoid condensation. The VC was tilted with a pneumatic cylinder connected to the cell by a push rod to enable sampling of the middle phase in the VLLE. The transfer tubes connecting the liquid- and gas-sampling valves to the inlet of the GC were heated to around 500 K by low-voltage mineral-insulated heater cables (custom made, Tempco Electric Heater Corp.) operating with thermocouple temperature sensors of Type K. During analysis, samples from the view cell were vaporized in these lines and transported to the GC by the carrier gas, helium. Helium was also pre-heated upstream of the sampling valves.

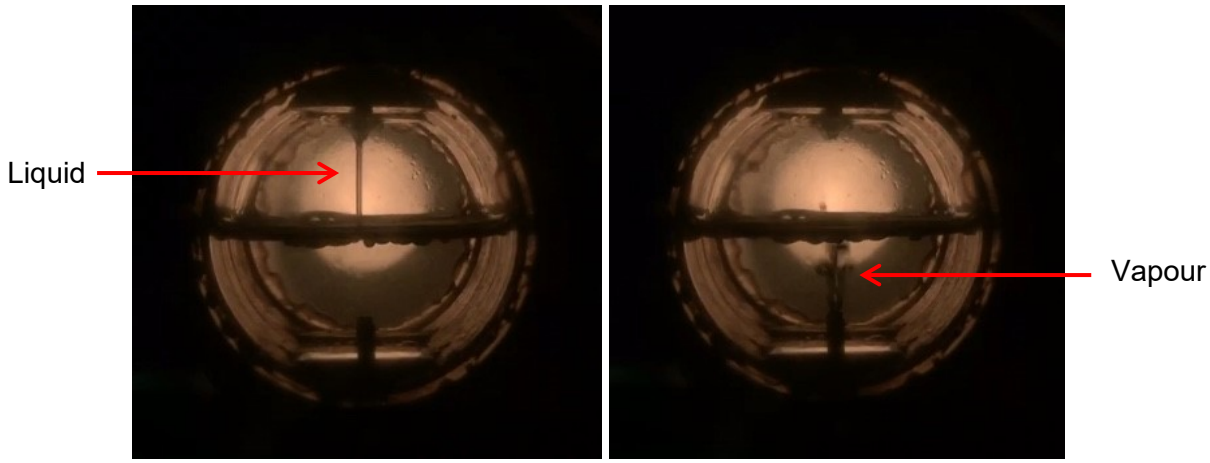

Figure 4.3: Images of the inside of the equilibrium cell showing circulation of liquid and vapour phases by means of the reciprocating recirculation pump.

The GC oven accommodated two parallel columns, a HayeSep Q packed column (80/100 mesh, 2 m long, 3.2 mm o.d., 2 mm i.d.) and a 5% OV-1 on C-WHP column having the same size of the first column. However, in this work the Hayesep Q column was used for the separation and analysis of all the components. The GC was equipped with one thermal conductivity detector (TCD) connected in series with two flame ionization detectors (FID), one for each column. The TCD works based on the variation of the thermal conductivity of the carrier gas when its composition changed while the electrical conductivity of the gas after its ionization is the basis of the FID response. The FID was ignited using a hydrogen (H_2) generator and a zero-grade air supplied by a precision air compressor and purifier (Peak Scientific Instruments Ltd) with H_2/air flow ratio of roughly 1:10. In the present work, the TCD was used to measure carbon dioxide and water, while the FID was used to measure methyl propanoate, butanoic acid, propionic acid, *tert*-butanol and toluene. A schematic diagram of the GC arrangement and the connection to the sampling valves is shown in Figure 4.4 [158].

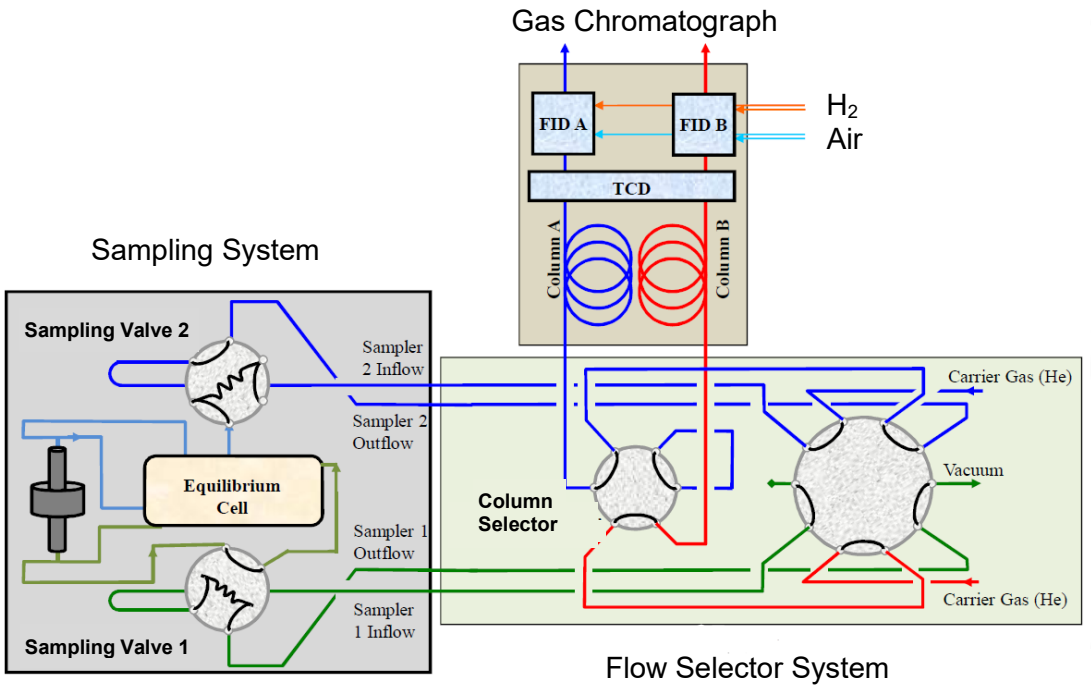

Figure 4.4: Schematic diagram of the GC and connection to the sampling valves [158].

The instrument conditions used for the GC analysis are detailed in Table 4.1. The refrigerated automatic syringe pump (Teledyne Isco, model 100DM, Teledyne Technologies Inc.), illustrated as E3 in Figure 4.1, was used for the injection of carbon dioxide into the view cell through valve V6, while the manual syringe pump E4 (Sitec model 750.110, SITEC-Sieber Engineering AG) was used to inject liquids through valve V9. The valves (V4, V7, and V9) were used for draining, flushing and evacuating the cell. The pressure was measured with a pressure transducer (Paroscientific Digiquartz model 410 KR-HT-101) positioned in the liquid inlet line. The temperature was measured by means of a platinum resistance thermometer (PRT) placed close to the cell in the silicone oil bath. The system was leak tested before and during the measurements to ensure the integrity of the apparatus.

Table 4.1: GC conditions and flow rates for the analysis of the mixtures being used in the experiments[a].

System	Injector		Oven	TCD		FID[c]
	$\dot{V}$ /($cm^3 \cdot min^{-1}$)	T/K	T/K	I/mA	T/K	T/K
Butanoic acid + CO_2	40	453.15	493.15	80	503.15	573.15
Methyl propanoate + CO_2	40	423.15	473.15	90	523.15	573.15
Methyl propanoate + propionic acid + CO_2	40	423.15	473.15	90	523.15	573.15
Tert-butanol + CO_2	40	423.15	443.15 – 518.15[b]	90	523.15	573.15
Toluene + water + CO_2	40	453.15	443.15 – 518.15[b]	80	503.15	573.15

[a]Notation: $\dot{V}$ is the carrier-gas flow rate, T is temperature, I is filament current.
[b]Notation: Ramp temperature program
[c]Notation: H_2/air flow ratio = 1:10

4.2 Materials

The details of the materials used in this work are provided in Table 4.2. Purities are stated as by the supplier.

Table 4.2: Description of chemical samples.

Chemical name	CAS number	Source	Purity as supplied[a]	Further purification
Carbon dioxide		BOC	$x \geq 0.99995$	none
Helium		BOC	$x \geq 0.99995$	none
Water		Millipore Direct-Q UV3	ρ_e > 18 MΩ.cm at T=298K	degassed under vacuum
Methyl propanoate	554-12-1	Sigma Aldrich	$w \geq 0.999$	none
Butanoic acid	107-92-6	Sigma Aldrich	$w \geq 0.997$	none
Tert-butanol	75-65-0	Sigma Aldrich	$w \geq 0.995$	none
Propionic acid	79-09-4	Sigma Aldrich	$w \geq 0.998$	none
Toluene	108-88-3	Sigma Aldrich	$w \geq 0.9997$	none
2-Propanol	67-63-0	Sigma Aldrich	$w \geq 0.9999$	none
Methanol	67-56-1	Sigma Aldrich	$w > 0.9999$	none

[a]Notation: x is mole fraction; w is mass fraction and ρ_e is electrical resistivity.

4.3 Experimental Procedure

The apparatus was initially cleaned, flushed with CO_2 and dried under vacuum. Then, a liquid (pure component or mixture) was loaded into the cell through valve V9 until it occupied roughly one-third of the cell volume. After that, at a given temperature, CO_2 was injected slowly through valve V6 until the desired pressure was reached. The system was then left to equilibrate for (two to three) hours, which varied between the systems studied, while the recirculation pump was running. In addition to the circulation pump used to promote mass transfer between the phases, a rocking mechanism for the cell within a range of ±40° was implemented. When the system was at equilibrium, the rocking was stopped, and samples were taken from the gas phase using the GSV and sent to the GC for compositional analysis. Then, the bottom liquid phase was sampled using the LSV. In the case of VLLE phase behaviour, the view cell was then tilted until the less-dense liquid phase could be sampled by means of the LSV. The recirculation pump was kept running as the LSV was located in the liquid re-circulation loop. For each phase, at least six samples were withdrawn to ensure reproducibility. The pressure was increased to the next point by injection of more CO_2, and the process was repeated for each isotherm.

4.4 Apparatus Calibration

The pressure transducer was calibrated previously [161] from (0.1 to 50) MPa against a pressure balance (Desgranges et Huot, model 26000) having a standard relative uncertainty of 0.005%. The overall standard uncertainty of pressure was estimated to be 10 kPa. Periodic adjustments for the pressure readings of the transducer were done to account for any sensor drift over time. The platinum resistance thermometer (PRT) was calibrated on ITS-90 at the temperature of the triple point of H_2O and by comparison with a standard PRT at temperatures up to 473.15 K. The overall standard uncertainty of cell temperature, after considering bath temperature fluctuations and calibration uncertainties, was estimated to be 0.05 K. The TCD and FID GC detectors were calibrated by an absolute-area method for each component individually using the LSV in which loop volume was assumed fixed, and therefore the amount of a component injected was proportional to the density of the calibration fluid under the conditions of the sampling. To obtain the calibration curves for CO_2, which is the only gas used in this work, both LSV and GSV were used. The calibrations were performed at the same GC conditions used for the experimental measurements and covered the full range of chromatographic peak areas that no extrapolation was required for either component.

The TCD for CO_2 was calibrated by injecting different amounts of CO_2 at different conditions of pressure and temperature in the equilibrium cell. The density of CO_2 was obtained from the EoS developed by Span and Wagner [162] with an estimated relative uncertainty of 0.025%. The calibrations of TCD and FID for H_2O, methyl propanoate, butanoic acid, *tert*-butanol and toluene were performed by filling the equilibrium cell with gravimetrically prepared mixtures of each component with appropriate solvents. The solvents used and the references of the density data used at the injection conditions are summarised in Table 4.3.

Table 4.3: Solvents used for calibrations of the GC detectors.

Component	Solvent	Density
Butanoic acid	Water	Measured in this work[a]
Propionic acid	Methyl propanoate	Measured in this work
Tert-butanol	Water	Egorovet al. [163]
Methyl propanoate	Methanol	Blanco-Marigorta [164]
Toluene	Hexane	Freire et al. [165]
Water	Isopropanol	Saleh et al. [166]

[a]Notation: Measured in this work by a densimeter [167] available in our lab with an estimated standard uncertainty of 1 $kg.m^{-3}$.

Optimised temperature ramp programs were used in the GC in order to avoid overlapping of (*tert*-butanol and water) and (toluene and water) response area peaks as shown in Table 4.1. The reproducibility in the GC peak area was examined by taking at least 6 samples. Considering uncertainties in temperature, pressure, and the EoS model, the standard relative uncertainties in the peak area and in the calculated amount of each component at each given pressure and temperature were estimated to be 1.0% and 0.1%, respectively. A nonlinear relationship between the response peak area and the amount of CO_2 injected was observed; hence a quadratic polynomial was used. The TCD peak area showed a linear response for water. A linear behaviour was observed between the FID peak response area and the amount of methyl propanoate, butanoic acid, propionic acid, toluene and *tert*-butanol injected. Most components in this work could be detected by TCD but FID was used due to its higher sensitivity. The calibration curves used in this work are shown in Figure 4.5.

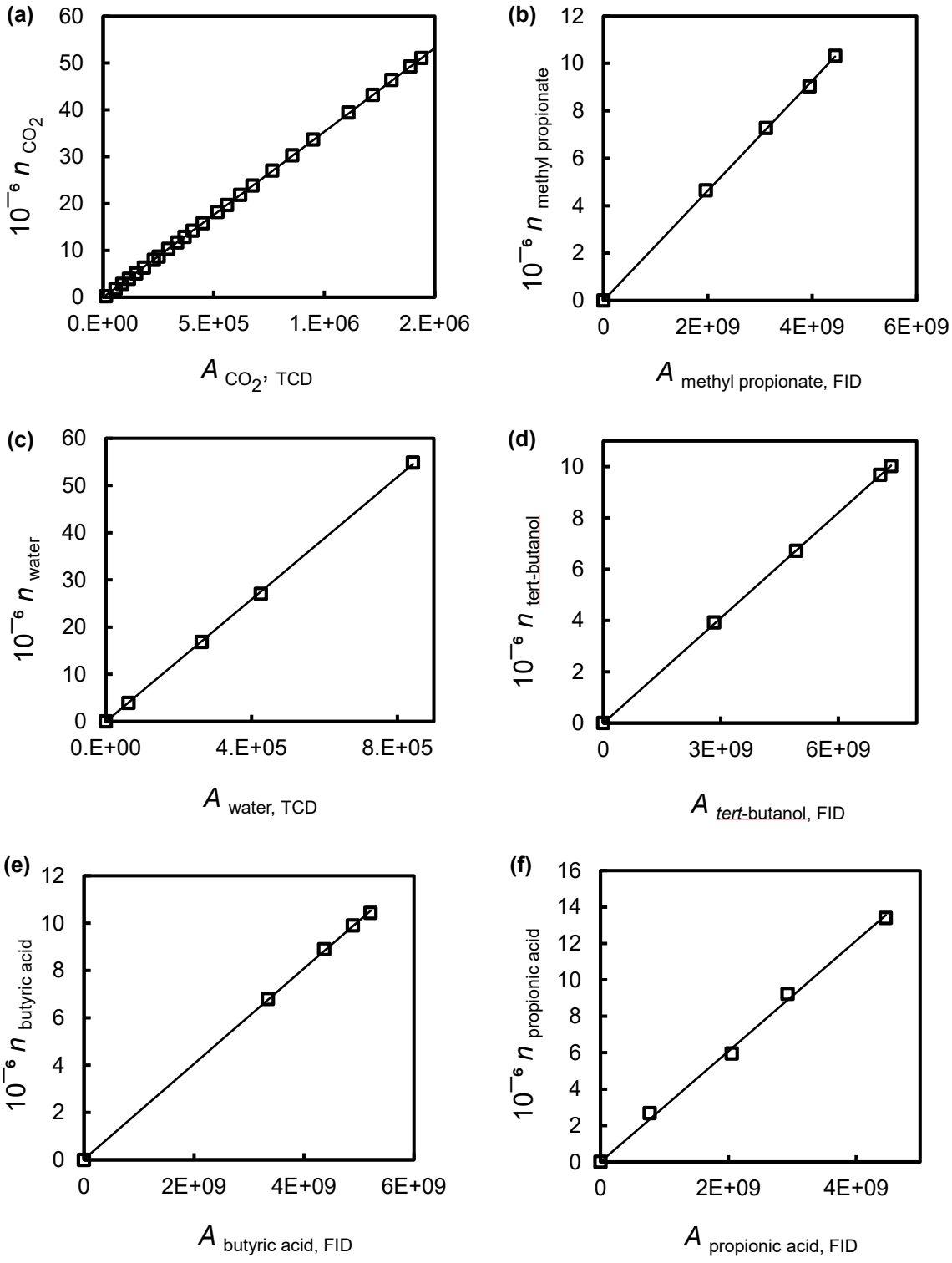
(a)
60
50
40
30
20
10
0
0.E+00
5.E+05
1.E+06
2.E+06
10⁻⁶ n CO2
A CO2, TCD
(b)
12
10
8
6
4
2
0
0
2E+09
4E+09
6E+09
10⁻⁶ n methyl propionate
A methyl propionate, FID
(c)
60
50
40
30
20
10
0
0.E+00
4.E+05
8.E+05
10⁻⁶ n water
A water, TCD
(d)
10
8
6
4
2
0
0
3E+09
6E+09
10⁻⁶ n tert-butanol
A tert-butanol, FID
(e)
12
10
8
6
4
2
0
0
2E+09
4E+09
6E+09
10⁻⁶ n butyric acid
A butyric acid, FID
(f)
16
14
12
10
8
6
4
2
0
0
2E+09
4E+09
10⁻⁶ n propionic acid
A propionic acid, FID

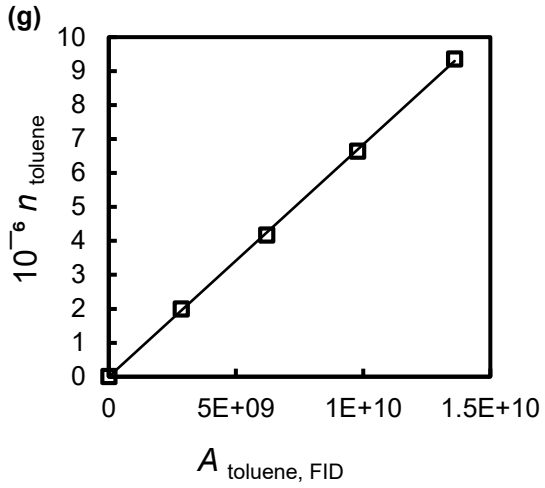

Figure 4.5: Amount of component (*n*) versus detector response area (*A*) graph showing the data points measured and the calibration curve obtained for the response of the detectors with: (a), CO_2 (TCD detector) ; (b), methyl propanoate (FID detector); (c), water (TCD detector); (d), *tert*-butanol (FID detector); (e), butanoic acid (FID detector); (f), propionic acid (FID detector); and (g), toluene (FID detector).

4.5 Uncertainty Analysis

The uncertainty of the determined phase compositions in this work was analyzed using the Guide to the Expression of Uncertainty in Measurement (GUM) [168]. The uncertainty has been studied in detail by Al Ghafri et al. [160]. The combined standard uncertainty of the mole fraction of each component in a given phase $u(x_i)$ was calculated by the following relation:

$$u^2(x_i) = \sum_{j=1}^{n} \left[\left(\frac{\partial x_i}{\partial z_j} \right)^2 u^2(z_j) \right], \tag{4.1}$$

where z_j (j = 1, 2, 3 … n) are the n independent measured variables upon which x_i is dependent, each associated with variance $u^2(z_j)$, and $(\partial x_i / \partial z_j)$ is the sensitivity coefficient of x_i with respect to z_j. The expanded uncertainty $U(x_i)$ is determined by multiplying the combined standard uncertainty $u(x_i)$ by a coverage factor which is normally 2 to represent 95% of confidence level.

In this work, an absolute area method was used for composition calculations in which the chromatographic peak area A_i associated with component i in the mixture is related to the amount n_i of that component in the sample. The parameters n_i and A_i are related to each other by

$$n_i = f_i A_i, \tag{4.2}$$

where f_i is the response factor. The mole fraction x_i of component i is given by

$$x_i = A_i f_i \Big/ \left(\sum_{k=1}^{N_c} A_k f_k \right), \tag{4.3}$$

where N_c is the number of components. The independent variables considered in the uncertainty analysis are temperature, pressure, chromatographic response peak area and the response factor, so the overall combined standard uncertainty of the mole fraction can be determined as follows:

$$\begin{aligned} u^2(x_i) = &\left[\left(\partial x_i / \partial T \right) u(T) \right]^2 + \left[\left(\partial x_i / \partial p \right)_T u(p) \right]^2 \\ &+ \sum_{j=1}^{N_c} \left(\frac{\partial x_i}{\partial n_j} \frac{\partial n_j}{\partial A_j} \right)^2 u^2(A_j) + \sum_{j=1}^{N_c} \left(\frac{\partial x_i}{\partial n_j} \frac{\partial n_j}{\partial f_j} \right)^2 u^2(f_j). \end{aligned} \tag{4.4}$$

The sensitivity coefficient ($\partial x_i / \partial n_j$) is given by

$$\left.\begin{aligned} \left(\frac{\partial x_i}{\partial n_j} \right) &= -\frac{x_i x_j}{n_j} \qquad (j \neq i) \\ &= (1 - x_i) \frac{x_i}{n_i} \quad (j = i) \end{aligned}\right\} \tag{4.5}$$

and the sensitivity coefficients ($\partial n_i / \partial A_j$) and ($\partial n_i / \partial f_j$) are given by

$$\left.\begin{aligned} \left(\frac{\partial n_j}{\partial A_j} \right) &= f_j \\ \left(\frac{\partial n_j}{\partial f_j} \right) &= A_j \end{aligned}\right\} \tag{4.6}$$

The overall standard uncertainty of x_i is therefore can be written as follows:

$$\begin{aligned} u^2(x_i) = &\left[x_i (1 - x_i) \right]^2 \left[u_r^2(f_i) + u_r^2(A_i) \right] + \sum_{j \neq i} (x_i x_j)^2 \left[u_r^2(f_j) + u_r^2(A_j) \right] + \left[\left(\partial x_i / \partial T \right)_p u(T) \right]^2 \\ &+ \left[\left(\partial x_i / \partial p \right)_T u(p) \right]^2 \end{aligned} . \tag{4.7}$$

Here, $u_r(f_i)$ is the standard *relative* uncertainty of the chromatographic response factor for component i, as determined in the calibration step, $u_r(A_i)$ is the standard *relative* uncertainty of the response peak area, as determined during the measurements, and $u(T)$ and $u(p)$ are the standard uncertainties of temperature and pressure, respectively. The differential coefficients $(\partial x_i / \partial T)_p$ and $(\partial x_i / \partial p)_T$ were estimated from the experimental data, and $u_r(f_j)$ was determined from the relation

$$u_r^2(f_j) = \left[u_r^2(n_j) + u_r^2(A_j)\right]_{cal}, \quad (4.8)$$

where $u_r(n_j)$ is the standard *relative* uncertainty of the calculated amount of each pure component j in the sampling loop and subscript 'cal' denotes the calibration condition. The standard relative uncertainty $u_r(n_j)$ is further related to the uncertainties of the pressure, temperature, and the EoS model used.

The standard uncertainties calculated for the systems studied in the work are included with experimental measurements which are provided in Chapters 6 and 7.

4.6 Apparatus Validation

The current apparatus was validated previously by measuring VLE of (CO_2 + $C_{10}H_{22}$) [161], (CO_2 + C_7H_{16}) [169], and (CO_2 + H_2O) [160], and they were found to be in good agreement with the literature data. As a further validation, phase behaviour data were measured for each mixture of interest in this work and the results were compared with available literature data measured at the same conditions. This is covered in Chapters 5 and 6 under Comparison of VLE Data with Literature Data sections.

4.7 Experimental Challenges and Issues

During the experimental work, we faced some difficulties and issues that caused some delay in the work progress. Examples of these issues are reported below.

4.7.1 Flame Ionization Detector (FID) Ignition Malfunction

As mentioned above, the GC is equipped with a Thermal Conductivity Detector (TCD) connected in series with two Flame Ionization Detectors (FIDs); one FID for each column. One of the FIDs could not be ignited. Referring to the troubleshooting procedure provided in the manual of Shimadzu, the FID parts (igniter, collector and jet) were disassembled as shown in Figure 4.6. It was found that the FID jet tip was clogged and dirty. The jet was cleaned, and the FID got to work properly.

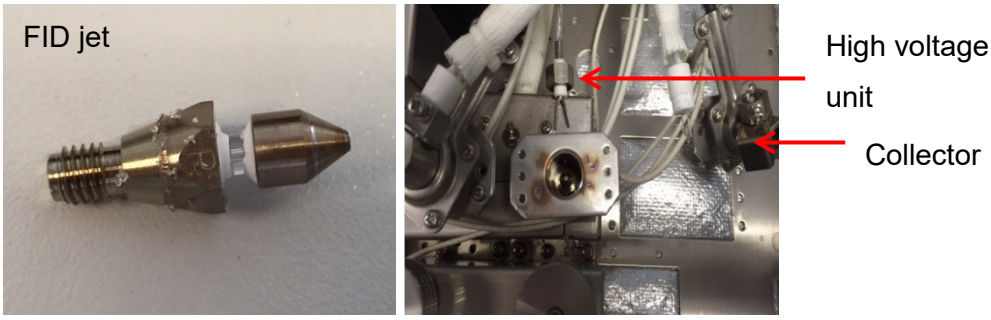

Figure 4.6: Schematic of the FID unit.

4.7.2 View Cell (VC) Sealing

The equilibrium view cell (VC) requires two O-rings with internal diameter of 29.74 mm for the two sapphire windows and four O-rings for the four plugs with internal diameter of 10.6 mm used for the sampling and re-circulation lines as shown in Figure 4.7 (right). The main type of O-ring used for sealing was Hydrogenated Nitrile (Elast-O-Lion 101, James Walker), which has typical operating temperatures from (233 to 433) K. However, Viton O-rings (fluorocarbon rubber, Polymax Ltd), which has capability of temperatures from (255 to 473) K, were also used in some systems. Both O-rings were frequently damaged and worn out due to different causes including compression and decompression process in the view cell and exposure to compounds that were not suitable to be used for these kinds of seals. This resulted in having leaks from one or both sapphire windows and plugs. A photo of the damaged O-rings is shown in Figure 4.7 (left).

Figure 4.7: Schematic of the O-rings in the VC. Left shows the damages, Right shows the locations of the sealing required in the VC.

4.7.3 Internal Piston Stuck in One End of Pump Nipple

The two-channel reciprocating recirculation pump, shown in Figure 4.8, is used to recirculate the equilibrium phases concurrently. The pump was magnetically coupled, and its body consisted of a stainless steel nipple of 6.4 mm external diameter, (3.00 ± 0.05) mm internal diameter and length of (100.0 ± 0.5) mm. The internal piston inside the nipple was fabricated from a magnetic stainless steel and was 15 mm in length and 2.95 mm in diameter. The nipple and internal piston are shown in Figure 4.9 (right). When the system was under vacuum and the external magnet was located close to one of the nipple ends (see Figure 4.9 left) the

coupling between the internal magnetic piston and the external magnet was broken and the external piston stuck to one end. The piston was released by disassembling the nipple from both ends. To avoid the occurrence of this issue the external magnet needs to be in the center of the nipple before putting the system under vacuum. The external magnet can be moved manually from the top of the push rod.

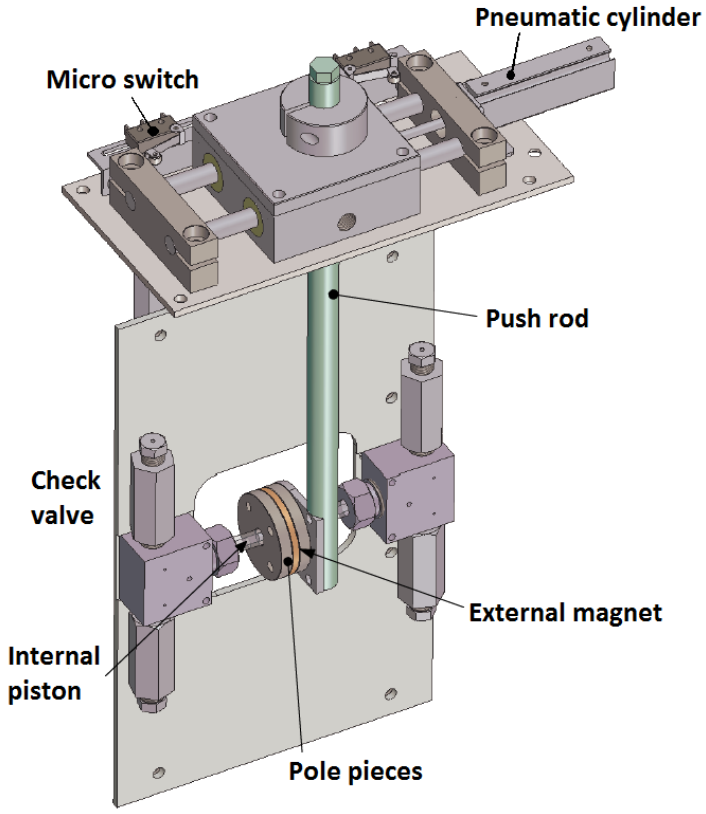

Figure 4.8: 3D view of the magnetic recirculation pump.

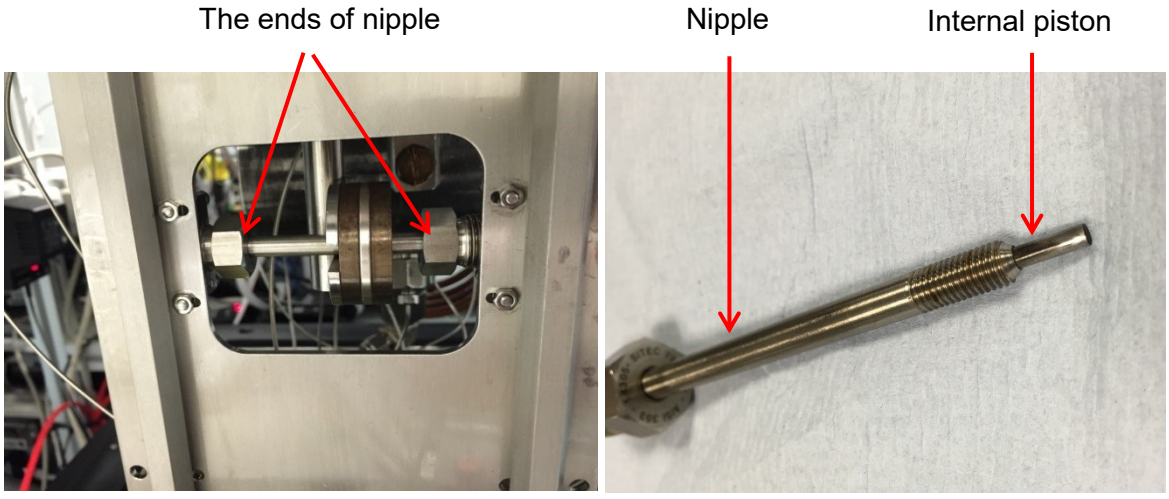

Figure 4.9: Images of the external magnet, nipple and internal piston.

Chapter 5: Phase Behavior Measurements of Binary Systems

5.1 Overview

In this Chapter, fluid-phase equilibrium measurements on the binary systems (methyl propanoate + carbon dioxide) and (butanoic acid + carbon dioxide) were carried out with the high-pressure analytical apparatus. The measurements for the (methyl propanoate + carbon dioxide) mixture, in collaboration with MSc student, Rami Bamagain, who performed some experimental work, were made along six isotherms at temperatures from (298.15 to 423.15) K and at pressures up to near the mixture critical pressure at each temperature while for the mixture (butanoic acid + carbon dioxide) the measurements were made along eight isotherms at temperatures from (323.13 to 423.2) K and pressures up to the mixture critical pressures. Vapour-liquid equilibrium (VLE) data obtained for the mixtures have been compared with the predictions of SAFT-γ Mie model. The group interaction parameters in SAFT-γ Mie reported in literature have been revised by fitting to the new experimental VLE data. After parameters optimisation, the model was found to be in a good agreement with the measured VLE data for both bubble and dew points. The experimental data were also compared with the description of the Peng Robinson equation of state (PR EoS) combined with the classical one-fluid mixing rules integrating one temperature-independent binary interaction parameter for (methyl propanoate + carbon dioxide) system and two temperature-independent binary interaction parameters for (butanoic acid + carbon dioxide) system. The results after tuning show that the PR EoS can also predict well the system measured data, except in the critical regions in which PR EoS shows overprediction.

5.2 (Methyl Propanoate + Carbon Dioxide) System

5.2.1 Introduction

In this work, the binary system (methyl propanoate + CO_2) was selected to represent (fatty acid methyl ester + CO_2). Methyl propanoate ($C_2H_5COOCH_3$, also known as propanoic acid methyl ester) is an ester containing the COO functional group found in fatty acid methyl esters, which are the major components of biodiesel. Hongling et al. [170] reported the VLE data for this system at pressures from (1 to 12) MPa and temperatures in the range from (313.15 to 373.15) K. The measurements were carried out in a cylindrical autoclave with a movable piston and observation window. To our knowledge, this is the only study of the phase behaviour for this system that has been published. There are a few published data for systems of the type

(fatty acids esters + CO_2) measured at conditions of low temperatures and pressures as summarised in Table 5.1. However, these phase behaviour data are still limited.

Table 5.1: The literature review of phase equilibrium for (fatty acids esters + CO_2)[a].

System	Formula	Temperatures and Pressures Ranges (Min – Max)[b]		Ref.
		T/K	*p*/MPa	
(Ethyl propanoate + CO_2)	$C_5H_{10}O_2$	303.15 – 373.00	1.74 – 10.97	[171, 172]
(Propyl propanoate + CO_2)	$C_6H_{12}O_2$	313.00 – 373.00	1.00 – 12.00	[170]
(Ethyl butyrate + CO_2)	$C_6H_{12}O_2$	323.20 – 393.20	10.0 – 28.70	[173, 174]

[a]Notation: Showing only works reporting measurements on both liquid and vapour phases.
[b]Notation: Minimum and maximum conditions reported in literature.

5.2.2 Comparison of VLE Data with Literature Data

To validate the calibration curves of (methyl propanoate and carbon dioxide) mixture, VLE measurements were made on the binary system ($CH_3CH_2COOCH_3$ + CO_2) at T = 373.15 K, and at pressures up to 12 MPa and the results were compared with the experimental study of Hongling et al. [170] as shown in Figure 5.1. As can been seen in the figure, good agreement is observed at high pressures for both bubble and dew points, but some discrepancies are observed at low pressures in the bubble point curve. The difference between the data reported in literature and the data in the current study might be due to different experimental methodologies for sampling, calibration and measurements.

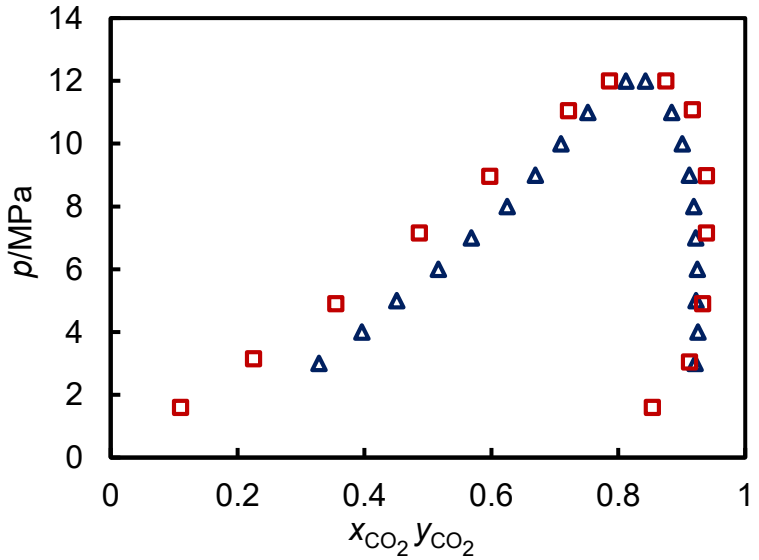

Figure 5.1: Isothermal pressure-composition (*p, x*) phase diagram for the (methyl propanoate + carbon dioxide) system at T = 373.15 K; □, this work; Δ, Hongling et al. [170].

5.2.3 Experimental Results

The binary system ($CH_3CH_2COOCH_3$ + CO_2) exhibits type I phase behaviour according to the classification of Van Konynenburg and Scott [48, 49] (described in Chapter 2, section 2.1.3) at temperatures in the range from (283.15 to 423.15) K and pressures from (1 to 12) MPa. Mixtures of this type show vapor-liquid equilibrium (VLE). The compositions of the coexisting fluid phases have been determined along six isotherms at temperatures of (298.15, 323.15, 348.15, 373.15, 398.15 and 423.15) K and pressures up to the mixture critical pressure for each isotherm. The experimental VLE measurements are given in Table 5.2 and shown graphically in Figure 5.2 as isothermal pressure-composition (p, x) phase diagram. The estimated standard uncertainties, which were obtained as described in Chapter 4 section 4.5, as well as K values, which are explained below in section 5.2.5, are included in Table 5.2.

Table 5.2: Experimental VLE data for [$CH_3CH_2COOCH_3$ (1) + CO_2 (2)] at temperatures T and pressures p[a].

p/MPa	x_1^{exp}	$u(x_1)$	y_1^{exp}	$u(y_1)$	K_1	K_2
			T = 298.15 K			
1.03	0.7907	0.0046	0.0073	0.0002	4.7434	0.0092
2.04	0.5822	0.0056	0.0002	0.0001	2.3933	0.0003
3.01	0.4259	0.0055	0.0001	0.0001	1.7418	0.0003
4.02	0.2709	0.0045	0.0002	0.0001	1.3714	0.0005
5.02	0.1369	0.0030	0.0002	0.0001	1.1585	0.0012
6.01	0.0279	0.0017	0.0091	0.0002	1.0193	0.3273
			T = 323.15 K			
1.07	0.8593	0.0032	0.0489	0.0010	6.7591	0.0569
2.07	0.7300	0.0044	0.0271	0.0006	3.6035	0.0372
3.05	0.6095	0.0051	0.0232	0.0005	2.5016	0.0381
4.03	0.4996	0.0053	0.0214	0.0004	1.9558	0.0428
5.46	0.3491	0.0048	0.0264	0.0005	1.4958	0.0757
7.08	0.2007	0.0035	0.0157	0.0005	1.2315	0.078
8.07	0.1183	0.0024	0.0188	0.0006	1.1129	0.1588
8.65	0.0759	0.0019	0.0254	0.0007	1.0547	0.3346
			T = 348.15 K			
1.56	0.8537	0.0029	0.0737	0.0014	6.3311	0.0863
3.00	0.7191	0.0043	0.0455	0.0009	3.3976	0.0633
4.61	0.5803	0.0051	0.0347	0.0007	2.2997	0.0599
6.08	0.4629	0.0051	0.0358	0.0007	1.7951	0.0774
7.54	0.3556	0.0047	0.0329	0.0006	1.5007	0.0925
9.13	0.2481	0.0039	0.0383	0.0008	1.2790	0.1545
10.55	0.1504	0.0027	0.0771	0.0015	1.0862	0.5130
			T = 373.15 K			
1.60	0.8893	0.0023	0.1459	0.0025	7.7136	0.1641
3.15	0.7742	0.0037	0.0875	0.0016	4.0417	0.1130

5.04	0.6447	0.0047	0.0668	0.0013	2.6267	0.1036
7.16	0.513	0.0051	0.0605	0.0011	1.9291	0.1180
8.96	0.4023	0.0049	0.0606	0.0012	1.5717	0.1506
11.05	0.2779	0.0041	0.083	0.0016	1.2700	0.2986
12.00	0.2135	0.0035	0.1247	0.0022	1.1128	0.5842
			T = 398.15 K			
3.06	0.8294	0.0030	0.1568	0.0027	4.9426	0.1890
4.50	0.7418	0.0039	0.1222	0.0022	3.3999	0.1648
5.90	0.6635	0.0046	0.1082	0.0019	2.6502	0.1630
7.59	0.5694	0.0050	0.0995	0.0018	2.0916	0.1747
9.05	0.4908	0.0051	0.0997	0.0018	1.7681	0.2032
10.39	0.4196	0.0049	0.1094	0.0020	1.5344	0.2607
12.15	0.3158	0.0044	0.1553	0.0027	1.2346	0.4917
12.60	0.278	0.0041	0.1847	0.0030	1.1293	0.6643
			T = 423.15 K			
4.00	0.8164	0.0031	0.2363	0.0037	4.1584	0.2895
5.50	0.7375	0.0040	0.1886	0.0031	3.0907	0.2558
7.00	0.6605	0.0046	0.1688	0.0028	2.4481	0.2555
8.50	0.5869	0.0049	0.1624	0.0027	2.0273	0.2768
10.00	0.5121	0.0051	0.1709	0.0029	1.6992	0.3337
11.48	0.4308	0.0050	0.1911	0.0031	1.4213	0.4435
12.47	0.3456	0.0046	0.2586	0.0039	1.1329	0.7484

[a]Notation: x_i and y_i denote the mole fraction of component i in the liquid phase, the mole fraction of component i in the vapour phase, respectively. K_i denotes the K values of component i. $u(x_i)$ and $u(y_i)$ denote standard uncertainty of x_i and y_i, respectively. $u(T)$ = 0.1 K and $u(p)$ = 0.01 MPa.

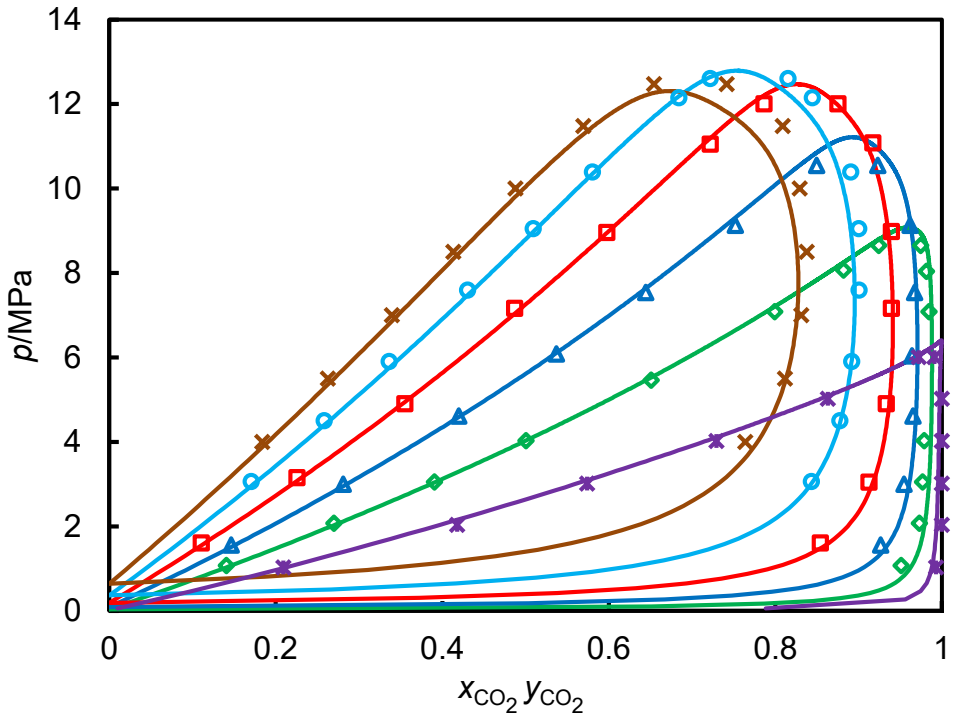

Figure 5.2: Isothermal pressure-composition (*p, x*) phase diagram for the (methyl propanoate + carbon dioxide) system: ✱, *T* = 298.15 K; ◇, *T* = 323.15 K; Δ, *T* = 348.15 K; □, *T* = 373.15 K; ○, *T* = 398.15 K; ×, *T* = 423.15 K. The continuous curves are the calculations from SAFT-γ Mie (indicated by colours at each temperature).

5.2.4 Modelling

In this work, SAFT-γ Mie model was used to describe the phase behaviour of this mixture. The data were also modelled using the Peng Robinson equation of state (PR EoS) combined with classical one-fluid mixing rules incorporating a temperature-independent binary interaction parameter k_{ij}. The SAFT-γ group contribution approach was described previously (Chapter 3 section 3.2.2) and a brief reference is made here for the particular mixture (methyl propionate + carbon dioxide). In the SAFT-γ Mie approach, the molecular properties are obtained by dividing the molecules into distinct functional groups representing the structure of a molecule. The parameters that fully describe the functional groups in this system are the number of identical segments that each group comprises, the shape factor S_k, the energy of interaction ε_{kk} between the segments, the segment diameter σ_{kk}, and the values λ_{kk}^{r} and λ_{kk}^{a} the repulsive and attractive exponents, respectively. Carbon dioxide is modelled by means of the molecular group CO_2 [157], and its like group parameters have been already published in literature [157]. Methyl propanoate ($CH_3CH_2COOCH_3$) is composed of two CH_3, one CH_2, and one COO. The

like and unlike functional group parameters for the mixture ($CH_3CH_2COOCH_3$ + CO_2) are collected in Table 5.3 and Table 5.4, respectively. The COO parameter is treated as non-associating as esters do not self-associate, however, association sites need to be included in some polar mixtures containing alkanols or water to capture the unlike associations [135, 175].

Table 5.3: SAFT-γ Mie like group parameters used in this work [44, 157].

group k	v^*_k	S_k	σ_{kk}/Å	(ε_{kk}/k_B)/K	λ^a_{kk}	λ^r_{kk}	Ref.
CH_3	1	0.57255	4.0773	256.77	6.000	15.050	[44]
CH_2	1	0.22932	4.8801	473.39	6.000	19.871	[44]
COO	1	0.65264	3.9939	868.92	6.000	31.189	[44]
COO	1	0.65264	3.9939	503.11	6.000	31.189	This work[a]
CO_2	2	0.84680	3.0500	207.89	5.055	26.408	[157]

[a]Notation: The parameter ε_{kk} of COO was only optimised in this approach.

Table 5.4: SAFT-γ Mie unlike group parameters used in this work [44, 157].

group k	group l	(ε_{kl}/k_B)/K	λ^r_{kl}	Ref.
CH_3	CH_2	350.77	CR	[44]
CH_3	CO_2	205.70	CR	[157]
CH_3	COO	402.75	CR	[44]
CH_3	COO	425.79	CR	This work[a]
CH_3	COO	532.50	22.46	This work[b]
CH_2	CO_2	276.45	CR	[157]
CH_2	COO	498.86	CR	[44]
CH_2	COO	447.02	CR	This work[a]
CH_2	COO	470.00	30.14	This work[b]

[a]Notation: Only ε_{kl} for COO-CH_3 and COO-CH_2 was refined.
[b]Notation: The parameters ε_{kl} and λ^r_{kl} for COO-CH_3 and COO-CH_2 as well as ε_{kk} for COO were refined.
CR indicates the parameter was determined from the combining rule. All other values given in the table have been estimated from experimental data.

The matrix of biodiesel functional groups explained in Chapter 3 section 3.2.3 is represented here in Table 5.5 for the particular functional groups comprising the mixture and it shows the group-group interaction parameters optimised in this work and those reported in literature.

Table 5.5: Groups developed within SAFT-γ Mie

	CH_3	CH_2	COO	CO_2
CH_3	O			
CH_2	O	O		
COO	✓	✓	✓	
CO_2	O	O	✓	O

Ticks indicate interaction parameters estimated and optimised in this work, while circle indicates the interactions reported in literature.

The like group parameters describing the functional group COO and the unlike interactions for COO-CH_3 and COO-CH_2 were estimated in literature using experimental vapour pressures (p_{vap}) and saturated-liquid densities (ρ_{sat}) of *n*-alkyl acetates (ethyl acetate to *n*-heptyle acetate). As reported in the work of Papaioannou et al. [135], the overall percentage average absolute deviations (Δ_{AAD}, Equation 3.22) are 0.83% for vapour pressures and 0.24% for saturated-liquid densities. However, there are other esters (*n*-alkyl propanoates, butanoates, and other esters) having the same number of functional groups (COO, CH_3, and CH_2) and are different in the chemical chain structure. Since SAFT-γ Mie describes systems based on their functional groups it is unable to distinguish between different esters having the same number and type of functional groups. Examples of the esters that have ($2CH_3$, $4CH_2$, 1COO) are pentyl acetate, butyl propanoate, propyl butyrate, ethyl valerate, and methyl caproate. The SAFT-γ Mie model describes vapour pressure and saturated-liquid density data of pentyl acetate well, but the prediction deviates from the experimental data for the other esters as shown graphically (black curves) in Figure 5.3.

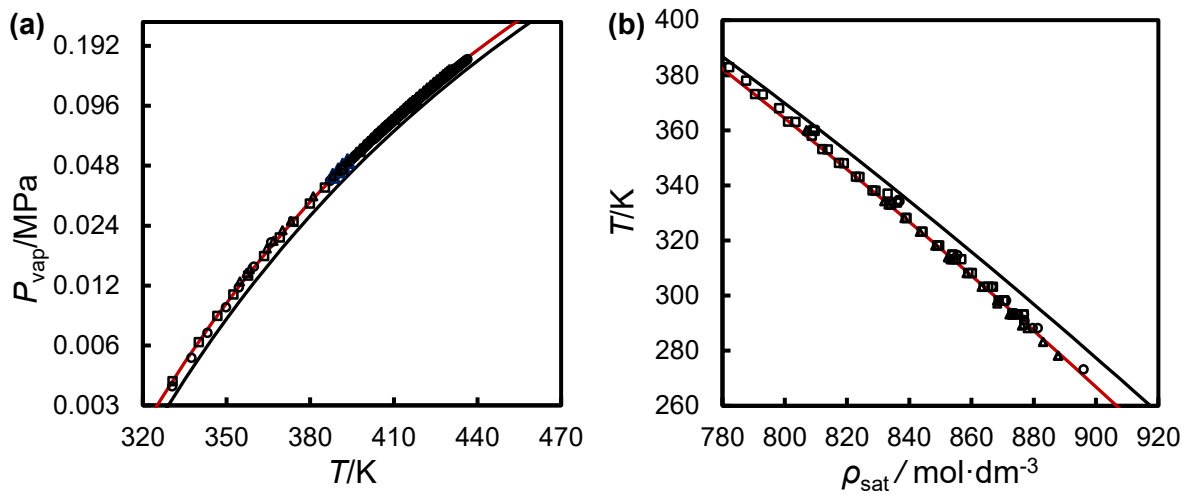

Figure 5.3: The description of optimised SAFT-γ Mie for the fluid-phase equilibria of *n*-alkyl esters having the same number of functional groups ($2CH_3$, $4CH_2$, 1COO) at temperatures from (273 to 436) K: (a) vapour pressures; and (b) saturated-liquid densities. The symbols are O: butyl propanoate [176-178]; Δ: propyl butyrate [177, 179]; □: ethyl valerate [180, 181]. The black continuous curve is the calculation from SAFT-γ Mie reported in literature. The red continuous curve is the calculation from SAFT-γ Mie after optimisation.

The overall deviations (Δ_{AAD}) were found to be 12.41% for vapour pressures and 0.51% for saturated-liquid densities. The same deviations were seen in the other esters that have the same number of functional groups (e.g. $2CH_3$, $3CH_2$, 1COO: butyl acetate, propyl propanoate, ethyl butyrate and methyl valerate). It has been noticed that these deviations made a difference in our cross interactions involving COO functional group and subsequently affected the description of the binary and ternary systems, therefore; an optimisation for the COO like parameters and cross interactions COO-CH_3 and COO-CH_2 was made in order to have more accurate prediction of thermodynamic data. As can be seen in Figure 5.3, the fluid-phase equilibria data of most of the esters apart from the *n*-alkyl acetates, which were used for parameters estimation in literature, are within the trend. Therefore, many adjustment approaches in parameters were carried out taking into account the phase behaviour data of these different esters. These optimisations included dispersion energies ε_{kl} between COO-CH_3 and COO-CH_2, dispersion energies ε_{kl} and repulsive exponent λ_{kl}^{r} between COO-CH_3 and COO-CH_2, segment energy of interaction ε_{kk} of COO and dispersion energies ε_{kl} and repulsive exponent λ_{kl}^{r} between COO-CH_3 and COO-CH_2, segment energy of interaction ε_{kl} of COO and dispersion energies ε_{kl} between COO-CH_3 and COO-CH_2. It was found that optimising the unlike dispersion energy ε_{kl} between COO-CH_3 and COO-CH_2 and keeping the other parameters unchanged as reported would predict well the fluid-phase equilibria of other esters as shown in Figure 5.3. The overall deviations (Δ_{AAD}) were found to be 2.56% for vapour

pressures and 0.20% for saturated-liquid densities. The deviations are summarised in Table 5.6.

Table 5.6: Percentage average absolute deviations (Δ_{AAD}) for vapour pressures $p_{vap}(T)$ and for saturated-liquid densities $\rho_{sat}(T)$ determined with SAFT-γ Mie for the *n*-alkyl esters having the same number of functional groups ($2CH_3$, $4CH_2$, 1COO).

Compound	T range/K	n	Δ_{AAD} (p_{vap}), literature SAFT	Δ_{AAD} (p_{vap}), optimised SAFT	T range/K	n	Δ_{AAD} (ρ_{sat}) literature SAFT	Δ_{AAD} (ρ_{sat}) optimised SAFT
Butyl-propanoate	306-436	145	11.17	2.77	273-359	13	0.34	0.26
Propyl-butyrate	355-430	50	15.73	1.89	278-360	18	0.65	0.14
Ethyl-valerate	331-418	20	13.02	2.69	298-423	42	0.52	0.18

After that, the cross interactions between COO and CO_2 were determined using our experimental VLE measured in this work for the binary mixture ($CH_3CH_2COOCH_3$ + CO_2). In this case, the optimised unlike dispersion energy ε_{kl} between COO-CH_3 and COO-CH_2 have been used. Using low, medium and high temperatures of the experimental data in parameters estimation, it was found that the best fitting of SAFT-γ Mie to the experimental data, as shown in Figure 5.2, was achieved at a value of 429.1 for ε_{kl}. The unlike repulsive exponent λ_{kl}^{r}, the unlike attractive exponent λ_{kl}^{a} and the segment diameter σ_{kl} between COO-CO_2 were calculated using appropriate combining rules which were described previously (Chapter 3, section 3.2.2).

The experimental data were also modelled using the Peng Robinson equation of state (PR EoS). The model and its interaction parameters were described previously in Chapter 3, sections 3.1.3 and 3.1.4. It was found that tuning the temperature-independent binary interaction parameter k_{ij} provides the best fit to the experimental VLE data of the binary mixture for all the isotherms as shown in Figure 5.4. The value of the optimised interaction parameter k_{ij} was found to be 0.0045.

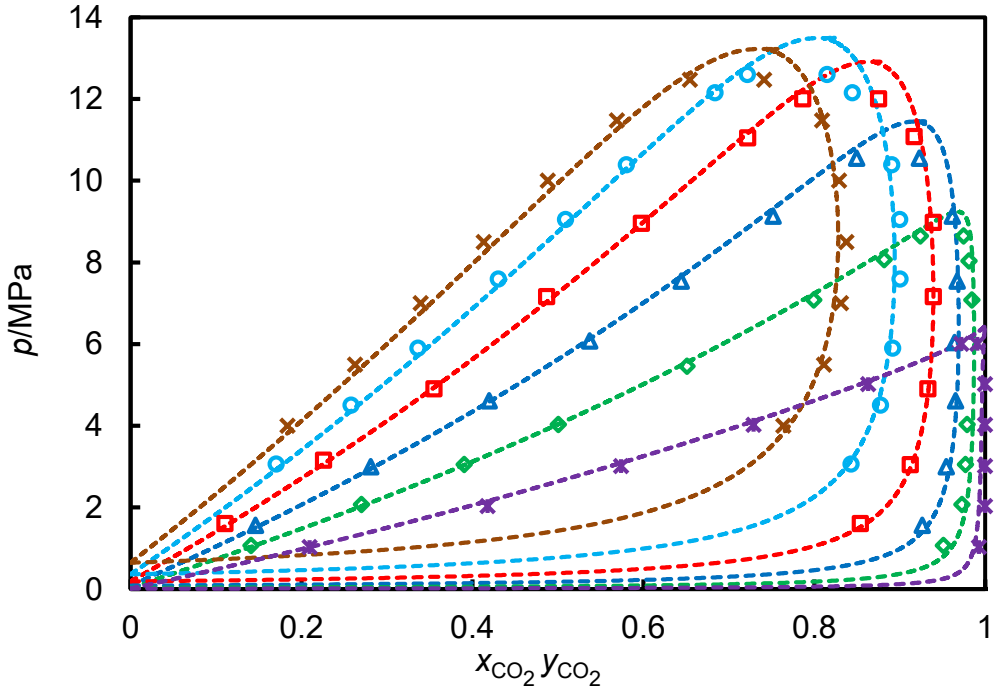

Figure 5.4: Isothermal pressure-composition (*p, x*) phase diagram for the (methyl propanoate + carbon dioxide) system: ✱, *T* = 298.15 K; ◇, *T* = 323.15 K; Δ, *T* = 348.15K; □, *T* = 373.15 K; ○, *T* = 398.15 K; ×, *T* = 423.15 K. The dashed curves are the calculations from PR EoS (indicated by colours at each temperature).

5.2.5 Discussion and Comparison with Experiments

It is clear from Figure 5.2 that SAFT-γ Mie model after parameters optimisations predicts well the bubble and dew points of the binary system (methyl propanoate + carbon dioxide) at all temperatures. A small deviation is observed in the dew curves near the critical region at high temperature isotherms e.g. 423 K and 398 K. This deviation could be minimized when we considered methyl propanoate only in parameters estimation, but SAFT-γ Mie approach is based on functional groups, and various fluid-phase equilibria experimental data for different compounds should be involved in order to make the model valid for all the systems comprising the functional groups. The description of PR EoS for the system, as shown in Figure 5.4, is good for all the isotherms, but deviations in the critical regions are observed especially at high temperatures.

Effect of temperature on the solubility of supercritical CO_2 in the ester. Figure 5.5 shows the isothermal pressure-composition (*p, x*) phase diagram for the (methyl propanoate + carbon dioxide) system in the CO_2-rich gas phase (Figure 5.5b and d) and in the ester-rich liquid phase (Figure 5.5a and c) at temperatures from (283.15 to 423.15) K. From these figures it

can be observed that the solubility of CO_2 in the ester decreases when temperature increases at constant pressure. On the other hand, the concentration of the ester in the CO_2-rich phase increases when temperature increases at constant pressure.

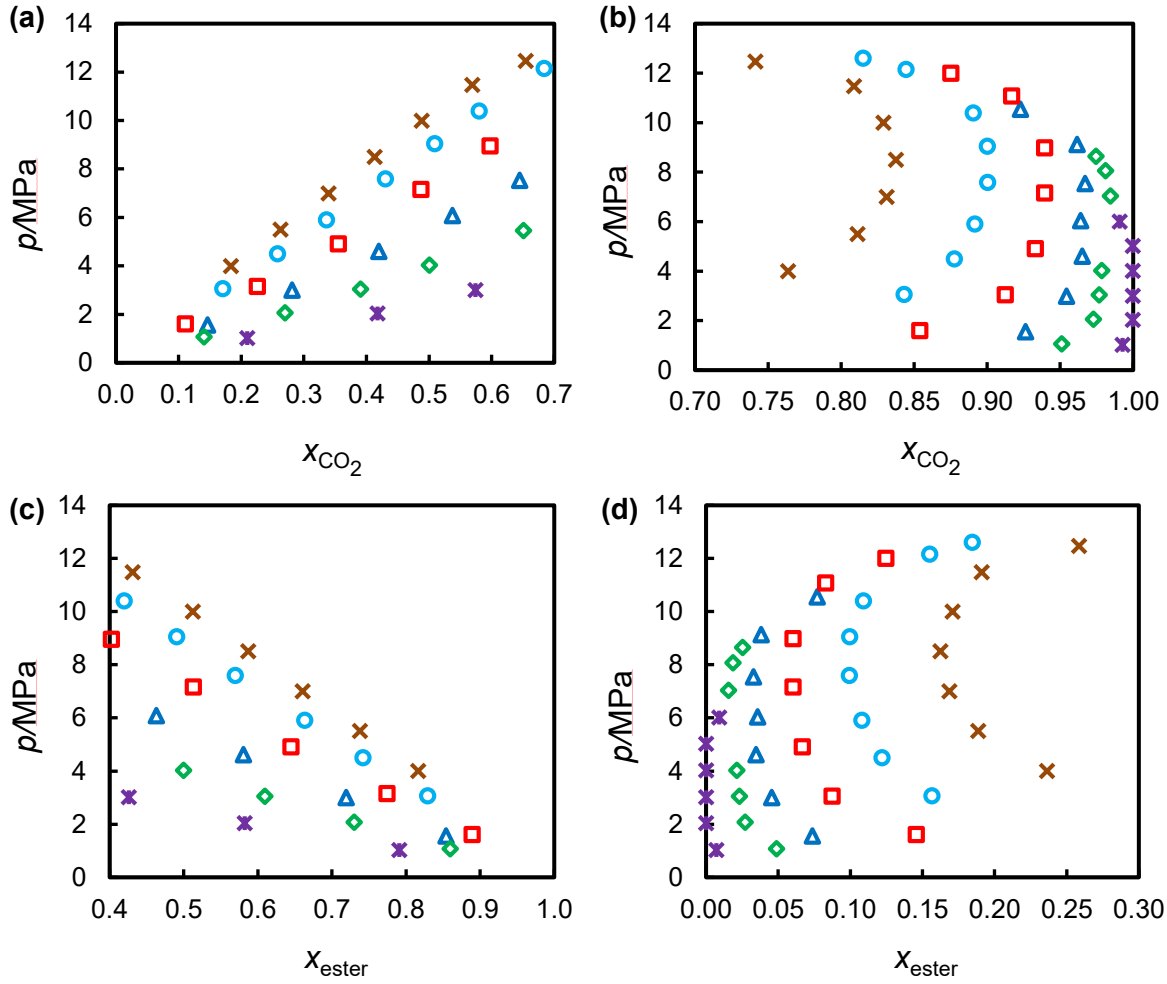

Figure 5.5: Isothermal pressure-composition (*p, x*) phase diagram for the (methyl propionate + carbon dioxide) system in the CO_2-rich gas phase (b, d) and in the Ester-rich liquid phase (a, c): ✱, T = 298.15 K; ◇, T = 323.15; Δ, T = 348.15 K; □, T = 373.15 K; ○, T = 398.15 K; ✖, T = 423.15 K.

The vapour-liquid ratios of $CH_3CH_2COOCH_3$ (1) and CO_2 (2) can be expressed as K values as follows:

$$K_1 = \frac{y_1}{x_1} \text{ and } K_2 = \frac{y_2}{x_2}. \tag{5.1}$$

The values of K_1 and K_2 are given in Table 5.2. They are also plotted against pressures at different isotherms (K-p) in Figure 5.6a, which includes SAFT-γ Mie prediction, and Figure 5.6b, which includes PR EoS prediction. As can be seen from the figures, K_1 decreases when

pressure increases for a constant temperature. K_2, on the other hand, increases with the rising pressures at constant temperatures.

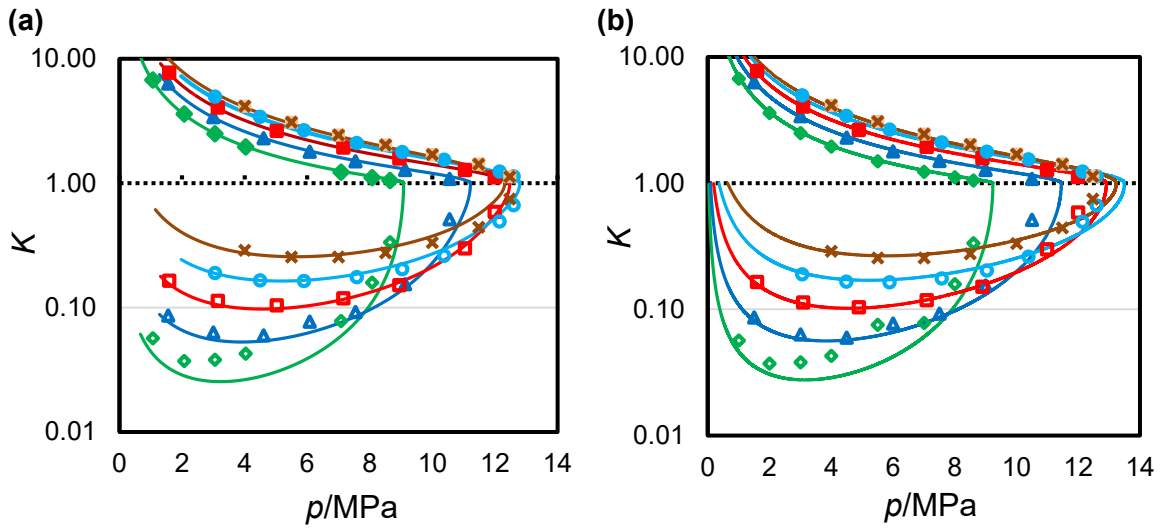

Figure 5.6: *K*-*p* for the (methyl propionate + carbon dioxide) system: ◇ and ◆ , T = 323.15; Δ and ▲, T = 348.15 K; □ and ■, T = 373.15 K; ○ and ●, T = 398.15 K; × and × , T = 423.15 K The continuous curves are: (a) optimised SAFT-γ Mie prediction and (b) optimised PR EoS at the corresponding temperatures (indicated by colours). Solid symbols indicate K_1 and unfilled symbols indicate K_2.

Effect of pressure on the solubility of supercritical CO_2 in the ester. The pressure effects on the system can also be seen in Figure 5.5 and Figure 5.6. The solubility of CO_2 in the ester increases when pressure increases at constant temperature. The concentration of the ester in the CO_2-rich phase at constant temperature decreases when pressure increases at low pressures and then starts increasing with pressure as a result of the decline in CO_2 concentration in the vapour phase.

Critical point estimation. In this particular system, the critical points in all isotherms were not observed and measured. Nevertheless, the critical points have been estimated using the scaling law for binary mixtures, as described by Westman et. al. [182] (more details are in references [183, 184]):

$$z_{CO_2} = z_{CO_2,c} + (\lambda_1 + \varepsilon\frac{\lambda_2}{2})(p_c - p) + \varepsilon\frac{\mu}{2}(p_c - p)^{\beta}, \tag{5.2}$$

where,

$$\varepsilon = \begin{cases} 1 \text{ for bubble points,} \\ -1 \text{ for dew points} \end{cases}.$$

Here, z_{CO_2} is the boiling point or dew point, CO_2 mole fraction at pressure p, p_c is the critical pressure, and $z_{CO_{2,c}}$ is the critical composition. β is a universal scaling exponent, which was fixed at 0.325. The other parameters of the equation were regressed by using data close to the critical point. The critical points were also estimated from SAFT-γ Mie calculation. These critical points obtained by the above scaling law and SAFT-γ Mie were provided in Table 5.7 and plotted in Figure 5.7 at the experimental isotherms from (323.15 to 423.15) K. As seen in Figure 5.7 and Table 5.7, the critical points calculated by Equation 5.2 deviates slightly from SAFT predictions, and this is probably due to the regression trials.

Table 5.7: Critical points estimated from SAFT-γ Mie and scaling law.

T/K	p_c, SAFT/MPa	p_c, Scaling Law /MPa	$z_{CO_{2,c}}$
323.15	9.1	8.9	0.96
348.15	11.5	11.0	0.89
373.15	12.5	12.3	0.81
398.15	12.8	12.7	0.77
423.15	12.3	12.5	0.70

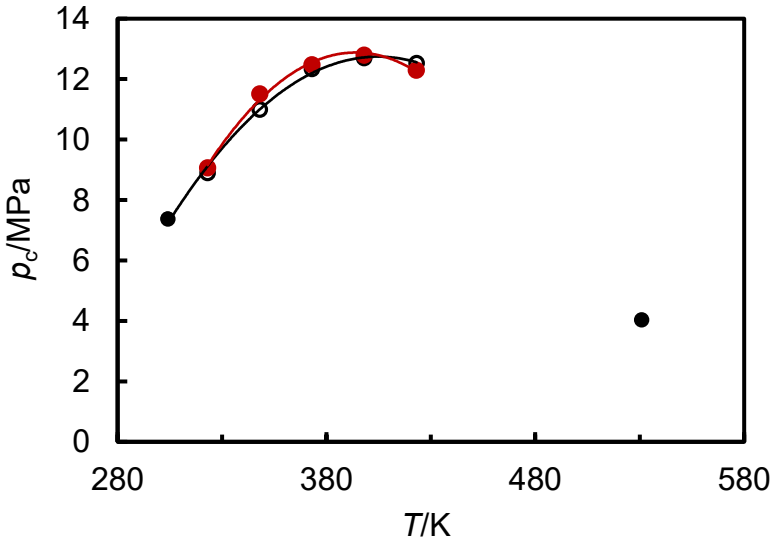

Figure 5.7: Critical point pressures as a function of temperature calculated by SAFT-γ Mie and scaling method for the (methyl propanoate + carbon dioxide) system: ●, SAFT-γ Mie prediction; O, scaling method (Equation 5.2); filled black symbols represent p_c for pure CO_2 and pure methyl propionate; solid lines represent polynomial fit to the data for the corresponding method (indicated by colours).

5.2.6 Conclusion

Experimental study of vapour-liquid equilibria for ($CH_3CH_2COOCH_3$ + CO_2) on six isotherms at temperatures from (298.15 to 423.15) K with pressures up to 12 MPa was reported. The unlike dispersion energy ε_{kl} between COO-CH_3 and COO-CH_2 has been adjusted using methyl propanoate and different series of esters. The cross interactions between COO and CO_2 were then determined using our experimental data. The experimental results have been compared with predictions of the optimised SAFT-γ Mie and PR equation of states. Both are in a good agreement with the experimental measurements.

5.3 (Butanoic acid + Carbon Dioxide) System

5.3.1 Introduction

In this work, the binary system (butanoic acid + carbon dioxide) was studied. Butanoic acid ($CH_3(CH_2)_2COOH$), also known as butyric acid, is a short fatty acid containing the COOH functional group found in the free fatty acids, which react with methanol in supercritical state to produce biodiesel (so-called esterification reaction as in Equation 2.14).

Vapour-liquid equilibrium data for this system was studied by Byun et al. [185] and to our knowledge it is the only published study of the phase behaviour for this system. However, there are a few published data for systems of the type (carboxylic acids + CO_2) measured at conditions of low temperature and pressures and some of the works are summarised in Table 5.8. These phase behaviour data are still limited.

Table 5.8: The literature review of phase equilibrium for (carboxylic acids + CO_2)[a].

System	Acid (C:D)	Temperatures and Pressures Ranges (Min – Max)[b]		Ref.
		T/K	*p*/MPa	
(Hexanoic acid + CO_2)	6:0	308.15 – 373.15	2.53 – 20.48	[185, 186]
(Octanoic acid + CO_2)	8:0	308.15 – 373.15	2.41 – 9.29	[185]
(Decanoic acid + CO_2)	10:0	323.20 – 393.20	10.0 – 28.70	[187]
(Oleic acid + CO_2)	18:1	313.15 – 353.15	3.36 – 33.60	[141, 142, 145]

[a]Notation: Showing only works reporting measurements on both liquid and vapour phases.
[b]Notation: Minimum and maximum conditions reported in literature.

5.3.2 Comparison of VLE Data with Literature Data

VLE measurements were made on the binary system (butanoic acid + carbon dioxide) at T = 353.18 K and T = 373.13 K and pressures up to the mixture critical points, and the results were compared with the experimental study of Byun et al. [185] as shown in Figure 5.8. As seen in the figure, the experimental data measured in this work agree well with the literature data at both isotherms. A small difference was seen at the critical region at T = 373.13 K.

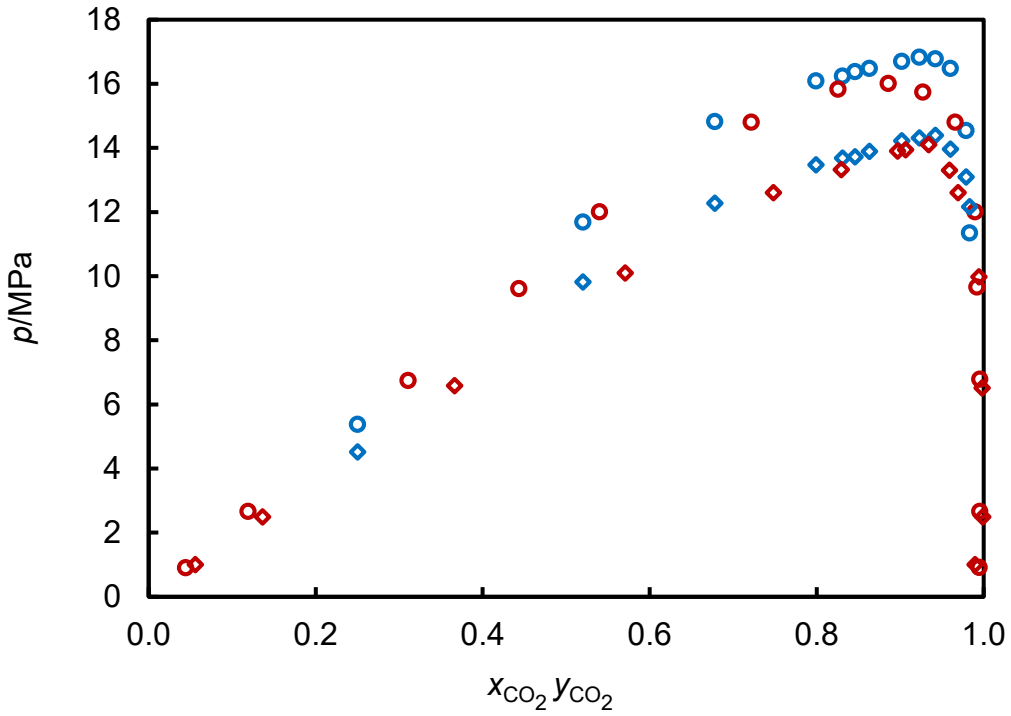

Figure 5.8: Isothermal pressure-composition (p, x) phase diagram for the (butanoic acid + carbon dioxide) system: circle, T = 373.13 K; diamond, T = 353.18 K. The RED symbols correspond to this work while the BLUE symbols correspond to literature data [185].

5.3.3 Experimental Results

The binary system ($CH_3(CH_2)_2COOH + CO_2$) exhibits type I phase behaviour according to the classification of Van Konynenburg and Scott [48, 49] at temperatures in the range from (323.13 to 423.2) K and pressures from (1 to 20) MPa. The compositions of the coexisting fluid phases have been determined along eight isotherms at temperatures of (323.13, 343.12, 353.18, 363.18, 373.13, 383.11, 403.2 and 423.2) K and pressures up to the mixture critical pressures. The experimental VLE measurements are given in Table 5.9 and Figure 5.9. The estimated standard uncertainties and K values are included in Table 5.9.

Table 5.9: Experimental VLE data for [$CH_3(CH_2)_2COOH$ (1) + CO_2 (2)] at temperatures T and pressures p[a].

p/MPa	x_1^{exp}	$u(x_1)$	y_1^{exp}	$u(y_1)$	K_1	K_2
			T = 323.13 K			
0.78	0.9341	0.0014	0.0000	0.0001	0.0000	15.1729
2.06	0.8268	0.0029	0.0000	0.0000	0.0000	5.7738
3.44	0.7091	0.0042	0.0000	0.0006	0.0000	3.4379
4.52	0.6162	0.0048	0.0000	0.0019	0.0000	2.6058
6.23	0.4614	0.0050	0.0004	0.0078	0.0008	1.8560
7.75	0.2983	0.0042	0.0024	0.0212	0.0080	1.4216
8.60	0.1844	0.0031	0.0030	0.0337	0.0162	1.2225
9.04	0.1013	0.0019	0.0087	0.0390	0.0857	1.1031
9.27	0.0706	0.0014	0.0108	0.0354	0.1523	1.0644
9.34	0.0562	0.0012	0.0181	0.0280	0.3216	1.0404
			T = 343.12 K			
1.50	0.9036	0.0061	0.0000	0.0001	0.0000	10.3728
2.05	0.8686	0.0063	0.0000	0.0001	0.0000	7.6098
3.49	0.7713	0.0068	0.0006	0.0001	0.0008	4.3699
6.57	0.5802	0.0076	0.0012	0.0004	0.0021	2.3791
8.47	0.4556	0.0077	0.0021	0.0011	0.0045	1.8332
10.56	0.2874	0.0071	0.0094	0.0024	0.0328	1.3901
11.58	0.1985	0.0066	0.0284	0.0033	0.1429	1.2122
12.19	0.1050	0.0061	0.0424	0.0040	0.4042	1.0699
12.21	0.1027	0.0061	0.1027	0.0044	1.0000	1.0000
			T = 353.18 K			
1.00	0.9443	0.0050	0.0105	0.0003	0.0111	17.7624
2.49	0.8637	0.0054	0.0012	0.0000	0.0014	7.3259
6.58	0.6336	0.0067	0.0020	0.0002	0.0032	2.7239
10.10	0.4293	0.0069	0.0058	0.0006	0.0134	1.7422
12.60	0.2518	0.0062	0.0307	0.0013	0.1220	1.2955
13.32	0.1705	0.0056	0.0412	0.0016	0.2415	1.1559
14.10	0.0661	0.0050	0.0661	0.0021	1.0000	1.0000
			T = 363.18 K			
0.83	0.9558	0.0051	0.0196	0.0006	0.0205	22.1619
3.10	0.8425	0.0057	0.0022	0.0001	0.0026	6.3364
5.05	0.7459	0.0063	0.0025	0.0001	0.0033	3.9260
7.05	0.6474	0.0068	0.0034	0.0001	0.0052	2.8262
8.66	0.5666	0.0070	0.0037	0.0004	0.0065	2.2987
10.50	0.4663	0.0071	0.0077	0.0014	0.0166	1.8594
11.87	0.3860	0.0069	0.0124	0.0029	0.0320	1.6085
13.97	0.2475	0.0062	0.0272	0.0072	0.1097	1.2928
14.64	0.1809	0.0058	0.0473	0.0091	0.2616	1.1631
14.77	0.0932	0.0053	0.0694	0.0096	0.7448	1.0262
			T = 373.13 K			
0.90	0.9556	0.0052	0.0055	0.0001	0.0058	22.4018

2.66	0.8810	0.0056	0.0044	0.0001	0.0050	8.3666
6.75	0.6892	0.0067	0.0047	0.0004	0.0068	3.2021
9.61	0.5568	0.0071	0.0080	0.0014	0.0144	2.2381
11.90	0.4600	0.0072	0.0103	0.0030	0.0223	1.8327
14.80	0.2783	0.0065	0.0341	0.0070	0.1226	1.3383
15.83	0.1745	0.0059	0.0728	0.0094	0.4172	1.1232
16.00	0.1142	0.0055	0.1142	0.0099	1.0000	1.0000
			T = 383.11 K			
0.83	0.9653	0.0053	0.0130	0.0003	0.0134	28.4576
3.10	0.8668	0.0058	0.0075	0.0002	0.0086	7.4487
5.00	0.7868	0.0063	0.0067	0.0002	0.0085	4.6592
7.10	0.7003	0.0067	0.0074	0.0006	0.0106	3.3119
9.06	0.6194	0.0071	0.0110	0.0014	0.0177	2.5985
11.49	0.5131	0.0073	0.0149	0.0031	0.0290	2.0234
13.92	0.4008	0.0071	0.0257	0.0059	0.0641	1.6262
15.66	0.3070	0.0068	0.0417	0.0085	0.1357	1.3829
16.46	0.2483	0.0065	0.0660	0.0098	0.2659	1.2425
16.82	0.1994	0.0062	0.0988	0.0105	0.4954	1.1257
16.90	0.1826	0.0061	0.1826	0.0109	1.0000	1.0000
			T = 403.20 K			
1.23	0.9653	0.0056	0.0296	0.0007	0.0310	21.2484
4.29	0.8668	0.0062	0.0162	0.0004	0.0193	6.0661
7.45	0.7868	0.0069	0.0172	0.0007	0.0238	3.5345
9.73	0.7003	0.0072	0.0175	0.0013	0.0275	2.7155
12.56	0.6194	0.0075	0.0238	0.0028	0.0447	2.0827
15.40	0.5131	0.0075	0.0311	0.0052	0.0683	1.7779
16.10	0.4008	0.0073	0.0483	0.0060	0.1279	1.5288
17.66	0.3070	0.0068	0.0794	0.0081	0.2873	1.2721
18.19	0.2483	0.0067	0.1044	0.0089	0.4248	1.1874
18.49	0.1994	0.0065	0.2083	0.0096	1.0000	1.0000
			T = 423.20 K			
0.85	0.9736	0.0059	0.0830	0.0017	0.0853	34.7568
4.10	0.8593	0.0063	0.0268	0.0006	0.0312	6.9162
7.17	0.7544	0.0069	0.0279	0.0006	0.0370	3.9573
10.62	0.6363	0.0075	0.0302	0.0007	0.0474	2.6668
13.90	0.5048	0.0077	0.0431	0.0009	0.0855	1.9324
17.09	0.4022	0.0076	0.0645	0.0014	0.1604	1.5649
18.35	0.3491	0.0074	0.0964	0.0020	0.2763	1.3881
18.94	0.3137	0.0073	0.1190	0.0024	0.3794	1.2836
19.38	0.2731	0.0071	0.1389	0.0027	0.5089	1.1845
19.57	0.2376	0.0069	0.2376	0.0036	1.0000	1.0000

[a]Notation: x_i and y_i denote the mole fraction of component i in the liquid phase, the mole fraction of component i in the vapour phase, respectively. K_i denotes the K values of component i. $u(x_i)$ and $u(y_i)$ denote standard uncertainty of x_i and y_i, respectively. $u(T)$ = 0.05 K and $u(p)$ = 0.01 MPa.

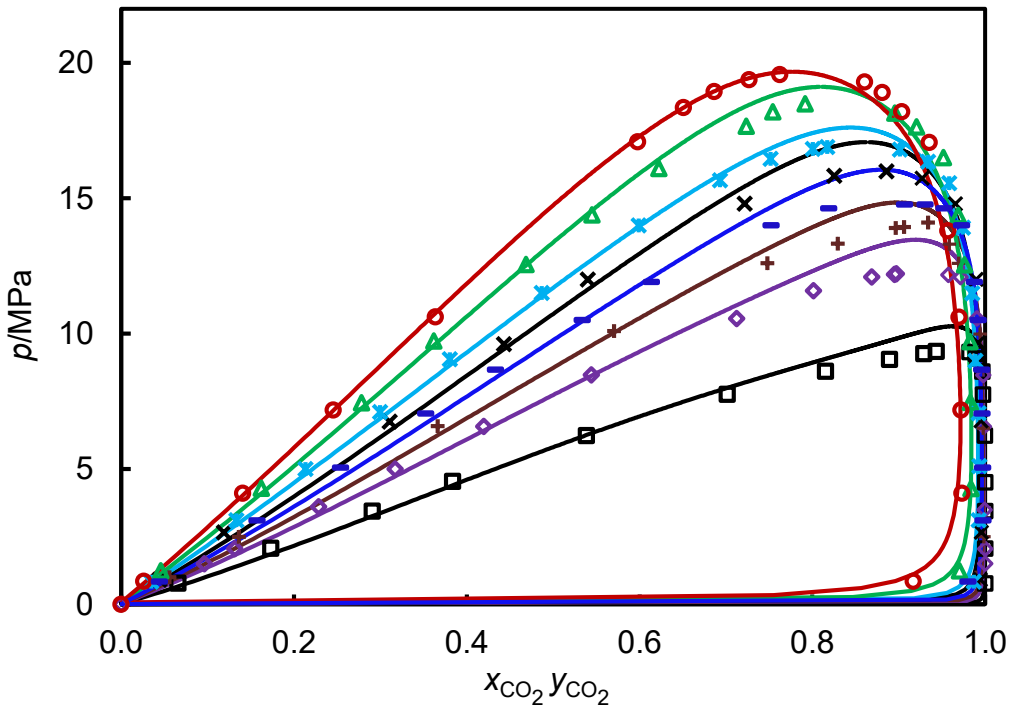

Figure 5.9: Isothermal pressure-composition (*p, x*) phase diagram for the (butanoic acid + carbon dioxide) system: □, *T* = 323.13 K; ◇, *T* = 343.12 K; +, *T* = 353.18 K; –, *T* = 363.18 K; ×, *T* = 373.13 K; ∗, *T* = 383.11 K; Δ, *T* = 403.2 K; and ○, *T* = 423.2 K. The continuous solid curves are the calculations from SAFT-γ Mie after optimisation.

5.3.4 Modelling

The modelling procedure for the (butanoic acid + carbon dioxide) binary system is similar to that followed for the (methyl propanoate + carbon dioxide) binary system. Butanoic acid ($CH_3(CH_2)_2COOH$) is composed of one CH_3, two CH_2, and one COOH. The like, associations and unlike parameters for the functional groups, which the system ($CH_3(CH_2)_2COOH$ + CO_2) is composed of, are collected in Table 5.10, Table 5.11 and Table 5.12, respectively. The parameters for the functional groups CH_3, CH_2 and CO_2 and their cross interactions were provided in section 5.2.

Table 5.10: SAFT-γ Mie like group parameters used in this work.

group *k*	v^*_k	S_k	σ_{kk}/Å	(ε_{kk}/k_B)/K	λ^a_{kk}	λ^r_{kk}	$N_{ST,K}$	$n_{k,h}$	$n_{k,e1}$	$n_{k,e2}$	Ref.
COOH	1	0.72312	3.8711	343.14	6.0	8.0	3	1	2	2	This work

Table 5.11: Estimated SAFT-γ Mie like and unlike group association energies (ε_{klab}^{HB}) and bonding volume (K_{klab}) parameters.

group *k*	group *l*	Site *a* of group *k*	Site *b* of group *l*	ε_{klab}^{HB}	K_{klab} [Å^3]	Ref.
COOH	COOH	*e*	*H*	3222.919	10.39	This work

Table 5.12: SAFT-γ Mie unlike group parameters used in this work.

group *k*	group *l*	(ε_{kl}/k_B)/K	λ_{kl}^r	Ref.
CH_3	COOH	274.4672	CR	This work
CH_2	COOH	320.9826	CR	This work
COOH	COOH	343.1426	8.000	This work
COOH	CO_2	200.0064	8.891	This work

CR indicates λ_{kl}^r was determined from the combining rule. All other values given in the table have been estimated from experimental data.

These groups are shown in Table 5.13 as a group matrix, which highlights the interactions that were estimated for this system.

Table 5.13: Groups developed within SAFT-γ Mie.

	CH_3	CH_2	COOH	CO_2
CH_3	O			
CH_2	O	O		
COOH	✓	✓	✓	
CO_2	O	O	✓	O

Ticks indicate interaction parameters estimated from experimental data in this work, while circle indicates the interactions reported in literature.

The COOH functional group is treated as self-associating; association site in CO_2 is inactive in the absence of water [156]. The like group parameters describing the functional group COOH and the unlike interactions for COO-CH_3 and COO-CH_2 were estimated using experimental vapour pressures (p_{vap}) and saturated-liquid densities (ρ_{sat}) of short carboxylic

acids such as acetic acid (CH_3COOH), propanoic acid (CH_3CH_2COOH), butanoic acid ($CH_3(CH_2)_2COOH$) and pentanoic acid ($CH_3(CH_2)_3COOH$). It has been observed that including acetic acid in parameters-estimation showed a better description for the fluid-phase behaviour of the fatty acids. As can be seen in Figure 5.10, Figure 5.11 and Figure 5.12, SAFT-γ Mie model shows a very accurate prediction for the vapour-liquid equilibrium of the pure carboxylic acids. The deviations (Δ_{AAD}) for the vapour pressures and the saturated-liquid densities are summarised in Table 5.14. The prediction of the model was extended to medium and long carboxylic acids such as stearic acid ($CH_3(CH_2)_{16}COOH$) and oleic acid ($C_{18}H_{34}O_2$), which are dominants in biodiesel feedstocks, and it showed quite good description as shown in Figure 5.10 and Figure 5.11.

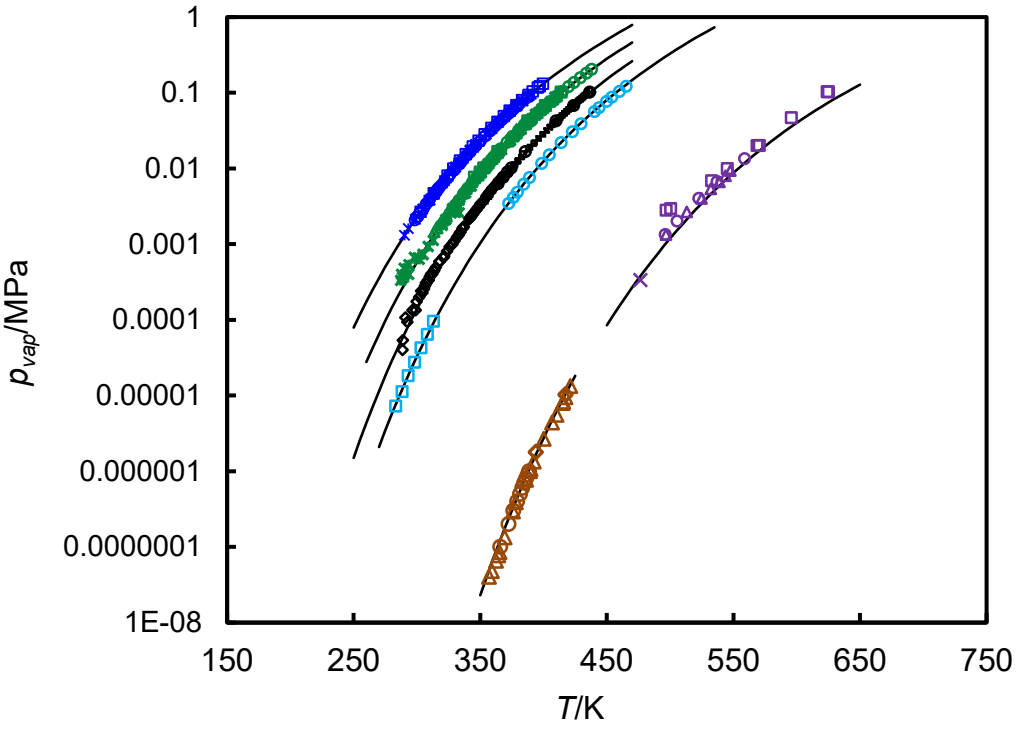

Figure 5.10: The description of SAFT-γ Mie for the experimental vapour pressures of free fatty acids. The colours are: Dark Blue, acetic acid [188, 189]; Green, propanoic acid [188, 190] ; Black, butanoic acid [191-193]; Blue, pentanoic acid [194, 195]; Purple, oleic acid [196-198]; and Dark Orange, stearic acid [196, 199, 200]. The black continuous curves are the calculation from SAFT-γ Mie after optimisation.

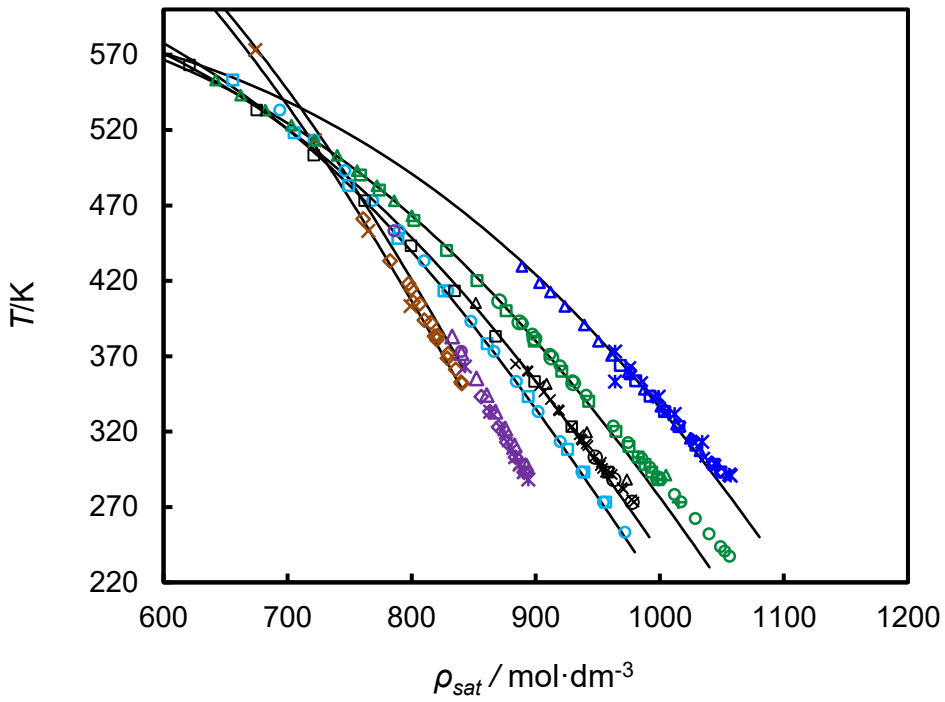

Figure 5.11: The description of SAFT-γ Mie for the experimental saturated-liquid densities of free fatty acids. The colours are: Dark Blue, acetic acid [201, 202]; Green, propanoic acid [203-205]; Black, n-butanoic acid [206, 207]; Blue, pentanoic acid [206, 208]; Purple, oleic acid [209-211]; and Dark Orange, stearic acid [203, 212]. The black continuous curves are the calculation from SAFT-γ Mie after optimisation.

Table 5.14: Percentage average absolute deviations (Δ_{AAD}) for vapour pressures $p_{vap}(T)$ and for saturated-liquid densities $\rho_{sat}(T)$ determined with SAFT-γ Mie for some fatty acids.

Compound	T range/ K	n	Δ_{AAD} (p_{vap}), optimised SAFT	T range/ K	n	Δ_{AAD} (ρ_{sat}) optimised SAFT
Acetic acid (CH_3COOH)	290-405	141	1.75	291-430	48	0.28
Propanoic acid (CH_3CH_2COOH)	287-438	155	4.18	237-642	53	0.63
Butanoic acid ($CH_3(CH_2)_2COOH$)	288-436	136	7.11	273-563	45	0.41

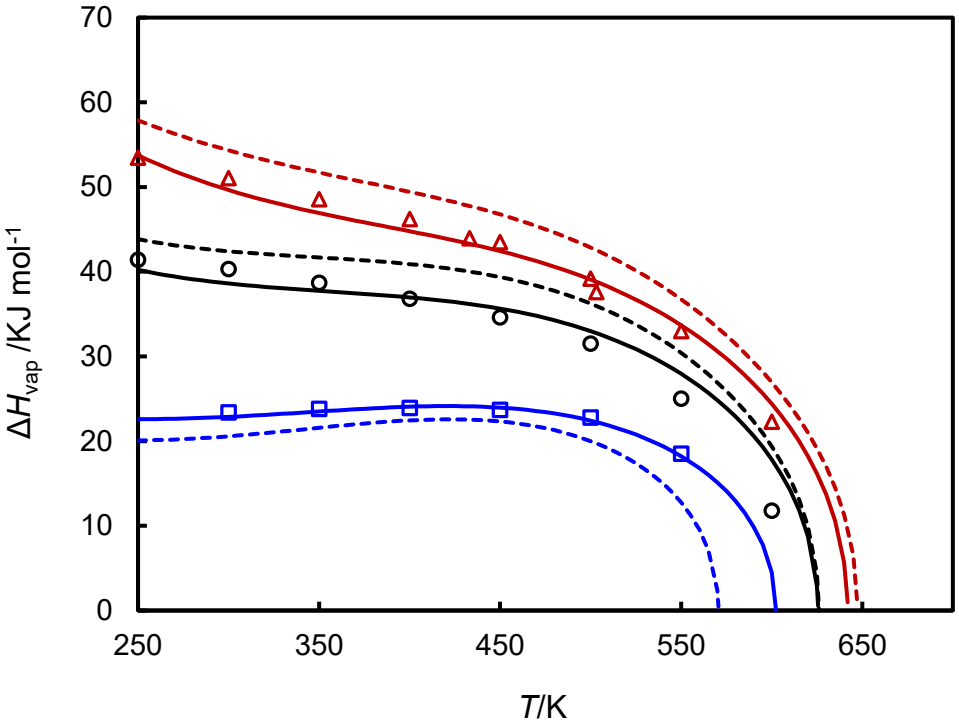

Figure 5.12: The description of SAFT-γ Mie for the heat of vaporization of free fatty acids. The symbols are: □, acetic acid [213]; O, butanoic acid [213], and Δ, n-pentanoic acid [213]. The continuous curves and the dashed curves are the calculation from SAFT-γ Mie after optimisation and SAFT-γ Mie reported in literature, respectively.

The unlike dispersion energy ε_{kl} and the unlike repulsive Mie exponent λ_{kl}^{r} for the CO_2-COOH were then estimated from our experimental VLE measurements of ($CH_3(CH_2)_2COOH$ + CO_2) system, and the values are provided in Table 5.12. All the remaining unlike interaction parameters were calculated using combining rules. The experimental VLE data of the binary system were also modelled using the Peng Robinson equation of state (PR EoS). Applying the PR EoS modelling approaches in the regression to the experimental data, it was found that considering the binary temperature-independent binary interactions ($k_{ij,0}$) and ($l_{ij,0}$) showed the best description for the phase envelope in all the isotherms as shown in Figure 5.13. The values of the optimised interaction parameters k_{ij} and l_{ij} were found to be 0.005 and 0.05, respectively.

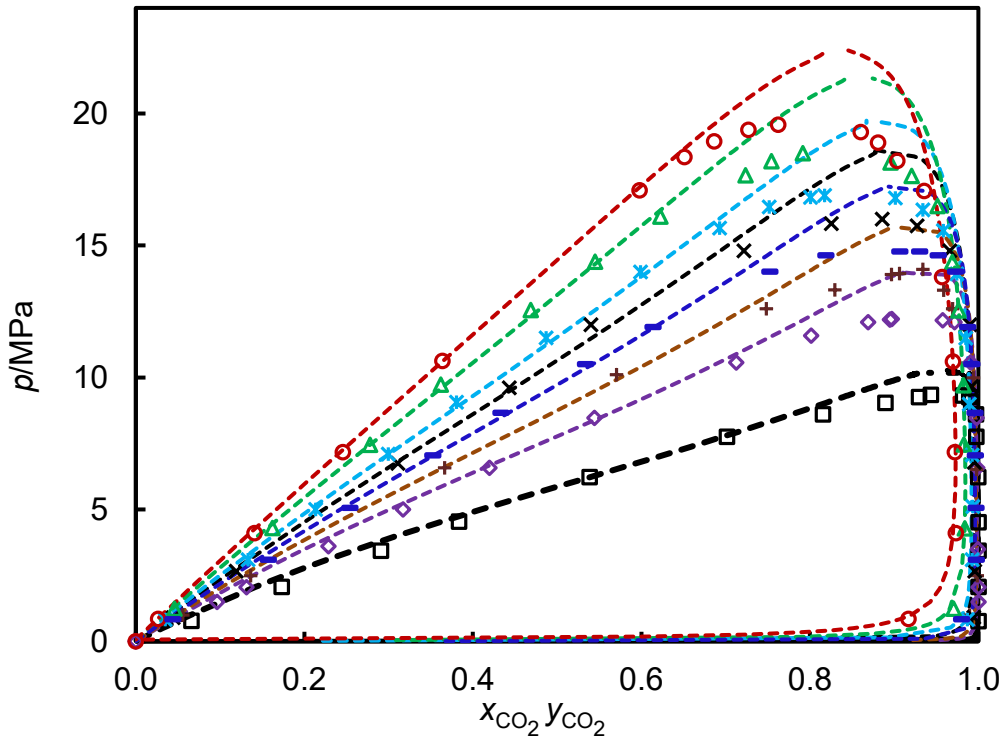

Figure 5.13: Isothermal pressure-composition (*p, x*) phase diagram for the (butanoic acid + carbon dioxide) system: □, *T* = 323.13 K; ◇, *T* = 343.12 K; +, *T* = 353.18 K; –, *T* = 363.18 K; ×, *T* = 373.13 K; ∗, *T* = 383.11 K; Δ, *T* = 403.2 K; and ○, *T* = 423.2 K. The dashed curves are the calculations from PR EoS after optimisation.

5.3.5 Discussion and Comparison with Experiments

As can be seen from Figure 5.9, SAFT-γ Mie model after parameters optimisations predicts well the bubble and dew points of the binary system (butanoic acid + carbon dioxide) at all temperatures except the critical region in which the model overpredicts the data especially at low temperatures. In this system, the critical point of the mixture for each isotherm was observed and measured. Figure 5.14 shows the critical opalescence phenomena from the interior of the view cell observed between the acid-rich liquid phase and CO_2-rich vapour phase.

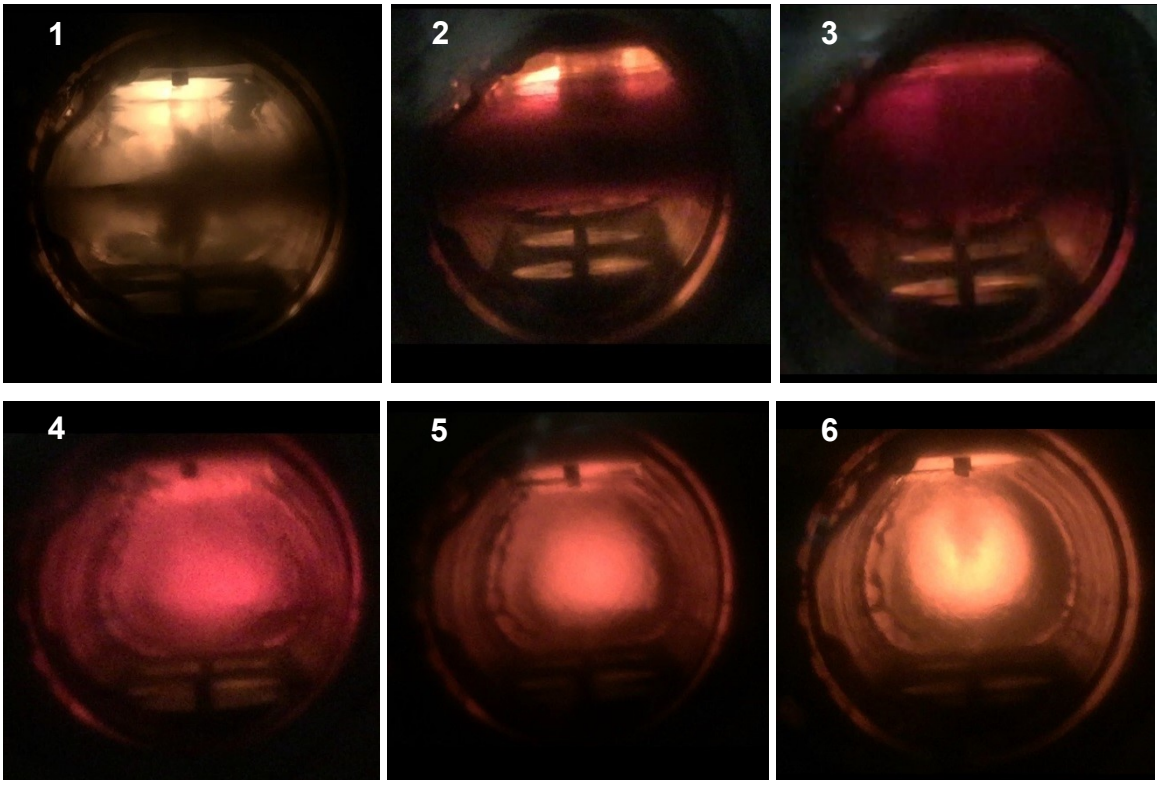

Figure 5.14: Images of the interior of the view cell showing the critical opalescene phenomena (CP) observed between the acid-rich liquid phase and CO_2-rich vapour phase at T= 343.12 K. Pressure is increased from (12.10 to 12.21) MPa from image 1 to image 6.

The critical points obtained for each isotherm from the experimental measurements as well as the SAFT-γ Mie model are provided in Table 5.15 and shown graphically in Figure 5.15 as (p, T) diagram.

Table 5.15: Critical points estimated from SAFT-γ Mie and experimental work.

T/K	p_c, SAFT/MPa	p_c, Experiments/MPa[a]
323.13	10.27	–
343.12	13.36	12.21
353.18	14.69	14.10
363.18	16.04	–
373.13	16.81	16.00
383.11	17.59	16.90
403.20	19.07	18.49
423.20	19.42	19.57

[a]Notation: critical points at temperatures of 323.13 K and 363.18 K could not be achieved.

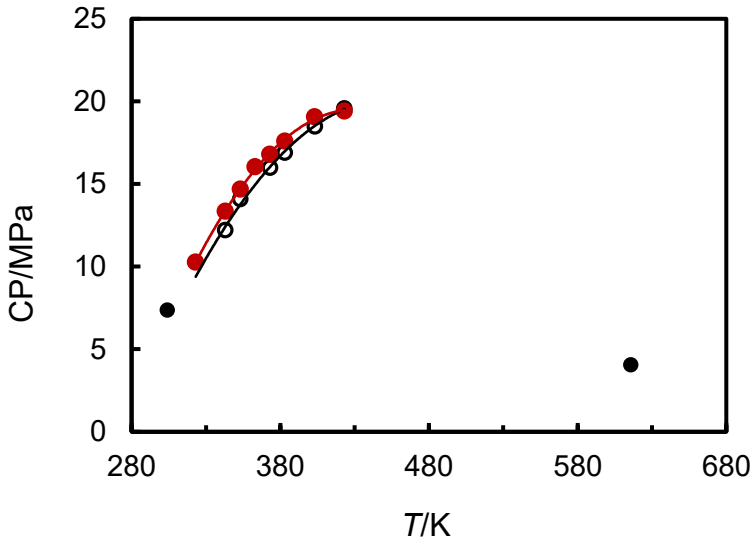

Figure 5.15: Critical point pressures as a function of temperature estimated from experimental measurements and calculated by SAFT-γMie for the (butanoic acid + carbon dioxide) system: ●, SAFT-γMie prediction; O, experimental measurements; filled symbols represent p_c for pure CO_2 and pure butanoic acid; solid lines represent polynomial fit to the data for the corresponding data (indicated by colours).

PR EoS again overpredicts the data at the critical region in all isotherms as shown in Figure 5.13.

It can be seen from Figure 5.9 that the solubility of CO_2 in the acid decreases when temperature is increased at constant pressure. On the other hand, the mole fraction of the acid in the CO_2-rich phase increases when temperature is increased at constant pressure. The effect of pressure on the system can also be observed in the figure. The concentration of CO_2 in the acid increases when pressure in the cell is raised at constant temperature. The mole fraction of the acid in the CO_2-rich phase increases when pressure is increased at constant temperature. They are also plotted against pressures at different isotherms in Figure 5.16, with SAFT-γMie and PR EoS predictions. As can be seen from the figure, K_1 decreases when pressures are increased for constant temperatures. K_2, on the other hand, increases with the rising pressures at constant temperatures.

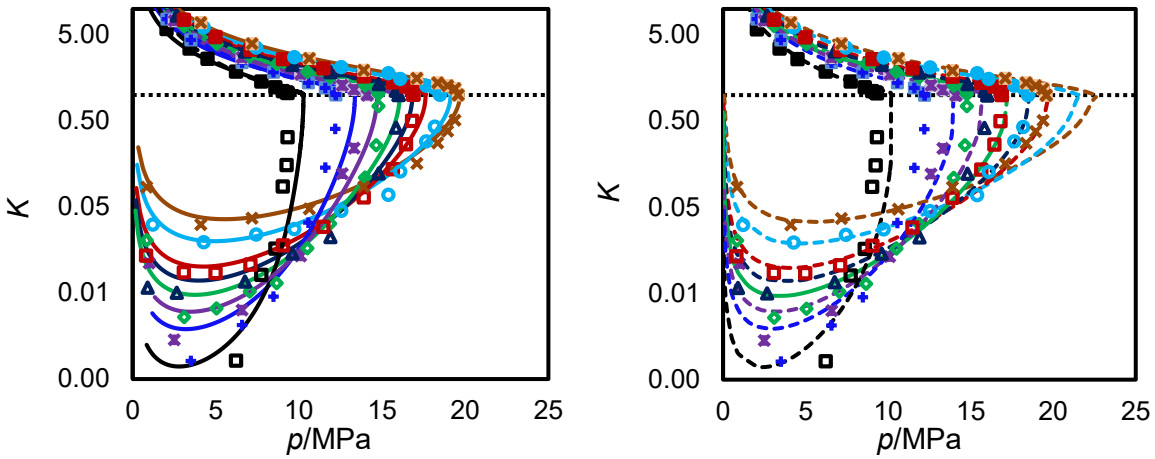

Figure 5.16: *K-p* for the (butanoic acid + carbon dioxide) system: ☐ and ■, T = 323.13 K; + and +, T = 343.12 K; ✱ and ✱, T = 353.18 K; ◇ and ◆, T = 363.18 K; Δ and ▲, T = 373.13 K; ☐ and ■, T = 383.11 K; ○ and ●, T = 403.2 K; × and ×, T = 423.2 K. The continuous solid curves and the dashed curves are the calculations from SAFT-γ Mie after optimisation and PR EoS, respectively.

5.3.6 Conclusion

The experimental study of vapour-liquid equilibria for (butanoic acid + carbon dioxide) was reported on eight isotherms at temperatures from (323.13 to 423.2) K with pressures up to 18.0 MPa. The like group parameters and self-associations parameters of SAFT-γ Mie for the functional group COOH have been estimated using VLE data of different fatty acids. The values obtained for COOH were tested for thermodynamic properties of long-chain carboxylic acids, and the model showed a good agreement with the experimental data. The unlike dispersion energy ε_{kl} and the unlike repulsive exponent λ_{kl}^{r} between COOH-CO_2 were adjusted using the experimental measurements obtained in this work. The model showed a good prediction for all the isotherms with a small deviation at the critical region. The experimental results have also been compared with description of PR equation of state after optimising the model interaction parameters, and the model was found to be in a good agreement with the experimental measurements with overprediction at the critical regions in all isotherms.

Chapter 6: Phase Behaviour Measurements of Ternary Systems

6.1 Overview

In this Chapter, fluid-phase equilibrium measurements on the ternary systems (methyl propanoate + propionic acid + carbon dioxide), (*tert*-butanol + water + carbon dioxide) and (toluene + water + carbon dioxide) carried out by the means of the high-pressure quasi-static analytical apparatus with compositional analysis using the gas chromatography were reported. The compositions of the present phases coexisting in vapour-liquid equilibrium (VLE) for (methyl propanoate + propionic acid + carbon dioxide) were measured along six isotherms at temperatures from (323.12 to 423.11) K and pressures from (1 to 20) MPa at equal feed molar ratio of (methyl propanoate + propionic acid). Phase behaviour measurements were also collected at different compositions of the mixture (methyl propanoate + propionic acid) at fixed temperatures and pressures. The experimental study of the phase behaviour of the ternary system (carbon dioxide + *tert*-butanol + water) was presented along five isotherms at temperatures of (283.2, 298.18, 323.13, 373.10 and 423.17) K and at pressures of (4, 8, 12 and 18) MPa with different known feed compositions of (*tert*-butanol + water) while the phase behaviour of the system (toluene + water + carbon dioxide) was investigated along four isotherms at temperatures from (338.15 to 413.15) K and pressures up to the UCEP. The data obtained for the ternary mixtures have been compared with the description of SAFT-γMie and Peng Robinson EoS.

6.2 Methyl Propanoate + Propionic Acid + Carbon Dioxide

6.2.1 Introduction

In biodiesel production, free fatty acids react with methanol to produce fatty acid methyl esters (FAME) and water (esterification reaction). Understanding the phase behaviour of the related systems under the use of the co-solvent, CO_2, is of great importance in the production and separation processes. In Chapter 5, the like and unlike group parameters were estimated for the functional groups COOH, COO and CO_2, which esters, fatty acids, glycerides and carbon dioxide are composed of, using our experimental measurements and some VLE literature data on pure and binary mixtures. The prediction of the model needs to be tested for the ternary system (fatty acid methyl ester + free fatty acid + carbon dioxide). In this work, methyl propanoate ($C_2H_5COOCH_3$) is selected to be a representative component for FAME and propionic acid (CH_3CH_2COOH) is selected to represent fatty acid. The phase behaviour of the ternary system (methyl propanoate + propionic acid + carbon dioxide) was investigated at two

different baths. First, the molar ratio of the mixture (methyl propanoate + propionic acid) was fixed to be 1:1 and six isotherms were measured at different CO_2 pressures. Second, the temperature and pressure were fixed and different compositions of the mixture (methyl propanoate + propionic acid + carbon dioxide) were injected. To our knowledge, there is no experimental data available in literature for this ternary system. The phase behaviour of the binary system (methyl propanoate + CO_2) was investigated in Chapter 5. The VLE of the binary system (propionic acid + CO_2) was studied by Adrian and Maurer [148] at temperatures between 298 K and 333 K. To the best of our knowledge, the study of Adrian and Maurer is the only study available in literature providing VLE data for the binary mixture. Very few VLE data at temperature of 313 K were reported by Willson (1988) in his PhD dissertation as cited by Adrian and Maurer. The data reported in literature were used to validate the calibration curves obtained for propionic acid as shown below in section 6.2.2. Butyric acid was not used in this mixture due to a complain raised previously during the phase behaviour study of (butyric acid + CO_2) about its bad smell in the laboratory.

6.2.2 Comparison of VLE Data with Literature Data

VLE data of (propionic acid + CO_2) were measured in this work at 333.19 K and pressures up to the mixture critical point and the results were compared with the work of Adrian and Maurer carried out at 333.15 K as shown in Figure 6.1 and summarised in Table 6.1. This system exhibits two coexisting fluid phases; propionic acid-rich liquid phase and CO_2-rich vapour phase. However, one composition of the vapour phase was only measured in the literature for one pressure near the critical point. As can be seen from the figure, the measured compositions in this work are in a very good agreement with the compositions reported in the literature over the entire pressures range.

Table 6.1: Comparison of VLE data for [CH_3CH_2COOH (1) + CO_2 (2)] between this work (at T = 333.19 K) and literature [148] (at T = 333.15 K) and pressures p.

T/K	p/MPa	$x_2^{\text{litrature}}$	$y_2^{\text{litrature}}$	T/K	p/MPa	$x_2^{\text{this work}}$	$y_2^{\text{this work}}$
333.15	2.010	0.1486		333.19	1.996	0.1414	
333.15	4.014	0.2919		333.19	3.980	0.2869	
333.15	6.013	0.4376		333.19	5.997	0.4359	
333.15	8.029	0.5992		333.19	8.011	0.6006	
333.15	8.986	0.6861		333.19	8.922	0.6850	
333.15	10.01	0.7963		333.19	10.030	0.8017	
333.15	10.50	0.8660	0.9752	333.19	10.513	0.8655	0.9850

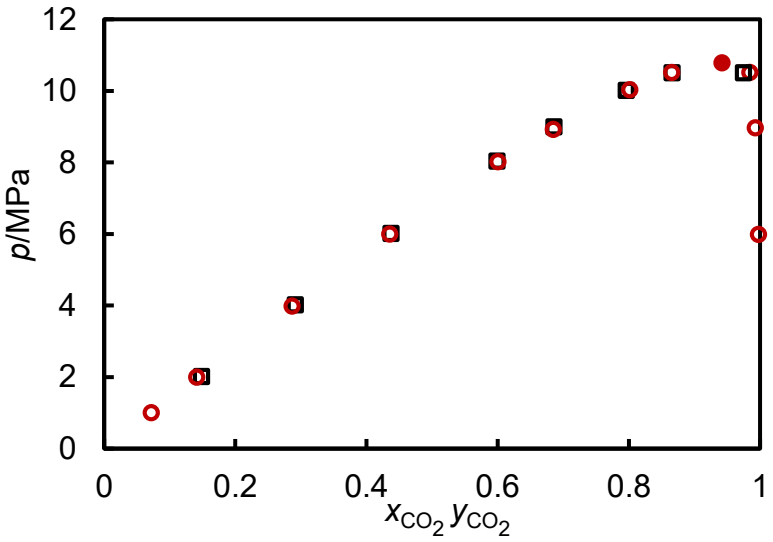

Figure 6.1: Isothermal pressure-composition (*p, x*) phase diagram for the (propionic acid + carbon dioxide) system: ○, *T* = 333.19 K (this work); □, *T* = 333.15 K [148]. Filled symbol represents the critical point measured in this work.

6.2.3 Experimental Results

Both binary systems (CH_3CH_2COOH + CO_2) and ($CH_3CH_2COOCH_3$ + CO_2) at temperatures from (323.15 to 423.15) K and pressures up to 20 MPa exhibit type I phase behaviour according to the classification of Van Konynenburg and Scott. The binary system (methyl propanoate + propionic acid) exhibits type I phase behaviour at pressure of 101.33 kPa and temperatures ranging from (352 to 413) K with no azeotrope [214]. Therefore, the ternary system (methyl propanoate + propionic acid + carbon dioxide) is expected to exhibit ternary class I phase behaviour according to the global ternary diagrams classification proposed by Bluma and Dieters (described in Chapter 2, section 2.1.4). The phase behaviour of the system was measured in two different baths as introduced previously. In the first bath, the molar ratio of the mixture (methyl propanoate + propionic acid) was fixed to be 1:1 and six isotherms at temperatures from (323.12 to 423.11) K were measured at different CO_2 pressures from (1 to 20) MPa, while in the second bath, the temperature and pressure of the equilibrium cell were fixed (*T* = 383.17 K and *p* = 4 MPa, *T* = 363.17 K and *p* = 6 MPa) and different compositions of the mixture (methyl propanoate + propionic acid + carbon dioxide) were injected starting from zero mole composition of methyl propionate to zero mole composition of propanoic acid in order to have a complete envelope. The experimental measurements for the first and second baths are provided in Table 6.2 and shown graphically in Figure 6.2, Figure 6.3 and Figure 6.4, respectively.

Table 6.2: Experimental VLE data for [$CH_3CH_2COOCH_3$ (1) + CH_3CH_2COOH (2) + CO_2 (3)] at temperatures T and pressures p[a].

phase	p/MPa	x_1^{exp}	$u(x_1)$	x_2^{exp}	$u(x_2)$	x_3^{exp}	$u(x_3)$
			T = 323.12 K				
L	1.07	0.3189	0.0062	0.5764	0.0062	0.1047	0.0063
V	1.07	0.0006	0.0000	0.0015	0.0000	0.9979	0.0000
L	3.00	0.2498	0.0053	0.4547	0.0054	0.2955	0.0055
V	3.00	0.0002	0.0000	0.0005	0.0000	0.9993	0.0000
L	4.42	0.1997	0.0046	0.3667	0.0046	0.4336	0.0048
V	4.40	0.0002	0.0000	0.0011	0.0000	0.9987	0.0000
L	6.00	0.1444	0.0035	0.2644	0.0036	0.5913	0.0039
V	5.98	0.0050	0.0002	0.0010	0.0002	0.9940	0.0002
L	7.27	0.0973	0.0026	0.1782	0.0027	0.7245	0.0030
V	7.41	0.0072	0.0003	0.0019	0.0003	0.9909	0.0003
L	8.10	0.0631	0.0018	0.1157	0.0020	0.8212	0.0024
V	8.07	0.0088	0.0004	0.0046	0.0004	0.9867	0.0004
L	8.92	0.0358	0.0011	0.0634	0.0014	0.9009	0.0020
V	8.90	0.0090	0.0004	0.0061	0.0004	0.9849	0.0004
CP	9.49	0.0153	0.0007	0.0225	0.0011	0.9622	0.0018
			T = 343.13 K				
L	2.07	0.4073	0.0069	0.4323	0.0069	0.1604	0.0069
V	2.14	0.0259	0.1609	0.0010	0.0315	0.9731	0.9865
L	4.02	0.3343	0.0063	0.3553	0.0063	0.3104	0.0064
V	3.92	0.0189	0.1377	0.0007	0.0271	0.9803	0.9901
L	5.96	0.2618	0.0055	0.2850	0.0055	0.4532	0.0056
V	5.98	0.0151	0.1231	0.0011	0.0338	0.9837	0.9918
L	8.10	0.1852	0.0043	0.2018	0.0043	0.6130	0.0045
V	8.12	0.0150	0.1225	0.0025	0.0499	0.9825	0.9912
L	9.01	0.1522	0.0037	0.1652	0.0037	0.6825	0.0039
V	9.02	0.0171	0.1306	0.0034	0.0583	0.9795	0.9897
L	9.94	0.1171	0.0030	0.1242	0.0030	0.7587	0.0032
V	9.97	0.0189	0.1376	0.0056	0.0746	0.9755	0.9877
L	10.92	0.0749	0.0020	0.0779	0.0021	0.8472	0.0024
V	10.94	0.0259	0.1611	0.0141	0.1186	0.9600	0.9798
CP	11.52	0.0541	0.0016	0.0542	0.0016	0.8917	0.0020
			T = 363.17 K				
L	2.08	0.4057	0.0068	0.4657	0.0068	0.1285	0.0069
V	2.14	0.0419	0.0019	0.0036	0.0019	0.9546	0.0019
L	3.92	0.3511	0.0065	0.4070	0.0065	0.2419	0.0065
V	4.03	0.0261	0.0012	0.0032	0.0012	0.9707	0.0012
L	5.99	0.2895	0.0058	0.3480	0.0059	0.3625	0.0059
V	5.98	0.0251	0.0011	0.0037	0.0011	0.9712	0.0012

L	7.97	0.2362	0.0051	0.2820	0.0051	0.4818	0.0052
V	8.00	0.0244	0.0011	0.0043	0.0011	0.9714	0.0011
L	10.08	0.1799	0.0042	0.2114	0.0042	0.6087	0.0043
V	10.05	0.0251	0.0012	0.0065	0.0012	0.9684	0.0012
L	11.61	0.1368	0.0034	0.1587	0.0034	0.7045	0.0035
V	11.45	0.0287	0.0013	0.0124	0.0013	0.9589	0.0013
L	12.43	0.1023	0.0027	0.1473	0.0027	0.7504	0.0028
V	12.58	0.0295	0.0013	0.0209	0.0013	0.9496	0.0014
CP	13.58	0.0507	0.0015	0.0587	0.0015	0.8906	0.0018
			T = 383.18 K				
L	2.09	0.4446	0.0070	0.4458	0.0070	0.1096	0.0070
V	2.00	0.0814	0.0035	0.0107	0.0035	0.9079	0.0035
L	4.01	0.3812	0.0067	0.4066	0.0067	0.2121	0.0067
V	4.03	0.0516	0.0023	0.0058	0.0023	0.9426	0.0023
L	6.46	0.3172	0.0062	0.3434	0.0062	0.3393	0.0062
V	6.51	0.0393	0.0018	0.0069	0.0018	0.9538	0.0018
L	8.78	0.2577	0.0054	0.2892	0.0054	0.4531	0.0055
V	8.84	0.0358	0.0016	0.0091	0.0016	0.9551	0.0016
L	10.84	0.2163	0.0048	0.2266	0.0048	0.5570	0.0049
V	10.84	0.0373	0.0017	0.0104	0.0017	0.9523	0.0017
L	13.22	0.1464	0.0036	0.1571	0.0036	0.6965	0.0037
V	13.39	0.0502	0.0022	0.0293	0.0022	0.9205	0.0023
CP	14.55	0.0923	0.0024	0.0894	0.0024	0.8183	0.0026
			T = 403.11 K				
L	2.00	0.4405	0.0070	0.4758	0.0070	0.0838	0.0070
V	2.02	0.1494	0.0060	0.0178	0.0060	0.8328	0.0060
L	4.49	0.3952	0.0068	0.4041	0.0068	0.2008	0.0068
V	4.43	0.0836	0.0036	0.0110	0.0036	0.9053	0.0036
L	6.91	0.3355	0.0063	0.3527	0.0063	0.3118	0.0064
V	6.92	0.0583	0.0026	0.0136	0.0026	0.9281	0.0026
L	9.44	0.2763	0.0057	0.3015	0.0057	0.4222	0.0057
V	9.46	0.0521	0.0023	0.0163	0.0023	0.9316	0.0023
L	12.00	0.2192	0.0049	0.2507	0.0049	0.5300	0.0049
V	11.99	0.0541	0.0024	0.0222	0.0024	0.9237	0.0024
L	13.91	0.1761	0.0041	0.1910	0.0041	0.6329	0.0042
V	13.80	0.0578	0.0026	0.0290	0.0026	0.9132	0.0026
CP	15.70	0.1088	0.0028	0.1209	0.0028	0.7703	0.0029
			T = 423.11 K				
L	1.96	0.4649	0.0071	0.4668	0.0071	0.0683	0.0071
V	1.90	0.2189	0.0049	0.0425	0.0048	0.7386	0.0049
L	4.32	0.4037	0.0068	0.4312	0.0068	0.1651	0.0069
V	4.33	0.1102	0.0028	0.0273	0.0028	0.8625	0.0028
L	6.90	0.3492	0.0065	0.3805	0.0064	0.2703	0.0065

V	6.98	0.0805	0.0021	0.0249	0.0021	0.8946	0.0021
L	9.07	0.3040	0.0060	0.3405	0.0060	0.3555	0.0060
V	8.85	0.0738	0.0019	0.0268	0.0019	0.8994	0.0019
L	11.51	0.2514	0.0054	0.3015	0.0053	0.4471	0.0054
V	11.31	0.0694	0.0018	0.0320	0.0018	0.8986	0.0018
L	14.05	0.1980	0.0045	0.2529	0.0045	0.5492	0.0045
V	13.95	0.0749	0.0020	0.0477	0.0020	0.8775	0.0020
L	15.41	0.1659	0.0039	0.2228	0.0039	0.6113	0.0040
V	15.34	0.0881	0.0023	0.0764	0.0023	0.8355	0.0023

[a]Notation: x_i, V, L, $u(x_i)$ denote the mole fraction of component *i* in any phase, the vapour phase, the liquid phase, and the standard uncertainty of x_i, respectively.

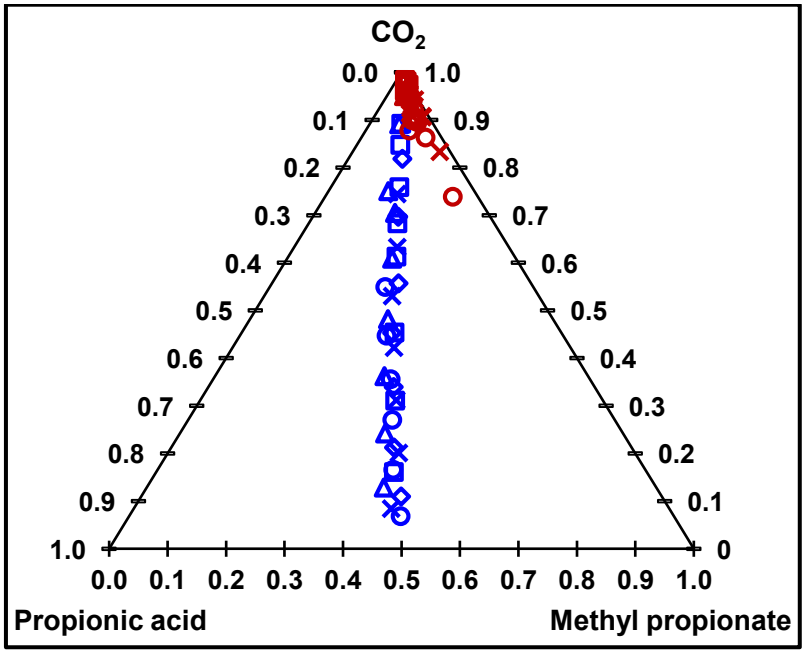

Figure 6.2: Phase equilibria for (methyl propanoate + propionic acid + carbon dioxide) system with molar ratio of (methyl propanoate and propionic acid) of 1:1. The symbols represent the VLE data measured in this work at the following temperatures: □, T = 343.13 K; Δ, T = 363.17 K; ◇, T = 383.18 K; ×, T = 403.12 K and O, T = 423.11K. BLUE symbols correspond to liquid phase and RED symbols represent vapour phase.

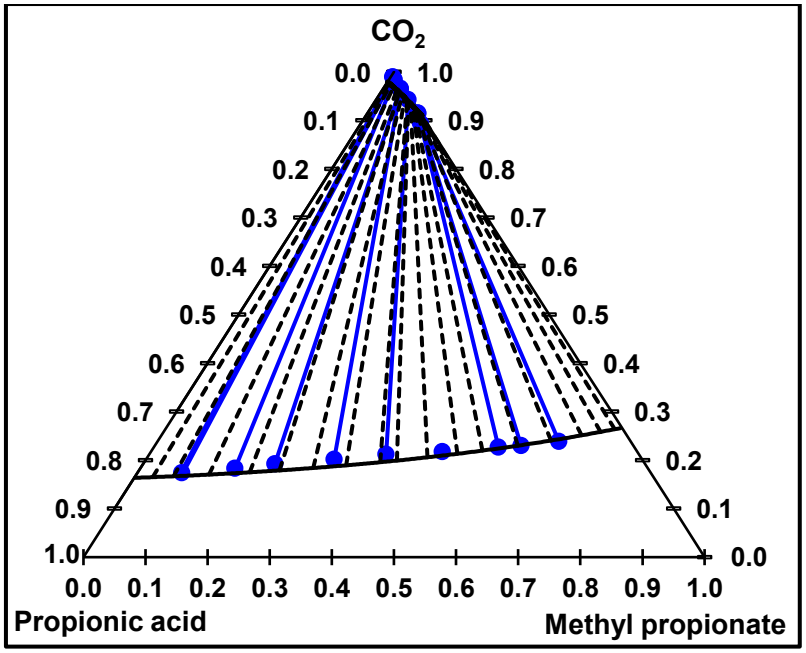

Figure 6.3: Phase equilibria for (methyl propanoate + propionic acid + carbon dioxide) system at T = 383.15 K and p = 4.0 MPa. The BLUE filled symbols represent the VLE data measured in this work. The BLUE continuous lines and BLACK dashed lines are the tie-lines between the coexisting phases measured experimentally and calculated by SAFT-γ Mie, respectively. The continuous curves are the phase boundaries calculated by SAFT-γ Mie.

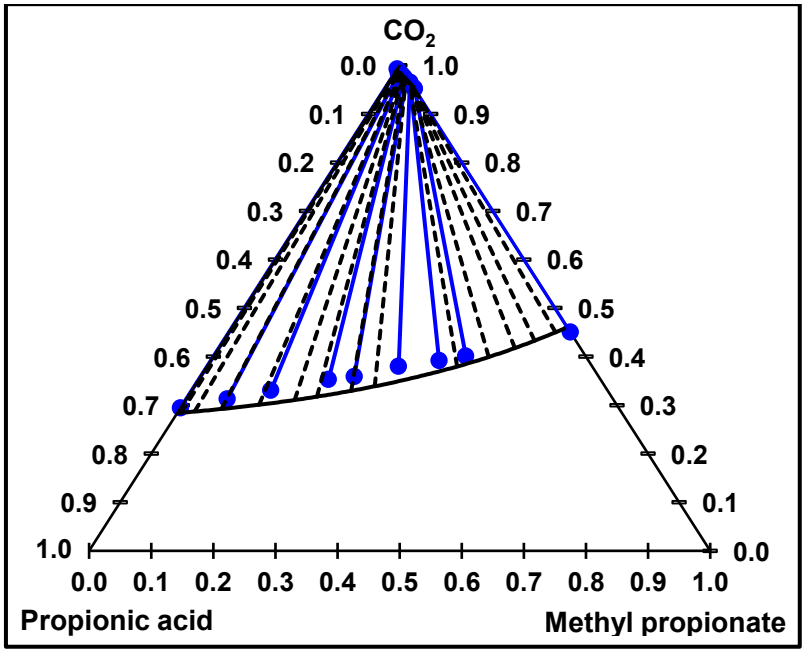

Figure 6.4: Phase equilibria for (methyl propanoate + propionic acid + carbon dioxide) system at T = 363.15 K and p = 6.0 MPa. The BLUE filled symbols correspond to the VLE data measured in this work. The BLUE continuous lines and BLACK dashed lines are the tie-lines between the coexisting phases measured experimentally and calculated by SAFT-γ Mie, respectively. The continuous curves are the phase boundaries calculated by SAFT-γ Mie.

6.2.4 Modelling

The experimental VLE data of this ternary system can be used to test the validity of the use of the like and unlike group parameters for the functional groups COO and COOH and their cross interactions with CO_2, CH_3 and CH_2, which have been estimated from the phase equilibrium data of the pure components and constituent binaries covered in Chapter 5. The unlike group parameters for COO-COOH are summarised in Table 6.3 (the other cross interactions have been provided previously). The model can be tested by describing the binary system (propionic acid + carbon dioxide) at T = 333.19 K. As can be seen in Figure 6.5, the model predicts the bubble and dew points of the binary system very well with a slight overprediction at the critical region. The cross interactions between COO and COOH can be calculated by the appropriate combining rules, but large deviations between the model calculations and the experimental data were seen. Therefore, the values for the unlike parameters ε_{kl} and λ_{kl}^{r} were estimated from binary mixtures of components having these functional groups. Isobaric vapour-liquid equilibrium (VLE) data were measured for the mixture (methyl propanoate + propionic acid) in a temperature range of (330.05 to 413.15) K at p = 101.3 kPa by Hsieh et al. [214]. The model was also used to describe isobaric vapour-liquid equilibrium (VLE) data of (methyl acetate + acetic acid) binary system measured at temperatures from (329.99 to 391.05) K and at a pressure of 101.33 kPa [215, 216]. The experimental VLE data and the calculations of SAFT-γ Mie are provided in Figure 6.6 and Figure 6.7 (represented by the solid curves). As can be seen in the figures, there is a large deviation seen between the experimental data and the predictions of SAFT-γ Mie (dashed curve) when using the parameter values of COO and COOH reported in literature even after optimising the unlike parameters ε_{kl} and λ_{kl}^{r}. This is due to the poor accuracy of the calculated properties of the pure components as highlighted by circles in Figure 6.6 and Figure 6.7 and summarised in Table 6.4. Using the parameters estimated for COO and COOH provided in Chapter 5 the model provides more accurate predictions for VLE data as shown in the figures by the solid black curves.

Table 6.3: SAFT-γ Mie unlike group parameters used in this work.

group k	group l	(ε_{kl}/k_B)/K	λ_{kl}^{r}	Ref.
COO	COOH	829.37	50.0	This work

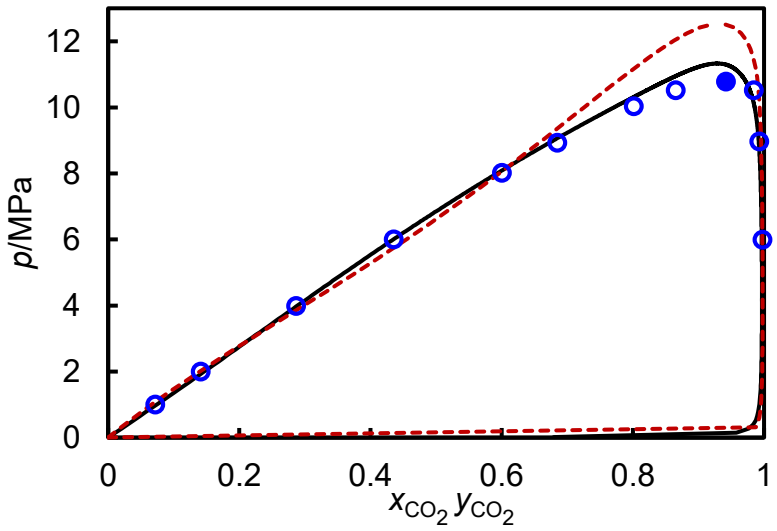

Figure 6.5: Isothermal pressure-composition (*p, x*) phase diagram for the (propionic acid + carbon dioxide) system: ○, This work at T = 333.19 K. Filled symbol corresponds to the critical point measured in this work. The solid and dashed curves are the calculation from the optimised SAFT-γ Mie and PR EoS, respectively.

Table 6.4: Boiling points of acids and esters reported in literature, calculated from SAFT-γ Mie (literature) and calculated From SAFT-γ Mie (optimised).

Component	Boiling Point at 101.325 kPa (literature)/ K	Ref.	SAFT calculation (literature)/ K	SAFT calculation (optimised)/ K
Propionic acid	413.60	[214]	409.17	414.42
Methyl propanoate	352.65	[214]	349.10	352.66
Acetic acid	391.05	[215]	372.75	391.47
Methyl acetate	329.99	[215]	325.26	329.89

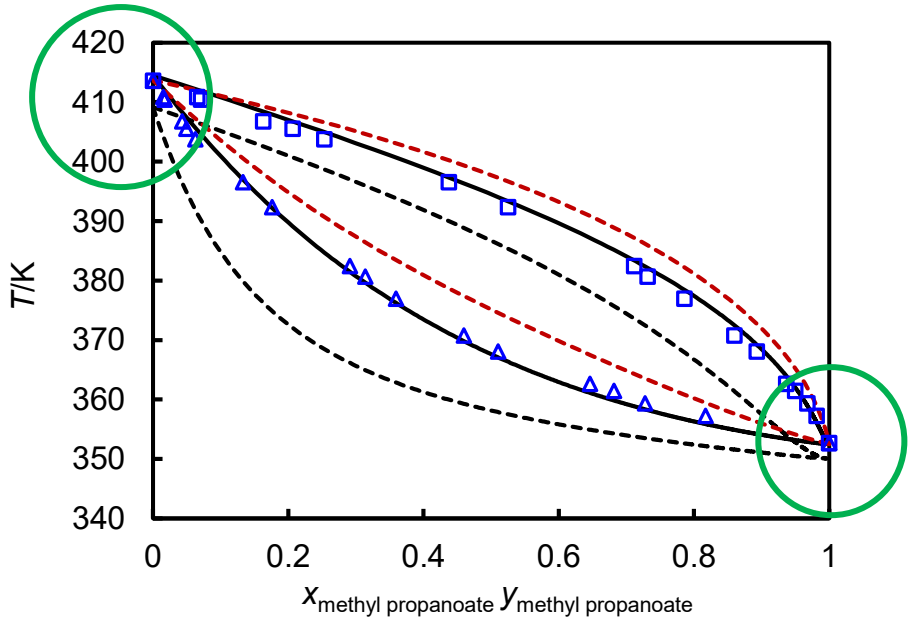

Figure 6.6: Isobaric temperature-composition (*T, x*) phase diagram for the (methyl propanoate + propionic acid) system [214]: □, dew points; △, bubble points. The black dashed curve is the calculation from SAFT-γ Mie using literature parameters and the solid curve is the calculation from SAFT-γ Mie using the optimised parameters. The red dashed curve corresponds to PR predictions. The open green circles show the deviation in the boiling points of the pure components.

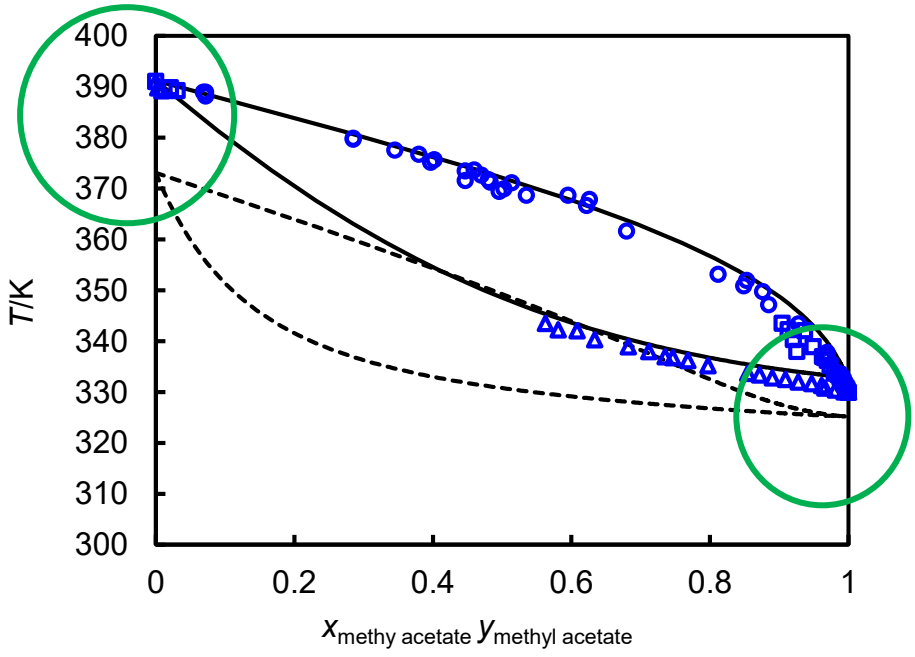

Figure 6.7: Isobaric temperature-composition (*T, x*) phase diagram for the (methyl acetate + acetic acid) system [215, 216]: □ and ○, dew points; △, bubble points. The dashed curve is the calculation from SAFT-γ Mie using literature parameters and the solid curve is the calculation from SAFT-γ Mie using the optimised parameters. The open green circles show the deviation in the boiling points of the pure components.

The Peng Robinson EoS was also used to predict the phase behaviour of the ternary system. The estimation of the binary interaction parameters for (methyl propanoate + CO_2) mixture was covered in Chapter 5. The binary interaction parameters for (propionic acid + CO_2) were estimated from the experimental VLE data measured in this work at 333.19 K while the interaction parameters for (methyl propanoate + propionic acid) were obtained by regression to the isobaric phase behaviour measurements at temperatures from the boiling point of the less volatile component (propionic acid) to that of the high volatile component (methyl propanoate) at atmospheric pressure. The PR EoS interaction parameters for these binaries are summarised in Table 6.5. The predictions of PR for (propionic acid + CO_2) and (methyl propanoate + propionic acid) systems are shown graphically in Figure 6.5 and Figure 6.6 (represented by the red dashed curves), respectively. As can be seen in the figures, the description of SAFT-γMie for the bubble and dew points in the phase envelopes of the binaries is more accurate than that of PR model.

Table 6.5: PR EoS binary interaction parameters estimated in this work.

Component *i*	Component *j*	k_{ij}	l_{ij}
Propionic acid	CO_2	0.023905	-0.101057
Methyl propanoate	CO_2	0.00450	0
Methyl propanoate	Propionic acid	-0.028011	0.057995

6.2.5 Discussion and Comparison with Experiments

Figure 6.2 shows the isothermal composition diagram for the ternary mixture (methyl propanoate + propionic acid + carbon dioxide) with a fixed equal molar ratio between methyl propanoate and propionic acid. To investigate the effect of temperature and pressure on the phase behaviour of each component in the phases, isothermal (p, x_i) diagrams, as shown in Figure 6.8, for the two coexisting phases are drawn from Figure 6.2. The mole fractions of CO_2, methyl propanoate and propionic acid in the liquid phase are shown in Figure 6.8a, c, and e while their mole fractions in the CO_2-rich phase are plotted in Figure 6.8b, d, and f. Predictions from SAFT and PR models are also included in the figures. As can be seen from Figure 6.8a and b, at constant temperature the concentration of CO_2 in the liquid phase increases when pressure is increased. The mole fractions of CO_2 in the CO_2-rich vapour phase show the same relationship until the conditions reach critical where CO_2 content starts to decrease. On the other hand, at constant pressure the mole fractions of CO_2 in the liquid and

vapour phases decrease when temperature increases. Figure 6.8c, d, e and f show a reverse dependence of the contents of methyl propanoate and propionic acid upon temperature and pressure as seen with CO_2 in both phases. The dependence of temperature and pressure on the phase behaviour predicted by SAFT in this approach agrees well with that measured in this work, but the predictions are not accurate as it always predicts equal molar ratio for (methyl propanoate + propionic acid) in the liquid phase at all isotherms, which is not matching with the experimental measurements. PR predictions have almost the same accuracy seen in SAFT. The comparisons between the mole fractions of methyl propanoate and that of propionic acid in the liquid and CO_2-rich vapour phases under conditions of VLE for the ternary system are shown in Figure 6.9a and b at temperatures of (343.13, 363.17 and 423.11) K. As can be seen from the graphs, at fixed temperature, pressure and molar ratio the content of propionic acid is more than that of the ester in the liquid phase and less in the vapour phase.

In Figure 6.3 and Figure 6.4, SAFT-γ Mie prediction is compared with the VLE data measured at temperature of 383.17 K and pressure of 4 MPa and VLE data measured at temperature of 363.17 K and pressure of 6 MPa for the ternary system (methyl propanoate + propionic acid + carbon dioxide). It can be seen that the SAFT model prediction is quite good for the bubble and dew points at both conditions. The vapour phase is rich in CO_2, but SAFT can also predict well the compositions of the components in this phase as can be seen in Figure 6.10, which is a close-up figure at the vapour phase. As seen in Figure 6.4, there is a small deviation between the SAFT predictions and the experimental liquid-phase equilibrium data in the ternary system at the temperature of 363.17 K and pressure of 6 MPa.

In Figure 6.11 and Figure 6.12, PR EoS prediction is compared with the VLE data measured at (T = 383.17 K and p = 4 MPa) and (T = 363.17 K and p = 6 MPa) for the ternary system (methyl propanoate + propionic acid + carbon dioxide). It can be seen that the PR EoS predictions and the experimental VLE data are in good agreement at both conditions. Figure 6.13 is a close-up figure showing the PR EoS predictions at the vapour phase in both conditions.

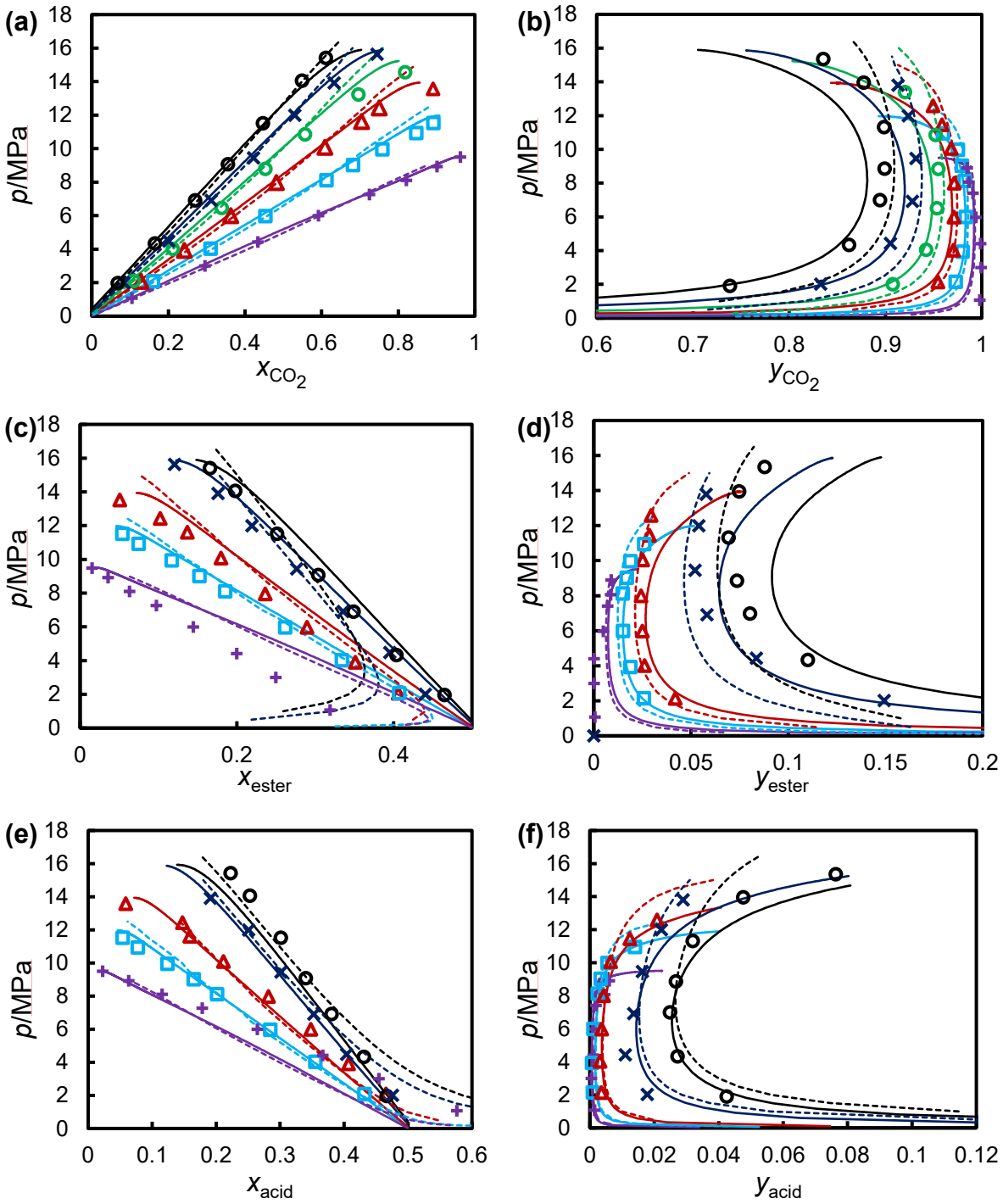

Figure 6.8: Isothermal pressure-composition (p, x) for the (methyl propanoate + propionic acid + carbon dioxide) system in the liquid phase (a, c, e) and CO_2-rich phase (b, d, f) under VLE conditions and molar ratio of (methyl propanoate + propionic acid) of 1:1. The symbols represent the experimental data at: +, T = 323.12 K; □, T = 343.13 K; Δ, T = 363.17 K; ×, T = 403.12 K; O, T = 423.11 K. The continuous curves and dashed curves are SAFT-γ Mie predictions and PR predictions at the corresponding temperatures indicated by colours.

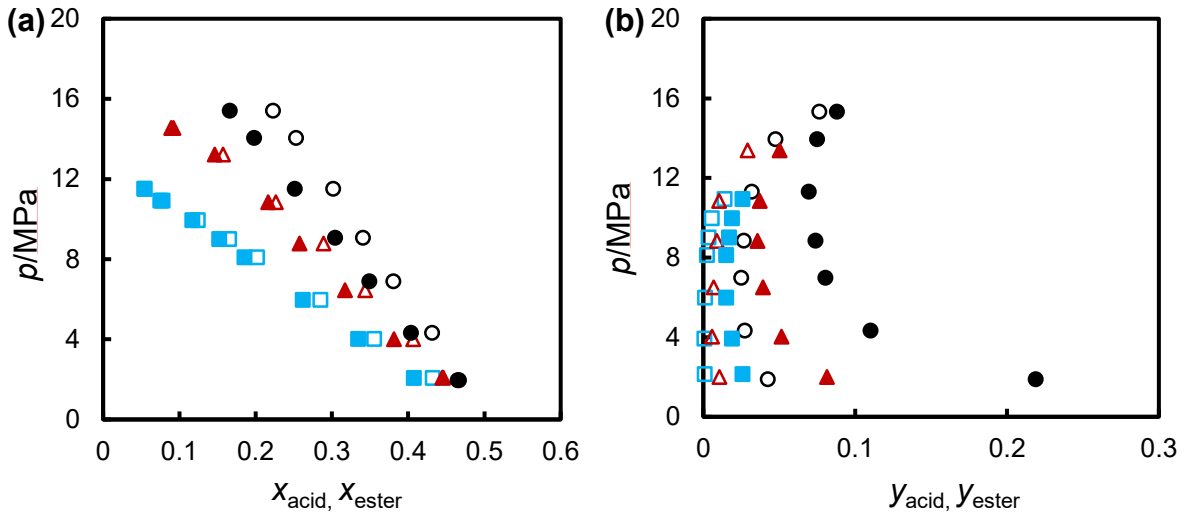

Figure 6.9: Isothermal pressure-composition (p, x) for methyl propanoate and propionic acid measured in the liquid phase (a) and CO_2-rich phase (b) under VLE conditions and molar ratio of (methyl propanoate + propionic acid) of 1:1 for (methyl propanoate + propionic acid + carbon dioxide) system. The symbols correspond to the VLE data measured at: □ and ■, T = 343.13 K; Δ and ▲, T = 363.17 K; and O and ●, T = 423.11 K. The filled symbols denote methyl propanoate and the open symbols denote propionic acid.

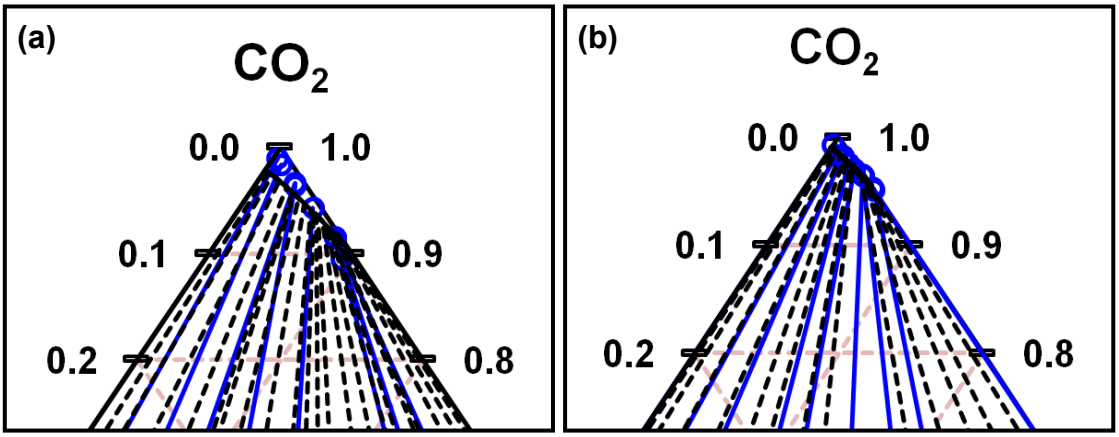

Figure 6.10: Phase equilibria for (methyl propanoate + propionic acid + carbon dioxide) system at: (a), T = 383.15 K and p = 4.0 MPa, and (b), T = 363.15 K and p = 6.0 MPa. The BLUE symbols denote the experimental data measured in the vapour phase. The BLUE continuous lines and BLACK dashed lines are the tie-lines between the coexisting phases measured experimentally and calculated by SAFT-γ Mie, respectively. The continuous curve is the vapour phase boundary calculated by SAFT-γ Mie.

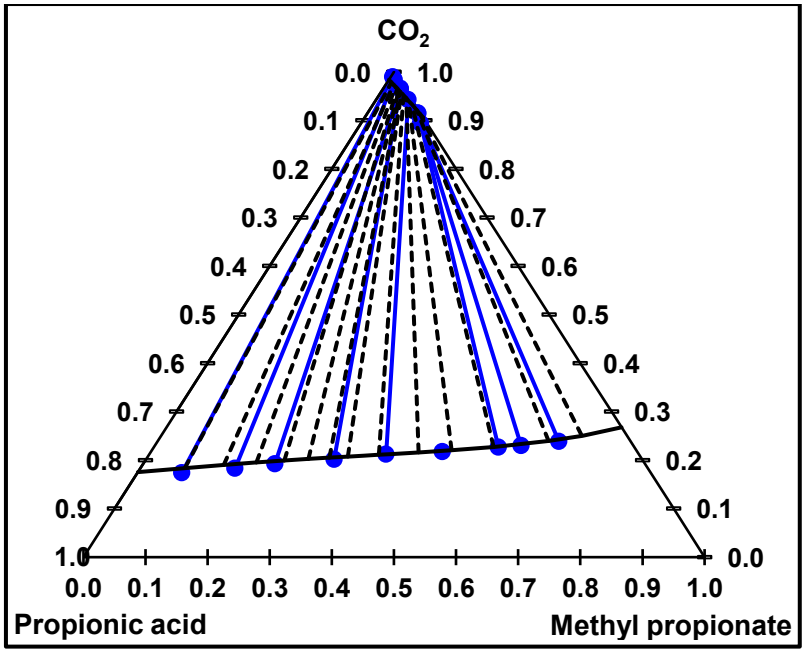

Figure 6.11: Phase equilibria for (methyl propanoate + propionic acid + carbon dioxide) system at T = 383.15 K and p = 4.0 MPa. The BLUE filled symbols correspond to the VLE data measured in this work. The BLUE continuous lines and BLACK dashed lines are the tie-lines between the coexisting phases measured experimentally and calculated by PR EoS, respectively. The continuous curves are the phase boundaries calculated by PR EoS.

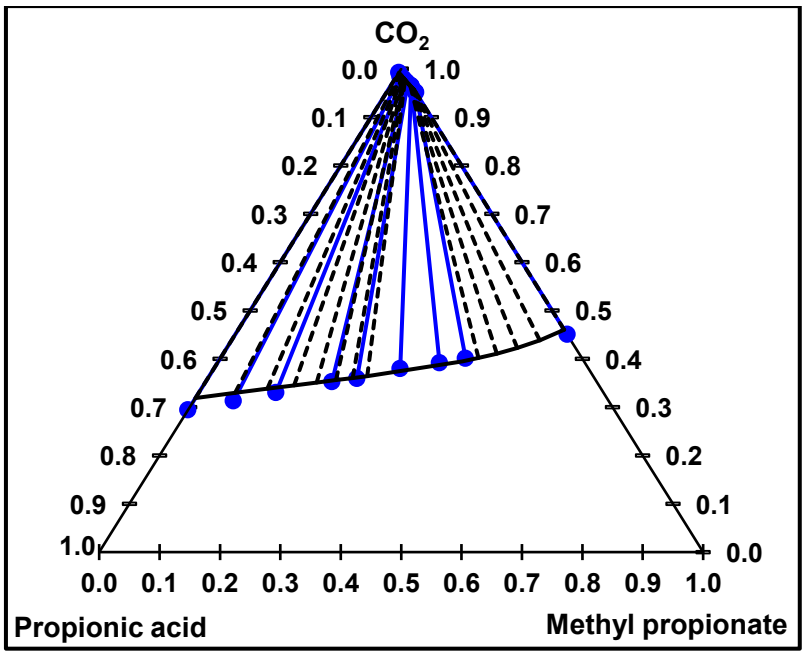

Figure 6.12: Phase equilibria for (methyl propanoate + propionic acid + carbon dioxide) system at T = 363.15 K and p = 6.0 MPa. The BLUE filled symbols correspond to the VLE data measured in this work. The BLUE continuous lines and BLACK dashed lines are the tie-lines between the coexisting phases measured experimentally and calculated by PR EoS, respectively. The continuous curves are the phase boundaries calculated by PR EoS.

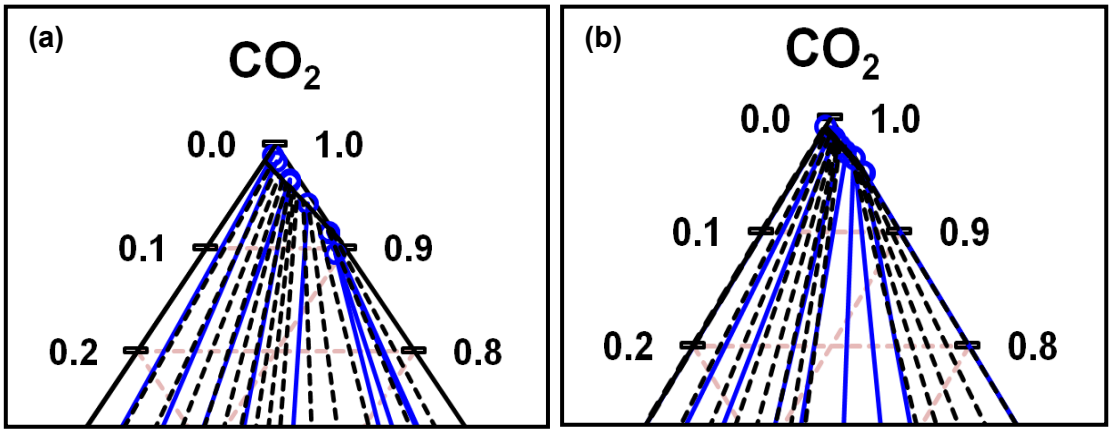

Figure 6.13: Phase equilibria for (methyl propanoate + propionic acid + carbon dioxide) system at: (a), T = 383.15 K and p = 4.0 MPa, and (b), T = 363.15 K and p = 6.0 MPa. The BLUE symbols represent the experimental data in the vapour phase. The BLUE continuous lines and BLACK dashed lines are the tie-lines between the coexisting phases measured experimentally and calculated by PR EoS, respectively. The continuous curve is the vapour phase boundary calculated by PR EoS.

6.2.6 Conclusion

The phase behaviour of the system was measured in two different baths. In the first bath, the molar ratio of the mixture (methyl propanoate + propionic acid) was fixed to be 1:1 and six isotherms at temperatures from (323.12 to 423.11) K were measured at different CO_2 pressures from (1 to 20) MPa, while in the second bath, the temperature and pressure of the equilibrium cell were fixed (T = 383.17 K and p = 4 MPa, T = 363.17 K and p = 6 MPa). The SAFT-γ Mie prediction was compared with the VLE data measured at temperature of 383.17 K and pressure of 4 MPa and VLE data measured at temperature of 363.17 K and pressure of 6 MPa for the ternary system (methyl propanoate + propionic acid + carbon dioxide) using the cross interactions between CO_2-COOH, CO_2-COO and COO-COO which were optimised previously. The SAFT model prediction was quite good for the bubble and dew points at both conditions. The PR EoS prediction was also compared with the VLE data measured and it showed a satisfactory description for the system in both conditions.

6.3 (*Tert*-butanol + Water + Carbon Dioxide)

6.3.1 Introduction

To the best of our knowledge, the system (*tert*-butanol + water + carbon dioxide) has only been studied by Kim et al. [155] at the single temperature of 323.2 K and at pressures from (6 to 12) MPa. Their results showed quite complex phase behaviour of the ternary system under CO_2 addition with extended three phase regions. Two other publications dealing with this particular system are limited to investigations at atmospheric pressure and temperature of 298 K [217] or p = (1.5 to 4.0) MPa and low temperatures ranging from (275 to 282) K [218]. In this work, in collaboration with a visiting research student, Kirsten Grübel, the phase behaviour of the ternary system (*tert*-butanol + water + carbon dioxide) was investigated over the temperature range from (283.2 to 423.17) K and pressures from (4 to 18) MPa.

6.3.2 Comparison of VLE Data with Literature Data

VLLE data for the ternary system were measured at T = 323.13 K, at pressures of 6.03 MPa, 8.02 MPa and 12.00 MPa, and the results, provided in Table 6.6, are compared with the results of the work of Kim et al. [155] carried out at similar conditions in Figure 6.14 a, b and c (p = 6.03 MPa, p = 8.02 MPa and p = 12.00 MPa, respectively). At a temperature of 323.13 K and 6.03 MPa CO_2 pressure, the ternary system exhibits three coexisting fluid phases. Analysis of the three phases indicates a water-rich phase and a CO_2-rich phase. The measured compositions are in very good agreement with the compositions reported by Kim et al. Analysis of the upper liquid phase with intermediate density show slight deviation, indicating a higher water content and lower *tert*-butanol content for the less dense phase measured in this work. A similar observation was seen for the measurements of the three-phase region at pressure of 8.02 MPa, where good agreement for the water- and CO_2-rich phase compositions can be seen. Generally, the herein presented measurements of the less-dense liquid phase compositions show good repeatability, even for investigations of different feed compositions. However, slight discrepancies for the compositions of this phase between literature and this work can be observed again. These deviations are in the same order of magnitude as the deviations for this phase at p = 6.03 MPa. They might be assigned to differences in experimental procedure, even though the group of Kim et al. used a quite similar recirculation type of analytical apparatus combined with an on-line gas chromatograph but with a single thermal conductivity detector for quantitative analysis of the sample components. Another reason for the slight deviations in analysis of the upper liquid phase with intermediate density might be minor differences in temperature and pressure readings at sampling conditions. As

seen in Figure 6.14a and b, by comparing the results at pressures of 6.03 and 8.02 MPa the composition of the phase with intermediate density changes significantly by increasing the pressure by 2 MPa. Thereby, small variances in pressure reading between this work and literature might lead to discrepancies in composition measurement for the given conditions. At p = 12 MPa and T = 323.13 K, the ternary system is in a two-phase area and the measured compositions of the two coexisting phases are in a very good agreement with literature data.

Table 6.6: Experimental VLLE data for [CO_2 (1) + $(CH_3)_3COH$ (2) + H_2O (3)] at temperatures T and pressures p.

p/MPa	V			L_1			L_2		
	y_1^{exp}	y_2^{exp}	y_3^{exp}	x_1^{exp}	x_2^{exp}	x_3^{exp}	x_1^{exp}	x_2^{exp}	x_3^{exp}
				T = 323.13 K					
6.03	0.9903	0.0080	0.0017	0.0188	0.0386	0.9426	0.1749	0.3110	0.5141
8.02	0.9879	0.0104	0.0017	0.0223	0.0285	0.9492	0.4793	0.2949	0.2257
12.00				0.8055	0.1428	0.0517	0.0210	0.0225	0.9565
12.01				0.8618	0.1050	0.0332	0.0239	0.0205	0.9556

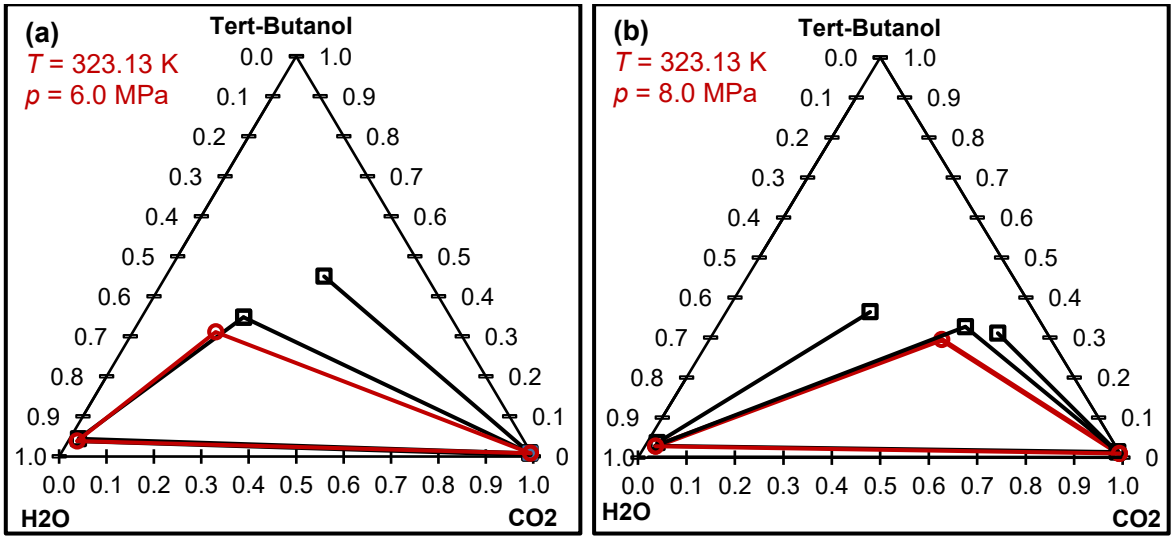

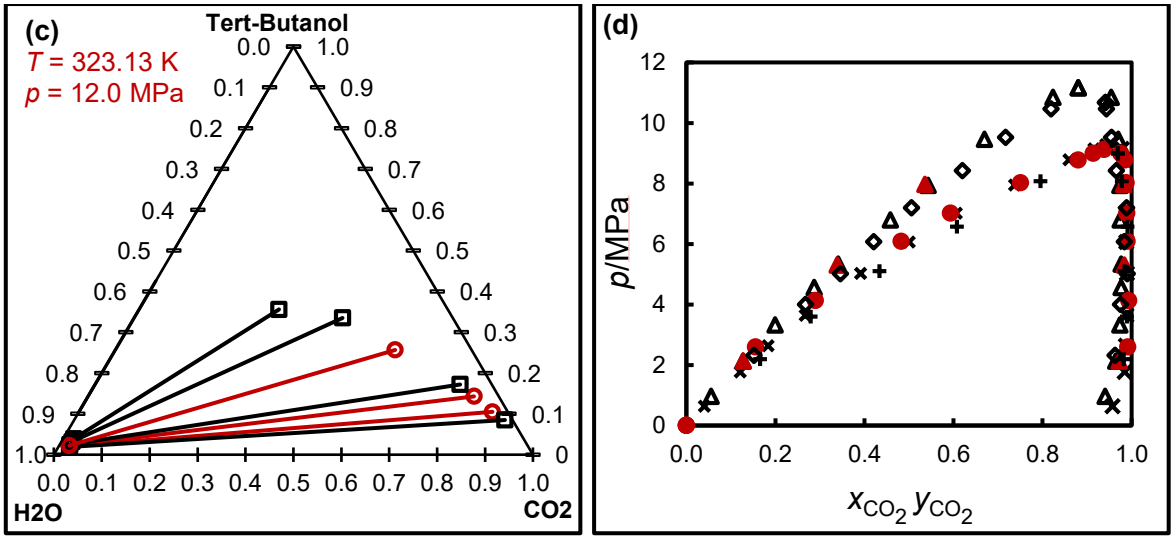

Figure 6.14: (a, b, and c): ternary diagram for (*tert*-butanol + water + carbon dioxide) system. (d): isothermal pressure-composition (*p, x*) phase diagram for the binary system (*tert*-butanol + carbon dioxide). The BLACK symbols and tie-lines represent literature data while the RED symbols and tie-lines represent the experimental data measured in this work at: (a), O: T = 323.13 K, p = 6 MPa (this work), □: T = 323.2 K, p = 6 MPa [155]; (b), O: T = 323.13 K, p = 8 MPa (this work), □: T = 323.2 K, p = 8 MPa [155]; (c), O: T = 323.13 K, p= 12 MPa (this work), □: T = 323.2 K, p = 12 MPa [155]; (d), ▲: T= 343.17 K (this work), ●: T = 323.13 K (this work); **Δ:** T = 343.2 K [155]**;** ◇: T = 343.15 K [219], **✖:** T = 323.2 K [155], and **+**: T = 323.15 K [219].

Further validation measurements were undertaken on the (CO_2 + $(CH_3)_3COH$) binary system at T = 323.13 K and T = 343.17 K. The results are given in Table 6.7 and compared in Figure 6.14d with the available literature data [155, 219]. As can be seen in the figure, there is a small deviation among the literature data especially on the bubble curves. The deviation might be due to different methodologies used in their experimental measurements. However, good agreement between this work and the literature data is observed over the entire pressure range.

Table 6.7: Experimental VLE data for [CO_2 (1) + $(CH_3)_3COH$ (2)] at temperatures T and pressures p[a].

p/MPa	x_1^{exp}	y_1^{exp}	p/MPa	x_1^{exp}	y_1^{exp}
T = 323.13 K			T = 343.17 K		
1.77	0.1102	0.9854	2.13	0.1274	0.9719
2.67	0.1730	0.9890	5.30	0.3383	0.9831
3.64	0.2497	0.9905	7.97	0.5356	0.9819
5.03	0.3670	0.9912			
6.09	0.4836	0.9901			
7.02	0.5933	0.9894			
8.02	0.7508	0.9879			
8.77	0.8796	0.9842			
8.99	0.9139	0.9756			
9.12	0.9383				

[a]Notation: x_1 and y_1 denote the mole fraction of CO_2 in the liquid phase and the mole fraction of CO_2 in the vapour phase, respectively.

6.3.3 Experimental Results

The binary system (CO_2+ H_2O) exhibits type III phase behaviour according to the classification of Van Konynenburg and Scott while the binary systems (CO_2 + $(CH_3)_3COH$) and (H_2O + $(CH_3)_3COH$) exhibit type I based on the measured and existing literature data [220]. Therefore, the ternary system (*tert*-butanol + water + carbon dioxide) is expected to exhibit ternary class III phase behaviour according to the global ternary diagrams classification proposed by Bluma and Dieters [57]. Mixtures of this class possess LLE immiscibility region, and therefore VLLE regions are expected. The system was studied along five isotherms at temperatures of (283.2, 298.18, 323.13, 373.10 and 423.17) K and at four pressures (4, 8, 12 and 18) MPa and at least three different starting compositions of (*tert*-butanol + water). The VLLE regions in which the three fluid phases coexist occurred over wide ranges of temperatures and pressures. The two- and three-phase equilibrium compositions are given in Table 6.8 and shown in Figure 6.15 in the form of isothermal triangular diagrams.

Table 6.8: Experimental VLLE data for [CO_2 (1) + $(CH_3)_3COH$ (2) + H_2O (3)] at temperatures T and pressures p[a].

phase	p/MPa	x_1^{exp}	$u(x_1)$	x_2^{exp}	$u(x_2)$	x_3^{exp}	$u(x_3)$
			T = 283.20 K				
V	4.10	0.9992	0.0000	0.0008	0.0000	0.0000	0.0000
L_1	4.10	0.4103	0.0082	0.2869	0.0092	0.3028	0.0080
L_2	4.10	0.4751	0.0221	0.3178	0.0114	0.2071	0.0209
			T = 298.18 K				
V	4.00	0.9980	0.0001	0.0020	0.0001	0.0000	0.0001
L_1	4.00	0.0254	0.0025	0.0726	0.0032	0.9020	0.0027
L_2	4.00	0.1308	0.0057	0.3199	0.0062	0.5492	0.0065
V	4.01	0.9968	0.0001	0.0032	0.0001	0.0000	0.0001
L_1	4.01	0.1698	0.0092	0.4191	0.0115	0.4110	0.0096
L_2							
V							
L_1	8.02	0.0261	0.0010	0.0265	0.0012	0.9474	0.0012
L_2	8.03	0.9161	0.0019	0.0666	0.0018	0.0173	0.0015
			T = 323.13 K				
V	4.02	0.9913	0.0003	0.0070	0.0003	0.0017	0.0003
L_1	4.02	0.0250	0.0033	0.0960	0.0042	0.8790	0.0036
L_2							
V	4.00	0.9572	0.0008	0.0160	0.0007	0.0268	0.0003
L_1	4.00	0.0497	0.0073	0.2754	0.0094	0.6749	0.0079
L_2							
V	4.03	0.9905	0.0003	0.0074	0.0031	0.0020	0.0003
L_1	4.03	0.1198	0.0088	0.4029	0.0113	0.4774	0.0094
L_2							
V	8.02	0.9879	0.0004	0.0104	0.0005	0.0017	0.0004
L_1	8.02	0.0223	0.0011	0.0285	0.0013	0.9491	0.0012
L_2	8.02	0.4793	0.0072	0.2949	0.0062	0.2257	0.0060
V							
L_1	12.01	0.0210	0.0008	0.0225	0.0009	0.9565	0.0009
L_2	12.01	0.8055	0.0029	0.1428	0.0027	0.0517	0.0023
V							
L_1	12.00	0.0239	0.0008	0.0205	0.0010	0.9556	0.0010
L_2	12.00	0.8630	0.0037	0.1050	0.0035	0.0320	0.0031
V							
L_1	12.00	0.0210	0.0008	0.0225	0.0010	0.9565	0.0010
L_2	12.00	0.5841	0.0058	0.2566	0.0054	0.1593	0.0051
			T = 373.10 K				
V	3.99	0.9291	0.0017	0.0422	0.0019	0.0287	0.0015
L_1	3.99	0.0163	0.0030	0.0881	0.0038	0.8956	0.0032
L_2							
V	4.08	0.9286	0.0031	0.0425	0.0032	0.0289	0.0030
L_1	4.00	0.0497	0.0073	0.2754	0.0094	0.6749	0.0079
L_2							
V	4.01	0.9267	0.0032	0.0478	0.0034	0.0254	0.0031
L_1	4.01	0.0819	0.0088	0.4149	0.0114	0.5032	0.0079
L_2							
V	8.01	0.9461	0.0015	0.0362	0.0016	0.0177	0.0013

L_1	8.00	0.0181	0.0013	0.0368	0.0017	0.9451	0.0015
L_2	8.01	0.1294	0.0052	0.2748	0.0057	0.5958	0.0060
V	8.04	0.9443	0.0015	0.0376	0.0017	0.0181	0.0013
L_1	8.04	0.1386	0.0079	0.3056	0.0100	0.5558	0.0084
L_2							
V	8.00	0.9467	0.0014	0.0362	0.0016	0.0171	0.0013
L_1	8.02	0.1877	0.0087	0.3664	0.0109	0.4459	0.0091
L_2							
V	12.02	0.9327	0.0012	0.0499	0.0023	0.0174	0.0018
L_1	12.02	0.0209	0.0009	0.0239	0.0011	0.9552	0.0010
L_2	12.02	0.3717	0.0063	0.3125	0.0061	0.3158	0.0061
V							
L_1	18.05	0.0219	0.0006	0.0143	0.0007	0.9638	0.0007
L_2	18.05	0.8264	0.0034	0.1256	0.0031	0.0480	0.0028
			T = 423.17 K				
V	4.15	0.6918	0.0059	0.1654	0.0065	0.1428	0.0053
L_1	4.15	0.0106	0.0027	0.0784	0.0034	0.9110	0.0029
L_2							
V	4.02	0.6842	0.0062	0.1790	0.0069	0.1367	0.0056
L_1	4.02	0.0295	0.0065	0.2357	0.0085	0.7348	0.0071
L_2							
V	3.99	0.6875	0.0062	0.1791	0.0069	0.1334	0.0056
L_1	4.00	0.0493	0.0085	0.3760	0.0110	0.5747	0.0091
L_2							
V	8.07	0.7862	0.0045	0.1209	0.0050	0.0929	0.0040
L_1	8.03	0.0172	0.0022	0.0521	0.0026	0.9307	0.0022
L_2	8.00	-		-		-	
V	7.99	0.8044	0.0042	0.1111	0.0046	0.0845	0.0037
L_1	7.99	0.0697	0.0063	0.2226	0.1070	0.7078	0.0089
L_2							
V	7.98	0.7913	0.0045	0.1212	0.0050	0.0875	0.0040
L_1	7.98	0.1210	0.0084	0.3478	0.0107	0.5312	0.0089
L_2							
V	12.02	0.8247	0.0043	0.1171	0.0049	0.0583	0.0038
L_1	12.02	0.0246	0.0015	0.0420	0.0019	0.9334	0.0017
L_2	12.03	0.2043	0.0057	0.2981	0.0059	0.4976	0.0063

[a]Notation: x_i, V, L_1 and L_2 denote the mole fraction of component i in any phase, the vapour phase, H_2O-rich phase, and the less-dense liquid phase, respectively. The experimental measurements taken at T = 323.13 K and p = 6.03 MPa were reported in Table 6.6 which compares the data of this work with the data published in the literature.

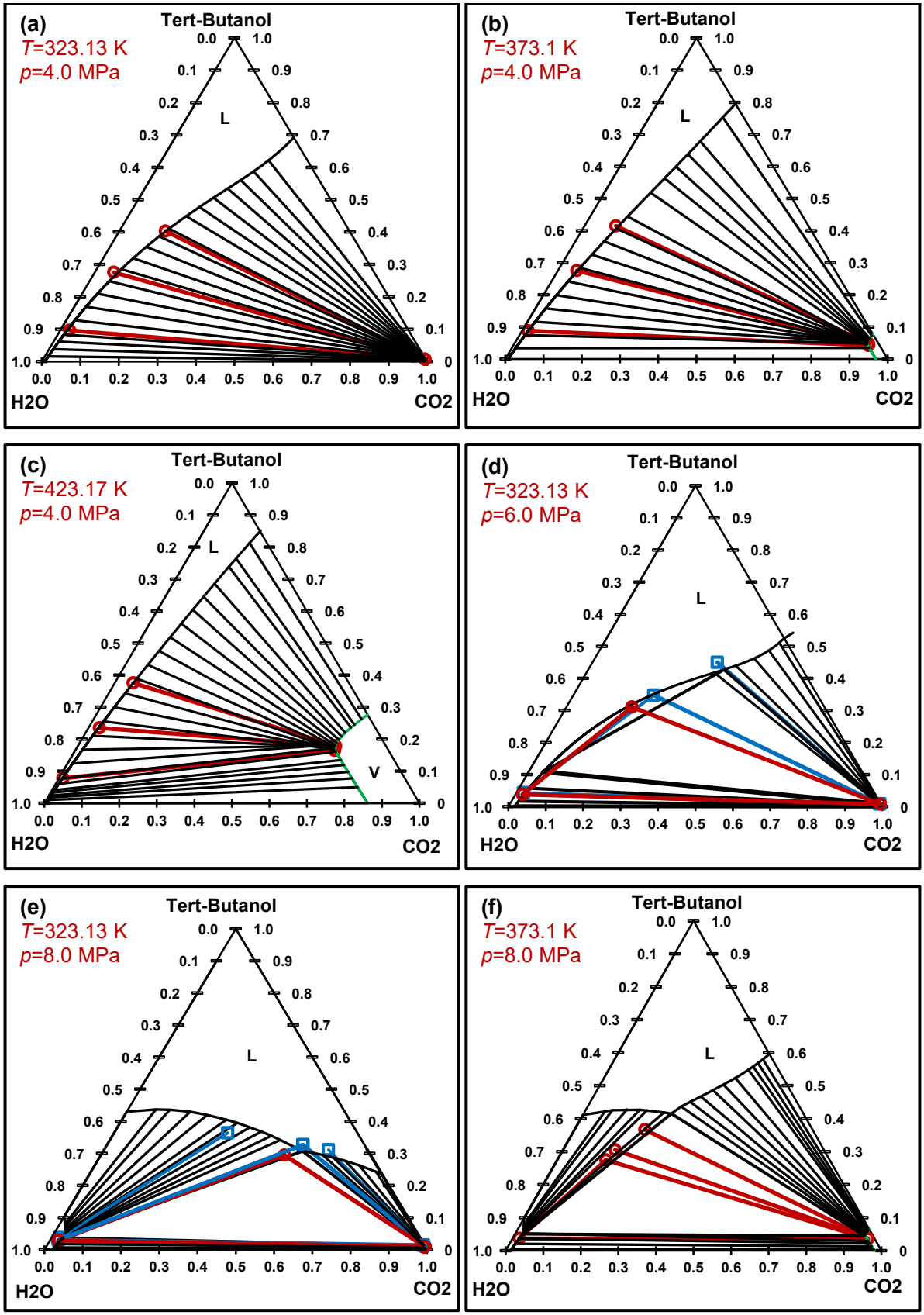
(a)
T=323.13 K
p=4.0 MPa
Tert-Butanol
L
H2O
CO2
(b)
T=373.1 K
p=4.0 MPa
Tert-Butanol
L
H2O
CO2
(c)
T=423.17 K
p=4.0 MPa
Tert-Butanol
L
V
H2O
CO2
(d)
T=323.13 K
p=6.0 MPa
Tert-Butanol
L
H2O
CO2
(e)
T=323.13 K
p=8.0 MPa
Tert-Butanol
L
H2O
CO2
(f)
T=373.1 K
p=8.0 MPa
Tert-Butanol
L
H2O
CO2

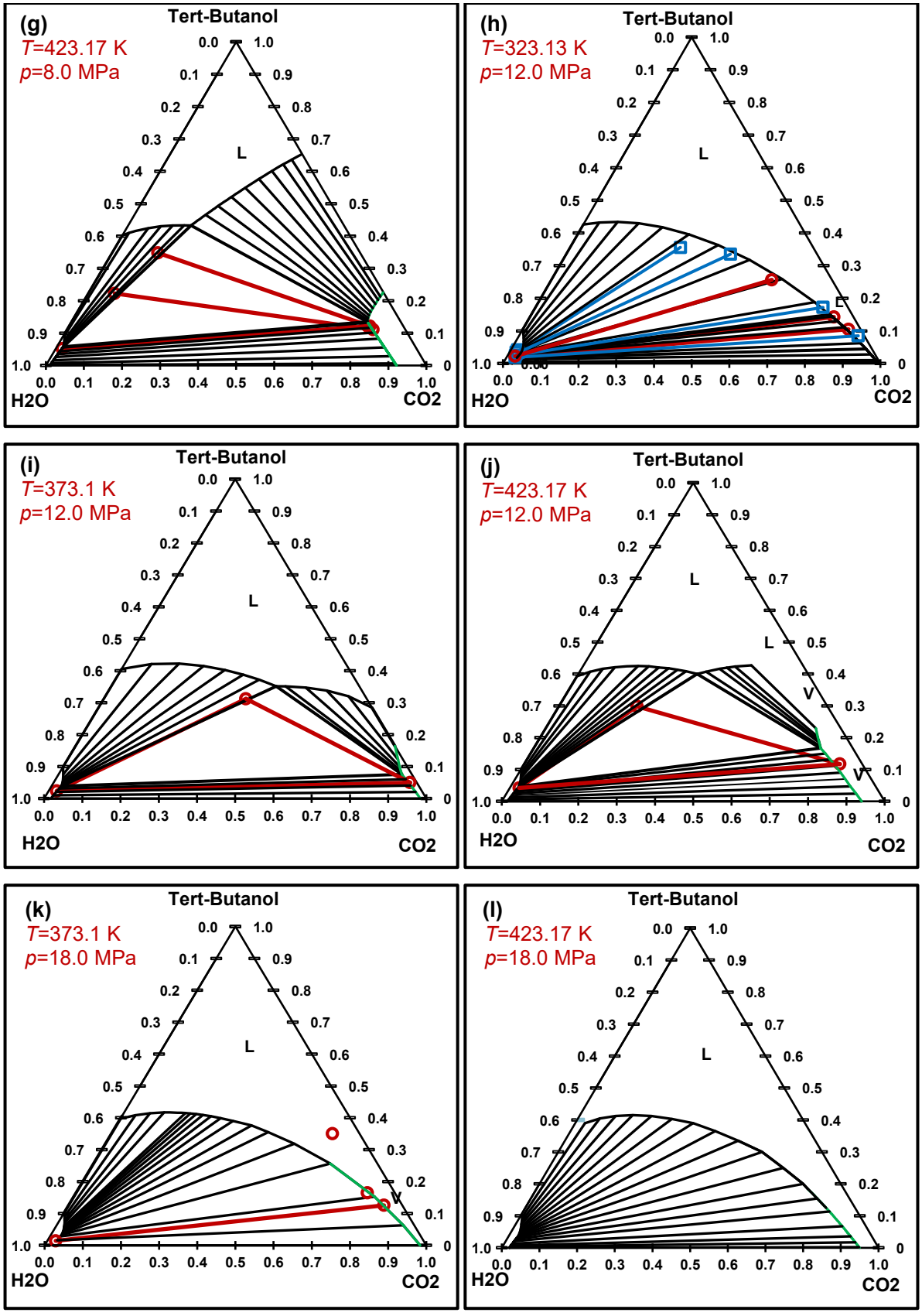
(g)
T=423.17 K
p=8.0 MPa
Tert-Butanol
L
H2O
CO2
(h)
T=323.13 K
p=12.0 MPa
Tert-Butanol
L
H2O
CO2
(i)
T=373.1 K
p=12.0 MPa
Tert-Butanol
L
H2O
CO2
(j)
T=423.17 K
p=12.0 MPa
Tert-Butanol
L
V
H2O
CO2
(k)
T=373.1 K
p=18.0 MPa
Tert-Butanol
L
V
H2O
CO2
(l)
T=423.17 K
p=18.0 MPa
Tert-Butanol
L
H2O
CO2

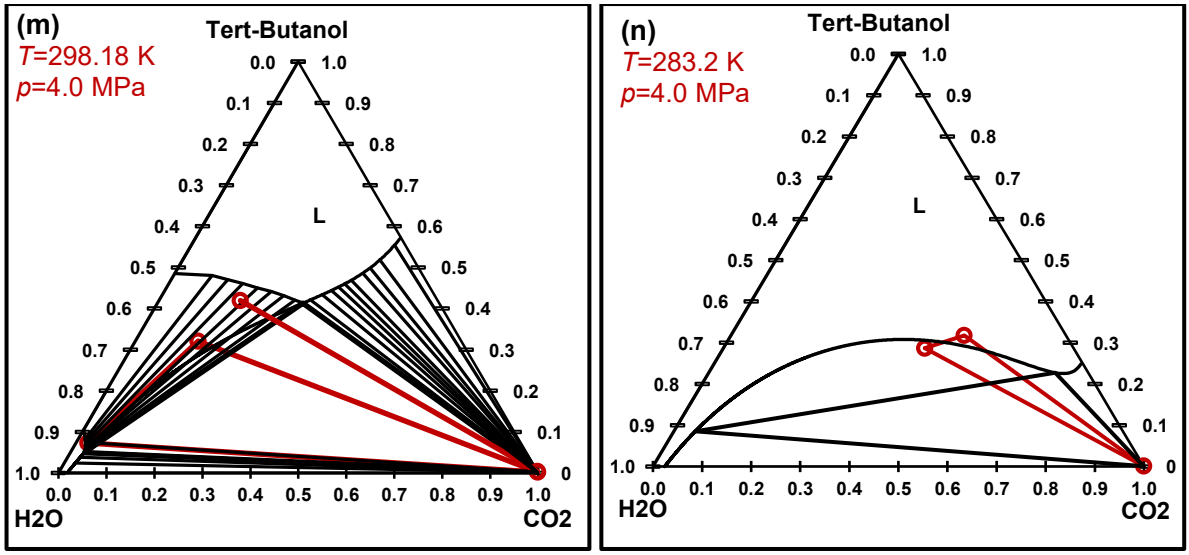

Figure 6.15: Ternary diagram for (*tert*-butanol + water + carbon dioxide) system: (a) T = 323.13 K and p = 4 MPa, (b) T = 373.10 K and p = 4 MPa, (c) T = 423.17 K and p = 4 MPa, (d) T = 323.13 K and p = 6 MPa, (e) T = 323.13 K and p = 8 MPa, (f) T = 373.10 K and p = 8 MPa, (g) T = 423.17 K and p = 8 MPa, (h) T = 323.13 K and p = 12 MPa, (i) T = 373.10 K and p = 12 MPa, (j) T = 423.17 K and p = 12 MPa, (k) T = 373.10 K and p = 18 MPa, (l) T = 423.17 K and p = 18 MPa, (m) T = 298.18 K and p = 4 MPa, and (n) T = 283.2K and p = 4 MPa. The symbols O and □ represent the experimental data and literature data, respectively. The continuous coloured lines are the experimental and literature tie-lines between coexisting phases. The continuous black lines are calculated by SAFT-γ Mie. The continuous black curves and the green curves are the liquid and vapour phases boundaries, respectively, calculated by SAFT-γ Mie.

The expected vapor-liquid-liquid equilibrium (VLLE) regions could be observed and quantified at temperature of 323.13 K from p = (6.03 to 8.02) MPa (Figure 6.15d and e), at T = 373.10 K from p = (8.00 to 12.02) MPa (Figure 6.15f and i), and at T = 423.17 K from p = (7.99 to 12.00) MPa (Figure 6.15g and j). Under these conditions, the system disaggregates into three phases, namely a water-rich liquid phase at the bottom of the view cell; a CO_2-rich vapor phase and a second liquid phase with intermediate density, immiscible with the water-rich phase, which contains the majority of the overall systems *tert*-butanol content (see Figure 6.16 left). From the experimental results, it becomes apparent that at higher system temperatures more CO_2 pressure is required for the occurrence of the three-phase area. This perception goes with the analysis at low temperatures of 283.20 K and 298.18 K, where three-phase areas could be indicated already at p = 4.08 MPa and p = 4.00 MPa, respectively (see Table 6.8 and Figure 6.15m and n).

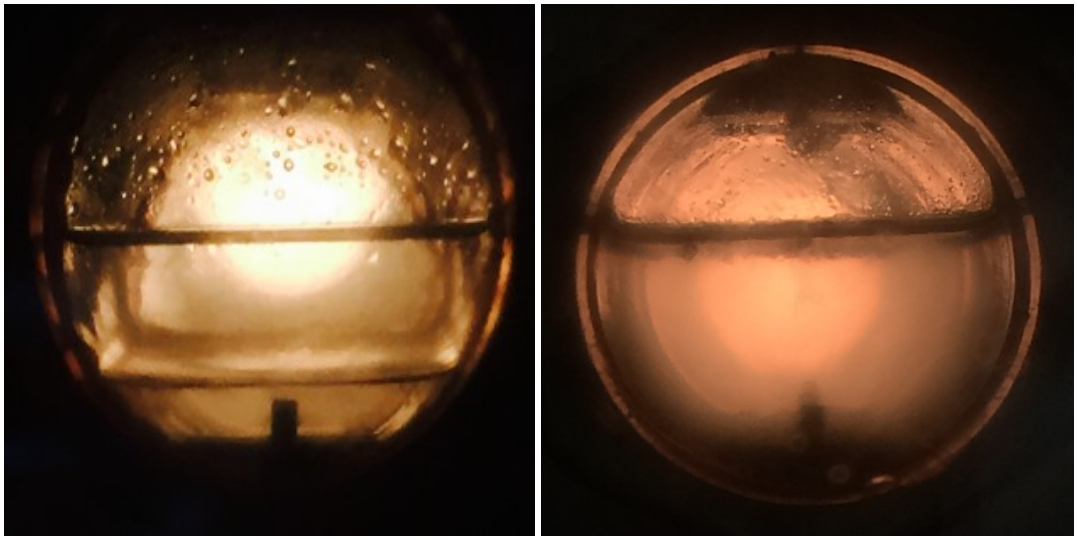

Figure 6.16: Images of the cell interior: three coexisting fluid phases (left), two coexisting fluid phases (right).

Beyond these VLLE pressure- and temperature-conditions, the system exhibits large two-phase regions with coexisting vapour-liquid phases (VLE) at lower pressure levels of about 4 MPa. Different tie-lines of these vapor-liquid equilibria at 323.13 K (Figure 6.15a), 373.10 K (Figure 6.15b), and 423.17 K (Figure 6.15c) could be recorded, indicating that the liquid phase mainly consisting of *tert*-butanol dissolved in water and the coexisting vapor phase is rich in CO_2. Regarding the phase behaviour of the ternary system at 4 MPa, it can be seen that the content of H_2O and *tert*-butanol in the CO_2-rich vapour phase increases remarkably by increasing temperature. When pressures exceed the conditions where VLLE areas are present in the phase diagrams (precisely 12 MPa at 323.13 K (Figure 6.15h), 18 MPa at 373.10 K and 423.17 K (Figure 6.15k and l)), the system exhibits liquid-liquid equilibrium with the liquid phase rich in water and a coexisting liquid phase consisting of *tert*-butanol dissolved in CO_2.

At some temperature and pressure conditions, not all phases could be sampled due to either a phase was too small or the phase occurred in the form of droplets or a thin layer on the surface of the cell. Figure 6.17a, b and c show the circulation process inside the cell, the small phases, and the droplets and phase layer formation on the cell surface, respectively. Measurements at the temperature of 423.15 K and at the pressure of 18 MPa were discarded as it seemed a component formed on the surface of the cell, as shown in Figure 6.18, which may affect the phase behaviour of the system. This observation was supported by the chromatographic analysis, where a new peak appeared in the chromatograms of the samples at mentioned condition of temperature and pressure. The emerging substance has not been investigated further, but it is presumed that isobutene has been formed by an acidic catalysed

dehydration of *tert*-butanol in the dense aqueous liquid phase at elevated temperatures [221-224]. However, the predictions from the SAFT-γ Mie and PR EoS are shown in Figure 6.15l and Figure 6.21l, respectively.

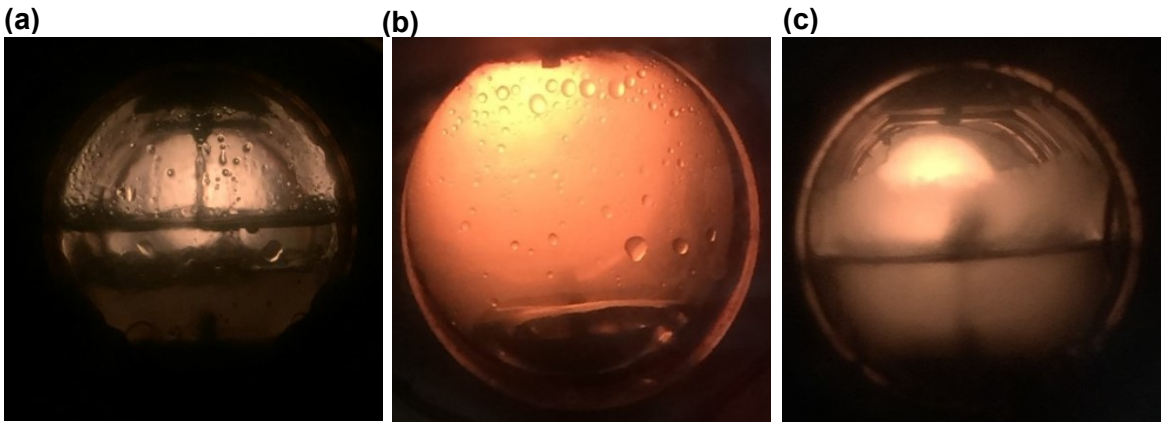

Figure 6.17: Images of the cell interior: (a) the circulation process inside the cell, (b) the small phases, (c) droplets and phase layer formation on the cell surface.

Figure 6.18: Formation of isobutene by an acidic catalysed dehydration of tert-butanol.

6.3.4 Modelling

The like group parameters of the functional groups H_2O and CO_2 have been obtained previously [44, 135, 157, 225] and collected in Table 6.9. These parameters are estimated using the experimental vapour pressure (p_{vap}) and saturated-liquid density (ρ_{sat}) data of the pure components. However, the COH functional group available in *tert*-butanol [$(CH_3)_3COH$] and its cross interactions with CH_3 have not been published in literature yet. The COH group is represented here as one spherical group with three association sites (one of type *H* and two of type *e*). In this work, the vapour pressure and saturated-liquid density data of pure *tert*-

butanol were used in the regression of the like group parameters, and the parameters values obtained are provided in Table 6.9.

Table 6.9: SAFT-γ Mie like group parameters used in this work [135, 157, 225].

group k	v^*_k	S_k	σ_{kk}/Å	(ε_{kk}/k_B) /K	λ^a_{kk}	λ^r_{kk}	$N_{ST,K}$	$n_{k,h}$	$n_{k,e}$	Ref.
CO_2	2	0.8468	3.050	207.89	5.055	26.408	1	1	0	[157]
H_2O	1	1.0000	3.006	266.68	6.000	17.020	2	2	2	[225]
COH	1	0.5180	3.524	791.42	6.000	32.252	3	1	2	This work

A graphical comparison of the SAFT-γ Mie description with the experimental data is shown for the vapour pressure data in Figure 6.19a and for saturated liquid densities in Figure 6.19b. As can be seen in these two figures, SAFT-γ Mie model provides a very accurate description for the vapour-liquid equilibrium of *tert*-butanol. The deviations (Δ_{AAD}) are 3.64% for the vapour pressure and 0.39% for the saturated-liquid density as summarised in Table 6.10.

Table 6.10: Percentage average absolute deviations (Δ_{AAD}) for vapour pressures $p_{vap}(T)$ and for saturated-liquid densities $\rho_{sat}(T)$ determined with SAFT-γ Mie for *tert*-butanol.

Compound	T range/K	n	Δ_{AAD} (p_{vap})	Ref.	T range/K	n	Δ_{AAD} (ρ_{sat})	Ref.
Tert-butanol	307-509	43	3.64	[226-228]	791-532	25	0.39	[205, 229]

The unlike group parameters for the Mie potential interactions and the association interaction parameters for the CO_2-COH and H_2O-COH were estimated from VLE experimental data of [$(CH_3)_3COH$ + CO_2] and [$(CH_3)_3COH$ + H_2O] binary systems, respectively. Here the unlike dispersion energy ε_{kl} and the unlike repulsive Mie exponent λ^r_{kl} were adjusted to fit the mixtures VLE data. The parameters values are provided in Table 6.11.

For the associating interactions between the associating functional groups, the energy ε^{HB}_{klab} and range of the association K_{klab} were adjusted and the values are provided in Table 6.12. All the remaining unlike interaction parameters were calculated using the combining rules as described previously.

Table 6.11: SAFT-γ Mie unlike group parameters used in this work [44, 135, 157, 225].

group *k*	group *l*	(ε_{kl}/k_B)/K	λ_{kl}^r	Ref.
CH_3	H_2O	274.80	CR	[44]
CH_3	CO_2	205.698	CR	[157]
CH_3	COH	436.38	16.088	This work
CO_2	CO_2	207.89	26.408	[157]
CO_2	H_2O	225.026	CR	[157]
CO_2	COH	268.75	8.268	This work
H_2O	H_2O	266.68	17.050	[225]
H_2O	COH	297.842	8.404	This work
COH	COH	791.423	32.252	This work

CR indicates λ_{kl}^r was determined from the combining rule. All other values given in the table have been estimated from experimental data.

Table 6.12: Estimated SAFT-γ Mie like and unlike group association energies (ε_{klab}^{HB}) and bonding volume (K_{klab}) parameters.

group *k*	group *l*	Site a of group *k*	Site b of group *l*	ε_{klab}^{HB}	K_{klab} [Å^3]	Ref.
H_2O	H_2O	*e*	*H*	1985.4	101.69	[44]
H_2O	CO_2	*e*	*H*	1398.141	91.419	[157]
COH	COH	*e*	*H*	2615.642	1.992	This work
H_2O	COH	*e*	*H*	3222.919	10.390	This work

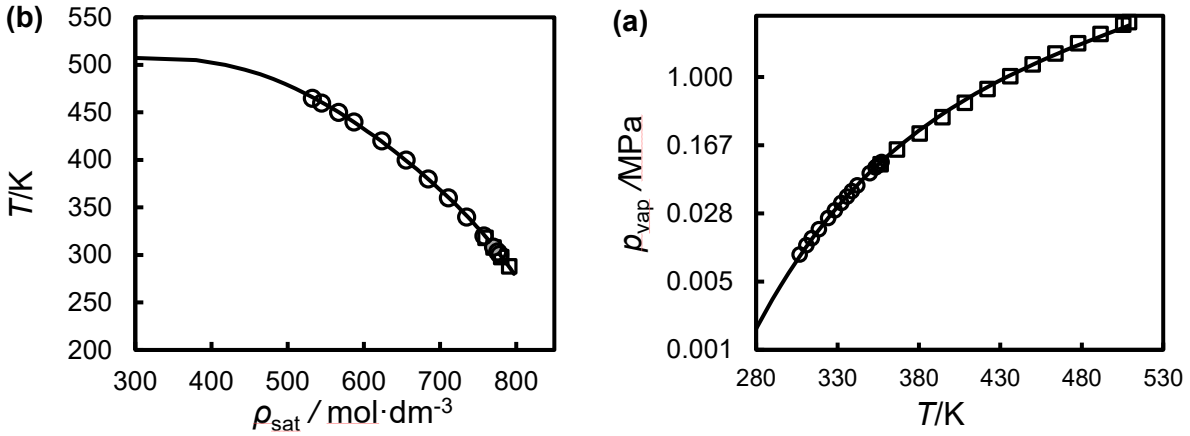

Figure 6.19: The description of SAFT-γ Mie for the fluid-phase equilibria of *tert*-butanol: (a) experimental vapour pressures; and (b) experimental saturated-liquid densities. The open symbols correspond to the experimental data [205, 226-229]. The continuous curves represent the calculation from SAFT-γ Mie.

The SAFT-γ Mie predictions of the phase behaviour of the binary systems (*tert*-butanol + carbon dioxide) and (*tert*-butanol + water) are shown in Figure 6.20a and b, respectively.

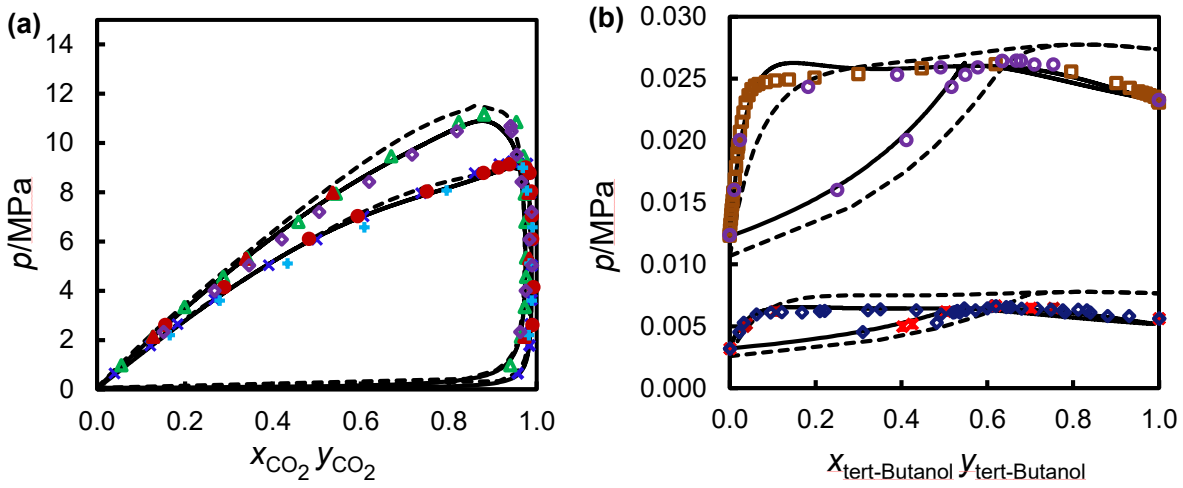

Figure 6.20: Isothermal pressure-composition (*p, x*) phase diagram: (a) binary system (*tert*-butanol + carbon dioxide) and (b) binary system (*tert*-butanol + water). The symbols represent the VLE data measured in this work and literature data at: ✱, T = 298.15K [230]; ◇, T = 298.15 K [220]; Δ, T = 343.2K [219] ; □, T = 323.13K [231]; ○, T = 323.15 K; ●, T = 323.13 K (this work); ▲, T = 343.17 K (this work); ✖, T = 323.2 K [155]; +: T = 323.15 K [219]; and ◇: T = 343.15 K [219]. The continuous curves are the calculations from SAFT-γ Mie. The dashed curves are the calculations from PR EoS.

As can be seen in the figures, very good agreement between the experimental data and model description is observed. After estimating all the cross interactions between the functional groups present in the ternary system (*tert*-butanol + water + carbon dioxide) the SAFT-γ Mie group contribution model was used to predict the phase behaviour of the mixture at temperatures from (283.2 to 423.17) K and pressures ranging from (4 - 18) MPa.

The binary interactions parameters for PR EoS have been estimated using the same VLE experimental data of [$(CH_3)_3COH$ + CO_2] and [$(CH_3)_3COH$ + H_2O] binary systems used for SAFT-γ Mie model, and the values obtained are presented in Table 6.13. The comparison between the description of SAFT-γ Mie and description of PR EoS for the binary systems (*tert*-butanol + water) and (*tert*-butanol + carbon dioxide) is shown in Figure 6.20a and b. As can be seen from the figure, SAFT-γ Mie describes the systems better in both bubble and dew curves. The estimated binary interaction parameters for PR EoS are used to describe and predict the phase behaviour of the ternary system (*tert*-butanol + water + carbon dioxide).

Table 6.13: Binary interaction parameters for use within PR EoS.

Component *i*	Component *j*	k_{ij}	l_{ij}	Source of parameters
tert-butanol	water	-0.1982	0.1935	This work
tert-butanol	carbon dioxide	0.1154	-0.0853	This work
water	carbon dioxide	0.1200	0.0000	ASPEN

6.3.5 Discussion and Comparison with Experiments

In Figure 6.15 a-n (except l), the experimental measurements of the ternary system (carbon dioxide + *tert*-butanol + water) were compared with the predictions of SAFT-γ Mie model. As detailed earlier, the cross interactions between the functional groups H_2O-CO_2, COH-H_2O and COH-CO_2, which the ternary system (*tert*-butanol + carbon dioxide + water) comprises, were estimated from the phase behaviour data of the binary sub-systems and implemented into SAFT-γ Mie model. At a pressure of 4 MPa and temperatures of (323.13, 373.10 and 423.18) K (Figure 6.15a, b, c, respectively), SAFT-γ Mie predicts very well the experimental VLE data, indicating extensive two phase vapour-liquid areas with a CO_2-rich vapour phase and complete miscibility of *tert*-butanol and water under given conditions in the liquid phase. The vapour region expands as the temperature increases at fixed pressure. As can be seen from the Figure 6.15h and k, the mole fractions of the components in the LLE area observed at higher pressures and temperatures (12 MPa at 323.13 K and 18 MPa at 373.10 K) are predicted well by the model. The two liquid phases in equilibrium were observed also at T = 423.17 K and p = 18 MPa and predicted by SAFT-γ Mie, but as mentioned previously, due to the side formation of unwanted components the results were not included. Contrary to the VLE, the LLE shows a miscibility gap between *tert*-butanol and water and full miscibility of *tert*-butanol in the CO_2-rich liquid phase. Interestingly, the LLE areas predicted by the model at the just mentioned conditions extend over nearly the same composition range, even though the temperature and pressure raise remarkably. In between the conditions of VLE and LLE phase behaviour three coexisting phases were experimentally and theoretically determined. SAFT-γ Mie prediction is in good agreement with the three-phase (VLLE) regions which appeared at conditions of medium temperatures and pressures (Figure 6.15d, e, f, g, i, j) except for the upper liquid phase with lower density, in which the model predicts more *tert*-butanol content. This deviation could be due to the fact, that the cross interactions of COH-CO_2 and COH-H_2O were estimated at lower temperatures that were available in the literature as detailed earlier. At conditions of temperature and pressure in which VLLE regions occur, the model predicts a CO_2-rich vapour phase and H_2O-rich liquid phase (VLE) when the content of *tert*-butanol in

the system is very low, and this phase behaviour could not be observed in the experiment. Three-phase regions were predicted also by the model at lower temperatures (283.20 K and 298.18 K) as can been seen in Figure 6.15m and n. The measured compositions of the CO_2-rich phase and the H_2O-rich phase at T = 298.18 K and p = 4 MPa are in a good agreement with the calculated compositions, similar to the observations of the VLLE that occurred at medium conditions, but again the less-dense liquid phase contains higher water content. Large deviations between the calculated and measured compositions of the two liquid phases are observed at T = 283.2 K and p = 4 MPa as seen in Figure 6.15n.

PR EoS model was also used to predict the ternary system (carbon dioxide + *tert*-butanol + water) at measured conditions as shown in Figure 6.21 a-n. As seen earlier, this model predicted well the binary systems (CO_2 + $(CH_3)_3COH$) and (H_2O + $(CH_3)_3COH$) (see Figure 6.20). As can be seen in Figure 6.21a, b and c, PR EoS predicts well the bubble and dew points of the VLE phase behaviour at pressure of 4 MPa and temperatures ranging from (323.13 to 423.17) K except the dew points at high temperature in which the model predicts more CO_2 and less *tert*-butanol contents in the CO_2-rich phase. The model can predict two coexisting liquid phases (LLE) at higher pressures and temperatures (12 MPa at 323.13 K, 18 MPa at 373.10 K and 423.17 K) as shown in Figure 6.21h, k, and l. However, under these conditions and when the *tert*-butanol concentration in the mixture is low the model, similar to SAFT-γ Mie prediction, shows VLE phase behaviour with CO_2-rich vapour phase and H_2O-rich liquid phase. At conditions of T = 323.13 K and p = 12 MPa, PR EoS predicts more *tert*-butanol in the upper less-dense liquid phase when *tert*-butanol in the mixture is increased.

PR EoS is also able to predict three-phase regions (VLLE) at medium conditions of temperatures and pressures (Figure 6.21d, e, f, i). Large deviation between the experimental data and PR prediction can be seen in all conditions at the upper less-dense liquid phase where PR predicts more content of *tert*-butanol and less water while smaller deviation is seen in the water-rich liquid phase (except at T = 283.2 K and p = 4 MPa in Figure 6.21n). The molar compositions of the three components in the system are predicted well by the model in the CO_2-rich vapour phase.

As can be seen in Figure 6.21g and j, PR EoS does not show the VLLE regions, which have been observed experimentally and predicted by SAFT-γ Mie at the temperature of 423.17 K and pressures of 8 and 12 MPa. Figure 6.22 shows the VLLE regions measured in this work and predicted by SAFT and PR models.

In general, SAFT-γ Mie model predicts the phase behaviour of the experimental VLE data better than that of PR EoS.

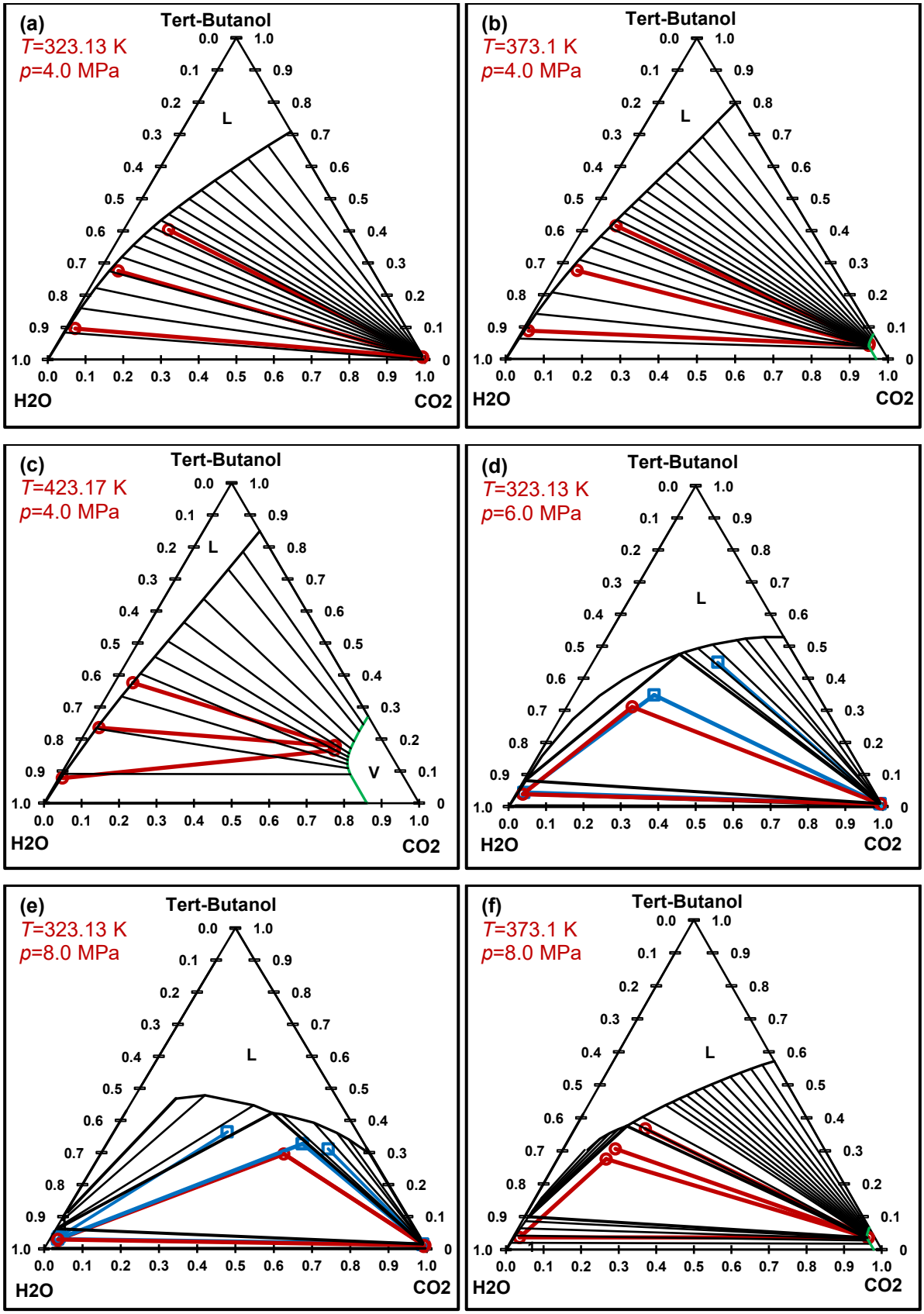
(a)
T=323.13 K
p=4.0 MPa
Tert-Butanol
L
H2O
CO2
(b)
T=373.1 K
p=4.0 MPa
Tert-Butanol
L
H2O
CO2
(c)
T=423.17 K
p=4.0 MPa
Tert-Butanol
L
V
H2O
CO2
(d)
T=323.13 K
p=6.0 MPa
Tert-Butanol
L
H2O
CO2
(e)
T=323.13 K
p=8.0 MPa
Tert-Butanol
L
H2O
CO2
(f)
T=373.1 K
p=8.0 MPa
Tert-Butanol
L
H2O
CO2

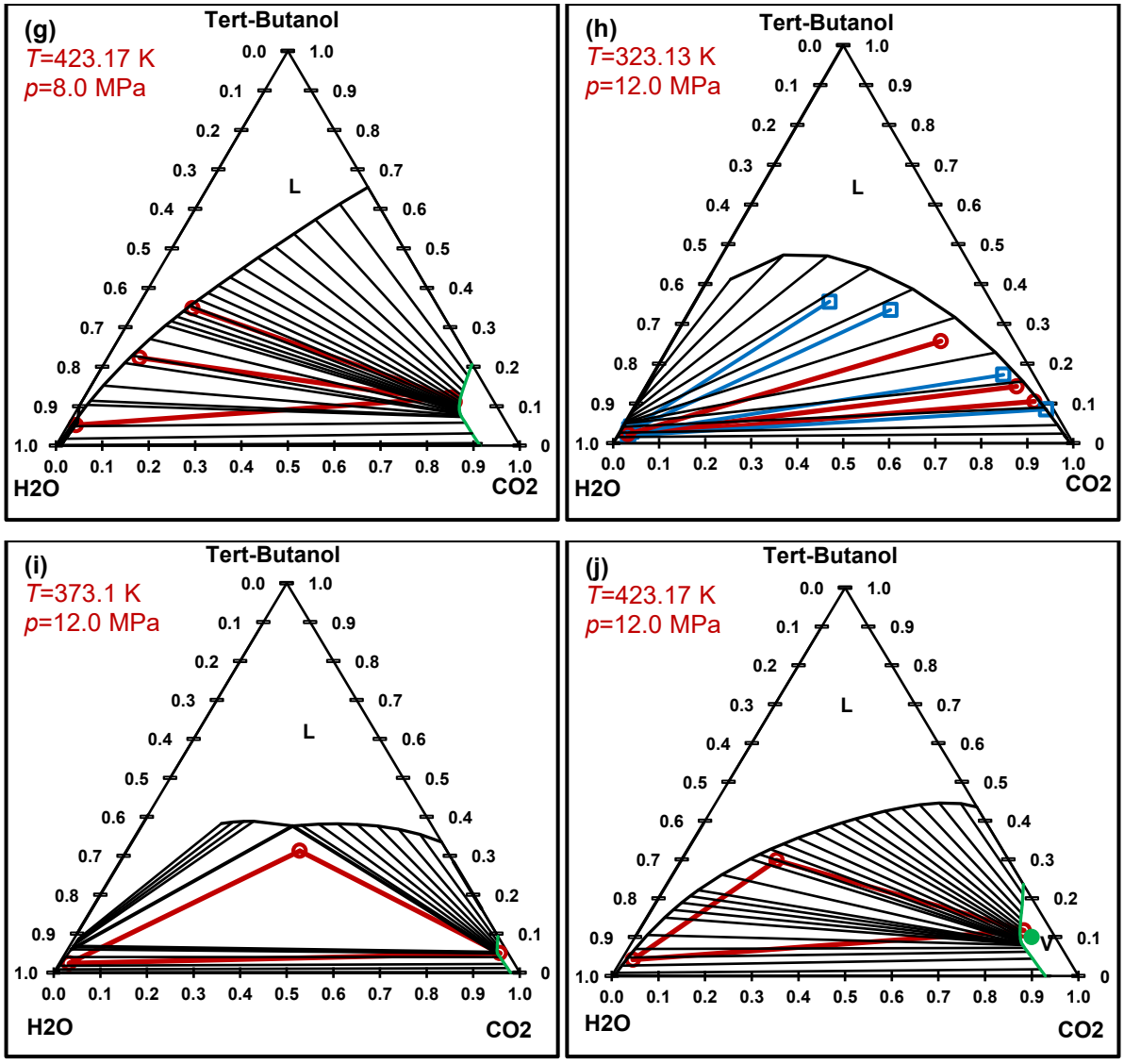
(g)
T=423.17 K
p=8.0 MPa
Tert-Butanol
L
H2O
CO2
(h)
T=323.13 K
p=12.0 MPa
Tert-Butanol
L
H2O
CO2
(i)
T=373.1 K
p=12.0 MPa
Tert-Butanol
L
H2O
CO2
(j)
T=423.17 K
p=12.0 MPa
Tert-Butanol
L
V
H2O
CO2

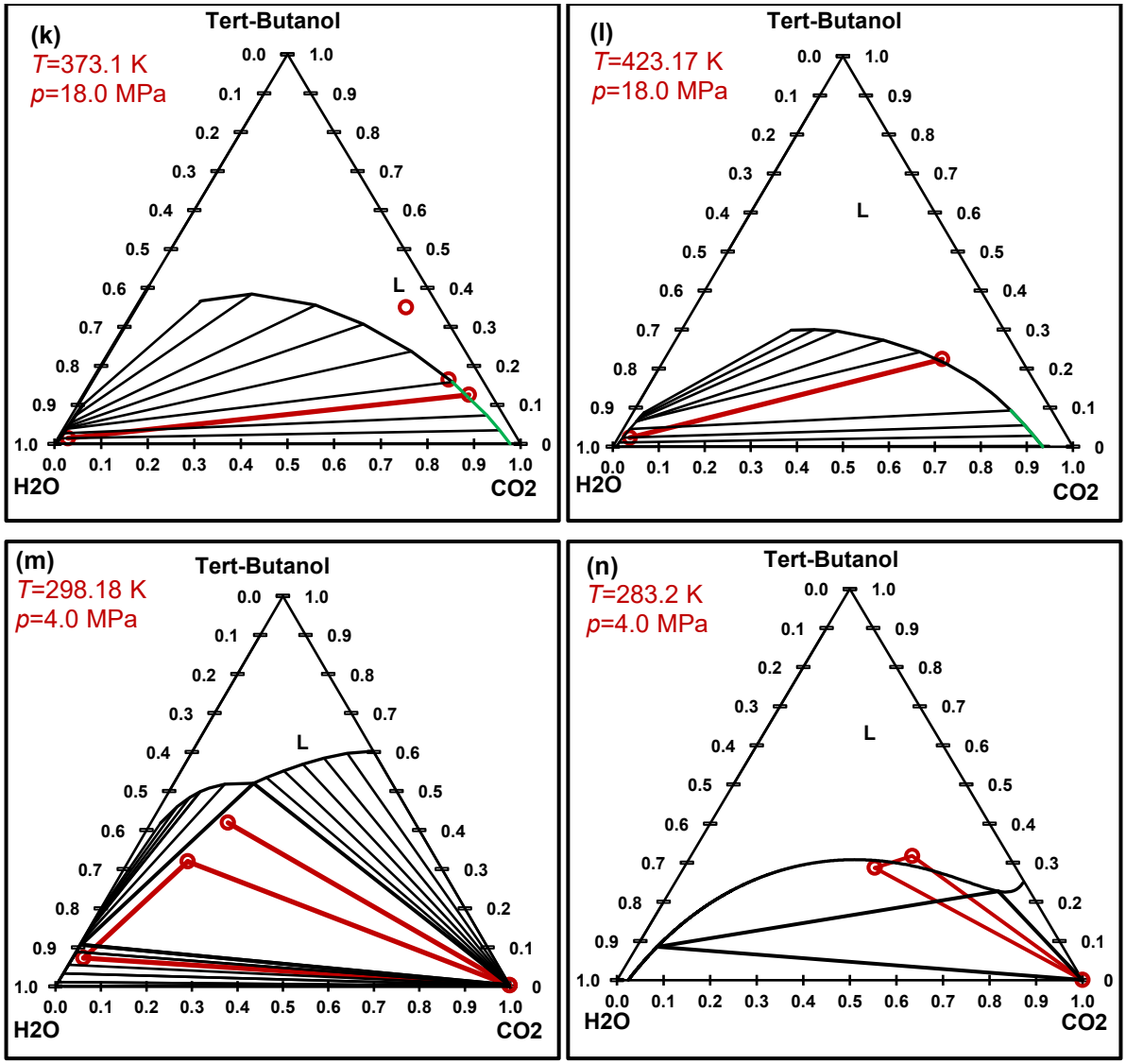

Figure 6.21: Ternary diagram for (*tert*-butanol + water + carbon dioxide) system: (a) T = 323.13 K and p = 4 MPa, (b) T = 373.10 K and p = 4 MPa, (c) T = 423.17 K and p = 4 MPa, (d) T = 323.13 K and p = 6 MPa, (e) T = 323.13 K and p = 8 MPa, (f) T = 373.10 K and p = 8 MPa, (g) T = 423.17 K and p = 8 MPa, (h) T = 323.13 K and p = 12 MPa, (i) T = 373.10 K and p = 12 MPa, (j) T = 423.17 K and p = 12 MPa, (k) T = 373.10 K and p = 18 MPa, (l) T = 423.17 K and p = 18 MPa, (m) T = 298.18 K and p = 4 MPa, and (n) T = 283.2 K and p = 4 MPa. The symbols O and □ represent the experimental data and literature data, respectively. The continuous coloured lines are the experimental and literature tie-lines between coexisting phases. The continuous black lines are calculated by PR EoS. The continuous black curves and the green curves are the Liquid and Vapour phases boundaries, respectively, calculated by PR EoS.

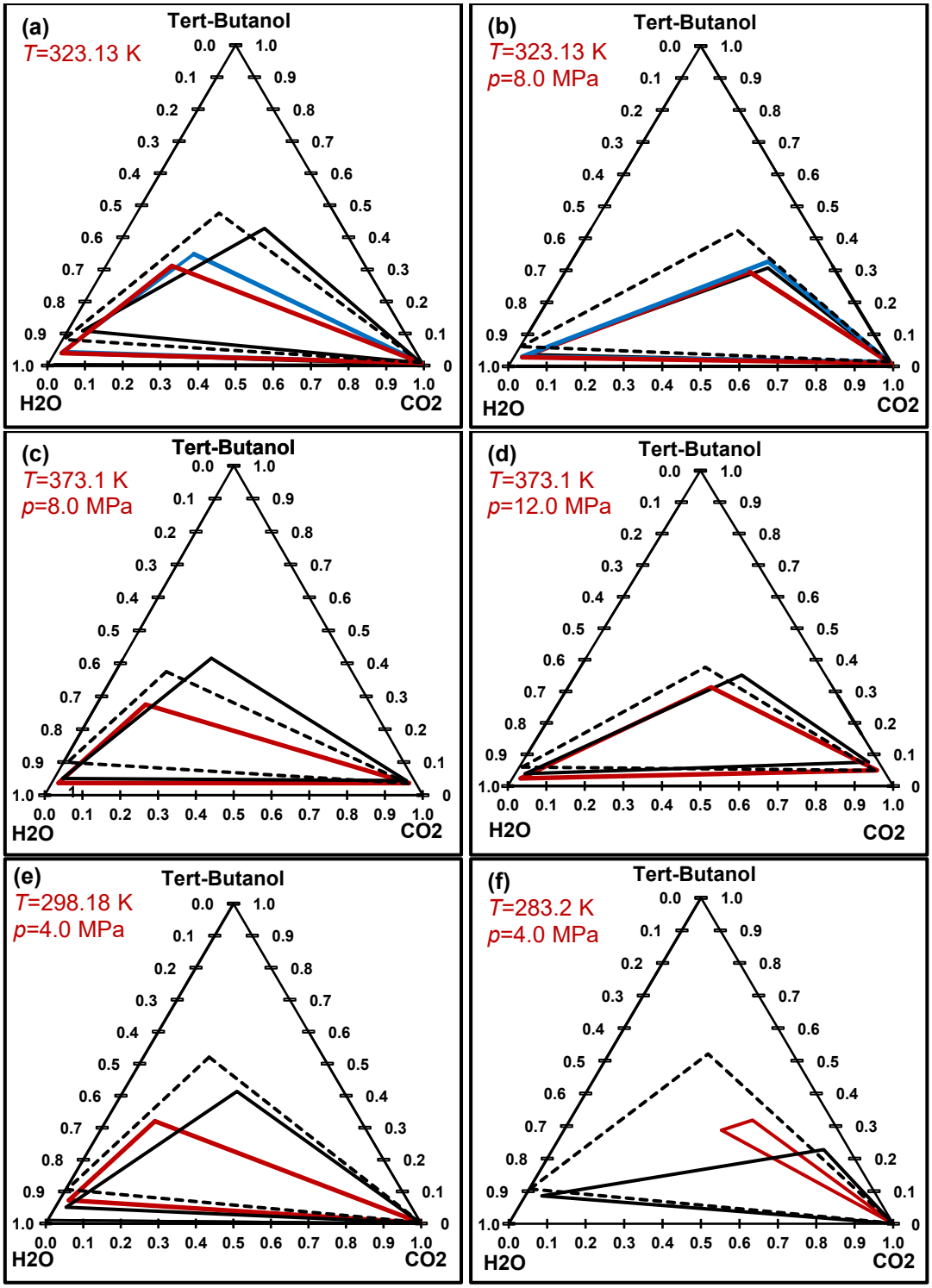

Figure 6.22: Three coexisting phases in the ternary diagram for (*tert*-butanol + water + carbon dioxide) system: (a) T = 323.15 K and p = 6 MPa, (b) T = 323.15 K and p = 8 MPa, (c) T = 373.15 K and p = 8 MPa, (d) T = 373.15 K and p = 12 MPa, (e) T = 298.18 K and p = 4 MPa, and (f) T = 283.2 K and p = 4 MPa. The solid RED and BLUE lines are the experimental and literature tie-lines, respectively. The continuous and dashed black lines are calculated by SAFT-γ Mie and PR EoS, respectively.

6.3.6 Conclusion

The experimental investigation of the phase behaviour of the ternary system (carbon dioxide + *tert*-butanol + water) was presented along five isotherms at temperatures of (283.2, 298.18, 323.13, 373.10 and 423.17) K and at pressures of (4, 8, 12 and 18) MPa with different known feed compositions of (*tert*-butanol + water). The like group parameters of the functional group (COH) for use within SAFT-γ Mie have been estimated from the fluid-phase behaviour data of pure *tert*-butanol. The model described very well the vapour pressure and saturated-liquid density data of *tert*-butanol. The cross interactions between the functional groups H_2O-CO_2, COH-H_2O and COH-CO_2, which the ternary system (*tert*-butanol + carbon dioxide + water) comprises, were estimated from the phase behaviour data of the binary sub-systems and the values of the parameters implemented into SAFT-γ Mie model. The VLLE, VLE and LLE experimental data of the ternary system have been compared with the descriptions of SAFT-γ Mie making use of the optimised like and unlike group parameters estimated in this work. The description of the model agrees well with the experimental data except the less-dense liquid phase in the three-phase regions where the model predicts more water and less *tert*-butanol contents. PR EoS model was also used to predict the phase behaviour of the ternary system (carbon dioxide + *tert*-butanol + water) after obtaining the binary parameters from the same sub-systems used for SAFT model. The model agrees with the VLE at low temperatures and pressures, but the predictions are not good at the three-phase regions (VLLE).

6.4 Toluene + Water + Carbon Dioxide

6.4.1 Introduction

The study of miscibility of CO_2 with hydrocarbons including both aliphatic and aromatic molecules and the knowledge of the phase behaviour of the mixtures in the presence of water is crucial in the design of Carbon Capture and Storage (CCS) processes and Enhanced Oil Recovery (CO_2-EOR) operations. CO_2 is also a supercritical solvent for extraction processes and it is nontoxic, has a natural character and low critical temperature. It is used for processing heavy hydrocarbons such as the separation of aromatic and paraffinic hydrocarbons. Experimental data for (aromatic hydrocarbons + H_2O + CO_2) mixtures are very scarce and limited. However, equilibrium data for the binary subsystems have been studied extensively. The (CO_2 + toluene) system has been studied by Lay and co-workers [232, 233] at temperatures up to 313 K, pressures up to 7.5 MPa and CO_2 composition over the range

(0.215 to 0.955) using an apparatus with a variable-volume cell. Tochigi et al. [234] also studied the system at temperatures up to 333 K, pressures up to 6.0 MPa and CO_2 composition over the range (0.080 to 0.889) using a static-type apparatus. Wu et al. [235] reached temperatures up to 572 K, pressures up to 16.6 MPa over CO_2 composition range of (0.01 to 0.78) using a dynamic synthetic method. More studies on the phase equilibria of this binary system can be found in references [236-240]. Phase behaviour studies on other benzene derivatives (e.g. benzene, xylenes, trimethylbenzene, phenol, *m*-cresol) with CO_2 have been surveyed by Pfohl et al. [241]. Most of these authors used the Peng Robinson EoS as a modelling tool except Saif et al. [242] who used SAFT-γ Mie to model the binary system using the literature data reported by the above authors. The phase equilibrium data for the binary system (H_2O + CO_2) is similarly plentiful in literature and the reader can refer to references [243-246]. Experimental phase behaviour data for the ternary system (benzene + water + carbon dioxide) were reported in literature by Brandt et al. [247]. They measured the molar compositions of the coexisting phases of the ternary system at temperatures up to 600 K and pressures up to 300 MPa using a synthetic method. Two- and three-phase equilibria in binary and ternary systems containing benzene derivatives, carbon dioxide and water at one temperature (373.15 K) and pressures up to 30 MPa were investigated by Pfohl et al. [241]. In this work, toluene was selected as a representative aromatic hydrocarbon and extended the investigation of (toluene + water + carbon dioxide) to high temperatures ranging from (338.15 to 413.15) K and pressures from 3 MPa to Upper Critical End Point (UCEP). This work is believed to be the first study covering a high range of temperatures and pressures to determining the phase behaviour envelope of the ternary system (C_7H_8 + H_2O + CO_2).

6.4.2 Comparison of VLE Data with Literature Data

The calibration curves for the ternary system (toluene + water + CO_2) were validated by measuring the phase behaviour of the binaries (toluene + carbon dioxide) and (water + carbon dioxide) at a temperature of 323.15 K and at different pressures within the phase envelope of the mixtures. The results were compared with the VLE data reported in literature [238, 243-245, 248, 249] as shown in Figure 6.23. As can been in the figure, there is a small deviation among the reported literature data but overall a good agreement between our data and the literature data is observed.

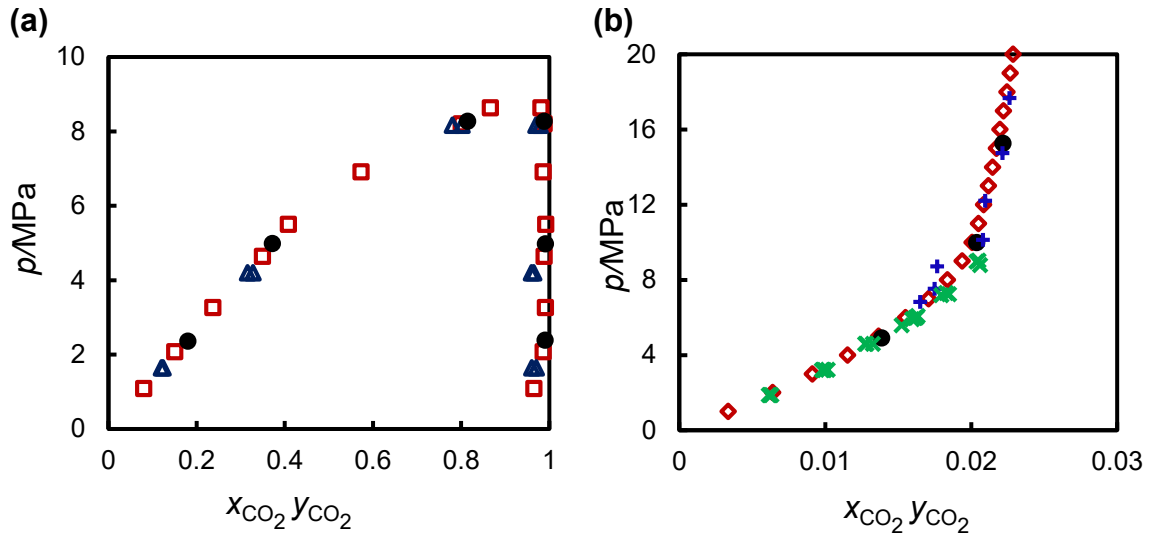

Figure 6.23: Isothermal pressure-composition (*p, x*) phase diagrams for: (a), (toluene + carbon dioxide) system and (b), (water + carbon dioxide) system. Filled circle symbols represent the data measured in this work at 323.15 K while open symbols (□, Δ,◇, ✕, +) represent the literature data at *T* = 323.15 K reported in the references [238, 243-245, 248, 249].

6.4.3 Experimental Results

Based on the phase behaviour reported in literature [238, 243, 250] and obtained in this work, the binary system (C_7H_8 + CO_2) exhibits type I phase behaviour while the binary systems (H_2O + CO_2) and (C_7H_8 + H_2O) fall within type III phase behaviour according to the classification of Van Konynenburg and Scott [48]. Therefore, the ternary system (C_7H_8 + H_2O + CO_2) is expected to exhibit ternary class IV phase behaviour according to the global ternary diagrams classification proposed by Bluma and Dieters [57]. A liquid-liquid equilibrium immiscibility region and vapour-liquid-liquid equilibrium region are expected to appear in mixtures of this type. The area within which the three coexisting phases is confined by the locus of UCEP (L_{C7H8} + L_{H2O} = V), above which there is a single nonaqueous phase in coexistence with the bottom water-rich liquid phase. The compositions of the three fluid phases that coexist in VLLE were measured along four isotherms at temperatures from (338.15 to 413.15) K and pressures up to the UCEP. The experimental data with the estimated standard uncertainties are provided in Table 6.14 and shown graphically in the form of isothermal triangular diagrams in Figure 6.24 (with SAFT-γ Mie predictions) and Figure 6.26 (with PR EoS predictions).

Table 6.14: Experimental VLLE data for [C_7H_8 (1) + H_2O (2) + CO_2 (3)] at temperatures T and pressures p[a].

phase	p/MPa	x_1^{exp}	$u(x_1)$ ($\times10^{-2}$)	x_2^{exp}	$u(x_2)$ ($\times10^{-2}$)	x_3^{exp}	$u(x_3)$ ($\times10^{-2}$)
			T = 338.15 K				
L_1	3.03	0.7903	0.4802	0.0177	0.4699	0.1920	0.4793
L_1	4.39	0.6985	0.6073	0.0150	0.5972	0.2865	0.6065
L_1	6.09	0.5736	0.7048	0.0149	0.6935	0.4115	0.7040
L_1	7.47	0.4629	0.7183	0.0150	0.7050	0.5221	0.7174
L_1	9.06	0.3104	0.6257	0.0153	0.6069	0.6743	0.6244
L_2	3.04	0.0002	0.0011	0.9927	0.0040	0.0071	0.0031
L_2	4.37	0.0004	0.0018	0.9903	0.0040	0.0093	0.0032
L_2	6.06	0.0004	0.0019	0.9873	0.0037	0.0123	0.0030
L_2	7.45	0.0005	0.0023	0.9851	0.0037	0.0145	0.0031
L_2	9.05	0.0002	0.0012	0.9836	0.0029	0.0161	0.0021
V	3.03	0.0143	0.0661	0.0083	0.0670	0.9775	0.1447
V	4.38	0.0120	0.0555	0.0060	0.0566	0.9821	0.1401
V	6.09	0.0106	0.0493	0.0047	0.0505	0.9847	0.1377
V	7.46	0.0119	0.0555	0.0042	0.0565	0.9838	0.1401
V	9.06	0.0155	0.0718	0.0037	0.0725	0.9808	0.1473
			T = 363.15 K				
L_1	3.04	0.8212	0.4232	0.0267	0.4164	0.1521	0.4222
L_1	5.45	0.6935	0.6086	0.0278	0.6027	0.2788	0.6079
L_1	7.89	0.5604	0.7047	0.0280	0.6985	0.4115	0.7041
L_1	10.45	0.4055	0.6913	0.0280	0.6836	0.5664	0.6906
L_1	12.66	0.2458	0.5373	0.0260	0.5257	0.7282	0.5365
L_2	3.06	0.0004	0.0020	0.9944	0.0037	0.0051	0.0032
L_2	5.44	0.0004	0.0020	0.9905	0.0035	0.0090	0.0030
L_2	7.88	0.0005	0.0022	0.9873	0.0035	0.0122	0.0029
L_2	10.45	0.0004	0.0019	0.9843	0.0031	0.0153	0.0025
L_2	12.65	0.0004	0.0019	0.9820	0.0030	0.0176	0.0023
V	3.06	0.0251	0.1152	0.0301	0.1155	0.9448	0.1816
V	5.45	0.0204	0.0941	0.0157	0.0946	0.9638	0.1721
V	7.89	0.0209	0.0960	0.0117	0.0963	0.9674	0.1766
V	10.45	0.0277	0.1272	0.0104	0.1268	0.9619	0.1988
V	12.66	0.0597	0.2639	0.0115	0.2634	0.9289	0.3070
			T = 388.15 K				

L_1	4.64	0.7627	0.5172	0.0460	0.5133	0.1913	0.5168
L_1	6.81	0.6679	0.6326	0.0476	0.6289	0.2845	0.6323
L_1	9.49	0.5468	0.7065	0.0484	0.7027	0.4048	0.7062
L_1	11.88	0.4322	0.7003	0.0467	0.6959	0.5211	0.6999
L_1	14.03	0.3174	0.6199	0.0462	0.6144	0.6364	0.6195
L_2	4.64	0.0006	0.0026	0.9929	0.0039	0.0065	0.0036
L_2	6.80	0.0006	0.0026	0.9902	0.0037	0.0093	0.0034
L_2	9.47	0.0006	0.0029	0.9868	0.0038	0.0126	0.0034
L_2	11.87	0.0007	0.0034	0.9834	0.0040	0.0159	0.0037
L_2	14.03	0.0006	0.0029	0.9828	0.0035	0.0165	0.0031
V	4.65	0.0391	0.1764	0.0409	0.1764	0.9200	0.2247
V	6.81	0.0354	0.1602	0.0298	0.1603	0.9348	0.2119
V	9.49	0.0382	0.1727	0.0246	0.1727	0.9371	0.2214
V	11.88	0.0493	0.2204	0.0230	0.2201	0.9277	0.2604
V	14.03	0.0801	0.3463	0.0240	0.3459	0.8959	0.3733
			T = 413.15 K				
L_1	3.08	0.8304	0.4027	0.0753	0.3994	0.0943	0.4026
L_1	6.04	0.7193	0.5752	0.0754	0.5725	0.2053	0.5752
L_1	8.70	0.6187	0.6715	0.0757	0.6689	0.3056	0.6716
L_1	12.04	0.4881	0.7112	0.0780	0.7085	0.4339	0.7114
L_1	15.19	0.3428	0.6422	0.0747	0.6388	0.5825	0.6426
L_2	3.09	0.0016	0.0075	0.9947	0.0080	0.0037	0.0079
L_2	6.03	0.0017	0.0078	0.9904	0.0082	0.0080	0.0081
L_2	8.66	0.0017	0.0080	0.9869	0.0083	0.0114	0.0082
L_2	12.02	0.0015	0.0069	0.9832	0.0072	0.0154	0.0071
L_2	15.17	0.0014	0.0065	0.9813	0.0067	0.0173	0.0066
V	3.09	0.0860	0.3693	0.1276	0.3698	0.7864	0.3982
V	6.04	0.0635	0.2793	0.0711	0.2797	0.8653	0.3149
V	8.70	0.0612	0.2699	0.0553	0.2700	0.8834	0.3058
V	12.04	0.0739	0.3215	0.0485	0.3212	0.8776	0.3521
V	15.19	0.1167	0.4842	0.0466	0.4837	0.8367	0.5056

[a]Notation: x_i, V, L_1, L_2, $u(x_i)$ denote the mole fraction of component i in any phase, the CO_2-rich vapour phase, the toluene-rich liquid phase, the water-rich liquid phase and the standard uncertainty of x_i, respectively.

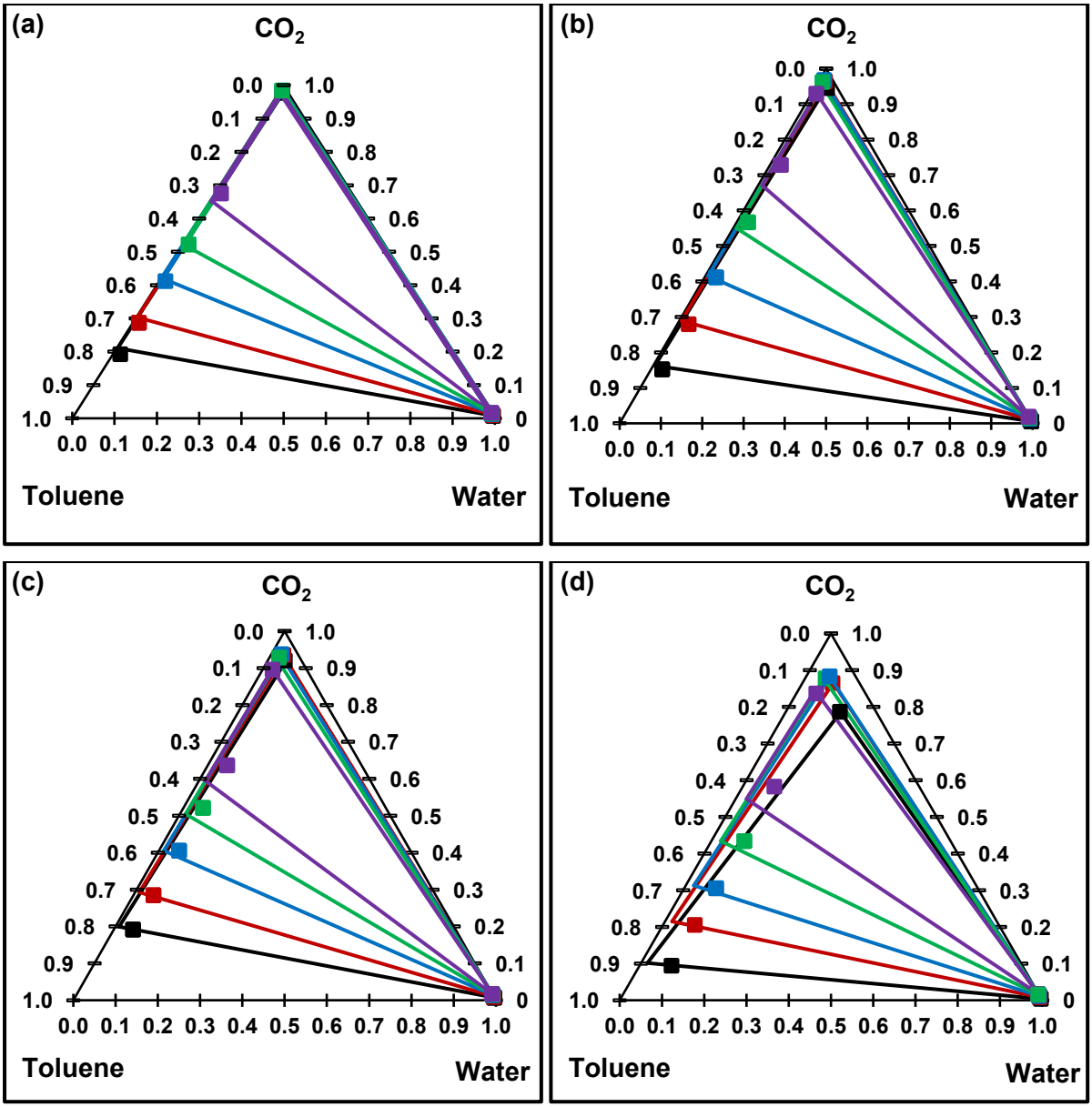

Figure 6.24: Isothermal composition diagram for the (C_7H_8 + H_2O + CO_2) system at (a) T = 338.15 K, (b) T = 363.15 K, (c) T = 388.15 K and (d) T = 413.15 K. The coloured square symbol corresponds to VLLE data measured in this work at the average pressures: (3.0, 3.0, 4.6, 3.1) MPa (BLACK); (4.4, 5.5, 6.8, 6.0) MPa (RED); (6.1, 7.9, 9.5, 8.7) MPa (BLUE); (7.5, 10.5, 11.9, 12.0) MPa (GREEN) and (9.1, 12.7, 14.0, 15.2) MPa (PURPLE) for a, b, c and d, respectively. The continuous coloured tie-lines are SAFT-γ Mie predictions for the three-phase equilibrium region for every pressure data point indicated by colours.

6.4.4 Modelling

In this work, we used SAFT-γ Mie group contribution model to predict the phase behaviour of the (C_7H_8 + H_2O + CO_2) ternary system. Toluene is modelled as (1× $aCCH_3$ and 5× aCH)

groups [157]. Carbon dioxide and water are modelled as molecular groups, e.g., the CO_2 group for carbon dioxide and H_2O group for water. The parameters of the individual functional groups that fully characterize the mixture are given in Table 6.15. These parameters were estimated previously in literature [44, 157, 225] by fitting saturated-liquid densities and vapour pressures of pure components, and in addition to these two properties excess enthalpies and volumes for the binary mixture (toluene + benzene) at ambient conditions were used in parameter-estimation for toluene [157]. The unlike dispersion energy ε_{kl} and the unlike repulsive Mie exponent λ^r_{kl} were calculated using the combining rules or estimated from VLE data. The cross interaction parameters for CO_2-aCH were determined by fitting to experimental VLE data for (benzene + CO_2) at temperatures from (298 to 393) K, while the CO_2-aCCH_3 were estimated by regression against experimental VLE data for (toluene + CO_2) at temperatures from (283 to 413) K [242]. All cross interactions between H_2O and aCCH_3 were calculated using combining rules. The other cross interactions parameters between the other functional groups are summarised in Table 6.16.

Table 6.15: SAFT-γ Mie like group parameters used in this work [44, 157].

group k	S_k	σ_{kk}/Å	(ε_{kk}/k_B)/K	λ^a_{kk}	λ^r_{kk}	$N_{ST,K}$	$n_{k,h}$	$n_{k,e}$	Ref.
aCH	0.3218	4.058	371.53	6.00	14.756				[44]
aCCH_3	0.3166	5.487	651.41	6.00	23.627				[157]

Table 6.16: SAFT-γ Mie unlike group parameters used in this work [44, 157, 242].

group k	group l	(ε_{kl}/k_B)/K	λ^r_{kl}	Ref.
aCH	aCCH_3	471.23	CR	[157]
aCH	CO_2	224.33	14.155	[242]
aCH	H_2O	357.78	38.640	[44]
aCCH_3	CO_2	309.36	CR	[242]
aCCH_3	H_2O	CR	CR	This work
CO_2	H_2O	226.38	CR	[157]

CR indicates parameter was determined from the combining rule. All other values given in the table have been estimated from experimental data.

In Figure 6.25a and b, the SAFT-γ Mie descriptions of the phase behaviour of (C_7H_8 + CO_2) at T = 338.15 K and T = 413.15 K and (CO_2 + H_2O) at T = 323.15 K are compared with the experimental VLE data measured at these temperatures. As seen in the figures by the solid curves, the model agrees well with the experimental VLE data. The model was then used to

predict the phase behaviour of the ternary system (toluene + water + carbon dioxide) at the measured conditions.

The experimental measurements of the ternary system were also compared with the predictions of the PR EoS combined with classical one-fluid mixing rules incorporating temperature-independent binary interaction parameter, k_{ij}. The values of this parameter for (CO_2 + H_2O) and (C_7H_8 + CO_2) were reported in Aspen databank as 0.1200 and 0.1056, respectively, so the values were used without any further optimisation. The predictions are shown by the dashed curves in Figure 6.25.

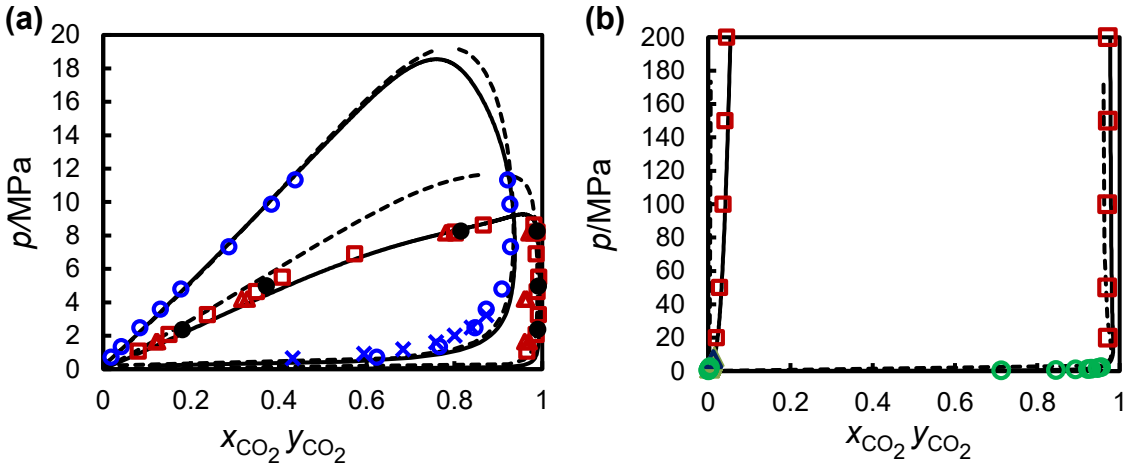

Figure 6.25: Isothermal pressure-composition (*p, x*) phase diagrams for (a): (toluene + carbon dioxide), (b): (water + carbon dioxide) binary systems at T = 413.15 K (X and O); T = 323.15 K (Δ, ◇ and ●); T = 373.15 K (□, O). The open symbols correspond to literature data [238, 243, 244, 248, 249] while the filled black symbols correspond to the data measured in this work. The solid curves are the calculations from the SAFT-γ Mie while the dashed curves are the predictions from PR EoS.

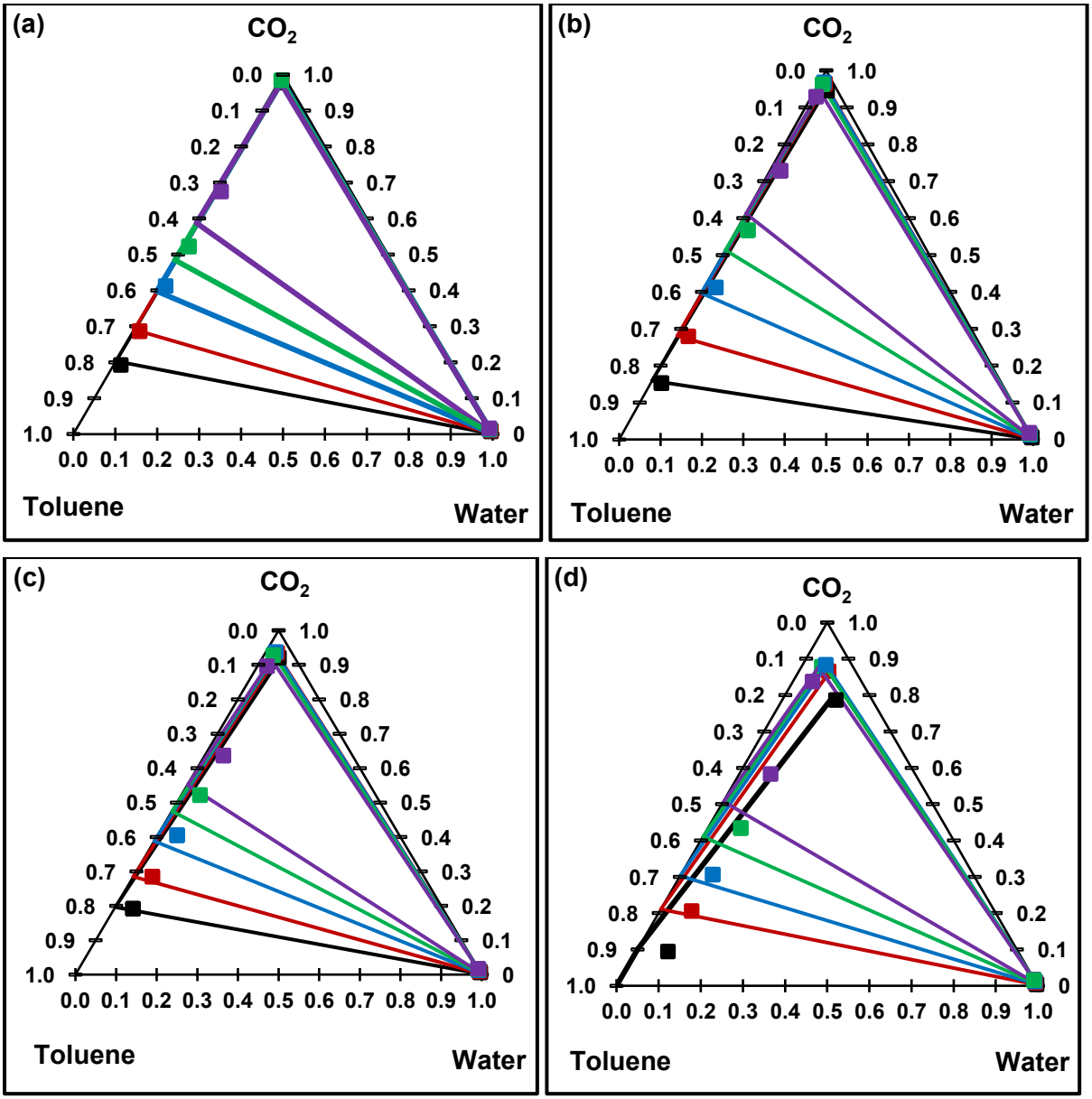

Figure 6.26: Isothermal composition diagram for the (C_7H_8 + H_2O + CO_2) system at (a) T = 338.15 K, (b) T = 363.15 K, (c) T = 388.15 K and (d) T = 413.15 K. The coloured square symbol corresponds to VLLE data measured in this work at the average pressures: (3.0, 3.0, 4.6, 3.1) MPa (BLACK); (4.4, 5.5, 6.8, 6.0) MPa (RED); (6.1, 7.9, 9.5, 8.7) MPa (BLUE); (7.5, 10.5, 11.9, 12.0) MPa (GREEN) and (9.1, 12.7, 14.0, 15.2) MPa (PURPLE) for a, b, c and d, respectively. The continuous coloured tie-lines are PR EoS predictions for the three-phase equilibrium region for every pressure data point indicated by colours.

6.4.5 Discussion and Comparison with Experiments

As can be seen in Figure 6.24, the VLLE region diminishes as we approach the critical point between CO_2-rich phase and C_7H_8-rich phase. The VLLE region diminishes also when the

temperature is increased. It can be seen in the figure, there is a good agreement between the experimental data and SAFT-γ Mie predictions especially in the CO_2-rich phase and water-rich phase. However, a deviation is observed in the toluene-rich phase where the model predicts less water in this phase. The underpredictions of PR for H_2O content in the toluene-rich phase are worse as can be seen in Figure 6.26. It can also be observed from the two figures that the deviation between the mole fractions of toluene in the toluene-rich phase measured experimentally and that calculated by the models increase when the pressure increases for the same temperature. PR predicted two coexisting phases (VLE) at pressure of 3 MPa and temperature of 413 K, which is not matching with what has been seen in the experiment. In general, SAFT-γ Mie shows more accurate predictions of mole fractions for all the phases in the system.

In Figure 6.27, the experimental VLLE data are compared with SAFT predictions by means of isothermal pressure-composition (p, x_i) phase diagram for the (C_7H_8 + H_2O + CO_2) system. Figure 6.27a and b show the H_2O and CO_2 mole fractions in the C_7H_8-rich phase, Figure 6.27c and d show the H_2O and C_7H_8 mole fractions in the CO_2-rich phase and the mole fractions of CO_2 and C_7H_8 in the H_2O-rich phase are shown in Figure 6.27e and f. As can be observed in the figures, the model predicts quite well the CO_2 content in the C_7H_8-rich phase but it underpredicts the H_2O mole fractions. The mole fractions of water and toluene in CO_2-rich phase are well predicted by SAFT-γ Mie model, but again the content of toluene in the H_2O-rich phase is underpredicted.

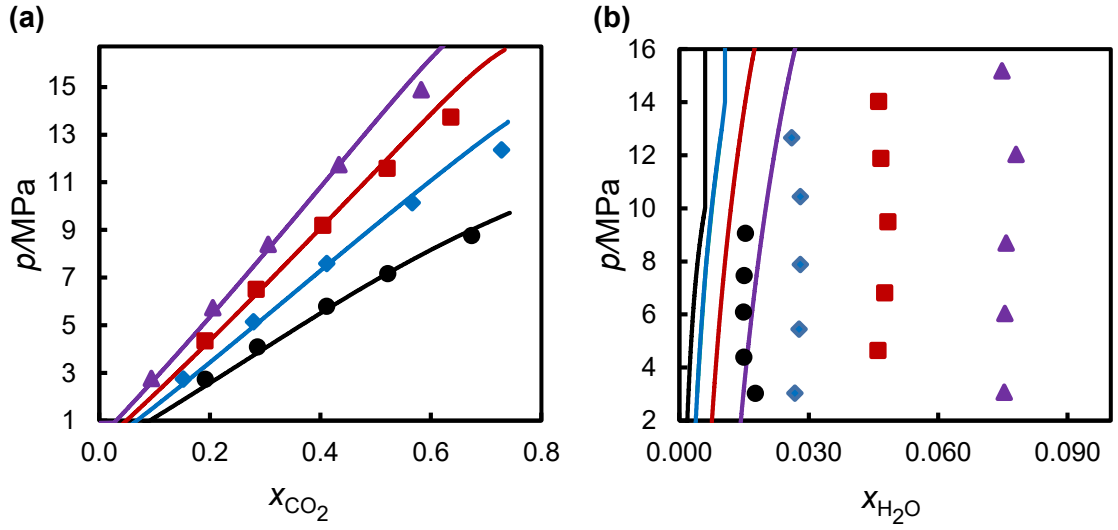

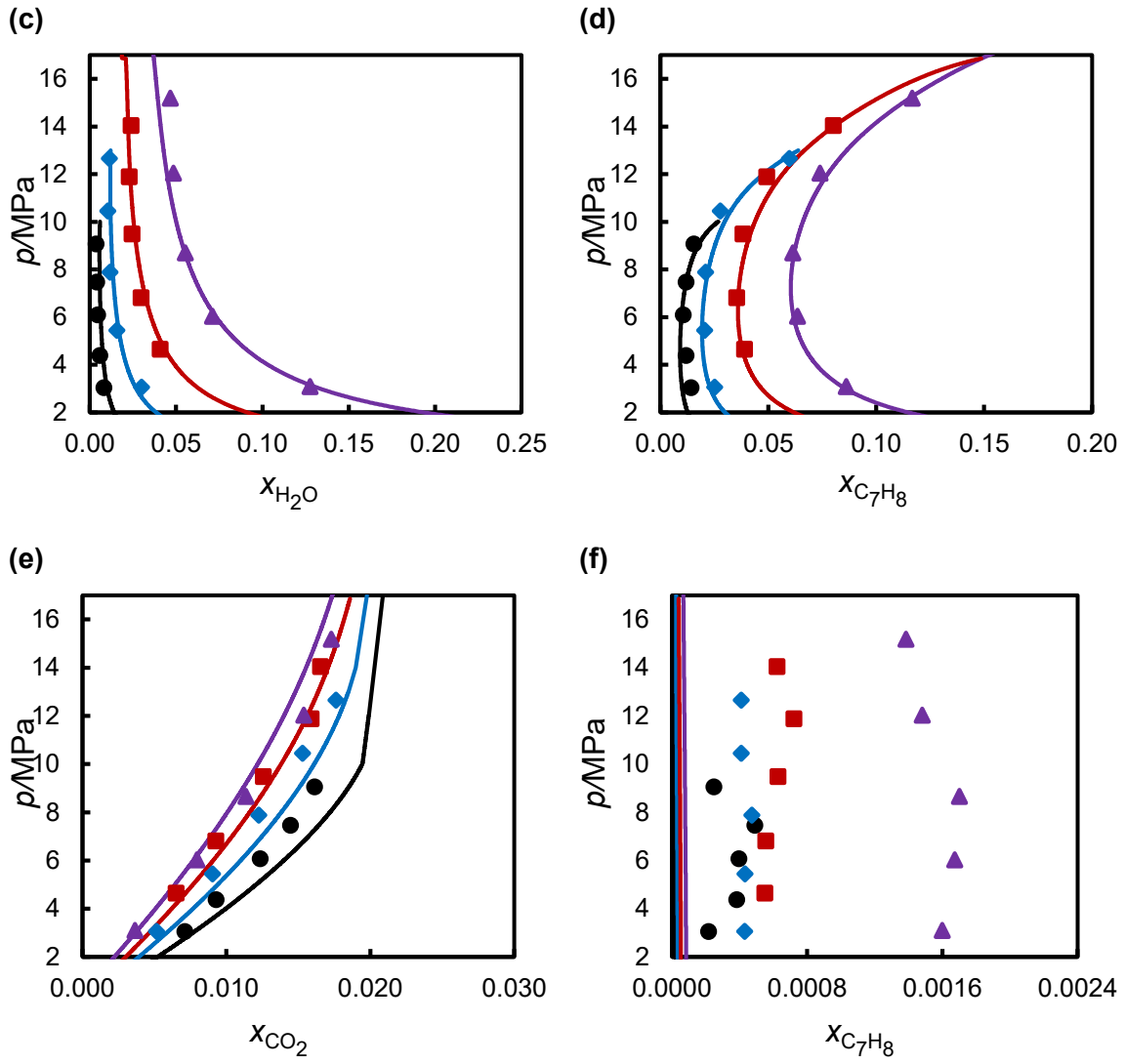

Figure 6.27: Isothermal pressure-composition (p, x) phase diagram for the (C_7H_8 + H_2O + CO_2) system in the toluene-rich phase (a, b), CO_2-rich phase (c, d) and water-rich phase (e, f) under VLLE conditions. The coloured symbols correspond to VLLE data measured in this work at the following temperatures: ●, T = 338.15 K; ◆, T = 363.15 K, ■, T = 388.15 K and ▲, T = 413.15 K. The continuous coloured curves are SAFT-γ Mie predictions for the three-phase equilibrium region at T = 338.15 K (BLACK), T = 363.15 K (BLUE), T = 388.15 K (RED) and T = 413.15 K (PURPLE).

In Figure 6.28, the effect of the addition of H_2O on the phase behaviour of (C_7H_8 + CO_2) was investigated by plotting the pressure as a function of the mole fractions of CO_2 in the C_7H_8-rich liquid phase and CO_2-rich vapour phase at the temperatures of (338.15 and 413.15) K measured for the ternary system (C_7H_8 + H_2O + CO_2) and comparing these experimental data with the VLE data of the binary system (C_7H_8 + CO_2) published in literature [238, 243, 250] at the same temperatures. It has been seen previously in Figure 6.27 that the mole fractions of H_2O in the C_7H_8-rich liquid phase and CO_2-rich vapour phase are small, so the effect of water

is expected to be small. It has been seen also in Figure 6.27 that the H_2O content in these two phases increases with temperature. As can be seen in Figure 6.28, the presence of water reduces very slightly the amount of CO_2 in the toluene-rich phase and a larger reduction of CO_2 is observed in the CO_2-rich phase. However, in general, the effect of the phase behaviour is relatively small. In this figure, predictions from SAFT-γ Mie are also provided for the ternary mixture (solid curves) and binary mixture (dashed curves). The model is in quite good agreement with the experimental data.

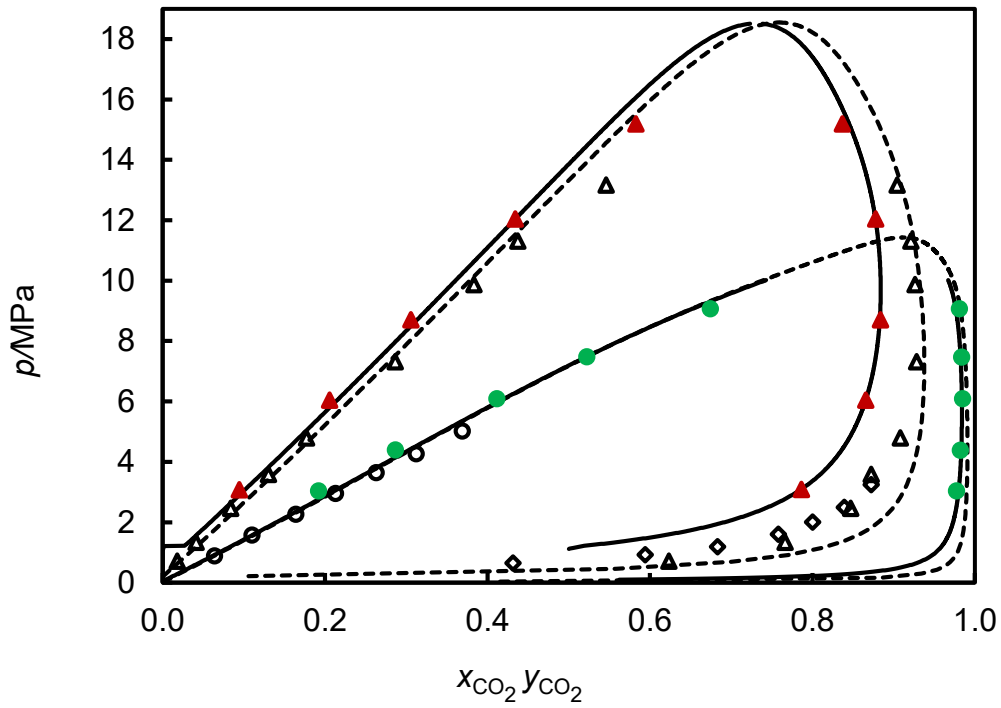

Figure 6.28: Isothermal pressure-composition phase diagram for the (C_7H_8 + H_2O + CO_2) system at T = 338.15 K (●) and T = 413.15 K (▲). The filled symbols represent coexisting-phase data measured in this work, continuous curves represent SAFT-γ Mie predictions for the ternary system, and dashed curves represent SAFT-γ Mie predictions for the binary system (C_7H_8 + CO_2). Open black symbols represent published data for the binary system (C_7H_8 + CO_2): ○, T = 338.15 K [250]; (◇ , △), T = 413.15 K [238, 243].

The effect of adding water in the (C_7H_8 + CO_2) system can be also analysed by comparing the UCEP data measured in the ternary system (C_7H_8 + H_2O + CO_2) with the experimental critical data for the (C_7H_8 + CO_2) as shown in Figure 6.29. It can be seen in the figure that water does not affect significantly the UCEP curve. This is due to the small solubility of water in the C_7H_8-rich liquid and CO_2-rich phases.

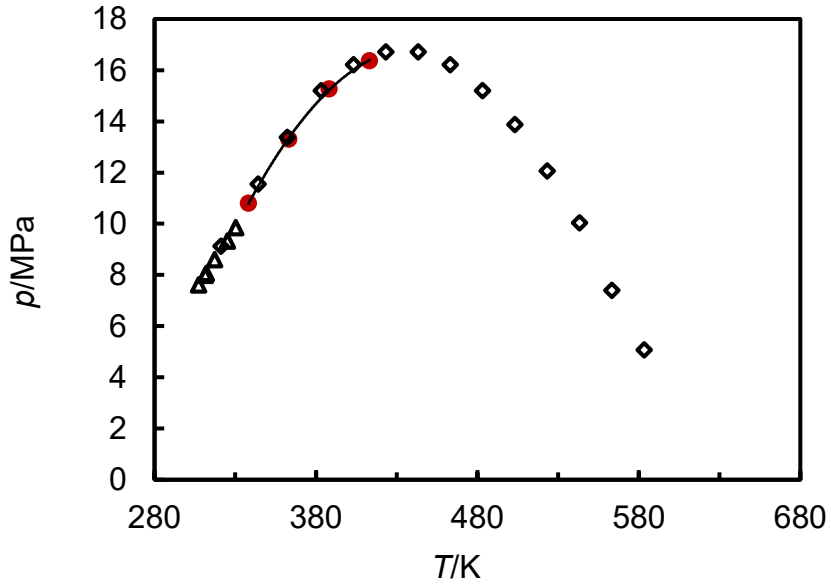

Figure 6.29: A plot showing the UCEP pressures as a function of temperatures. The red filled symbols (●) represent the data measured in this work for the (C_7H_8 + H_2O + CO_2) system while the open symbols (◇), ref [251] and (Δ), ref [248] represent the critical data published in literature for the binary system (C_7H_8 + CO_2). The solid black line corresponds to a polynomial fit to UCEP data measured in this work.

6.4.6 Conclusion

The phase behaviour of the system (toluene + water + carbon dioxide) was investigated along four isotherms at temperatures from (338.15 to 413.15) K and pressures up to the UCEP. The effect of the addition of H_2O on the phase behaviour of (C_7H_8 + CO_2) was also investigated by plotting the pressure as a function of the mole fractions of CO_2 in the C_7H_8-rich liquid phase and CO_2-rich vapour phase at the temperatures of (338.15 and 413.15) K measured for the ternary system (C_7H_8 + H_2O + CO_2) and comparing these experimental data with the VLE data of the binary system (C_7H_8 + CO_2) published in literature at the same temperatures. It was found that the effect of the phase behaviour was relatively small. The effect of adding water in the (C_7H_8 + CO_2) system was studied as well by comparing the UCEP data measured in the ternary system (C_7H_8 + H_2O + CO_2) with the experimental critical data for the (C_7H_8 + CO_2) and found that water did not affect significantly the UCEP curve. The vapour-liquid-liquid equilibrium (VLLE) data obtained for the mixture have been compared with the predictions of the optimised SAFT-γ Mie model and PR EoS, and in general the models were found to be in a good agreement with the measured data, but the accuracy of SAFT was more satisfactory especially in calculations of the mole compositions of the components in the less-dense liquid phase.

Chapter 7: Parameter Estimation for Cross Interactions Within SAFT-γ Mie

7.1 Overview

This chapter presents the cross interactions for (COOH - CH_3OH), (OH_GI - CH_3OH), (CO_2 - CH=), (CH_3OH - CH=), (COOH - CH=) and (H_2O - CH=) which were estimated in this work by regression to fluid-phase behaviour data published in literature. The comparison between the predictions of SAFT-γ Mie reported in literature (dashed curves in the figures) and those of SAFT-γ Mie after refining the parameters (solid curves in the figures) are shown.

7.2 Introduction

The databank for SAFT-γ Mie provided by PSE is encrypted and the values of the cross interactions for the groups in question are probably estimated using the combining rules or fitted to experimental data but have not been published in literature. As described previously, in the SAFT-γ Mie group contribution model the unlike segment diameter σ_{kl} and the unlike attractive exponent λ_{kl}^{a} interactions between unlike groups *k* and *l* are always given by the combining rules described in Chapter 3. The other cross interactions can be also estimated from the combining rules but may not provide accurate predictions of the fluid-phase behaviour of biodiesel mixtures. The estimates can be improved by regression against experimental data. However, some compounds of interest such as oleic acid and methyl oleate have not been defined in the encrypted databank and hence; to compare the predictions of SAFT-γ Mie reported in literature and those of SAFT-γ Mie after optimisation a customized databank was created using the published values of like and unlike parameters of the functional groups. In this customized databank, the compounds of mixtures of interest were defined. The values of the like group parameters describing each functional group are given in Table 7.1; the values of the unlike group parameters for the Mie potential interactions are summarised in Table 7.2; and those for the associations are provided in Table 7.3.

7.3 Modelling

7.3.1 (OH_GI - CH_3OH)

In biodiesel production, glycerol is a by-product and its phase behaviour with other components in the system needs to be predicted well by the model in order to have accurate thermodynamic and separation calculations. Glycerol is modelled as 3× OH_GI, 2× CH_2 and 1× CH groups. The hydroxyl group (OH_GI) is unique for glycerol. The like group parameters of the (OH_GI) have been estimated from the VLE of pure glycerol, both vapour pressures and saturated liquid densities. In Figure 7.1, the experimental data for the isobaric vapour-liquid equilibria (VLE) [252] and isothermal VLE of the binary mixture (methanol + glycerol) [253-255] are compared with the corresponding SAFT-γ Mie calculations after optimising the unlike Mie potential interactions (ε_{kl} and λ_{kl}^{r}) and considering the association parameters (energy and bonding volume). The model provides a satisfactory description of the phase equilibria of the system. On the other hand, large deviation is seen when using the encrypted databank in SAFT as shown by the dashed curves.

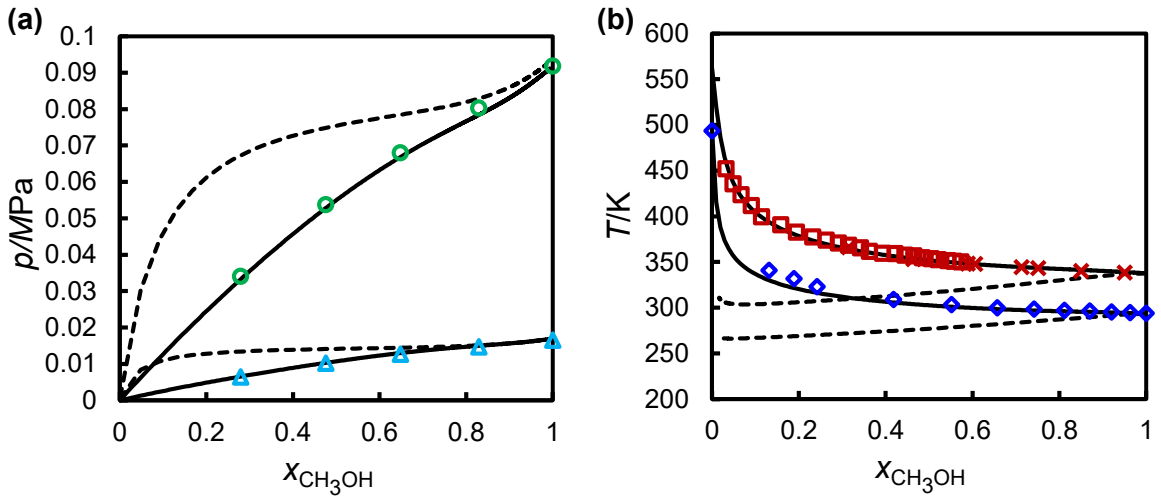

Figure 7.1: Fluid-phase behaviour data for (glycerol + methanol) binary system: (a), isothermal pressure-composition diagram and (b), isobaric temperature-composition diagram. The open symbols correspond to published literature data at: ○, T = 335.65 K [252]; Δ, T = 298.15 K [252]; □, p = 0.10133 MPa [253]; X, p = 0.10130 MPa [254] and ◇, p = 0.0133 [255]. The solid curves are the predictions from the SAFT-γ Mie after optimisation while the dashed curves are predictions using the encrypted databank in SAFT.

7.3.2 (CO_2 - CH=)

As mentioned previously the fatty acids in biodiesel production can be saturated with no C=C double bonds or unsaturated with one or more C=C double bonds. Triglycerides derived from unsaturated acids and methyl esters produced from unsaturated acids also contain C=C double bonds. Oleic acid is one of the most dominant acids that occur naturally in various animal and vegetable fats and oils. Its chemical structure can be written as ($CH_3(CH_2)_7CH=CH(CH_2)_7COOH$). To obtain more accurate predictions for the phase behaviour of mixtures containing unsaturated acids and CO_2 the cross interactions of (CO_2 - CH=) are estimated by fitting to experimental data. Fluid-phase behaviour (VLE) data for (oleic acid + CO_2) binary mixture reported in literature [141, 142, 145] were used in the regression. In Figure 7.2, the theoretical description after parameters optimisation is compared to both the experimental data and the SAFT-γ Mie using the values reported in literature. It is clear that the SAFT-γ Mie predictions are in good agreement with the experimental data for the fluid-phase equilibria of the binary system. The predictions of SAFT-γ Mie reported in literature are not satisfactory especially in the bubble curve.

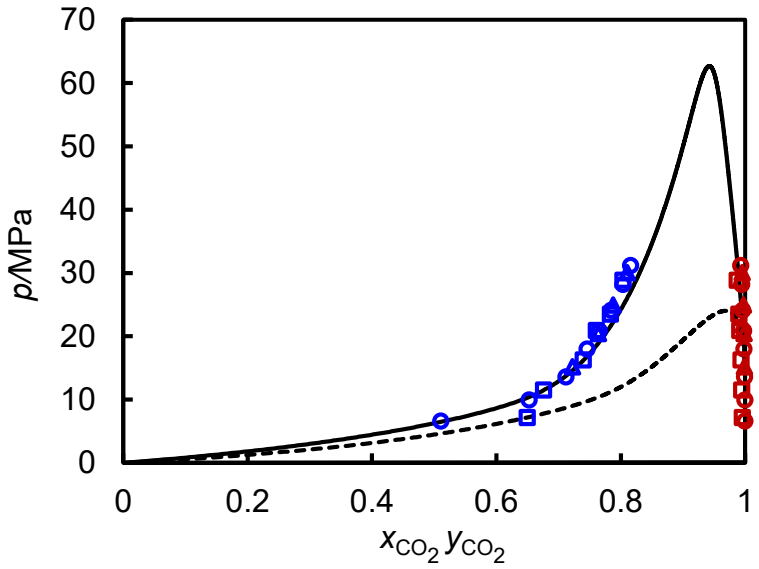

Figure 7.2: Isothermal pressure-composition (*p, x*) phase diagrams for (oleic acid + carbon dioxide) binary system at 333.15 K. The open symbols correspond to published literature data: ☐, [141]; **Δ**, [145] and **O**, [142]. The (BLUE) symbols represent bubble points and (RED) symbols represent dew points. The solid curves are the predictions from the SAFT-γ Mie after optimisation while the dashed curves are predictions from SAFT-γ Mie reported in literature.

7.3.3 (COOH - CH_3OH)

Fatty acids, which the feedstocks of biodiesel contain, are composed of the carboxyl (COOH) group as well as the methyl CH_3 and methylene CH_2 groups. The parameters for COOH and its cross interactions with CH_3 and CH_2 groups were estimated from experimental data for carboxylic acids (see Chapter 5). Methanol is modelled with CH_3OH molecular group comprising two fused Mie segments and three association sites (two sites of type *e* and one site of type *H*). As mentioned before, fatty acids react with methanol to produce biodiesel. Therefore, the cross interactions between COOH and CH_3OH are crucial in order to predict the phase behaviour of the mixture accurately. Currently, the unlike group parameters for the Mie potential interactions are estimated using the combining rules while the association interactions are not considered. This is not sufficient as both functional groups have induced association sites that are active in the mixture. The unlike dispersion energy ε_{kl} and the unlike repulsive Mie exponent λ_{kl}^{r} as well as the association interactions, energy ε_{klab}^{HB} and bonding volume K_{klab} for COOH-CH_3OH were estimated from isobaric temperature-composition phase behaviour data (VLE) of the binary system (CH_3COOH + CH_3OH) at temperatures ranging from pure acetic acid boiling point to pure methanol boiling point [216, 256-258] as shown in Figure 7.3.

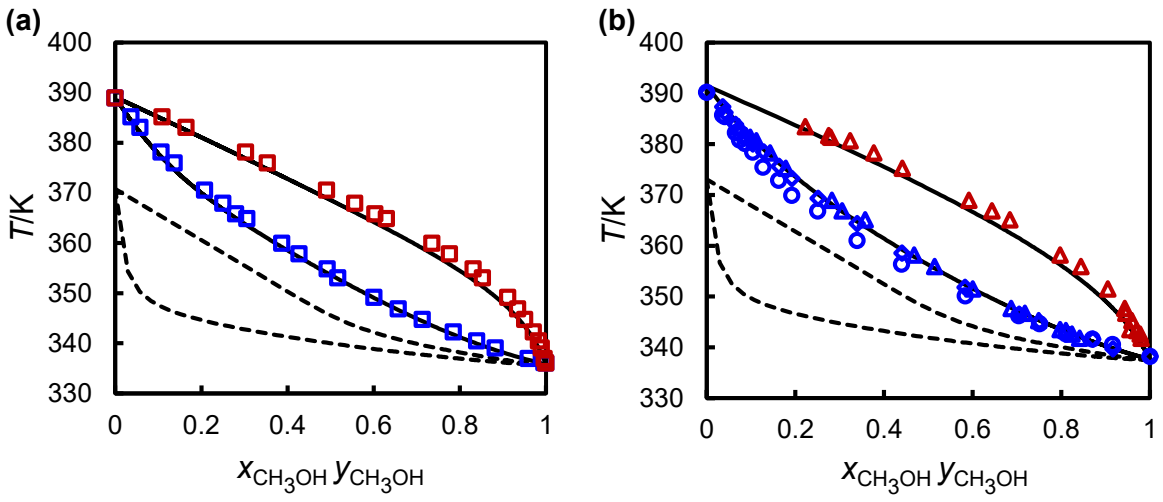

Figure 7.3: Isobaric temperature-composition (*T, x*) phase diagrams for (acetic acid + methanol) binary system: (a), p = 0.094130 MPa and (b), p = 1.01300 MPa. The open symbols correspond to published literature data: ☐, [256]; **Δ**, [216]; ◇, [258] and **O**, [257]. The (BLUE) symbols represent bubble points and (RED) symbols represent dew points. The solid curves are the predictions from the SAFT-γ Mie after optimisation while the dashed curves are predictions from SAFT-γ Mie reported in literature.

As seen in the figure, the SAFT-γ Mie model predicts the bubble and dew points of the mixture pretty well. The SAFT-γ Mie reported in literature fails to describe accurately the phase envelope of the mixture at both conditions.

7.3.4 (COO - CH_3OH)

As mentioned before, COO group is the main functional group forming fatty acid methyl esters (biodiesel) as well as glycerides. The cross interactions for (COO - CH_3OH) were obtained by regression to experimental VLE data of a binary mixture containing methanol and an ester with COO functional group. Experimental isothermal VLE (p, x) data at different temperatures and isobaric (T, x) data at pressure of 1.0133 MPa for the mixture of methyl laurate ($CH_3(CH_2)_{10}COOCH_3$) and CH_3OH published in literature [72, 259, 260] were used in the parameters-estimation. In Figure 7.4, it is apparent that the model after tuning the cross interactions provides a good representation of the experimental phase behaviour except for the dew points where the theoretical curve deviates from the experimental data. It is observed from the figure that the deviation is increased as the temperature increases. A good prediction can be achieved by the theoretical model using the values of parameters reported in literature for the vapour-liquid equilibria of the system except when the content of methanol is low in the liquid phase at constant pressure in which the model underpredicts the compositions of methanol as shown in Figure 7.4b.

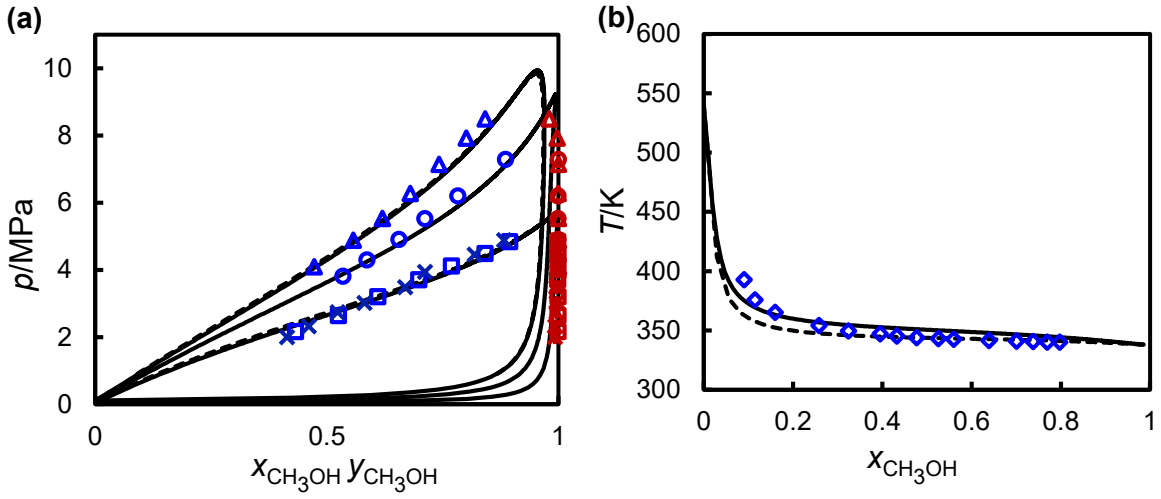

Figure 7.4: Vapour-liquid equilibria for (methanol + methyl laurate) binary mixture: (a), isothermal pressure-composition (p, x) phase diagram and (b), isobaric temperature-composition (T, x) diagram. The open symbols correspond to published literature data at: □, T = 493 K [72]; **X**, T = 493.2 K [259]; **O**, T = 523 K [72]; **Δ**, T = 543 K [72] and ◇, p = 1.0133 MPa [260]. The (BLUE) open symbols represent bubble points and (RED) symbols represent dew points. The solid curves are the predictions from the SAFT-γ Mie after optimisation.

7.3.5 (CH_3OH - CH=)

The interactions for (CH_3OH - CH=) here were obtained from the VLE data of (oleic acid + methanol) and (methyl oleate + methanol) mixtures. Methyl oleate is a fatty acid methyl ester (FAME) resulting from the condensation of the carboxy group of oleic acid with methanol. It derives from an oleic acid. As seen in Figure 7.5, a good satisfactory prediction of the phase equilibria of the mixtures is apparent. The literature SAFT-γ Mie model, on the other hand, shows a poor description for the (oleic acid + methanol) mixture as shown in Figure 7.5a, but a good prediction is seen for the (methyl oleate + methanol) mixture as shown in Figure 7.5b.

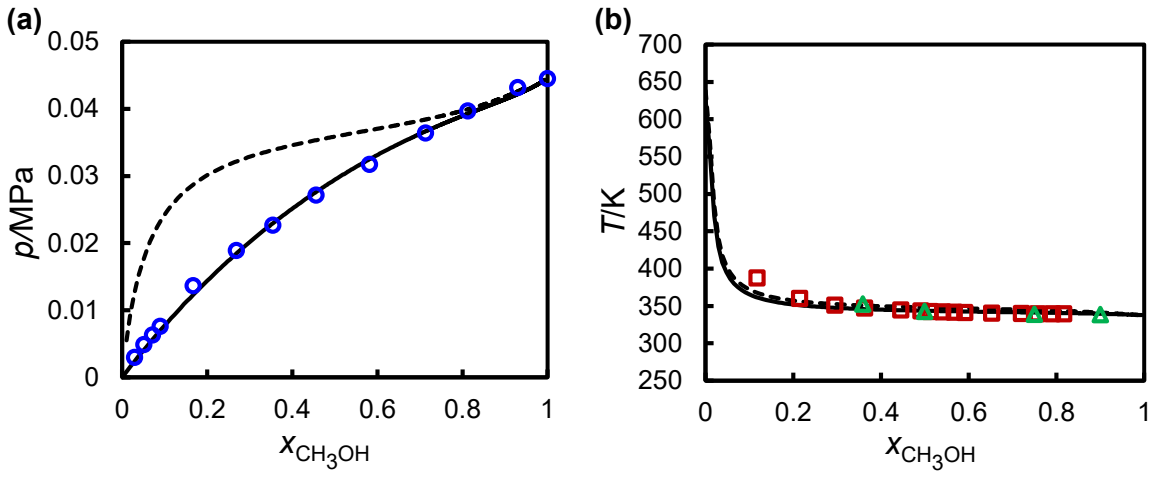

Figure 7.5: Fluid-phase behaviour data for: (a), (oleic acid + methanol) binary mixture and (b), (methyl oleate + methanol) binary mixture. The open symbols correspond to published literature data: ○, T = 318.15 K [261]; Δ, p = 1.0133 MPa [254] and □, p = 1.0133 MPa [260]. The solid curves are the predictions from SAFT-γ Mie after optimisation while the dashed curves are predictions from SAFT-γ Mie reported in literature.

The model using the refined parameters was tested to model the isothermal VLE of (methanol + propylene) mixture at T = 298.15 K as shown in Figure 7.6. Propylene chemical structure is $CH_3CH{=}CHCH_2$. As can be seen from the figure, the model agrees with the experimental data except at the critical region where it underpredicts the mole fractions of propylene in the liquid phase.

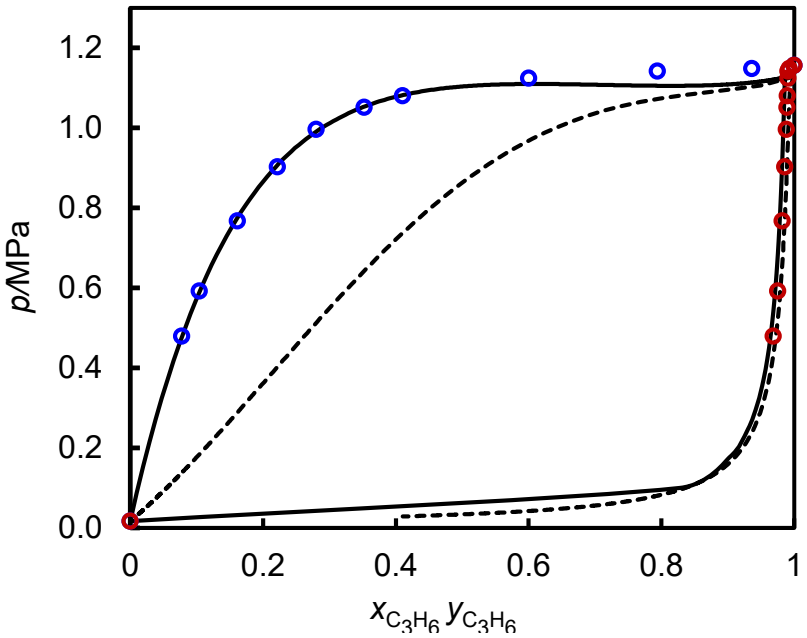

Figure 7.6: Isothermal pressure-composition (*p, x*) phase diagram for (methanol + propylene) binary system at 298.15 K reported in literature [262]. The (BLUE) open symbols (O) represent bubble points and (RED) symbols (O) represent dew points. The solid curves are the predictions from the SAFT-γ Mie while the dashed curves are predictions using the encrypted databank in SAFT.

7.3.6 (H_2O - CH=)

The cross interactions between H_2O group and CH= group can be estimated by fitting the phase behaviour data for (propylene + water) mixture at different temperatures as shown in Figure 7.7a and b. The unlike dispersion energy ε_{kl} was only refined to allow the model to accurately predict the mixture fluid-phase equilibria. The model is able to predict the very low content of propylene in the liquid phase as show in Figure 7.7b. The theoretical model using the encrypted databank can also predict the system in both bubble and dew curves with small deviation in the bubble curve at high pressures.

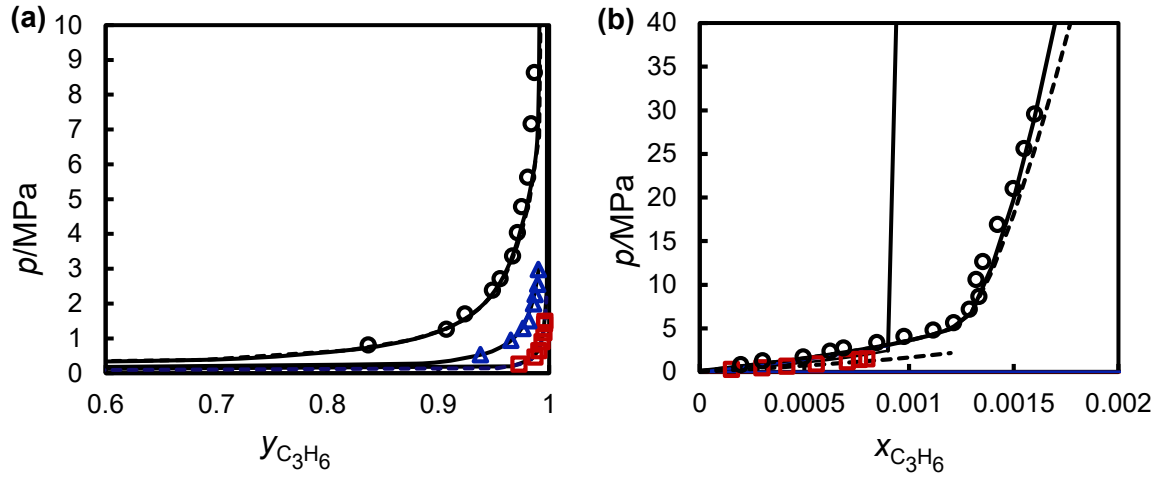

Figure 7.7: Fluid-phase behaviour data for (propylene + water) binary mixture. The open symbols correspond to published literature data [262]: **O**, T = 377.7 K; **Δ**, T = 344.4 K and **□**, T = 310.96 K. The solid curves are the predictions from SAFT-γ Mie while the dashed curves are predictions using the encrypted databank in SAFT.

7.3.7 (OH_GI - CO_2)

To predict the fluid-phase behaviour for the mixtures including (CO_2 + glycerol) more accurately, the cross interactions of (OH_GI - CO_2) need to be optimised. For this case, the unlike dispersion energy ε_{kl} was only tuned to have a satisfactory description as shown in Figure 7.8. The figure is an isothermal pressure-composition diagram for the mixture at temperatures of (313.15, 333.15 and 413.15) K reported in literature [263, 264]. It can be seen also in the figure that the theoretical model available in literature fails to predict the bubble points for the system accurately at all isotherms.

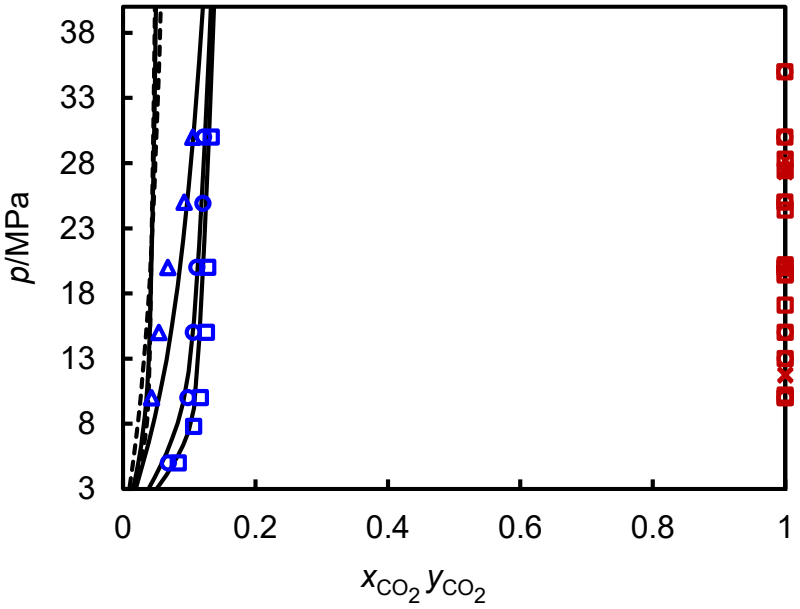

Figure 7.8: Isothermal pressure-composition (*p, x*) phase diagram for (glycerol + CO_2) binary system reported in literature at: ☐, T = 315.15 K [263]; **O**, T = 333.15 K [263]; **Δ**, T = 413.15 K [263] and **X**, T = 333.2 K [264]. The (BLUE) open symbols represent bubble points and (RED) symbols represent dew points. The solid curves are the predictions from the SAFT-γ Mie while the dashed curves are predictions using the encrypted databank in SAFT.

Table 7.1: SAFT-γ Mie like group parameters used in this work [44].

group *k*	S_k	σ_{kk}/Å	(ε_{kk}/k_B)/K	λ^a_{kk}	λ^r_{kk}	$N_{ST,K}$	$n_{k,h}$	$n_{k,e}$	Ref.
CH_3OH	0.83517	3.25	307.69	6.000	19.235	2	1	2	[44]
CH=	0.20037	4.75	952.54	6.000	15.974				[44]
OH_GI	0.87980	2.80	410.31	6.000	20.702	2	1	2	Databank

Table 7.2: SAFT-γ Mie unlike group parameters used in this work.

group *k*	group *l*	(ε_{kl}/k_B)/K	λ_{kl}^r	Ref.
COOH	CH_3OH	328.804	11.431	This work
COO	CH_3OH	497.733	CR	This work
OH_GI	CH_3OH	343.085	CR	This work
OH_GI	CO_2	298.639	CR	This work
CH=	CO_2	355.088	49.968	This work
CH=	CH_3OH	438.171	21.005	This work
CH=	H_2O	255.747	CR	This work

CR indicates parameter was determined from the combining rule. All other values given in the table have been estimated from experimental data.

Table 7.3: Estimated SAFT-γ Mie like and unlike group association energies (ε_{klab}^{HB}) and bonding volume (K_{klab}) parameters.

group *k*	group *l*	Site a of group *k*	Site b of group *l*	ε_{klab}^{HB}	K_{klab} [Å^3]	Ref.
CH_3OH	COOH	*e*	*H*	3982.392	106.29	This work
CH_3OH	OH_GI	*e*	*H*	2400.279	205.76	This work

7.4 Conclusion

The SAFT-γ Mie model available in literature provided poor descriptions for the mixtures comprising the cross interactions of (COOH - CH_3OH), (OH_GI - CH_3OH), (CO_2 - CH=), (CH_3OH - CH=), (COOH - CH=) and (H_2O - CH=). The unlike parameters between these functional groups were estimated in this work by fitting to fluid-phase behaviour data published in literature. The SAFT-γ Mie model after obtaining the cross interactions showed a quite good prediction for the mixtures involved in the biodiesel system. The accurate predictions of the model for these systems are crucial in order to have accurate thermodynamic and separation calculations.

Chapter 8: Process Simulation Using gPROMS

8.1 Overview

In this chapter, a preliminary process flowsheet for the one-step non-catalytic process (transesterification) for biodiesel production under supercritical conditions was suggested and simulated using gPROMS ProcessBuilder software. The one-step process using CO_2 as a co-solvent was simulated using reaction kinetics published in literature. Process flow sheets for the two-step processes (hydrolysis and esterification) were simulated. Detailed operating conditions for each process were obtained. No economic analysis was performed in all the processes and this will be a scope for future work.

8.2 Introduction

Process simulation is of great importance for the design and operation of chemical plants and it helps analyse, optimise and improve the performance of the process and quality of products. Biodiesel can be produced from vegetable oil and animal fats through catalyst-free transesterification (one-step) of triglycerides with supercritical methanol as explained earlier in Chapter 1. Esterification reaction between free fatty acids (FFA), which are available in the vegetable oil and animal fats, and supercritical methanol to produce biodiesel can occur simultaneously with the transesterification reaction. Preliminary design of industrial plant of the one-step process has been focused in a few studies published in literature, as summarised in Table 8.1, in which different thermodynamic models, kinetics data and assumptions were used in the simulations. Oleic acid, triolein and methyl oleate were used as the key components to represent free fatty acid, triglycerides and fatty acid methyl ester (biodiesel), respectively in all of these simulations. The authors also assumed that the reaction is irreversible and of first order.

Table 8.1: Simulations of the one-step process published in literature.

Reference	Simulation tool	Thermodynamic model	Reactor conditions			
			T/K	*p*/MPa	MeOH/Oil molar ratio	Conversion %
West et al. [265]	HYSYS	NRTL/UNIFAC[a]	623	20	42:1	98
Lee et al. [266]	HYSYS	NRTL/UNIFAC[a] /PR EoS[b]	623	19	42:1 and 24:1[c]	96[d]
Glisic and Skala [267]	HYSYS	UNIQUAC/RK Aspen EoS	573	20	42:1	97

[a]Notation: UNIFAC was used to estimate some interaction parameters.
[b]Notation: PR EoS was used in units operating at pressures greater than 1 MPa.
[c]Notation: Methanol to oil ratio of 24:1 was used in a modified process.
[d]Notation: The conversion of triolein and oleic acid are 96% and 100%, respectively.

Kusdiana and Saka [268] proposed a catalyst-free two-step supercritical methanol process which consists of hydrolysis of triglycerides to fatty acids in subcritical water and then methyl esterification of fatty acids to methyl esters (biodiesel) in supercritical methanol. They found that triglycerides were converted to biodiesel in shorter reaction time and milder reaction conditions (543 K/7-20 MPa) than the one-step process.

In this work, gPROMS ProcessBuilder software, developed by Process Systems Enterprise Limited (PSE), was used to simulate the process flowsheets of the one-step and two-step processes for biodiesel production using the SAFT-γ Mie developed in this work.

8.3 One-Step Process (Transesterification)

The one-step process consists of four main steps: pressurizing and heating methanol and triglycerides, transesterification reaction (and esterification reaction if free fatty acids in feedstocks are taken into account), methanol recovery (and co-solvent if it is used) and purification of biodiesel. The process flowsheet for the one-step process proposed in this work is shown in Figure 8.1. The process was simulated in gPROMS using the same inlet feed rates and reactor conditions used by West et al. [265] in their simulation and the comparison of outputs are summarised in Table 8.2. The simulation results obtained from gPROMS are provided in detail in Table 8.3. West et al. in his work made an assessment of biodiesel production processes including the supercritical method using HYSYS and due to lack of kinetics data of some processes a

conversion reactor (98% conversion) was assumed to operate continuously in the one-step process and the mono- and di-glycerides intermediates reactions were neglected. The annual plant capacity was specified to be 8000 metric tonnes per year of biodiesel production.

Table 8.2: Comparison of results between the simulation of one-step process built in this work and that published in literature.

	West et al. [265]	This work
Software	HYSYS	gPROMS
Thermodynamic model	NRTL/UNIFAC	SAFT-γ Mie
Transesterification		
T (K)	623.15	623.15
p (MPa)	20	20
Feed mass (%)	95%Triolein + 5% Oleic acid	95%Triolein + 5% Oleic acid
Methanol to Oil ratio	42:1	42:1
Residence time (hr)	0.333	0.333
Conversion (%)	98	98
Methanol Recovery		
Reflux ratio	3.42	3.42
Number of stages	12	12
Condenser/reboiler pressure (MPa)	0.1013/0.1053	0.1013/0.1053
Recovery (%)	99.3	99.3
Distillate flowrate (kg/h)	1239.7	1239.7
Distillate purity (%)	99.99	99.74
Glycerol Separation		
T (K)	298.15	298.15
p (MPa)	0.1053	0.1047
Molar flow (kmol/h)	1.44	1.32
Mass flow (kg/h)	110.1	108.5
Glycerol mass fraction	0.918	0.936
Biodiesel Purification		
Reflux ratio	2	2
Number of stages	8	8
Condenser/reboiler pressure (MPa)	0.1013/0.1113	0.1013/0.1113
Recovery (%)	99.9	99.9
Final purity	99.65	99.70

Methanol and oil were pressurized to 20 MPa by pumps (P_1) and (P_2) and then heated up to 534 K and 618 K in heat exchangers (E_1) and (E_2), respectively, in which hot stream of the reaction product was utilized. Both streams were then heated to 623 K by heater (E_3) and fed to the reactor where transesterification and esterification reactions took place. A distillation column with 12 theoretical stages was used to separate and recover the unreacted methanol. The

temperatures and pressures of the condenser and reboiler were (314.8 K/0.1013 MPa) and (456.8 K/0.1057 MPa), respectively. The recovery of methanol was 99.3% with a distillate mass flow rate of 1239.7 $kg \cdot h^{-1}$. The recovered methanol was recycled and mixed with the fresh methanol. The bottom of the distillation column was cooled to a temperature of 298.15 K and hence two liquid phases were formed: methyl oleate-rich phase and glycerol-rich phase. These phases were separated in a decanter where 93.6 wt.% of glycerol was separated in the bottom. The upper layer from the decanter consisted of 97.8 wt.% methyl oleate (biodiesel), 1.9 wt.% triolein, 0.1 wt.% oleic acid and 0.2 wt.% water. Biodiesel was purified further to 99.7 wt.% with a top liquid recovery of 99.9% in a distillation column equipped with eight theoretical stages. The purity of biodiesel meets both the ASTM D6751 and EN 14214 standards provided in Chapter 1, section 1.2.2. As seen in Table 8.2, the simulation results in this work agree well with those reported by West et al. [265].

Kinetics of transesterification reaction reported by Kusdiana and Saka [87] based on experimental results from rapeseed oil in a batch reactor were also used in the present work. An activation energy of 47.1 $kJ \cdot mol^{-1}$ and pre-exponential factor of 145.87 s^{-1} [266] were obtained from the Arrhenius plot. A plug flow reactor (PFR) was reported to be the preferred option for continuous large-scale production of biodiesel and, hence it was selected [267, 269]. The transesterification reaction was carried out at a temperature of 623 K, a pressure of 20 MPa, residence time of 4 min and a methanol to oil molar ratio of 42:1. The conversion of triolein to methyl oleate in the reactor was 93%, which was less than the conversion reported by Kusdiana and Saka (95%), and this could be due to the use of the key components in the simulation instead of the real biodiesel. A distillation column (Distillation_1) with four stages and reflux ratio of 3.45 was found enough to recover 99% of methanol from the reaction product. After separating the by-product glycerol in a decanter, biodiesel with a purity of 99.63 wt.% was obtained from a distillation column (Distillation_2) containing eight theoretical stages and reflux ratio of two. The reboiler and condenser pressures in the distillation column were set to 0.015-0.02 MPa in order to avoid thermal decompositions of the methyl ester. Depending on the molar ratio of alcohol to triglycerides, pressures and reaction time the thermal decompositions of methyl esters, glycerol and triglycerides can occur at temperatures above 573 K after 1 hr before reaching conversion of 96% [88, 270, 271]. The temperatures of the reboiler and condenser were 569 K and 323 K, respectively. The recovery of methyl oleate in the top of the distillation column was relaxed to be 90% in order to reduce the reboiler and condenser duties.

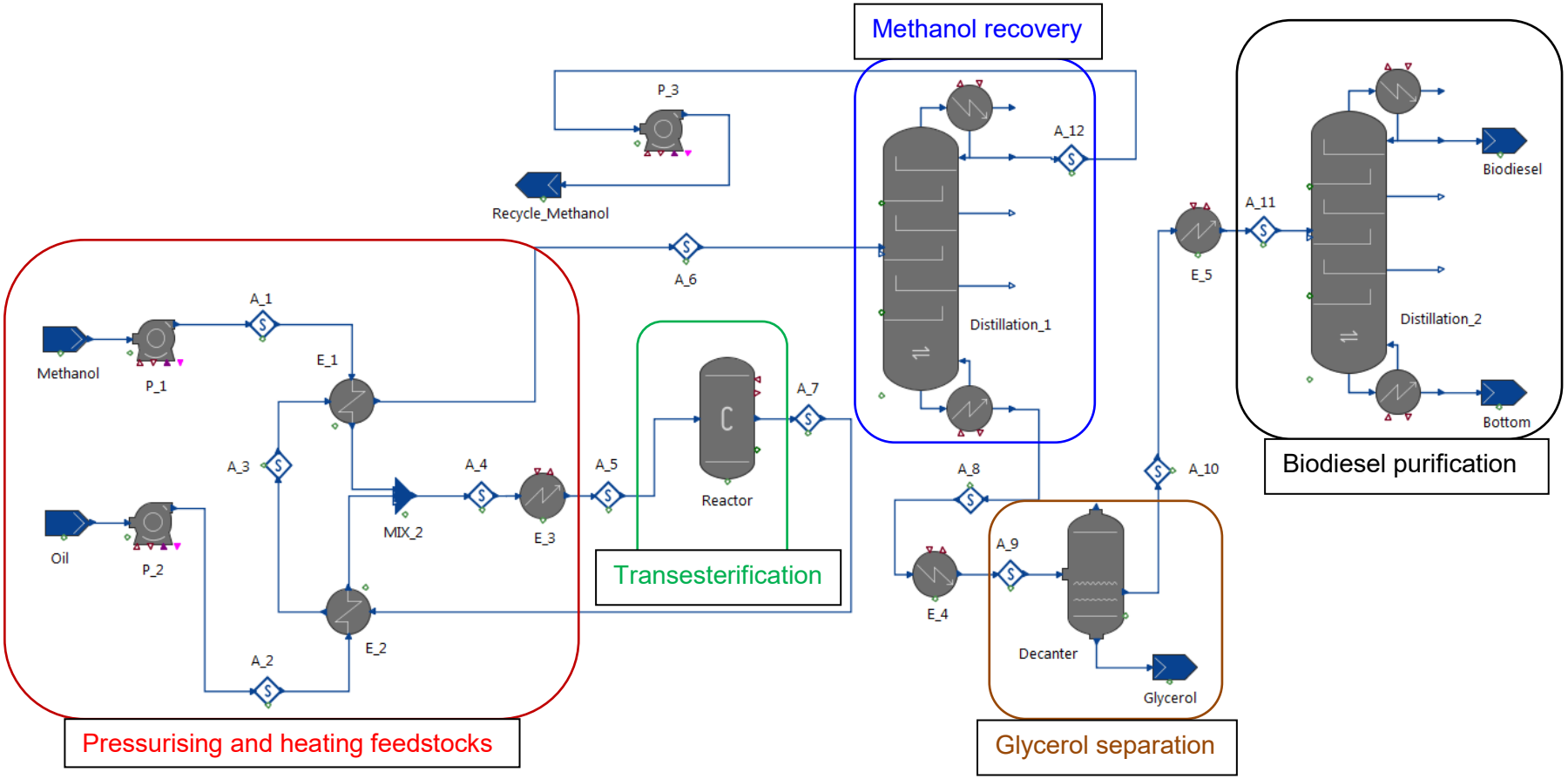

Figure 8.1: Flowsheet of the one-step process (simulation snapshot from gPROMS). Colours indicate the steps of the process.

Table 8.3: Properties of main streams of the one-step process.

Steam	Methanol	Oil	A_1	A_2	A_3	A_4
Pressure (MPa)	0.1	0.1	20	20	20	20
Temperature (K)	298.15	298.15	302.1	301.2	539.0	557.7
Mass flow (kg/h)	1357.50	1050	1357.5	1050	2407.5	2407.5
Molar flow (kmol/hr)	42.37	1.31	42.37	1.31	43.68	43.68
Component mass fraction						
Triolein	0	0.95	0	0.95	0.0083	0.4143
Methanol	1	0	1	0	0.5174	0.5639
Methyl Oleate	0	0	0	0	0.4303	0.0000
Oleic acid	0	0.05	0	0.05	0.0004	0.0218
Glycerol	0	0	0	0	0.0422	0.0000
Water	0	0	0	0	0.0014	0.0000

Steam	A_5	A_6	A_7	A_8	A_12	A_9
Pressure (MPa)	20	20	20	0.106	0.101	0.106
Temperature (K)	623.15	396.14	623.15	456.78	314.8	298.15
Mass flow (kg/h)	2407.5	2407.5	2407.5	1167.8	1239.7	1167.8
Molar flow (kmol/hr)	43.68	43.68	43.68	4.91	38.77	4.91
Component mass fraction						
Triolein	0.4143	0.0083	0.0083	0.0171	0.0000	0.0171
Methanol	0.5639	0.5174	0.5174	0.0078	0.9974	0.0078
Methyl Oleate	0.0000	0.4303	0.4303	0.8871	0.0000	0.8871
Oleic acid	0.0218	0.0004	0.0004	0.0009	0.0000	0.0009
Glycerol	0.0000	0.0422	0.0422	0.0871	0.0000	0.0871
Water	0.0000	0.0014	0.0014	0.000	0.0026	0.0000

Steam	A_10	Glycerol	A_11	Biodiesel	Bottom
Pressure (MPa)	0.105	0.105	0.105	0.101	0.113
Temperature (K)	305.14	305.14	338.15	480.07	825.3
Mass flow (kg/h)	1059.3	108.6	1059.3	1038.3	20.99
Molar flow (kmol/hr)	3.59	1.32	3.59	3.56	0.03
Component mass fraction					
Triolein	0.0188	0.0000	0.0188	0.0000	0.9506
Methanol	0.0020	0.0643	0.0020	0.0021	0.0000
Methyl Oleate	0.9780	0.0002	0.9780	0.9968	0.0494
Oleic acid	0.0010	0.0000	0.0010	0.001	0.0000
Glycerol	0.0012	0.9357	0.0012	0.0001	0.0000
Water	0.0000	0.0000	0.0000	0.0000	0.0000

Addition of CO_2 co-solvent in the one-step process:

As mentioned in Chapter 2, section 2.2.5, Cao et al. [94] added the co-solvent CO_2 to the reaction mixture to decrease the conditions required for the supercritical process. They demonstrated that at a reaction temperature of 553 K, a pressure of 14.3 MPa, methanol to oil molar ratio of 24:1 and methanol to CO_2 molar ratio of 10:1 a yield of 98% of methyl esters (biodiesel) was obtained in a reaction time of 10 min. A simulation proposed in this work for the process flowsheet using these reported conditions is shown in Figure 8.2. Fresh and recycled streams of methanol and oil stream were pumped to 14.3 MPa and warmed up in heat exchangers using the hot stream of the reaction product. Fresh and recycled streams of the co-solvent CO_2 were compressed to 14.3 MPa and mixed with methanol so that the molar ratio of methanol to CO_2 is 10:1. After the transesterification reaction, 100% of CO_2 and 98% of methanol were recovered in a distillation column (Distillation_1) containing six theoretical stages with a reflux ratio of one and recycled back to the feed. Glycerol was separated in a decanter and methyl oleate (biodiesel) in the top liquid phase was purified further in a distillation column (Distillation_2) having six theoretical stages and reflux ratio of 2. The purity of biodiesel obtained was 99.67% which meets the ASTM D6751 and EN 14214 standards. The outputs of the simulation are shown in Table 8.5.

8.4 Two-Step Process (Hydrolysis + Esterification)

The reaction kinetics reported by Alenezi et al. [100, 101] for the non-catalytic hydrolysis of sunflower oil with subcritical water and the non-catalytic esterification of free fatty acids with supercritical methanol, which were provided in Chapter 2 section 2.2.5, were used in the simulations of the two steps using gPROMS.

8.4.1 Hydrolysis Step

As per Alenezi et al. [101], sunflower oil consisted of 77 wt.% triglycerides, 20 wt.% diglycerides, 2.5 wt.% monoglycerides, and around 0.5 wt.% FFA. Therefore, triolein, diolein, monoolein, and oleic acid were used in the simulation to represent triglycerides, diglycerides, monoglycerides and free fatty acids, respectively. In the hydrolysis reaction, the intermediates (di- and mono-glycerides) were considered: triglycerides were hydrolyzed to diglycerides, the diglycerides were hydrolyzed to monoglycerides, and finally the monoglycerides were hydrolyzed to glycerol, and in each step fatty acids were generated. The volume ratio of water to oil required in this step was 1:1, and hence the reaction was assumed a pseudo-homogenous first order reaction because of the excess of water. The pressure was constant at 20 MPa and the temperatures were varied

from (543 - 623) K. The proposed simulation for the hydrolysis step is shown in Figure 8.3. The reaction temperature and the time of reaction were varied in the simulation and the conversion of triglycerides was measured as summarised in Table 8.4. The reaction temperature of 573 K, pressure of 20 MPa and residence time of 0.333 hr were used in the simulation of hydrolysis due to the high conversion obtained.

Table 8.4: Sensitivity analysis for the triglycerides conversion in the hydrolysis reaction.

Temperature (K)	Pressure (MPa)	Reaction time (min)	Triglycerides conversion (%)	Yield of fatty acid (mol%)
543	20	5	54.0	16.5
		10	69.0	32.0
		20	97.2	59.9
573	20	5	83.4	40.5
		10	96.8	67.0
		20	99.8	83.7
623	20	5	99.9	78.5
		10	100	85.6

The reaction product consisted of about 45.9% by wt. oleic acid, 46.9% water, 0.1% triolein, 1.4% diolein, 0.2% monoolein and 5.6% glycerol. The product was cooled by a cooler from 573 K to 453 K and the pressure was reduced to 0.1 MPa in order to separate water as vapour, glycerol and oil (oleic acid and unconverted intermediates) as two liquid phases in a three-phase separator. It was observed that cooling the product to a temperature less than 453 K resulted in formation of three liquid phases which were hard to be separated. The third liquid phase was expected to be the intermediates. The outlets of the top vapour and the bottom liquid from the three-phase separator contained 98.9 wt.% water and 100 wt.% glycerol, respectively. The second top liquid phase was rich in oleic acid (94.5 wt.%) and contained some intermediates. The oleic acid was purified to 96.4 wt.% in a distillation column (Distilation_column_1) with four theoretical stages and reflux ratio of 4. It was purified further to 100 wt.% in a second distillation column (Distilation_column_2). Both distillation columns were operated under vacuum in order to reduce the reboiler temperatures to avoid degradation of the components. The results of the simulation are shown in detail in Table 8.6.

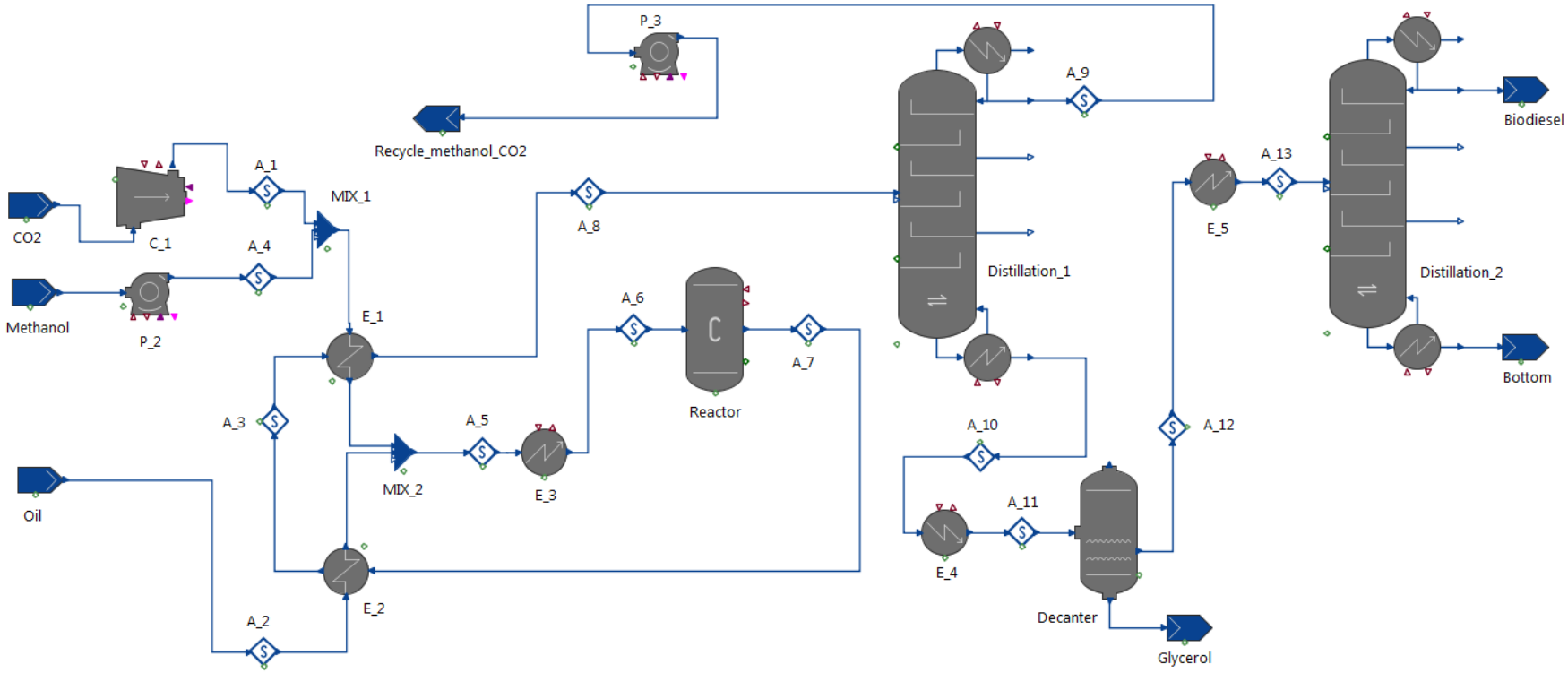

Figure 8.2: Flowsheet of the one-step process using CO_2 as a co-solvent (simulation snapshot from gPROMS).

Table 8.5: Properties of main streams of the one-step process using CO_2 as a co-solvent.

Stream	A_1	A_2	A_3	A_4	A_5	A_6
Pressure (MPa)	14.3	14.3	14.3	14.3	14.3	14.3
Temperature (K)	314.8	298.2	462.0	302.3	486.8	553.2
Mass flow (kg/h)	111.9	1050	1976.4	814.5	1976.4	1976.4
Molar flow (kmol/hr)	2.54	1.19	29.15	25.42	29.15	29.15
Component mass fraction						
Triolein	0	1	0.0106	0	0.5313	0.5313
Methanol	0	0	0.3556	1	0.4121	0.4121
Methyl Oleate	0	0	0.5230	0	0.0000	0.0000
Glycerol	0	0	0.0542	0	0.0000	0.0000
CO_2	1	0	0.0566	0	0.0566	0.0566

Stream	A_7	A_8	A_9	A_10	A_11	Glycerol
Pressure (MPa)	14.3	14.3	0.101	0.107	0.107	0.106
Temperature (K)	553.2	383.1	205.4	440.8	298.2	305.1
Mass flow (kg/h)	1976.4	1976.4	800.6	1175.8	1175.8	117.7
Molar flow (kmol/hr)	29.15	29.15	24.04	5.11	5.11	1.50
Component mass fraction						
Triolein	0.0106	0.0106	0.0000	0.0179	0.0179	0.0000
Methanol	0.3556	0.3556	0.8603	0.0120	0.0120	0.0925
Methyl Oleate	0.5230	0.5230	0.0000	0.8792	0.8792	0.0000
Glycerol	0.0542	0.0542	0.0000	0.0910	0.0910	0.9075
CO_2	0.0566	0.0566	0.1397	0.0000	0.0000	0.0000

Stream	A_13	Biodiesel	Bottom
Pressure (MPa)	0.106	0.015	0.019
Temperature (K)	338.2	325.6	578.8
Mass flow (kg/h)	1058.1	1026.7	31.34
Molar flow (kmol/hr)	3.61	3.55	0.06
Component mass fraction			
Triolein	0.0198	0.0000	0.6701
Methanol	0.0020	0.0031	0.0000
Methyl Oleate	0.9770	0.9967	0.3299
Glycerol	0.0002	0.0002	0.0000
CO_2	0.0000	0.0000	0.0000

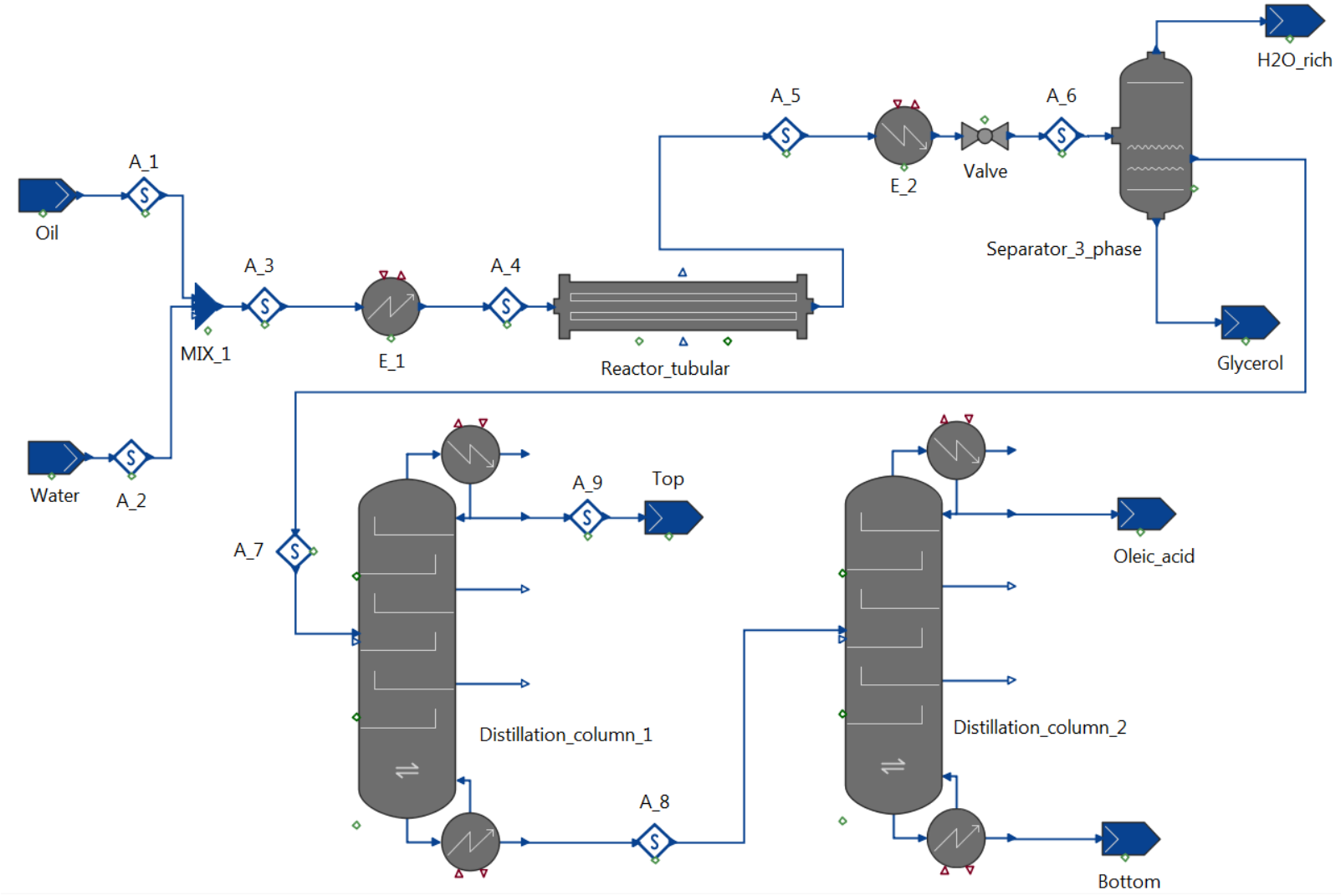

Figure 8.3: Flowsheet of the hydrolysis step (simulation snapshot from gPROMS).

Table 8.6: Properties of main streams of the hydrolysis step.

Stream	A_1	A_2	A_4	A_5	A_6	H_2O_rich
Pressure (MPa)	20	20	20	20	0.1	0.1
Temperature (K)	298.2	298.2	573.2	573.2	457.0	435.0
Mass flow (kg/h)	1320.7	1309.1	2629.9	2629.9	2629.9	1229.3
Molar flow (kmol/hr)	1.69	72.67	74.36	74.36	74.36	67.64
Component mass fraction						
Triolein	0.7700	0	0.3867	0.0005	0.0005	0.0000
Diolein	0.2000	0	0.1004	0.0144	0.0144	0.0000
Monoolein	0.0250	0	0.0126	0.0022	0.0022	0.0000
Oleic acid	0.0050	0	0.0025	0.4586	0.4586	0.0004
Water	0.0000	1	0.4978	0.4687	0.4687	0.9892
Glycerol	0.0000	0	0.0000	0.0556	0.0556	0.0105

Stream	Glycerol	A_7	A_8	A_9	Bottom	Oleic_acid
Pressure (MPa)	0.1	0.1	0.02	0.01	0.015	0.010
Temperature (K)	435.0	435.0	573.0	290.8	566.0	550.8
Mass flow (kg/h)	125.15	1275.5	1249.3	26.1	285.6	963.7
Molar flow (kmol/hr)	1.36	5.36	4.34	1.02	0.93	3.41
Component mass fraction						
Triolein	0.0000	0.0010	0.0010	0.0000	0.0043	0.0000
Diolein	0.0000	0.0297	0.0303	0.0000	0.1326	0.0000
Monoolein	0.0000	0.0045	0.0046	0.0000	0.0197	0.0001
Oleic acid	0.0000	0.9453	0.9641	0.0462	0.8434	0.9999
Water	0.0007	0.0130	0.0000	0.6363	0.0000	0.0000
Glycerol	0.9993	0.0065	0.0000	0.3175	0.0000	0.0000

8.4.2 Esterification Step

In the esterification step, free fatty acids obtained from the hydrolysis step are mixed with methanol to produce methyl esters (biodiesel) and water. Oleic acid, which represents FFA in the simulation of both hydrolysis and esterification processes, obtained from the previous hydrolysis step was mixed with fresh methanol (molar ratio of methanol to FFA was 7:1 as per the studies of Kusdiana and Saka [268] and Alenezi et al. [100]). The reaction conditions selected for the simulation were T = 543 K, p = 10 MPa and reaction time of 10 min. The methyl oleate yield obtained was 91%. The simulation of the process is shown in Figure 8.4 and the results are provided in Table 8.7. As can been from the figure, the hot stream of reaction product was utilized

to warm up fresh methanol and fatty acid inlets to 458.2 K and 437.1 K through heat exchangers (E_1) and (E_2), respectively before they were mixed and heated up to the desired temperature (543.2 K) by heater (E-3). The stream of the reaction product was then cooled down to room temperature by cooler (E-4) and depressurized to 0.1 MPa so that two liquid phases were formed (water-rich liquid phase and lower dense liquid phase containing mainly methanol and methyl oleate) and separated in a decanter. The upper liquid phase was heated up to 363 K and fed into a distillation column (Distillation_column_1) operating at atmospheric pressure and having four theoretical stages in which 99.75% of methanol was recovered as distillate. The bottom of the distillation column contained 90.92 wt.% methyl oleate, 8.90 wt.% oleic acid and 0.18 wt.% methanol. Methyl oleate was purified to 97.0 wt.% in a second distillation column equipped with 34 theoretical stages and a reflux ratio of four, and operating under vacuum (0.05/0.06 MPa) to avoid the degradation of biodiesel. The bottom recovery of methyl oleate was relaxed to be 60% to reduce the utility costs in the column. However, when the reaction temperature was increased to 593 K the conversion of oleic acid in the reactor was 97% (Alenezi et al. [100]), hence the purity of methyl oleate in the bottom of the first distillation column (12 theoretical stages and reflux ratio of 4) was 97.2 wt.% which meets the ASTM D6751 and EN 14214 standards. Therefore, there was no need for a second distillation column.

Table 8.7: Properties of main streams of esterification step.

Stream	A_1	A_2	A_3	A_4	A_5	A_6
Pressure (MPa)	10	10	10	10	10	10
Temperature (K)	433.9	320.2	463.2	432.6	543.2	460.0
Mass flow (kg/h)	622.4	705.6	1328.1	1328.1	1328.1	1328.1
Molar flow (kmol/hr)	19.4	2.5	21.9	21.9	21.9	21.9
Component mass fraction						
Oleic acid	0	1	0.0495	0.5313	0.5313	0.0495
Water	0	0	0.0307	0.0000	0.0000	0.0307
Methyl oleate	0	0	0.5057	0.0000	0.0000	0.5057
Methanol	1	0	0.4140	0.4687	0.4687	0.4140

Stream	A_7	A_8	Water_rich	A_10	A_11	Biodiesel
Pressure (MPa)	10	0.1	0.1	0.1	0.1	0.06
Temperature (K)	542.6	299.5	299.5	311.0	541.0	600.9
Mass flow (kg/h)	1328.1	1288.4	39.6	549.7	738.8	413.5
Molar flow (kmol/hr)	21.9	19.7	2.2	17.2	2.5	1.4
Component mass fraction						
Oleic acid	0.0183	0.0510	0.0000	0.0000	0.0890	0.0300
Water	0.0113	0.0009	0.9997	0.0021	0.0000	0.0000
Methyl oleate	0.1866	0.5213	0.0000	0.0000	0.9092	0.9700
Methanol	0.1527	0.4268	0.0003	0.9979	0.0018	0.0000

8.5 Conclusion

The preliminary designs of the one-step process (transesterification) and the two-step processes (hydrolysis and esterification) were simulated using gPROMS tool. The CO_2 co-solvent effect on the one-step process based on literature data was examined by a process flowsheet. There is no kinetics data available in literature for the effect of the CO_2 co-solvent on the two-step processes, so the simulation was not carried out. A comparative economic assessment including total capital investment and manufacturing costs needs to be conducted between the processes in order to find the best cost-effective process that can be economically competitive with the conventional process of biodiesel production.

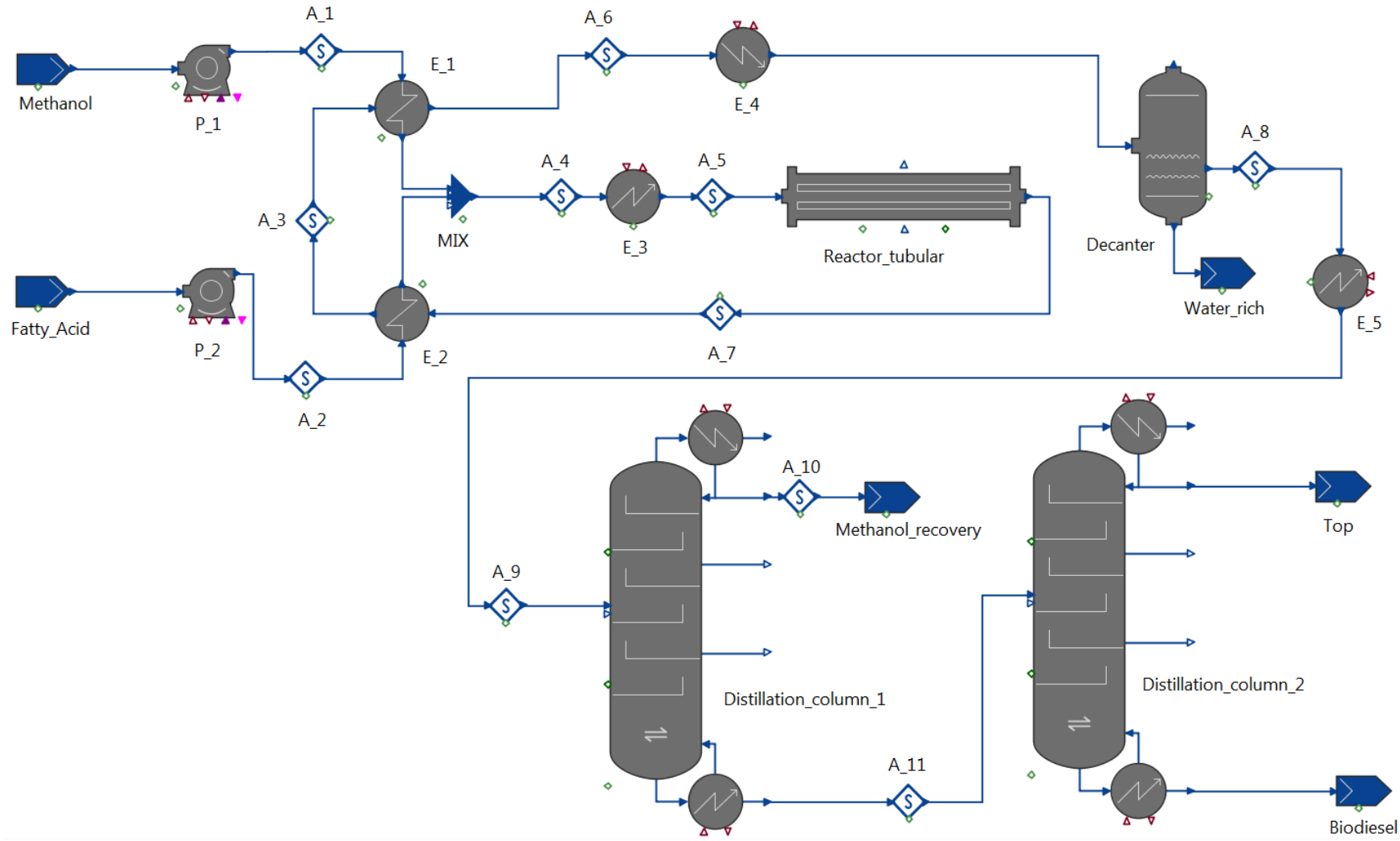

Figure 8.4: Flowsheet of the esterification step (simulation snapshot from gPROMS).

Chapter 9: Conclusions and Recommendations for Future Work

9.1 Summary and Conclusions

In this work, the phase behavior of different binary and ternary mixtures containing representative carboxylic acids, methyl esters and carbon dioxide has been studied over a wide temperature range of T = (298.15 to 423.15) K and pressures up to 20 MPa. The experimental measurements in this research were carried out by means of a quasi-static analytical apparatus having a maximum operating temperature of 433.15 K and a maximum operating pressure of 20 MPa. The apparatus consisted of a high pressure equilibrium view cell (VC) fitted with axially opposed sapphire windows to enable observation of the interior, and hence the critical points were measured experimentally. The overall standard uncertainty of the cell temperature, after considering bath temperature fluctuations and calibration uncertainties, was estimated to be 0.05 K while the overall standard uncertainty of the cell pressure was estimated to be 10 kPa. The experimental VLE and VLLE data measured in the present work were compared with calculations based on the SAFT-γ Mie and the Peng Robinson equations of state, both of which use group contribution approaches for parameters estimations. The VLE data were used to optimise cross interaction parameters for some of the functional groups comprising these mixtures. Other unlike parameters for functional groups that are of interest were estimated using VLE data reported in literature (see Chapter 7). The developed SAFT-γ Mie group contribution model containing the optimised like and unlike parameters was used as the physical property package in gPROMS ProcessBuilder simulation.

The fluid-phase equilibrium measurements on the binary systems (methyl propanoate + carbon dioxide) and (butanoic acid + carbon dioxide) were carried out with the high-pressure analytical apparatus. The measurements for the (methyl propanoate + carbon dioxide) mixture were made along six isotherms at temperatures from (298.15 to 423.15) K and at pressures up to near the mixture critical pressure at each temperature while for the mixture (butanoic acid + carbon dioxide) the measurements were made along eight isotherms at temperatures from (323.13 to 423.2) K and pressures up to the mixture critical pressures. The like group parameters and self-associations parameters for the functional group COOH have been estimated using VLE data of different fatty acids. The values obtained for COOH were tested for thermodynamic properties of long-chain carboxylic acids, and the model showed a good agreement with the experimental data.

The unlike dispersion energy ε_{kl} and the unlike repulsive exponent λ_{kl}^{r} between COOH-CO_2 were adjusted using the experimental measurements obtained in this work. The unlike dispersion energy ε_{kl} between COO-CH_3 and COO-CH_2 has been adjusted using methyl propanoate and different series of esters. The cross interactions between COO and CO_2 were then determined using the experimental data measured in this work. The vapour-liquid equilibrium (VLE) data obtained for the mixtures have been compared with the predictions of the optimised SAFT-γ Mie model. The model was found to be in a good agreement with the measured VLE data for both bubble and dew points with a small deviation at the critical region at low temperature in the case of (butanoic acid + carbon dioxide) system. The experimental data were also compared with the description of the Peng Robinson equation of state (PR EoS) combined with the classical one-fluid mixing rules integrating one temperature-independent binary interaction parameter for (methyl propanoate + carbon dioxide) system and two temperature-independent binary interaction parameters for (butanoic acid + carbon dioxide) system. The results after tuning show that the PR EoS can also predict well the system measured data, except in the critical regions in which PR EoS shows overprediction (at high temperatures for the binary mixture, methyl propanoate + carbon dioxide, and in all the isotherms for the mixture, butanoic acid + carbon dioxide).

The compositions of the phases coexisting in vapour-liquid equilibrium (VLE) for (methyl propanoate + propionic acid + carbon dioxide) were measured along six isotherms at temperatures from (323.12 to 423.11) K and pressures from (1 to 20) MPa at equal feed molar ratio of (methyl propanoate + propionic acid) at different CO_2 pressures. Phase behaviour measurements were also collected at fixed temperatures and pressures (T = 383.17 K and p = 4 MPa, T = 363.17 K and p = 6 MPa) and at different compositions of the mixture (methyl propanoate + propionic acid) starting from zero mole composition of methyl propionate to zero mole composition of propanoic acid. The vapour-liquid equilibrium (VLE) data obtained for the mixture have been compared with the predictions of the optimised SAFT-γ Mie model and PR EoS, and the models were found to be in a good agreement with the measured VLE data.

The experimental study of the phase behaviour of the ternary system (carbon dioxide + *tert*-butanol + water) was also presented along five isotherms at temperatures of (283.2, 298.18, 323.13, 373.10 and 423.17) K and at pressures of (4.0, 8.0, 12.0 and 18.0) MPa with different known feed compositions of (*tert*-butanol + water). The like group parameters of the functional group (COH) have been estimated from the fluid-phase behaviour data of pure *tert*-butanol. The model described very well the vapour pressure and saturated-liquid density data of *tert*-butanol. The cross interactions between the functional groups H_2O-CO_2, COH-H_2O and COH-CO_2, which

the ternary system (*tert*-butanol + carbon dioxide + water) comprises, were estimated from the phase behaviour data of the binary sub-systems and the values of the parameters implemented into SAFT-γ Mie model. The VLLE, VLE and LLE experimental data of the ternary system have been compared with the descriptions of SAFT-γ Mie making use of the optimised like and unlike group parameters estimated in this work. The description of the model agreed well with the experimental data except the less-dense liquid phase in the three-phase regions where the model predicted more water and less *tert*-butanol contents. PR EoS model was also used to predict the phase behaviour of the ternary system (carbon dioxide + *tert*-butanol + water) after obtaining the binary parameters from the same sub-systems used for SAFT model. The model agreed with the VLE at low temperatures and pressures, but the predictions were not good at the three-phase regions (VLLE).

The phase behaviour of the ternary system (toluene + water + carbon dioxide) was also investigated along four isotherms at temperatures from (338.15 to 413.15) K and pressures up to the UCEP. In this work, toluene was selected as a representative aromatic hydrocarbon and believed to be the first study covering a high range of temperatures and pressures to determining the phase behaviour envelope of the ternary system (C_7H_8 + H_2O + CO_2). The effect of the addition of H_2O on the phase behaviour of (C_7H_8 + CO_2) was also investigated by plotting the pressure as a function of the mole fractions of CO_2 in the C_7H_8-rich liquid phase and CO_2-rich vapour phase at the temperatures of (338.15 and 413.15) K measured for the ternary system (C_7H_8 + H_2O + CO_2) and comparing these experimental data with the VLE data of the binary system (C_7H_8 + CO_2) published in literature at the same temperatures. It was found that the effect of the phase behaviour was relatively small. The effect of adding water in the (C_7H_8 + CO_2) system was studied as well by comparing the UCEP data measured in the ternary system (C_7H_8 + H_2O + CO_2) with the experimental critical data for the (C_7H_8 + CO_2) and found that water did not affect significantly the UCEP curve. The vapour-liquid-liquid equilibrium (VLLE) data obtained for the mixture have been compared with the predictions of the optimised SAFT-γ Mie model and PR EoS, and in general the models were found to be in a good agreement with the measured data, but the accuracy of SAFT was more satisfactory especially in calculations of the mole compositions of the components in the less-dense liquid phase.

The cross interactions for (COOH - CH_3OH), (OH_GI - CH_3OH), (CO_2 - CH=), (CH_3OH - CH=), (COOH - CH=) and (H_2O - CH=) were estimated in this work by regression to fluid-phase behaviour data published in literature. The SAFT-γ Mie model available in literature provided poor descriptions for the mixtures comprising these functional groups. The SAFT-γ Mie model after

obtaining the cross interactions showed a quite good prediction for mixtures involved in the biodiesel system.

Finally, the preliminary designs of the one-step process (transesterification) and the two-step processes (hydrolysis and esterification) were simulated using gPROMS tool. The CO_2 co-solvent effect on the one-step process based on literature data was examined also by a process flowsheet. There is no kinetics data available in literature for the effect of the CO_2 co-solvent on the two-step processes, so the simulation was not carried out. A comparative economic assessment including total capital investment and manufacturing costs needs to be conducted between the processes in order to find the best cost-effective process that can be economically competitive with the conventional process of biodiesel production.

9.2 Contributions of This Work

The research provides new and accurate experimental data of fluid-phase behavior of mixtures that are relevant to biodiesel production under elevated temperatures and pressures. The experimental data offer inputs to develop more accurate thermodynamic models for process simulations. The work is an important step forward in understanding biodiesel production using supercritical methanol. The main contributions are summarised as follows:

- The production of a large set of experimental phase behavior data for the mixtures (butanoic acid + CO_2), (methyl propanoate + CO_2), (propionic acid + methyl propanoate + CO_2), (tert-butanol + water + CO_2) and (toluene + water + CO_2) over wide ranges of temperatures and pressures covering VLE, VLLE and LLE.
- The assessment and evaluation of the capability of SAFT-γ Mie and PR EoS models by means of comparison with the experimental data measured in this work. The experimental data were used to estimate and optimise many cross interactions between different functional groups for SAFT-γ Mie group contribution model; this represents a major contribution of the work.
- Providing new experimental data for mixtures at conditions of high temperature and pressure with detailed uncertainty analyses. These data are of great importance in filling gaps in the open literature and in the development of thermodynamic models for biodiesel production and other industrial processes.
- Preliminary designs for the one-step and the two-step processes of biodiesel production under supercritical conditions, which can play as useful basis for further

designing and retrofit. The simulation tool developed in this work can be used to optimise and evaluate the process.

9.3 Recommendations for Future Work

9.3.1 Further Experimental Investigations

In this work, phase behavior of binary and ternary mixtures of CO_2 and compounds related to biodiesel have been investigated under conditions of high temperatures and pressures. The mixtures studied were representatives of the real and heavy compounds available in the feedstocks and products, and the experimental data collected have been used in the optimisation of parameters in the thermodynamic models. This research has provided a fundamental basis for the understanding of the fluid phase behaviour of biodiesel system by use of the predictive capabilities of SAFT-γ Mie group contribution approach. However, real biodiesel contains several mixtures of fatty acid methyl esters (saturated and unsaturated) and hence the thermophysical properties of biodiesel are still difficult to be described by the predictive models. Further measurements on fluid mixtures comprising of biodiesel (real or synthetic) and other relative compounds under elevated temperatures and pressures would be highly beneficial in understanding the real process. Literature review on chemistry of the substances that are of interest should be made to avoid the occurrence of reactions. There was an interest to test biodiesel derived from oils extracted from date pits which are largely produced in Gulf Cooperation Council (GCC) countries including Oman. The total production of dates in the GCC countries is estimated to be 2.34×10^6 metric tons per year, with 23% of the total production is considered as waste [4]. An investigation on the biodiesel produced from the extracted date pits oil has been started by a research team in Sultan Qaboos University in Oman focusing on chemical kinetics, so a cooperation with this research team to cover the thermophysical properties of the mixtures of interest would benefit the project. The extraction of oils from date pits or any other sources (preferably non-edible) can also be carried out by an extraction equipment available in one of our laboratories.

9.3.2 Further Apparatus Improvements

The maximum operating pressure and temperature for the current high-pressure analytical apparatus are 433.15 K and 20 MPa, respectively. The equilibrium view cell was designed to

handle pressures higher than 100 MPa, but the sapphire windows limit the operating pressure to 70 MPa, and a further limitation in the maximum operating pressure for the apparatus was set to be 20 MPa due to the sampling valves. There are verity of sampling valves (VICI AG International) operating at high pressures and temperatures in which the existing valves can be replaced with. The capability of the apparatus to perform measurements at high pressure would allow to investigate the phase behaviour of more complex mixtures that may have critical points higher than 20 MPa. Also, the maximum operating temperature is limited by the silicon oil used as the thermal fluid inside the stainless steel bath. Silicon oil baths provide more constant heat compared to other heating devices, but their disadvantages include: silicone oil expands when temperature is increased so the level of the oil needs to be controlled, and since there is loss of oil with time because of the expansion the bath level needs to be observed and necessary top-up with fresh oil is carried out so that the bath covers fully the upper parts of the cell like the sampling valves to avoid any condensation. In addition to these drawbacks, fixing a leak in the view cell or the parts covered by the silicone oil took very long period of time due to the need to clean the surfaces of these parts from oil and the difficulty to use the electronic leak detectors which can be damaged if the surface of the equipment is wet. Replacing the oil bath with a furnace with higher operating temperature could be a good alternative. As a result, an extra development for the materials insulating the heating transfer tubes, which connect the sampling valves to the GC, would most likely be required to reach higher temperatures to avoid condensation of heavy compounds in their journey to the GC.

As mentioned earlier, some phases could not be sampled for compositional analysis at some conditions because the phases were too small or were in form of droplets on the view cell surface. Making the sampling capillary tubes in the cell movable or integrating smarter sampling techniques would lead to obtain more experimental measurements and hence better understanding for phase equilibria of mixtures under study.

9.3.3 Further Simulation Improvements

The simulations carried out in this research are preliminary but provide a fundamental basis to understanding the process and finding rooms for optimisation. Further sensitivity analyses, heat recovery, optimisations and use of different co-solvents can be carried out in these simulations. A comparative economic assessment including total capital investment and manufacturing costs

needs to be conducted between the processes in order to find the best cost-effective process that can be economically competitive with the conventional process of biodiesel production.

Bibliography

1. IEA, *Global Energy & CO2 Status Report* 2017, International Energy Agency Paris, France.
2. Ho, D.P., H.H. Ngo, and W. Guo, *A mini review on renewable sources for biofuel.* Bioresource Technology, 2014. **169**: p. 742-749.
3. Cellura, M., et al., *Energy and environmental impacts of energy related products (ErP): a case study of biomass-fuelled systems.* Journal of Cleaner Production, 2014. **85**: p. 359-370.
4. Jamil, F., et al., *Optimization of oil extraction from waste "Date pits" for biodiesel production.* Energy Conversion and Management, 2016. **117**: p. 264-272.
5. Food and a.o.o.t.U.N.F. department, *UBET - Unified bioenergy terminology*. 2004: Food and agriculture organization of the United States.
6. Guo, M., W. Song, and J. Buhain, *Bioenergy and biofuels: History, status, and perspective.* Renewable and Sustainable Energy Reviews, 2015. **42**: p. 712-725.
7. IEA, *Biofuels for transport: Tracking Clean Energy Progress*. 2018, International Energy Agency Paris, France.
8. EC. *Directive 2009/28/EC of The European Parliament and of the Council of 23 April 2009 on the Promotion of the Use of Energy from Renewable Sources and Amending and Subsequently Repealing Directives 2001/77/EC and 2003/30/EC*. 20 Jan 2019]; Available from: https://eur-lex.europa.eu/LexUriServ/LexUriServ.do?uri=OJ:L:2009:140:0016:0062:EN:PDF
9. de Man, R. and L. German, *Certifying the sustainability of biofuels: Promise and reality.* Energy Policy, 2017. **109**: p. 871-883.
10. Saladini, F., et al., *Guidelines for emergy evaluation of first, second and third generation biofuels.* Renewable and Sustainable Energy Reviews, 2016. **66**: p. 221-227.
11. Alam, F., S. Mobin, and H. Chowdhury, *Third Generation Biofuel from Algae.* Procedia Engineering, 2015. **105**: p. 763-768.
12. Joshi, G., et al., *Challenges and opportunities for the application of biofuel.* Renewable and Sustainable Energy Reviews, 2017. **79**: p. 850-866.
13. Mohr, A. and S. Raman, *Lessons from first generation biofuels and implications for the sustainability appraisal of second generation biofuels.* Energy Policy, 2013. **63**: p. 114-122.
14. Demirbas, A., *Political, economic and environmental impacts of biofuels: A review.* Applied Energy, 2009. **86**: p. S108-S117.
15. Demirbas, A., *Biorefineries: Current activities and future developments.* Energy Conversion and Management, 2009. **50**(11): p. 2782-2801.
16. Atadashi, I.M., M.K. Aroua, and A.A. Aziz, *Biodiesel separation and purification: A review.* Renewable Energy, 2011. **36**(2): p. 437-443.
17. Patil, P.D. and S. Deng, *Optimization of biodiesel production from edible and non-edible vegetable oils.* Fuel, 2009. **88**(7): p. 1302-1306.
18. Demirbas, A., *Biodiesel from waste cooking oil via base-catalytic and supercritical methanol transesterification.* Energy Conversion and Management, 2009. **50**(4): p. 923-927.
19. Schwab, A.W., M.O. Bagby, and B. Freedman, *Preparation and properties of diesel fuels from vegetable oils.* Fuel, 1987. **66**(10): p. 1372-1378.
20. Vijayaraj, K. and A.P. Sathiyagnanam, *Experimental investigation of a diesel engine with methyl ester of mango seed oil and diesel blends.* Alexandria Engineering Journal, 2016. **55**(1): p. 215-221.
21. Ma, F. and M.A. Hanna, *Biodiesel production: a review1.* Bioresource Technology, 1999. **70**(1): p. 1-15.

22. Singh, S.P. and D. Singh, *Biodiesel production through the use of different sources and characterization of oils and their esters as the substitute of diesel: A review.* Renewable and Sustainable Energy Reviews, 2010. **14**(1): p. 200-216.
23. Gonzalez, S.L., et al., *Continuous Catalyst-Free Production of Biodiesel through Transesterification of Soybean Fried Oil in Supercritical Methanol and Ethanol.* Energy & Fuels, 2013. **27**(9): p. 5253-5259.
24. Madras, G., C. Kolluru, and R. Kumar, *Synthesis of biodiesel in supercritical fluids.* Fuel, 2004. **83**(14-15): p. 2029-2033.
25. Hajar, M., S. Shokrollahzadeh, and F. Vahabzadeh, *A review on biodiesel production processes*. Vol. 21. 2009. 45-57.
26. Rathore, V. and G. Madras, *Synthesis of biodiesel from edible and non-edible oils in supercritical alcohols and enzymatic synthesis in supercritical carbon dioxide.* Fuel, 2007. **86**(17-18): p. 2650-2659.
27. Sonntag, N.O.V., *Structure and composition of fats and oils*. Bailey's industrial oil and fat products,. Vol. Vol 1 4th edition, ed. 1979: Swern, D. John Wiley and Sons, New York,.
28. Gonfa Keneni, Y. and J. Marchetti, *Oil extraction from plant seeds for biodiesel production*. Vol. 5. 2017. 316-340.
29. Saka, S. and D. Kusdiana, *Biodiesel fuel from rapeseed oil as prepared in supercritical methanol.* Fuel, 2001. **80**(2): p. 225-231.
30. Demirbaş, A., *Biodiesel fuels from vegetable oils via catalytic and non-catalytic supercritical alcohol transesterifications and other methods: a survey.* Energy Conversion and Management, 2003. **44**(13): p. 2093-2109.
31. Bunyakiat, K., et al., Energy Fuels, 2006. **20**: p. 812.
32. He, H., T. Wang, and S. Zhu, *Continuous production of biodiesel fuel from vegetable oil using supercritical methanol process.* Fuel, 2007. **86**(3): p. 442-447.
33. He, H., et al., *Transesterification Kinetics of Soybean Oil for Production of Biodiesel in Supercritical Methanol.* Journal of the American Oil Chemists' Society, 2007. **84**(4): p. 399-404.
34. Silva, C., et al., *Continuous Production of Fatty Acid Ethyl Esters from Soybean Oil in Compressed Ethanol.* Industrial & Engineering Chemistry Research, 2007. **46**(16): p. 5304-5309.
35. Mohibbe Azam, M., A. Waris, and N.M. Nahar, *Prospects and potential of fatty acid methyl esters of some non-traditional seed oils for use as biodiesel in India.* Biomass and Bioenergy, 2005. **29**(4): p. 293-302.
36. Bhuiya, M.M.K., et al., *Prospects of 2nd generation biodiesel as a sustainable fuel—Part: 1 selection of feedstocks, oil extraction techniques and conversion technologies.* Renewable and Sustainable Energy Reviews, 2016. **55**: p. 1109-1128.
37. Atabani, A.E., et al., *A comprehensive review on biodiesel as an alternative energy resource and its characteristics.* Renewable and Sustainable Energy Reviews, 2012. **16**(4): p. 2070-2093.
38. Marchetti, J.M., V.U. Miguel, and A.F. Errazu, *Possible methods for biodiesel production.* Renewable and Sustainable Energy Reviews, 2007. **11**(6): p. 1300-1311.
39. Demirbas, A., Energy Convers. Manage., 2002. **43**: p. 2349.
40. Demirbas, A., *Biodiesel production from vegetable oils via catalytic and non-catalytic supercritical methanol transesterification methods.* Progress in Energy and Combustion Science, 2005. **31**(5-6): p. 466-487.
41. *Standard Specification for Biodiesel Fuel Blend Stock (B100) for Middle Distillate Fuels*.
42. Jääskeläinen, H. *Biodiesel Standards & Properties*. 2009; Available from: https://www.dieselnet.com/tech/fuel_biodiesel_std.php
43. Xu, J., et al., *A review of multi-phase equilibrium studies on biodiesel production with supercritical methanol.* RSC Advances, 2014. **4**(45): p. 23447.

44. Dufal, S., et al., *Prediction of Thermodynamic Properties and Phase Behavior of Fluids and Mixtures with the SAFT-γ Mie Group-Contribution Equation of State.* Journal of Chemical & Engineering Data, 2014. **59**(10): p. 3272-3288.
45. Brainard, A.J., *Thermodynamics for chemical engineers, K. E. Betts, J. S. Rowlinson, and G. Saville. The MIT Press, Cambridge, Massachusetts, 1975, 505 pages.$19.95.* he American Institute of Chemical Engineers 1977. **23**(2): p. 213-213.
46. Soave, G., *Equilibrium constants from a modified Redlich-Kwong equation of state.* Chemical Engineering Science, 1972. **27**(6): p. 1197-1203.
47. Prausnitz, J.M.L., Ruediger M.; Azevedo, Edmund Gomes de., *Molecular thermodynamics of fluid-phase equilibria* ed. r. ed. 1999: Upper Saddle River, NJ : Prentice Hall
48. Scott, R.L.a.P.H.v.K., *Static properties of solutions. Van der Waals and related models for hydrocarbon mixtures.* Discuss. Faraday Soc, 1970. **49(0)**: p. 87-97.
49. Scott, P.H.V.K.a.R.L., *Critical Lines and Phase Equilibria in Binary Van Der Waals mixtures.* Philos. Trans. R. Soc. A, 1980. **298**: p. 495-540.
50. Webster, L.A. and A.J. Kidnay, *Vapor−Liquid Equilibria for the Methane−Propane−Carbon Dioxide Systems at 230 K and 270 K.* Journal of Chemical & Engineering Data, 2001. **46**(3): p. 759-764.
51. Vitu, S., et al., *Predicting the phase equilibria of CO2+hydrocarbon systems with the PPR78 model (PR EOS and kij calculated through a group contribution method).* The Journal of Supercritical Fluids, 2008. **45**(1): p. 1-26.
52. Al Ghafri, S.Z., *Phase Behaviour and Physical Properties of Reservoir Fluids Under Addition of Carbon Dioxide*, in *Department of Chemical Engineering*. 2013, Imperial College London. p. 305.
53. McCabe, C., A. Gil-Villegas, and G. Jackson, *Predicting the High-Pressure Phase Equilibria of Methane + n-Hexane Using the SAFT-VR Approach.* The Journal of Physical Chemistry B, 1998. **102**(21): p. 4183-4188.
54. Quirion, F., L.J. Magid, and M. Drifford, *Aggregation and critical behavior of 2-butoxyethanol in water.* Langmuir, 1990. **6**(1): p. 244-249.
55. Gubbins, K.E., *Theory and computer simulation studies of liquid mixtures.* Fluid Phase Equilibria, 1985. **20**: p. 1-25.
56. Forte, E., *Measurement and Prediction of the Phase Behaviour of Carbon Dioxide, Alkane and Water Mixtures at Reservoir Conditions*, in *Chemical Engineering*. 2011, Imperial College London.
57. Bluma, M. and U. K. Deiters, *A classification of phase diagrams of ternary fluid systems.* Physical Chemistry Chemical Physics, 1999. **1**(18): p. 4307-4313.
58. Van der Waals, J.D., *On the Continuity of the Gas and Liquid State*. 1873, University of Leiden, Leiden.
59. Glišić, S.B. and D.U. Skala, *Phase transition at subcritical and supercritical conditions of triglycerides methanolysis.* The Journal of Supercritical Fluids, 2010. **54**(1): p. 71-80.
60. Skala D , G.S., Lukić I, Orlović A, *A new concept of biodiesel production - transesterification with supercritical methanol.* Chem Ind, 2004. **58**: p. 76-185.
61. Glisic, S., et al., *Vapor-liquid equilibria of triglycerides-methanol mixtures and their influence on the biodiesel synthesis under supercritical conditions of methanol.* Journal of the Serbian Chemical Society, 2007. **72**(1): p. 13-27.
62. Almagrbi, A.M., S.B. Glisic, and A.M. Orlovic, *The phase equilibrium of triglycerides and ethanol at high pressure and temperature: The influence on kinetics of ethanolysis.* The Journal of Supercritical Fluids, 2012. **61**: p. 2-8.
63. Freeman B, B.R., Pryde EH *Transesterification kineticsofsoybean.* J Am Oil Chem Soc 1986: p. 63:1375–80.
64. Asakuma, Y., et al., *Theoretical study of the transesterification of triglycerides to biodiesel fuel.* Fuel, 2009. **88**(5): p. 786-791.

65. Weber W, P.S., Brunner G., *Vapour–liquid-equilibria and calculations using the Redlich–Kwong-Aspen-equation of state for tristearin, tripalmitin, and triolein in CO2 and propane.* Fluid Phase Equilibria, 1999: p. 158-160:695–706.
66. Tang, Z., et al., *Phase equilibria of methanol–triolein system at elevated temperature and pressure.* Fluid Phase Equilibria, 2006. **239**(1): p. 8-11.
67. Negi, D.S., et al., *Liquid−Liquid Phase Equilibrium in Glycerol−Methanol−Methyl Oleate and Glycerol−Monoolein−Methyl Oleate Ternary Systems.* Industrial & Engineering Chemistry Research, 2006. **45**(10): p. 3693-3696.
68. Fang, T., et al., *Phase equilibria for the mixtures of supercritical methanol+C18 methyl esters and supercritical methanol+α-tocopherol.* The Journal of Supercritical Fluids, 2008. **47**(2): p. 140-146.
69. Andreatta AE, C.s.L., Hegel P, Bottini SB, Brignole EA, *Phase Equilibria in Ternary Mixtures of Methyl Oleate, Glycerol, and Methanol.* Ind Eng Chem Res, 2008. **47**: p. 5157–64.
70. Glisic, S., et al., *Vapor–liquid equilibria of triglycerides – methanol mixture and its influence on the biodiesel synthesis under supercritical conditions of methanol.* J. Serb. Chem. Soc., 2007. **72**: p. 13-27.
71. Hegel, P., et al., *High pressure phase equilibria of supercritical alcohols with triglycerides, fatty esters and cosolvents.* Fluid Phase Equilibria, 2008. **266**(1-2): p. 31-37.
72. Shimoyama, Y., et al., *Measurement and correlation of vapor–liquid equilibria for methanol+methyl laurate and methanol+methyl myristate systems near critical temperature of methanol.* Fluid Phase Equilibria, 2007. **257**(2): p. 217-222.
73. Shimoyama, Y., et al., *Measurement and correlation of vapor–liquid equilibria for ethanol+ethyl laurate and ethanol+ethyl myristate systems near critical temperature of ethanol.* Fluid Phase Equilibria, 2008. **264**(1-2): p. 228-234.
74. Shimoyama, Y., et al., *Measurement and calculation of vapor–liquid equilibria for methanol+glycerol and ethanol+glycerol systems at 493–573K.* Fluid Phase Equilibria, 2009. **284**(1): p. 64-69.
75. Srinophakun, T. and B. Phithakchokchai, *Phase equilibrium modeling of triglycerides in supercritical fluids.* The Journal of Chemical Thermodynamics, 2011. **43**(3): p. 471-478.
76. Pinto, L.F., et al., *Phase equilibrium data and thermodynamic modeling of the system (CO2+biodiesel+methanol) at high pressures.* The Journal of Chemical Thermodynamics, 2012. **44**(1): p. 57-65.
77. Pinto, L.F., et al., *Phase equilibrium data of the system CO2+glycerol+methanol at high pressures.* The Journal of Supercritical Fluids, 2011. **59**: p. 1-7.
78. Glisic, S.B. and A.M. Orlovic, *Modelling of non-catalytic biodiesel synthesis under sub and supercritical conditions: The influence of phase distribution.* The Journal of Supercritical Fluids, 2012. **65**: p. 61-70.
79. Benson, S.W., *The foundations of chemical kinetics*. McGraw-Hill series in advanced chemistry 1960 McGraw-Hill.
80. Boundless, *Boundless Chemistry*. The Collision Theory. 2015.
81. Brown, T.L.L., H. Eugene (Harold Eugene), 1940-; Bursten, Bruce Edward, *Chemistry : the central science* 2000: Upper Saddle River, N.J. : Prentice Hall
82. Eldredge, B.A.a.P. *General Chemistry: Principles, Patterns, and Applications*. 2016 25/01/2016].
83. Laidler, K.J., *The development of the Arrhenius equation.* Journal of Chemical Education, 1984. **61**(6): p. 494.
84. Wenzel, B., Tait, M., Modenes, A. and Kroumov, A, *Modelling chemical kinetics of soybean oil transesterification process for biodiesel production: An analysis of molar ratio between alcohol and soybean oil temperature changes on the process conversion rate.* Bioautomation, 2006: p. pp. 13-22. .
85. Varma, M.N. and G. Madras, *Synthesis of Biodiesel from Castor Oil and Linseed Oil in Supercritical Fluids.* Industrial & Engineering Chemistry Research, 2007. **46**(1): p. 1-6.

86. Diasakou, M., A. Louloudi, and N. Papayannakos, *Kinetics of the non-catalytic transesterification of soybean oil.* Fuel, 1998. **77**(12): p. 1297-1302.
87. Kusdiana, D. and S. Saka, *Kinetics of transesterification in rapeseed oil to biodiesel fuel as treated in supercritical methanol.* Fuel, 2001. **80**(5): p. 693-698.
88. Glisic, S.B. and A.M. Orlović, *Review of biodiesel synthesis from waste oil under elevated pressure and temperature: Phase equilibrium, reaction kinetics, process design and techno-economic study.* Renewable and Sustainable Energy Reviews, 2014. **31**: p. 708-725.
89. Dasari, M.A., M.J. Goff, and G.J. Suppes, J. Am. Oil Chem. Soc., 2003. **80**(2): p. 189.
90. Pinnarat, T. and P.E. Savage, *Assessment of Noncatalytic Biodiesel Synthesis Using Supercritical Reaction Conditions.* Industrial & Engineering Chemistry Research, 2008. **47**(18): p. 6801-6808.
91. Warabi, Y., D. Kusdiana, and S. Saka, *Reactivity of triglycerides and fatty acids of rapeseed oil in supercritical alcohols.* Bioresource Technology, 2004. **91**(3): p. 283-287.
92. Kusdiana, D. and S. Saka, Fuel, 2001. **80**: p. 225.
93. Bunyakiat, K., et al., *Continuous Production of Biodiesel via Transesterification from Vegetable Oils in Supercritical Methanol.* Energy & Fuels, 2006. **20**(2): p. 812-817.
94. Cao, W., H. Han, and J. Zhang, *Preparation of biodiesel from soybean oil using supercritical methanol and co-solvent.* Fuel, 2005. **84**(4): p. 347-351.
95. Han, H., W. Cao, and J. Zhang, *Preparation of biodiesel from soybean oil using supercritical methanol and CO2 as co-solvent.* Process Biochemistry, 2005. **40**(9): p. 3148-3151.
96. Sawangkeaw, S.N.a.R., *Transesterification in Supercritical Conditions*, in *Biodiesel - Feedstocks and Processing Technologies*, D.M. Stoytcheva, Editor. 2011.
97. Busto, M., et al., Energy Fuels, 2006. **20**: p. 2642.
98. Koh, A.D.A., *PhD thesis: Two-step biodiesel production using supercritical methanol and ethanol.* 2011.
99. Minami, E. and S. Saka, *Kinetics of hydrolysis and methyl esterification for biodiesel production in two-step supercritical methanol process.* Fuel, 2006. **85**(17-18): p. 2479-2483.
100. Alenezi, R., et al., *Esterification kinetics of free fatty acids with supercritical methanol for biodiesel production.* Energy Conversion and Management, 2010. **51**(5): p. 1055-1059.
101. Alenezi, R., et al., *Hydrolysis kinetics of sunflower oil under subcritical water conditions.* Chemical Engineering Research and Design, 2009. **87**(6): p. 867-873.
102. Peng, D.Y. and D.B. Robinson, *A New Two-Constant Equation of State.* Ind. Eng. Chem. Fundam., 1976. **15**: p. 59-64.
103. Redlich, O. and J.N.S. Kwong, *On the Thermodynamics of Solutions. V. An Equation of State. Fugacities of Gaseous Solutions.* Chemical Reviews, 1949. **44**(1): p. 233-244.
104. Pitzer, K.S., et al., *The Volumetric and Thermodynamic Properties of Fluids. II. Compressibility Factor, Vapor Pressure and Entropy of Vaporization1.* Journal of the American Chemical Society, 1955. **77**(13): p. 3433-3440.
105. Lopez-Echeverry, J.S., S. Reif-Acherman, and E. Araujo-Lopez, *Peng-Robinson equation of state: 40 years through cubics.* Fluid Phase Equilibria, 2017. **447**: p. 39-71.
106. Shibata, S.K. and S.I. Sandler, *Critical evaluation of equation of state mixing rules for the prediction of high-pressure phase equilibria.* Industrial & Engineering Chemistry Research, 1989. **28**(12): p. 1893-1898.
107. Hansen, J.-P. and I.R. McDonald, *Chapter 5 - Perturbation Theory*, in *Theory of Simple Liquids (Third Edition)*, J.-P. Hansen and I.R. McDonald, Editors. 2006, Academic Press: Burlington. p. 109-146.
108. Zhou, S. and J.R. Solana, *Progress in the Perturbation Approach in Fluid and Fluid-Related Theories.* Chemical Reviews, 2009. **109**(6): p. 2829-2858.

109. S. Wertheim, M., *Thermodynamic Perturbation Theory of Polymerization*. Vol. 87. 1987. 7323-7331.
110. S. Wertheim, M., *Fluids with Highly Directional Attractive Forces. IV. Equilibrium Polymerization*. Vol. 42. 1986. 477-492.
111. Wertheim, M.S., *Fluids with highly directional attractive forces. II. Thermodynamic perturbation theory and integral equations.* Journal of Statistical Physics, 1984. **35**(1): p. 35-47.
112. S. Wertheim, M., *Fluids with highly directional attractive forces. I. Statistical thermodynamics*. Vol. 35. 1984. 19-34.
113. S. Wertheim, M., *Fluids of Dimerizing Hard Spheres, and Fluid Mixtures of Hard Spheres and Dispheres*. Vol. 85. 1986. 2929-2936.
114. Gubbins, K.E., *Perturbation theories of the thermodynamics of polar and associating liquids: A historical perspective.* Fluid Phase Equilibria, 2016. **416**: p. 3-17.
115. Chapman, W.G., et al., *SAFT: Equation-of-state solution model for associating fluids.* Fluid Phase Equilibria, 1989. **52**: p. 31-38.
116. Chapman, W.G., et al, *New reference equation of state for associating liquids.* Ind. Eng. Chem. Res., 1990. **29(8)**: p. 1709-1721.
117. Kraska, T. and K.E. Gubbins, *Phase Equilibria Calculations with a Modified SAFT Equation of State. 2. Binary Mixtures of n-Alkanes, 1-Alkanols, and Water.* Industrial & Engineering Chemistry Research, 1996. **35**(12): p. 4738-4746.
118. Kraska, T. and K.E. Gubbins, *Phase Equilibria Calculations with a Modified SAFT Equation of State. 1. Pure Alkanes, Alkanols, and Water.* Industrial & Engineering Chemistry Research, 1996. **35**(12): p. 4727-4737.
119. Mueller, E.A. and K.E. Gubbins, *An Equation of State for Water from a Simplified Intermolecular Potential.* Industrial & Engineering Chemistry Research, 1995. **34**(10): p. 3662-3673.
120. Huang, S.H. and M. Radosz, *Equation of state for small, large, polydisperse, and associating molecules.* Industrial & Engineering Chemistry Research, 1990. **29**(11): p. 2284-2294.
121. Galindo, A., A. Davies, and A. Gil-Villegas, *The Thermodynamics of Mixtures and the Corresponding Mixing Rules in the SAFT-VR Approach for Potentials of Variable Range*. Vol. 93. 1998. 241-252.
122. Gil-Villegas, A., et al., *Statistical Associating Fluid Theory for Chain Molecules with Attractive Potentials of Variable Range*. Vol. 106. 1997. 4168-4186.
123. Blas, F.J. and L.F. Vega, *Prediction of Binary and Ternary Diagrams Using the Statistical Associating Fluid Theory (SAFT) Equation of State.* Industrial & Engineering Chemistry Research, 1998. **37**(2): p. 660-674.
124. Blas, F. and L. Vega, *Critical Behavior and Partial Miscibility Phenomena in Binary Mixtures of Hydrocarbons by the Statistical Associating Fluid Theory*. Vol. 109. 1998. 7405-7413.
125. Gross, J. and G. Sadowski, *Perturbed-Chain SAFT: An Equation of State Based on a Perturbation Theory for Chain Molecules.* Industrial & Engineering Chemistry Research, 2001. **40**(4): p. 1244-1260.
126. Gross, J. and G. Sadowski, *Modeling Polymer Systems Using the Perturbed-Chain Statistical Associating Fluid Theory Equation of State.* Industrial & Engineering Chemistry Research, 2002. **41**(5): p. 1084-1093.
127. A. Barker, J. and D. Henderson, *Perturbation Theory and Equation of State for Fluids: The Square-Well Potential*. Vol. 47. 1967. 2856-2861.
128. A. Barker, J. and H. D. J, *Perturbation Theory and Equation of State for Fluids. II. A Successful Theory of Liquids*. Vol. 47. 1967. 4714-4721.
129. Skjold-Joergensen, S., *Group contribution equation of state (GC-EOS): a predictive method for phase equilibrium computations over wide ranges of temperature and pressures up to 30 MPa.* Industrial & Engineering Chemistry Research, 1988. **27**(1): p. 110-118.

130. A. Fredenslund, J.G., and P. Rasmussen: , *Vapor-Liquid equilibria using UNIFAC - a group-contribution method*. Vol. 82. 1977: Isevier Scientific Publishing Company.
131. Fredenslund, A., L. Jones Russell, and M. Prausnitz John, *Group-contribution estimation of activity coefficients in nonideal liquid mixtures.* AIChE Journal, 2004. **21**(6): p. 1086-1099.
132. Lymperiadis, A., et al., *A heteronuclear group contribution method for associating chain molecules (SAFT-γ)*. Vol. 25. 2008.
133. Lymperiadis, A., et al., *A group contribution method for associating chain molecules based on the statistical associating fluid theory (SAFT-gamma).* J Chem Phys, 2007. **127**(23): p. 234903.
134. Lymperiadis, A., et al., *A Generalisation of the SAFT-Gamma Group Contribution Method for Groups Comprising Multiple Spherical Segments*. Vol. 274. 2008. 85-104.
135. Papaioannou, V., et al., *Group contribution methodology based on the statistical associating fluid theory for heteronuclear molecules formed from Mie segments.* J Chem Phys, 2014. **140**(5): p. 054107.
136. Müller, E.A. and K.E. Gubbins, *Molecular-Based Equations of State for Associating Fluids: A Review of SAFT and Related Approaches.* Industrial & Engineering Chemistry Research, 2001. **40**(10): p. 2193-2211.
137. McCabe, C. and A. Galindo, *Chapter 8 SAFT Associating Fluids and Fluid Mixtures*, in *Applied Thermodynamics of Fluids*. 2010, The Royal Society of Chemistry. p. 215-279.
138. Chapman, W.G., et al., *SAFT: Equation-of-state solution model for associating fluids.* Fluid Phase Equilibria, 1989. **52**(Supplement C): p. 31-38.
139. Papaioannou, V., et al., *Group Contribution Methodologies for the Prediction of Thermodynamic Properties and Phase Behavior in Mixtures*, in *Process Systems Engineering*. 2011, Wiley-VCH Verlag GmbH & Co. KGaA. p. 135-172.
140. Lockemann, C.A., *High-pressure phase equilibria and densities of the binary mixtures carbon dioxide—oleic acid, carbon dioxide—methyl myristate, and carbon dioxide—methyl palmitate and of the ternary mixture carbon dioxide—methyl myristate—methyl palmitate.* Chemical Engineering and Processing: Process Intensification, 1994. **33**(3): p. 171-187.
141. Zou, M., et al., *Fluid-Liquid phase equilibria of fatty acids and fatty acid methyl esters in supercritical carbon dioxide.* The Journal of Supercritical Fluids, 1990. **3**(1): p. 23-28.
142. Yu, Z.-R., S.S.H. Rizvi, and J.A. Zollweg, *Phase equilibria of oleic acid, methyl oleate, and anhydrous milk fat in supercritical carbon dioxide.* The Journal of Supercritical Fluids, 1992. **5**(2): p. 114-122.
143. Hong, S.-A., et al., *Phase equilibria of palm oil, palm kernel oil, and oleic acid+supercritical carbon dioxide and modeling using Peng–Robinson EOS.* Journal of Industrial and Engineering Chemistry, 2010. **16**(5): p. 859-865.
144. Schwarz, C.E. and J.H. Knoetze, *Phase equilibrium measurements of long chain acids in supercritical carbon dioxide.* The Journal of Supercritical Fluids, 2012. **66**: p. 36-48.
145. Bharath, R., et al., *Phase equilibrium study for the separation and fractionation of fatty oil components using supercritical carbon dioxide.* Fluid Phase Equilibria, 1992. **81**: p. 307-320.
146. Garlapati, C. and G. Madras, *Solubilities of palmitic and stearic fatty acids in supercritical carbon dioxide.* The Journal of Chemical Thermodynamics, 2010. **42**(2): p. 193-197.
147. Iwai, Y., et al., *Solubilities of myristic acid, palmitic acid, and cetyl alcohol in supercritical carbon dioxide at 35.degree.C.* Journal of Chemical & Engineering Data, 1991. **36**(4): p. 430-432.
148. Adrian, T. and G. Maurer, *Solubility of Carbon Dioxide in Acetone and Propionic Acid at Temperatures between 298 K and 333 K.* Journal of Chemical & Engineering Data, 1997. **42**(4): p. 668-672.
149. Maheshwari, P., et al., *Solubility of fatty acids in supercritical carbon dioxide.* Journal of the American Oil Chemists' Society, 1992. **69**(11): p. 1069-1076.

150. Foster, N.R., S.L.J. Yun, and S.S.T. Ting, *Solubility of oleic acid in supercritical carbon dioxide.* The Journal of Supercritical Fluids, 1991. **4**(2): p. 127-130.
151. Yin, J.-Z., M. Xiao, and J.-B. Song, *Biodiesel from soybean oil in supercritical methanol with co-solvent.* Energy Conversion and Management, 2008. **49**(5): p. 908-912.
152. Imahara, H., J. Xin, and S. Saka, *Effect of CO2/N2 addition to supercritical methanol on reactivities and fuel qualities in biodiesel production.* Fuel, 2009. **88**(7): p. 1329-1332.
153. Sapkale, G.N., et al., *Supercritical fluid extraction - a review*. Vol. 8. 2010. 729-743.
154. Royon, D., et al., *Enzymatic production of biodiesel from cotton seed oil using t-butanol as a solvent.* Bioresource Technology, 2007. **98**(3): p. 648-653.
155. Kim, J.-S., J.-H. Yoon, and H. Lee, *High-pressure phase equilibria for carbon dioxide-2-methyl-2-propanol and carbon dioxide-2-methyl-2-propanol—water: Measurement and prediction.* Fluid Phase Equilibria, 1994. **101**: p. 237-245.
156. Sadeqzadeh, M., et al., *The development of unlike induced association-site models to study the phase behaviour of aqueous mixtures comprising acetone, alkanes and alkyl carboxylic acids with the SAFT-γ Mie group contribution methodology.* Fluid Phase Equilibria, 2016. **407**: p. 39-57.
157. Papaioannou, V., et al., *Application of the SAFT-γ Mie group contribution equation of state to fluids of relevance to the oil and gas industry.* Fluid Phase Equilibria, 2016. **416**(Special Issue): p. 104-119.
158. Forte, E., A. Galindo, and J.P.M. Trusler, *Experimental and molecular modelling study of the three-phase behaviour of (propane+carbon dioxide+water) at reservoir conditions.* The Journal of Supercritical Fluids, 2013. **75**: p. 30-42.
159. Al Ghafri, S.Z.S., et al., *Experimental and Modeling Study of the Phase Behavior of (Methane + CO_2 + Water) Mixtures.* The Journal of Physical Chemistry B, 2014. **118**(49): p. 14461-14478.
160. Al Ghafri, S.Z., et al., *Experimental and modeling study of the phase behavior of (methane + CO2 + water) mixtures.* J Phys Chem B, 2014. **118**(49): p. 14461-14478.
161. Forte, E., A. Galindo, and J.P.M. Trusler, *Experimental and Molecular Modeling Study of the Three-Phase Behavior of (n-Decane + Carbon Dioxide + Water) at Reservoir Conditions.* The Journal of Physical Chemistry B, 2011. **115**(49): p. 14591-14609.
162. Span, R. and W. Wagner, *A New Equation of State for Carbon Dioxide Covering the Fluid Region from the Triple-Point Temperature to 1100 K at Pressures Up to 800 MPa*. 1996.
163. Egorov, G.I., D.M. Makarov, and A.M. Kolker, *Liquid phase PVTx properties of (water+tert-butanol) binary mixtures at temperatures from 278.15 to 323.15K and pressures from 0.1 to 100MPa: I. Experimental results, excess and partial molar volumes.* The Journal of Chemical Thermodynamics, 2013. **61**: p. 161-168.
164. Blanco Marigorta, A.M., *Analysis of the liquid-vapor equilibrium at 141.3 kPa of binary mixtures containing methanol with n-alkanes (C5, C6) and alkyl esters* Universidad de Las Palmas de Gran Canaria, 1997.
165. Freire, S., et al., *Physical properties of (propyl propanoate+hexane+toluene) at 298.15K.* The Journal of Chemical Thermodynamics, 2007. **39**(4): p. 621-626.
166. Saleh, M.A., et al., *Excess Molar Volumes of Aqueous Solutions of 1-Propanol, 2-Propanol, Allyl Alcohol and Propargyl Alcohol.* Physics and Chemistry of Liquids, 1998. **36**(1): p. 53-65.
167. Tay, W.J., *Thermophysical Properties of Hydrocarbons with Dissolved Carbon Dioxide*, in *Department of Chemical Engineering*. 2017, Imperial College London: Imperial College London.
168. *Evaluation of measurement data-Guide to the expression of uncertainty in measurement.* JCGM 100:2008; Joint Committee for Guides in Metrology, BIPM: Sèvres, France 2008.

169. Al Ghafri, S.Z.S., et al., *Experimental and Modeling Study of the Phase Behavior of (Heptane + Carbon Dioxide + Water) Mixtures.* Journal of Chemical & Engineering Data, 2015. **60**(12): p. 3670-3681.
170. Hongling, L., et al., *Vapor−Liquid Equilibrium Data of (Carbon Dioxide + Methyl Propionate) and (Carbon Dioxide + Propyl Propionate) at Pressures from (1.00 to 12.00) MPa and Temperatures from (313.0 to 373.0) K.* Journal of Chemical & Engineering Data, 2009. **54**(5): p. 1510-1517.
171. Wagner, Z., *Vapour-liquid equilibrium in the carbon dioxide ‧ ethyl propanoate system at pressures from 2 to 9 MPa and temperatures from 303 to 323 K*. Vol. 112. 1995. 125-129.
172. Tian, Y.-L., et al., *Vapor−Liquid Equilibria of the Carbon Dioxide + Ethyl Propanoate and Carbon Dioxide + Ethyl Acetate Systems at Pressure from 2.96 MPa to 11.79 MPa and Temperature from 313 K to 393 K*. Vol. 49. 2004.
173. Feng, L.-C., et al., *Vapor–liquid equilibria of carbon dioxide with ethyl benzoate, diethyl succinate and isoamyl acetate binary mixtures at elevated pressures*. Vol. 21. 2001. 111-121.
174. Hongling, L., et al., *Vapor−Liquid Equilibrium Data of the Carbon Dioxide + Ethyl Butyrate and Carbon Dioxide + Propylene Carbonate Systems at Pressures from (1.00 to 13.00) MPa and Temperatures from (313.0 to 373.0) K*. Vol. 56. 2011. 1148–1157.
175. Kleiner, M. and G. Sadowski, *Modeling of Polar Systems Using PCP-SAFT: An Approach to Account for Induced-Association Interactions.* The Journal of Physical Chemistry C, 2007. **111**(43): p. 15544-15553.
176. Timmermans, J.H.-R., *Travaux du bureau international d'etalons physico-chimiques.* J. Chim. Phys. Phys. Chim. Biol., 1959: p. 984-1023.
177. Krammer, P. and H. Vogel, Supercrit. Fuids., 2000. **16**: p. 189.
178. Mathews, J.H., *The accurate measurement of the heats of vaporization of liquids.* J. Am. Chem. Soc., 1926. **48**: p. 562-576.
179. Khimenko, M.T.Z., V.P.;Kapushina,S.A., *Estimation of polarizability and dipole moments of the molecules of some liquid esters.* Zh. Fiz. Khim., 1989. **63**(5).
180. Ihmels, E.C., *Entwicklung computergesteuerter Messapparaturen fuer druck- und temperaturabhaengige Dichten mit einem Biegeschwinger-Prototyp und fuer temperaturunabhaengige Viskositaeten mit einem Ubbelohde-Kapillarviskosimeter.* Master's Thesis, 1998: p. 1-120.
181. Costa, H.F.G., R.L.;Johnson,I.;Fonseca,I.M.A.;Ferreira,A.G.M., *PVT Property Measurements for Ethyl Propionate, Ethyl Butyrate, and Ethyl Pentanoate Esters from 298 to 393 K and up to 35 MPa.* J. Chem. Eng. Data, 2009. **54**(2): p. 256-262.
182. Westman, S.F., et al., *Vapor–liquid equilibrium data for the carbon dioxide and nitrogen (CO2 + N2) system at the temperatures 223, 270, 298 and 303 K and pressures up to 18 MPa.* Fluid Phase Equilibria, 2016. **409**: p. 207-241.
183. Lachet, V., et al., *Thermodynamic behavior of the CO2+SO2 mixture: Experimental and Monte Carlo simulation studies.* Energy Procedia, 2009. **1**(1): p. 1641-1647.
184. Philippe Ungerer, B.T., Anne Boutin, *Applications of Molecular Simulation in the Oil and Gas Industry - Monte-Carlo Methods*. Technip, Paris, France ed. 2005.
185. Byun, H.-S., K. Kim, and M.A. McHugh, *Phase Behavior and Modeling of Supercritical Carbon Dioxide−Organic Acid Mixtures.* Industrial & Engineering Chemistry Research, 2000. **39**(12): p. 4580-4587.
186. Bharath, R., et al., *Phase equilibria of supercritical CO2 - fatty oil component binary systems.* Fluid Phase Equilibria, 1993. **83**: p. 183-192.
187. Poehler, H., *Fluid phase equilibria of binary and ternary mixtures of carbon dioxide with low volatile organic substances at temperatures from 303 K to 393 K and pressures from10 MPa to 100 MPa*. 1994, Ruhr-University Bochum: Ruhr-University Bochum. p. 1-179.
188. Schmidt, G.C., *Investigations on the vapor pressures of homologous compounds. I. The vapor tension of the homologous series of fatty acids.* Z. Phys. Chem. Stoechiom. Verwandtschaftsl., 1891. **7**: p. 433-467.

189. Richardson, A., *Determinations of Vapor-pressures of Alcohols and Organic Acids, and the Relations existing between the Vapor-pressures of the Alcohols and Organic Acids.* Journal of the Chemical Society 1886. **49**: p. 761-776.
190. Ambrose, D., et al., *Thermodynamic properties of organic oxygen compounds LI. The vapour pressures of some esters and fatty acids.* The Journal of Chemical Thermodynamics, 1981. **13**(8): p. 795-802.
191. Kahlbaum, G.W.A. and P. Schroeter, *Studies on vapor tension measurements. I. Section.* Monograph, 1893: p. 1-315.
192. Kahlbaum, G.W.A. and C.G. von Wirkner, *Studies on vapor stress measurements. 2nd section 1st part* Monograph, 1897. **2a**: p. 1-222.
193. Dreisbach, R.R. and S.A. Shrader, *Vapor Pressure–Temperature Data on Some Organic Compounds.* Industrial & Engineering Chemistry, 1949. **41**(12): p. 2879-2880.
194. Ambrose, D. and N.B. Ghiassee, *Vapour pressures and critical temperatures and critical pressures of some alkanoic acids: C1 to C10.* The Journal of Chemical Thermodynamics, 1987. **19**(5): p. 505-519.
195. Verevkin, S.P., *Measurement and Prediction of the Monocarboxylic Acids Thermochemical Properties.* Journal of Chemical & Engineering Data, 2000. **45**(5): p. 953-960.
196. Jantzen, E. and W. Erdmann, *The boiling points of fatty acids.* Fette Seifen Anstrichmittel 1952. **54**(4): p. 197-201.
197. Matricarde Falleiro, R.M., et al., *Vapor pressure data for fatty acids obtained using an adaptation of the DSC technique.* Thermochimica Acta, 2012. **547**: p. 6-12.
198. Krafft, F. and H. Noerdlinger, *On some boiling points in the oxalic acid and the oleic acid series.* Berichte der Deutschen Chemischen Gesellschaft, 1889. **22**: p. 816-820.
199. Spizzichino, C., *Contribution a l'Etude des Tensions de Vapeur et des Chaleurs de Vaporisation des Acides Gras, Esters Methyliques et Alcools Gras a des Pressions Inferieures A 1 mm de Mercure.* CNRS Le journal 1956. **34**: p. 1-24.
200. de Kruif, C.G., et al., *Thermodynamic properties of the normal alkanoic acids. III. Enthalpies of vaporization and vapor pressures of 13 normal alkanoic acids.* The Journal of Chemical Thermodynamics, 1982. **14**: p. 791-798.
201. Faust, O., *The internal Friction of liquid Mixtures, its Dependence on Temperature and the Relationship between the internal Friction of Liquids and their Vapor Pressure.* Z. Phys. Chem. Stoechiom. Verwandtschaftsl., 1912. **79**: p. 97-123.
202. Howard, K.S. and F.P. Pike, *Viscosities and Densities of Acetone - Benzene and Acetone - Acetic Acid Systems up to Their Normal Boiling Points.* Journal of Chemical Engineering Data, 1959. **4**: p. 331-333.
203. Hunten, K.W. and O. Maass, *Investigation of surface tension constants in an homologous series from the point of view of surface orientation.* Journal of American Chemical Society, 1929. **51**: p. 153-165.
204. von Hirsch, R.F., *Determination of density of saturated vapors and liquids.* Annals of Physics, 1899. **305**: p. 456-478.
205. Hales, J.L., H.A. Gundry, and J.H. Ellender, *Liquid densities from 288 to 490 K of four organic oxygen compounds.* The Journal of Chemical Thermodynamics, 1983. **15**(3): p. 211-215.
206. Liessmann, G., W. Schmidt, and S. Reiffarth, *Recommended Thermophysical Data.* Data compilation of the Saechsische Olefinwerke Boehlen Germany, 1995: p. 1.
207. Vogel, A.I., *Physical properties and chemical constitution. Part XX. Aliphatic alcohols and acids.* Journal of Chemical Society 1948: p. 1814-1819.
208. Costello, J.M. and S.T. Bowden, *The temperature variation of orthobaric density difference in liquid-vapour systems. III. Alcohols.* Recueil des Travaux Chimiques des Pays-Bas 1958. **77**: p. 803-810.
209. Albert, O., *Viscosity measurements on homologues ester series with special consideration of the relationship of Thorpe and Roger.* Zeitschrift für Physikalische Chemie A, 1938. **182**: p. 421-429.

210. Noureddini, H.T., B.C.; Clements, L.D., *Densities of Vegetable Oils and Fatty Acids.* Journal of the American Oil Chemists' Society, 1992. **69**(12): p. 1184-1188.
211. Keffler, L.J.P. and J.H. MacLean, *Homology in Long-chain Compounds - Oleic Acid and the n-Alkyl Oleates.* Journal of the Society of Chemical Industry London Transactions and Communications 1935. **54**: p. 178-185.
212. Berchiesi, G., M.A. Berchiesi, and G. Gioia-Lobbia, *Density and viscosity in the binary system octadecanoic acid-hexanedioic acid.* Journal of Chemical & Engineering Data, 1981. **26**(1): p. 20-22.
213. Andereya, E. and J.D. Chase, *The implications of carboxylic acid properties.* Chemical Engineering & Technology 1990. **13**: p. 304-312.
214. Hsieh, C.-T., M.-J. Lee, and H.-m. Lin, *Multiphase Equilibria for Mixtures Containing Acetic Acid, Water, Propylene Glycol Monomethyl Ether, and Propylene Glycol Methyl Ether Acetate.* Industrial & Engineering Chemistry Research, 2006. **45**(6): p. 2123-2130.
215. Fu, H., et al., *Vapor Liquid Equilibria of Formic Acid - Acetic Acid - Methyl Acetate Ternary System.* Zhejiang Daxue Xuebao 1987. **21**: p. 52-62.
216. Sawistowski, H. and P.A. Pilavakis, *Vapor-liquid equilibrium with association in both phases. Multicomponent systems containing acetic acid.* Journal of Chemical & Engineering Data, 1982. **27**(1): p. 64-71.
217. Kruus, P. and C.A. Hayes, *Solubility of carbon dioxide in water–t-butanol solutions.* Canadian Journal of Chemistry, 1985. **63**(12): p. 3403-3410.
218. Kim, E., et al., *Enclathration of tert-butyl alcohol in sII hydrates and its implications in gas storage and CO2 sequestration.* Fuel, 2016. **164**: p. 237-244.
219. Sima, S., et al., *New high-pressures vapor-liquid equilibrium data for the carbon dioxide + 2-methyl-2-propanol binary system.* Central European Journal of Chemistry, 2014. **12**(9): p. 893-900.
220. Edwards, D., et al., *Activités thermodynamiques d'alcools aliphatiques dans l'eau et le liquide de Rinqer.* J. Chim. Phys., 1966. **63**: p. 239-241.
221. Xu, X. and M.J. Antal, *Kinetics and mechanism of isobutene formation from T-butanol in hot liquid water.* AIChE Journal, 1994. **40**(9): p. 1524-1534.
222. Bothe, D., A. Steinkemper, and H.-J. Warnecke, *Modeling the Dehydration of tert-Butyl Alcohol and Avoidance of the Formation of Oligomers.* Industrial & Engineering Chemistry Research, 2006. **45**(9): p. 2986-2993.
223. Honkela, M.L., T. Ouni, and A.O.I. Krause, *Thermodynamics and Kinetics of the Dehydration of tert-Butyl Alcohol.* Industrial & Engineering Chemistry Research, 2004. **43**(15): p. 4060-4065.
224. Grana, R., et al., *An experimental and kinetic modeling study of combustion of isomers of butanol.* Combustion and Flame, 2010. **157**(11): p. 2137-2154.
225. Dufal, S., et al., *Developing intermolecular-potential models for use with the SAFT-VRMie equation of state.* AIChE journal, 2015. **61**(9): p. 2891-2912.
226. Biddiscombe, D.P., et al., *364. Thermodynamic properties of organic oxygen compounds. Part VIII. Purification and vapour pressures of the propyl and butyl alcohols.* Journal of the Chemical Society (Resumed), 1963(0): p. 1954-1957.
227. Krone, L.H.J., R.C., *Thermodynamic properties of tertiary butyl alcohol.* AIChE J., 1956. **2**(4): p. 552-554.
228. Sachek, A.I.P., A.D.; Markovnik, V.S.; Ralko, O.V.; Andreevskii, D.N.; Leonteva, A.A., *Temperature dependence of the vapor pressure of butanols.* Termodinam. Organ. Soedin., 1982: p. 94-98.
229. Kipkemboi, P.K. and A.J. Easteal, *Densities and viscosities of binary aqueous mixtures of nonelectrolytes: tert -Butyl alcohol and tert -butylamine.* Canadian Journal of Chemistry, 1994. **72**(9): p. 1937-1945.
230. Kenttaemaa, J.T., E.; Martti, M., *Some Thermodynamic Properties of the System tert-Butanol and Water.* Suom. Tiedeakat. Toim. Sar. A2, 1953. **93**: p. 1-20.

231. Fischer, K. and J. Gmehling, *P-x and .gamma..infin. Data for the Different Binary Butanol-Water Systems at 50.degree.C.* Journal of Chemical & Engineering Data, 1994. **39**(2): p. 309-315.
232. Lay, E.N., *Measurement and Correlation of Bubble Point Pressure in (CO2 + C6H6), (CO2 + CH3C6H5), (CO2 + C6H14), and (CO2 + C7H16) at Temperatures from (293.15 to 313.15) K.* Journal of Chemical & Engineering Data, 2010. **55**(1): p. 223-227.
233. Lay, E.N., V. Taghikhani, and C. Ghotbi, *Measurement and Correlation of CO2 Solubility in the Systems of CO2 + Toluene, CO2 + Benzene, and CO2 + n-Hexane at Near-Critical and Supercritical Conditions.* Journal of Chemical & Engineering Data, 2006. **51**(6): p. 2197-2200.
234. Tochigi, K., et al., *Vapor−Liquid Equilibria for the Carbon Dioxide + Pentane and Carbon Dioxide + Toluene Systems.* Journal of Chemical & Engineering Data, 1998. **43**(6): p. 954-956.
235. Wu, W., J. Ke, and M. Poliakoff, *Phase Boundaries of CO2 + Toluene, CO2 + Acetone, and CO2 + Ethanol at High Temperatures and High Pressures.* Journal of Chemical & Engineering Data, 2006. **51**(4): p. 1398-1403.
236. Ng, H.-J. and D.B. Robinson, *Equilibrium-phase properties of the toluene-carbon dioxide system.* Journal of Chemical & Engineering Data, 1978. **23**(4): p. 325-327.
237. Sebastian, H.M., et al., *Gas-liquid equilibrium in mixtures of carbon dioxide + toluene and carbon dioxide + m-xylene.* Journal of Chemical & Engineering Data, 1980. **25**(3): p. 246-248.
238. Morris, W.O. and M.D. Donohue, *Vapor-liquid equilibria in mixtures containing carbon dioxide, toluene, and 1-methylnaphthalene.* Journal of Chemical & Engineering Data, 1985. **30**(3): p. 259-263.
239. Chang, C.J., *The solubility of carbon dioxide in organic solvents at elevated pressures.* Fluid Phase Equilibria, 1992. **74**: p. 235-242.
240. Muhlbauer, A.L. and J.D. Raal, *Measurement and thermodynamic interpretation of high-pressure vapour—liquid equilibria in the toluene · CO2 system.* Fluid Phase Equilibria, 1991. **64**: p. 213-236.
241. Pfohl, O., P. Avramova, and G. Brunner, *Two- and three-phase equilibria in systems containing benzene derivatives, carbon dioxide, and water at 373.15 K and 10–30 MPa.* Fluid Phase Equilibria, 1997. **141**(1): p. 179-206.
242. Al Ghafri, S.Z.S., G.C. Maitland, and J.P.M. Trusler, *Phase Behavior of the System (Carbon Dioxide + n-Heptane + Methylbenzene): A Comparison between Experimental Data and SAFT-γ-Mie Predictions.* Journal of Chemical & Engineering Data, 2017. **62**(9): p. 2826-2836.
243. Müller, G., *Experimental Study of the Vapor-Liquid Equilibrium in the System Ammonia - Carbon Dioxide - Water from 100 to 200 °C at Pressures up to 90 bar*. 1983, University of Kaiserslautern, Germany p. 1-174.
244. Toedheide, K. and E.U. Franck, *The Two-Phase Region and the Critical Curve in the System Carbon Dioxide - Water up to Pressures of 350 bar* International journal of research in physical chemistry & chemical physics. , 1963. **37**: p. 387-401.
245. Patel, M.R., et al., *Thermophysical properties of gaseous carbon dioxidewater mixtures.* Fluid Phase Equilibria, 1987. **36**: p. 279-299.
246. Teng, H., et al., *Solubility of liquid CO2in water at temperatures from 278 K to 293 K and pressures from 6.44 MPa to 29.49 MPa and densities of the corresponding aqueous solutions.* The Journal of Chemical Thermodynamics, 1997. **29**(11): p. 1301-1310.
247. Brandt, E., et al., *Phase behaviour of carbon dioxide–benzene–water ternary mixtures at high pressures and temperatures up to 300 MPa and 600 K.* Physical Chemistry Chemical Physics, 2000. **2**(18): p. 4157-4164.
248. Chen, D., et al., *High pressure vapor-liquid equilibrium of carbon dioxide and reformed naphtha* Journal of Chemical Industry and Engineering (China) 2010. **61**(4): p. 805-811.

249. Tochigi, K., et al., *Vapor-Liquid Equilibria for the Carbon Dioxide + Pentene and Carbon Dioxide + Toluene Systems* The Journal of Chemical & Engineering Data 1998. **43**: p. 954-956.
250. Zirrahi, M., et al., *Measuring and Modeling the Solubility and Density for CO2-Toluene and C2H6-Toluene Systems.* The Journal of Chemical & Engineering Data 2015. **60**(6): p. 1592-1599.
251. Ziegler, J.W., et al., *Estimation of Liquid-Vapor Critical Loci for CO&sub2; - Solvent Mixtures Using a Peak-Shape Method* Analytical Chemistry 1995. **67**: p. 456-461.
252. Dulitskaya, K.A., *Vapor Pressure of some Binary Systems. Report I. .* Russian Journal of General Chemistry 1945. **15**(1-2): p. 9-21.
253. Oliveira, M.B., et al., *Phase equilibria of glycerol containing systems and their description with the Cubic-plus-association (CPA) Equation of State.* Fluid Phase Equilibria 2009. **280**(1-2): p. 22-29.
254. Barreau, A., et al., *Measurements of Liquid-Liquid Equilibria for a Methanol + Glycerol + Methyl Oleate System and Prediction Using Group Contribution Statistical Associating Fluid Theory.* Industrial & Engineering Chemistry Research, 2010. **49**(12): p. 5800-5807.
255. Veneral, J.G., et al., *Thermophysical properties of biodiesel and related systems. Part I. Vapor-liquid equilibrium at low pressures of binary and ternary systems involving methanol, ethanol, glycerol, water and NaCl.* The Journal of Chemical Thermodynamics 2013. **58**: p. 398-404.
256. Macarron, A., *Determination of the Diagrams of Vapor-Liquid Equilibria in Binary Systems with Chemical Reaction.* Matemáticas, of the Review of the Royal Academy of Exact, Physical and Natural Sciences 1959. **53**: p. 607-624.
257. Gao, D., et al., *Isobaric Vapor−Liquid Equilibria for Binary and Ternary Mixtures of Methanol, Ethanoic Acid, and Propanoic Acid.* Journal of Chemical & Engineering Data, 2010. **55**(9): p. 4002-4009.
258. Gao, D., et al., *Computation of Isobaric Vapor-Liquid Equilibrium Data for Binary and Ternary Mixtures of Methanol, Water, and Ethanoic Acid from , , , and Measurements.* Journal of Thermodynamics, 2012. **2012**: p. 13.
259. Shang, Q., et al., *Measurement and correlation of ternary vapor-liquid equilibria for methanol + glycerol + fatty acid methyl ester (methyl laurate, methyl myristate, methyl palmitate) systems at elevated temperatures and pressures.* Fluid Phase Equilibria, 2016. **425**: p. 15-20.
260. Oliveira, M.B., et al., *Phase Equilibria of Ester + Alcohol Systems and Their Description with the Cubic-Plus-Association Equation of State.* Industrial & Engineering Chemistry Research, 2010. **49**(7): p. 3452-3458.
261. Eduljee, G.H. and A.P. Boyes, *Excess Gibbs energy for eight oleic acid-solvent and triolein-solvent mixtures at 318.15 K.* Journal of Chemical & Engineering Data, 1981. **26**(1): p. 55-57.
262. Ohgaki, K., et al., *Phase equilibria for four binary systems containing propylene.* Fluid Phase Equilibria, 1988. **43**(1): p. 105-113.
263. Medina-Gonzalez, Y., et al., *Phase equilibrium of the CO2/glycerol system: Experimental data by in situ FT-IR spectroscopy and thermodynamic modeling.* The Journal of Supercritical Fluids, 2013. **73**: p. 97-107.
264. Sovová, H., J. Jez, and M. Khachaturyan, *Solubility of squalane, dinonyl phthalate and glycerol in supercritical CO2.* Fluid Phase Equilibria, 1997. **137**(1): p. 185-191.
265. West, A.H., D. Posarac, and N. Ellis, *Assessment of four biodiesel production processes using HYSYS.Plant.* Bioresource Technology, 2008. **99**(14): p. 6587-6601.
266. Lee, S., D. Posarac, and N. Ellis, *Process simulation and economic analysis of biodiesel production processes using fresh and waste vegetable oil and supercritical methanol.* Chemical Engineering Research and Design, 2011. **89**(12): p. 2626-2642.
267. Glisic, S. and D. Skala, *The problems in design and detailed analyses of energy consumption for biodiesel synthesis at supercritical conditions.* The Journal of Supercritical Fluids, 2009. **49**(2): p. 293-301.

268. Kusdiana, D. and S. Saka, *Two-step preparation for catalyst-free biodiesel fuel production.* Applied Biochemistry and Biotechnology, 2004. **115**(1): p. 781-791.
269. P Nisworo, A., *Biodiesel by supercritical transesterification:process design and economic feasibility*. 2005.
270. Shin, H.-Y., et al., *Thermal decomposition and stability of fatty acid methyl esters in supercritical methanol.* Journal of Analytical and Applied Pyrolysis, 2011. **92**(2): p. 332-338.
271. Quesada-Medina, J. and P. Olivares-Carrillo, *Evidence of thermal decomposition of fatty acid methyl esters during the synthesis of biodiesel with supercritical methanol.* The Journal of Supercritical Fluids, 2011. **56**(1): p. 56-63.